FABRIC TENSORS AND EFFECTIVE PROPERTIES OF GRANULAR MATERIALS WITH APPLICATION TO SNOW

by

Richard Hayden Shertzer

A dissertation submitted in partial fulfillment
of the requirements for the degree

of

Doctor of Philosophy

in

Engineering

MONTANA STATE UNIVERSITY
Bozeman, Montana

July 2011

© Copyright

by

Richard Hayden Shertzer

2011

All Rights Reserved

APPROVAL

of a dissertation submitted by

Richard Hayden Shertzer

This dissertation has been read by each member of the dissertation committee and has been found to be satisfactory regarding content, English usage, format, citations, bibliographic style, and consistency, and is ready for submission to The Graduate School.

Dr. Edward E. Adams

Approved for the Department of Civil Engineering

Dr. Brett W. Gunnink

Approved for The Graduate School

Dr. Carl A. Fox

STATEMENT OF PERMISSION TO USE

In presenting this dissertation in partial fulfillment of the requirements for a doctoral degree at Montana State University, I agree that the Library shall make it available to borrowers under rules of the Library. I further agree that copying of this dissertation is allowable only for scholarly purposes, consistent with "fair use" as prescribed in the U.S. Copyright Law. Requests for extensive copying or reproduction of this dissertation should be referred to ProQuest Information and Learning, 300 North Zeeb Road, Ann Arbor, Michigan 48106, to whom I have granted "the exclusive right to reproduce and distribute my dissertation in and from microform along with the non-exclusive right to reproduce and distribute my abstract in any format in whole or in part."

Richard Hayden Shertzer

July 2011

ACKNOWLEDGEMENTS

I have thoroughly enjoyed my tenure at Montana State University. This was primarily due to the research autonomy granted to me by my graduate committee. In particular I would like to thank Drs. Adams, Miller, McKittrick, and Edens for their advice and encouragement. I am also grateful to Dr. Schneebeli at the Swiss Federal Institute for Snow and Avalanche Research for providing the microstructural imagery used in this research. Additionally, I have benefited from enthusiastic research group members. Andrew Slaughter, Patrick Staron, and David Walters have participated in countless hours of interesting and valuable conversation with me regarding the fascinating subject of snow.

The unique laboratories at Montana State designed for cold regions study—the Subzero Science and Engineering Research Facility—were made possible by the National Science Foundation and M. J. Murdock Charitable Trust. My personal financial support was provided by the United States Air Force. As such I am required to include the following disclaimer: "the views expressed in this article are those of the author and do not reflect the official policy or position of the United States Air Force, Department of Defense, or the U.S. Government." I would like to express my gratitude for this unique career experience to my sponsoring agency and its head: Col. Yoder of the Department of Engineering Mechanics at the United States Air Force Academy.

I must also recognize the roles of my faith, friends, parents, and other extended family. The most dear to me are my wife and two young boys. Not only have they provided love and support, but they served as constant reminders of that which is truly important in life.

TABLE OF CONTENTS

1. INTRODUCTION AND BACKGROUND 1

1.1 Introduction 1
1.2 Micromechanics and Constitutive Modeling 4
1.2.1 Micromechanics 5
1.2.2 RVE Selection and Implications 7
1.2.3 Constitutive Modeling of Snow 8
1.2.3.1 Transport Models—Energy 13
1.2.3.2 Transport Models—Mass 15
1.2.3.3 Deformation Models 16
1.3 Research Framework and Objectives 18

2. MICROMECHANICS AND FABRIC TENSORS 20

2.1 Micromechanics 20
2.1.1 Homogenization Schemes 21
2.1.1.1 Periodic Media: Perturbation Theory 23
2.1.1.2 Randomly Distributed Media: Mean Field Theory 24
2.1.2 Localization Implications 27
2.1.3 Representation Theorems 29
2.1.4 Micromechanics Summary 32
2.2 Fabric Tensors 34
2.2.1 Directional Data 35
2.2.2 Tensors Derived from Granular Contacts 37
2.2.3 Symmetry of Directional Data and Principal Orientation 41
2.2.4 Decomposition and Interpretation 43
2.2.5 Tensors Derived from Mean Intercept Length 53
2.2.6 Tensors Derived from Void Parameters 57
2.3 Summary 58

3. EFFECTIVE PROPERTIES: ENERGY AND MASS TRANSPORT 60

3.1 Transport Properties 60
3.2 Mean Field Theory and Two-Constituent Microstructures 64
3.3 Thermal Conductivity 69
3.4 Diffusivity 78
3.5 Permeability 87
3.6 Summary 92

4. EFFECTIVE PROPERTIES: ELASTIC STIFFNESS 95

4.1 Elastic Stiffness Coefficients 95
4.1.1 Kinematic Localization: Voigt's Hypothesis 96

TABLE OF CONTENTS – CONTINUED

4.1.2 Static Averaging: Love Operation 97
4.1.3 Contact Law 99
4.1.3.1 Axial Stiffness 100
4.1.3.2 Shear Stiffness 103
4.1.4 Isotropic Elastic Stiffness Coefficients 104
4.2 Elastic Stiffness Coefficients: Anisotropy 106
4.3 Summary 111

5. EFFECTIVE PROPERTIES: COMPARISON TO EXISTING MODELS & DATA 113

5.1 Thermal Conductivity 113
5.2 Diffusivity 117
5.3 Permeability 122
5.4 Elastic Stiffness 128
5.4.1 Other Analytical Models 129
5.4.2 A Numerical Model and CT Data 132
5.5 Summary 139

6. EXPERIMENTS AND METHODS 141

6.1 Microstructural Experiments and Data 141
6.1.1 EHC: Effective Heat Conductivity 141
6.1.2 CT Images 142
6.1.3 Other Microstructural Data 142
6.1.4 Experimental Samples 144
6.1.5 Modeling Changes in EHC 145
6.2 Stereological Analysis 146
6.3 Conductivity Model Parameters 149
6.3.1 k: Grain Conductivity 149
6.3.2 $(1/f)\,\mathbf{F}$: Normalized Contact Tensor 150
6.3.2.1 2-D Directional Data and Tensors 150
6.3.2.2 3-D Tensor from 2-D Data 151
6.3.2.3 Experimental Considerations 155
6.3.3 ϕ: Solid Volume Fraction 160
6.3.4 $\hat{\rho}/\hat{R}$: Mean 3-D Bond and Grain Radii 160
6.3.5 $\mathcal{N}$: 3-D Coordination Number 161
6.4 Summary 162

TABLE OF CONTENTS – CONTINUED

7. RESULTS AND DISCUSSION 164

7.1 Sample 4 164
7.1.1 Scalar Conductivity Model Parameters 164
7.1.2 Contact Tensor: Center-to-Center Orientation 167
7.1.3 Contact Tensor: Skeleton Tangent Orientation 176
7.1.4 Discussion 178
7.2 Sample 6 182
7.2.1 Scalar Conductivity Model Parameters 182
7.2.2 Contact Tensor: Center-to-Center Orientation 182
7.2.3 Contact Tensor: Skeleton Tangent Orientation 186
7.2.4 Discussion 190
7.3 Summary 193

8. CONCLUSIONS AND RECOMMENDATIONS 195

8.1 Research Summary and Conclusions 195
8.2 Recommendations for Future Work 198

REFERENCES CITED 201

APPENDICES 213

APPENDIX A: Water Vapor Diffusion, Phase Change & Energy Flux 214
APPENDIX B: Notes on Other Elastic Stiffness Models 225
APPENDIX C: Example Stereological Output Tables 229
APPENDIX D: Calculating 3-D Tensor Coefficients from Orthogonal Planes 234
APPENDIX E: MATLAB Code 242

LIST OF TABLES

Table Page

2.1 Examples of common constitutive "laws" where a gradient and flux are linearly related through a coefficient of proportionality. 25

5.1 Parameter definitions used in calculating the density dependence of the scalar thermal conductivity models in Equations (5.1b) and (5.4). 116

6.1 Characteristics of the high density snow samples in Schneebeli and Sokratov (2004). 145

C.1 Stereology Data File 1: Bonds & Grains 231

C.2 Stereology Data File 2: 2-D Connectivity 232

C.3 Stereology Data File 3: Test Line and Intercept Data 233

LIST OF FIGURES

Figure Page

2.1 General scheme of homogenization theories. 22

2.2 The general homogenization scheme applied here to snow as a granular material. This algorithm highlights a localization assumption in scaling the kinematic variables from the macro to micro scale, a microscopic constitutive law, and an averaging operation in scaling the static variables from the micro to macro scale. 28

2.3 On the left, a lithograph plate from Gray's Anatomy of the anterior surface of the right femur. Modern images of the femoral head and femoral condyle microstructures are shown on the right. These images were produced with a scanning electron microscope and were taken from Gibson (1985)..... 31

2.4 A granular assembly with example directional quantities: $\bar{l}$, a unit vector along the major axis of a void cell ellipse; $\bar{m}$, a unit vector between centers of connected grains; and $\bar{n}$, a unit vector normal to a contact plane connecting grains. 35

2.5 An example of snow microstructure where the ice is identified by black pixels and the void space by white. 36

2.6 An example of two granular assemblies with N=8 contact normal vectors: (a) 2-D with half of the contact normal vectors ($\bar{n}^{\alpha}$) in the $\pm x_1$ direction and half in the $\pm x_2$ direction. (b) 3-D with all contact normal vectors oriented in the $\pm x_1$ direction. 40

2.7 An example granular assembly with four contact planes. This example capitalizes on the symmetry of the directional data, considering only four contact normal vectors rather than eight. All contact normal vectors are oriented 60° clockwise from the $+x_1$ direction..... 42

2.8 A regular empirical distribution density of $\bar{n}$ and the various functions to approximate $P(\bar{n})$ using a series solution comprised of Cartesian tensors. The empirical data were drawn from the example assembly in Figure 2.6a..... 48

2.9 Empirical distribution densities of $\bar{n}$ and the various functions to approximate $P(\bar{n})$ using a series solution comprised of Cartesian tensors. The empirical data in (a)–(c) were drawn from an isotropic population while the data in (d)–(f) were drawn from an anisotropic population. 50

LIST OF FIGURES – CONTINUED

Figure Page

2.10 An example image of an anisotropic microstructure with test line segments at two different orientations. The number of intersections with the solid constituent is labeled with the corresponding test line segment. The graphic was taken from SkyScan (2009). 54

3.1 An idealized granular assembly and associated quantities for calculating effective thermal conductivity, as applied in Equation 3.29. 73

3.2 Homogenization Scheme for Thermal Conductivity 75

3.3 A void cell with idealized grains and associated quantities for calculating apparent conductivity, as applied in Equation (3.47) 80

3.4 Time-lapse microscopic photography of the recrystallization of ice hemispheres subject to a 520 $^{\mathrm{K}}/_{\mathrm{m}}$ temperature gradient. These images are taken from Akitaya (1985), Figure 5. 82

3.5 Homogenization Scheme for Apparent Conductivity 85

3.6 Homogenization Scheme for Permeability 92

3.7 On the left is an idealized microstructure and directional data for a reference grain exchanging energy with three neighboring grains: with 1 and 2 via phase change/vapor diffusion and with 3 via conduction. The sketch on the right shows the simplified points on the surface of the reference grain where these exchanges occur. Also displayed are the microscopic heat (H) and mass (M) flows at these points that contribute to the macroscopic energy flux. 94

4.1 Undeformed contact geometry identifying the local Cartesian coordinates on the contact plane and the undeformed branch vector. 100

4.2 Contact geometry as a result of a hypothetical axial load. The schematic highlights the undeformed branch vector and the axial contact displacement. 102

4.3 Contact geometry as a result of a hypothetical shearing load. The schematic highlights the shearing strain and deformation. 103

4.4 Homogenization Scheme for Linear Elastic Stiffness 104

LIST OF FIGURES – CONTINUED

Figure Page

5.1 Density dependence of effective thermal conductivity comparing (a) the analytical approach of Batchelor and O'Brien (1977), and (b) the analytical approach of Adams and Sato (1993) to the empirical relation of Sturm *et al.* (1997). The dashed envelope represents the ±33% variation of $\hat{\rho}/\hat{R} = 0.15$ applied to the micromechanical models. 116

5.2 Evolution of density and MIL fabric tensor coefficients during temperature gradient experiment of Srivastava *et al.* (2010). The figures are reproduced from Figure 4a. and Figure 4d. in Srivastava *et al.* (2010). . 134

5.3 Normalized MIL fabric tensor coefficients. Each coefficient is normalized by the trace of the measured MIL fabric tensor coefficients in Figure 5.2b: $\mathrm{MIL}_1 + \mathrm{MIL}_2 + \mathrm{MIL}_3$ 135

5.4 Evolution of elastic stiffness coefficients during temperature gradient experiment of Srivastava *et al.* (2010). The moduli were numerically simulated with a finite element model. The figures are reproduced from Figure 5a. and Figure 5b. in Srivastava *et al.* (2010). 136

5.5 Evolution of stiffness coefficients predicted by Equation (5.18a) based on density and fabric changes with $\hat{\rho}/\hat{R} = 0.36$: this ratio was fixed to mimic the numerical results in Figure 5.4 on Day 0. 136

5.6 Evolution of stiffness coefficients predicted by Equation (5.18b) based on density and fabric changes. As above, $\hat{\rho}/\hat{R}$ was fixed at 0.36. 137

5.7 Evolution of stiffness coefficients predicted by Equation (5.18c) based on density and fabric changes. In this model there are no other microstructural variables. The empirically determined coefficients were taken from Srivastava *et al.* (2010), Table 4. They were determined as the best fit to the data in Figure 5.4. 137

6.1 Example of a grayscale reconstructed volume of high density snow (490 $\mathrm{kg/m^3}$) with reference axes. $+x_1$ is the direction of heat flow given the idealized applied unidirectional temperature gradient. The physical dimensions of the pictured volume are 5 x 5 x 4.85 mm^3. 143

6.2 A sample image processing chronology: (a) a binary microstructural image of snow where white pixels represent ice, (b) the skeletonization of (a), and (c) the final, segmented image where the lines overlaid on (a) represent the 2-D bonds. 147

LIST OF FIGURES – CONTINUED

Figure Page

6.3 Examples of 2-D images or slices extracted from the 3-D reconstructed volume. Ten slices at each planar orientation are used for stereological analysis. This figure uses the $x_1 - x_3$ plane to illustrate the sampling technique. 149

6.4 On the left, a 3-D bonded grain system with shaded circular bond and contact normal vector. An example of an $x_1 - x_3$ plane of section through the 3-D system is on the right. The 2-D image illustrates that planes of section through spherical grains and circular bonds are circles and lines, respectively. $\bar{n}^{(2\text{-D})}$ shares direction with the projection of $\bar{n}^{(3\text{-D})}$ onto the $x_1 - x_3$ plane. However, $\left|\bar{n}^{(2\text{-D})}\right|$ equals one whereas the magnitude of the projection of $\bar{n}^{(3\text{-D})}$ onto the $x_1 - x_3$ plane is less than one. 152

7.1 The scalar conductivity model parameters evaluated from sample 4 microstructural images. 165

7.2 The scalar conductivity model $k^* = k^*_{B\&O}$ based on stereologically determined parameters from sample 4 images compared to EHC derived from experimental data. 167

7.3 The 2-D contact tensor coefficients calculated from sample 4 images using grain center-to-grain center orientation as the source of directional data: (a) the diagonal components, and (b) the off-diagonal component of the three planar tensors. 168

7.4 The "fit" of the sample 4 planar contact tensors calculated from center-to-center data. The fit parameter is defined by Equation (6.9). 170

7.5 The 3-D contact tensor coefficients calculated from sample 4 images using grain center-to-grain center orientation as the source of directional data: (a) the diagonal components, and (b) the off-diagonal components. 171

7.6 DA from Schneebeli and Sokratov (2004) compared to the DA calculated from sample 4 center-to-center 3-D contact tensor coefficients. Hollow markers indicate that either F_{22} or F_{33} was the largest magnitude principal value. Solid markers indicate that F_{11} was the greatest principal value. 172

LIST OF FIGURES – CONTINUED

Figure Page

7.7 The modeled conductivity tensor $\mathbf{k}^*$ based on stereologically determined parameters from sample 4 images: (a) k_{11}^* component compared to EHC derived from experimental data, and (b) the diagonal/principal components. The contact tensor is calculated from center-to-center directional data. 173

7.8 The evolution in thermal conductivity for two different temperature gradient metamorphism experiments. The conductivity is measured by multiple heated probe instruments: (a) snow density of $130\,^{\mathrm{kg}}/_{\mathrm{m}^3}$ subject to $200\,^{\mathrm{K}}/_{\mathrm{m}}$ temperature gradient, (b) snow density of $240\,^{\mathrm{kg}}/_{\mathrm{m}^3}$ subject to a $100\,^{\mathrm{K}}/_{\mathrm{m}}$ temperature gradient. 175

7.9 The 2-D contact tensor coefficients calculated from sample 4 images using the tangent to the skeleton as the source of directional data: (a) the diagonal components, and (b) the off-diagonal component of the three planar tensors. 177

7.10 The "fit" of the sample 4 planar contact tensors calculated from skeleton tangent data. The fit parameter is defined by Equation(6.9). 178

7.11 The 3-D contact tensor coefficients calculated from sample 4 images using the tangent to the skeleton as the source of directional data: (a) the diagonal components, and (b) the off-diagonal components. 179

7.12 DA from Schneebeli and Sokratov (2004) compared to the DA calculated from sample 4 skeleton tangent 3-D contact tensor coefficients. Hollow markers indicate that either F_{22} or F_{33} was the largest magnitude principal value. Solid markers indicate that F_{11} was the greatest principal value. 180

7.13 The modeled conductivity tensor $\mathbf{k}^*$ based on stereologically determined parameters from sample 4 images: (a) k_{11}^* component compared to EHC derived from experimental data, and (b) the diagonal/principal components. The contact tensor is calculated from skeleton tangent directional data. 181

7.14 The scalar conductivity model parameters evaluated from sample 6 microstructural images. 183

7.15 The scalar conductivity model $k^* = k_{B\&O}^*$ based on stereologically determined parameters from sample 6 images compared to EHC derived from experimental data. 184

LIST OF FIGURES – CONTINUED

Figure Page

7.16 The 2-D contact tensor coefficients calculated from sample 6 images using grain center-to-grain center orientation as the source of directional data: (a) the diagonal components, and (b) the off-diagonal component of the three planar tensors. 185

7.17 The "fit" of the sample 6 planar contact tensors calculated from center-to-center data. The fit parameter is defined by Equation (6.9). 186

7.18 The 3-D contact tensor coefficients calculated from sample 6 images using grain center-to-grain center orientation as the source of directional data: (a) the diagonal components, and (b) the off-diagonal components.187

7.19 The modeled conductivity tensor $\mathbf{k}^*$ based on stereologically determined parameters from sample 6 images: (a) k_{11}^* component compared to EHC derived from experimental data, and (b) the diagonal/principal components. The contact tensor is calculated from center-to-center directional data. 188

7.20 The 2-D contact tensor coefficients calculated from sample 6 images using the tangent to the skeleton as the source of directional data: (a) the diagonal components, and (b) the off-diagonal component of the three planar tensors. 189

7.21 The "fit" of the sample 6 planar contact tensors calculated from skeleton tangent data. The fit parameter is defined by Equation(6.9). 190

7.22 The 3-D contact tensor coefficients calculated from sample 6 images using the tangent to the skeleton as the source of directional data: (a) the diagonal components, and (b) the off-diagonal components..... 191

7.23 The modeled conductivity tensor $\mathbf{k}^*$ based on stereologically determined parameters from sample 6 images: (a) k_{11}^* component compared to EHC derived from experimental data, and (b) the diagonal/principal components. The contact tensor is calculated from skeleton tangent directional data. 192

D.1 An example of a possible 3-D state of stress and the associated orthogonal planes in Cartesian coordinates. 238

LIST OF SYMBOLS

A	notation for a scalar
$\bar{A}$	notation for a vector with A_i Cartesian components
$\mathbf{A}$	notation for a 2^{nd} order tensor with A_{ij} Cartesian components
$\mathbb{A}$	notation for a 4^{th} order tensor with A_{ijkl} Cartesian components
∇	del operator
$\otimes$	dyadic product
$\langle\,\rangle$	volume average
:	scalar or double-dot product between two dyads
f, f_{vap}, f_{void}	isotropic value of proposed fabric tensors: $1/2$ in 2-D, $1/3$ in 3-D
h	center-to-center grain/particle spacing (pixels, mm)
k, $\mathbf{k}$	thermal conductivity ($^{\text{W}}/_{\text{m·K}}$)
k_n	microscopic axial contact stiffness ($^{\text{N}}/_{\text{m}}$)
k_s	microscopic shear contact stiffness ($^{\text{N}}/_{\text{m}}$)
p_{sat}	saturation pressure of water vapor (Pa)
p_{vap}	partial pressure of water vapor (Pa)
r	microscopic void channel radius (pixels, mm)
D, $\mathbf{D}$	diffusivity ($^{\text{m}^2}/_{\text{s}}$)
E	Young's modulus (Pa)
G	shear modulus/Lamé's second parameter (Pa)
H	microscopic heat flow ($^{\text{J}}/_{\text{s}}$)
I	number of intersections with test lines in MIL analysis
L_s	latent heat of H_20 sublimation ($^{\text{J}}/_{\text{kg}}$)
M	microscopic mass flow ($^{\text{kg}}/_{\text{s}}$)

LIST OF SYMBOLS – CONTINUED

P	total pressure (Pa)
$P(\bar{n})$	distribution density function of $\bar{n}$ $(-)$
Q	microscopic volume flow ($^{m^3}/_{s}$)
R	3-D grain/particle radius (pixels, mm)
$R_{(2\text{-D})}$	2-D grain/particle radius (pixels, mm)
R_{vap}	gas constant for water vapor ($^{J}/_{kg\cdot K}$)
R_{void}	3-D pore/void cell radius (pixels, mm)
V	volume of macroscopic/representative volume element (m^3)
$\mathcal{C}$	mean number of $\bar{n}_{void}$ per spherical pore/void cell $(-)$
$\mathcal{N}$	mean 3-D coordination number $(-)$
$\mathcal{N}_{(2\text{-D})}$	mean 2-D coordination number $(-)$
$\mathcal{Q}$	mean number of $\bar{n}_{cent}$ per spherical grain/particle $(-)$
$\bar{\mathrm{d}}$	Darcy flux/superficial velocity ($^{m}/_{s}$)
$\bar{f}$	general microscopic flux
$\bar{\mathrm{f}}$	microscopic contact force (N)
$\bar{g}$	general microscopic gradient
$\bar{n}$	unit vector normal to plane of granular contact
$\bar{n}_{cent}$	unit vector defining center-to-center intergranular direction
$\bar{n}_{void}$	unit vector defining void channel direction
$\bar{q}$	heat flux ($^{W}/_{m^2}$)
$\bar{q}_c$	heat flux due to conduction ($^{W}/_{m^2}$)
$\bar{q}_{vap}$	apparent heat flux due to vapor diffusion/phase change ($^{W}/_{m^2}$)
$\bar{u}$	average advective velocity ($^{m}/_{s}$)

LIST OF SYMBOLS – CONTINUED

$\bar{F}$	general macroscopic flux
$\bar{G}$	general macroscopic gradient
$\overline{J}$	mass or molar flux $\left({}^{\mathrm{kg}}/_{\mathrm{m}^2\cdot\mathrm{s}}\right)$ $\left({}^{\mathrm{mol}}/_{\mathrm{m}^2\cdot\mathrm{s}}\right)$
$\bar{L}$	branch vector (pixles, mm)
$\bar{R}$	general dipole strength of a pore/void cell
$\bar{S}$	general dipole strength of a grain/particle
$\mathbf{A}$	anisotropy tensor used in bone mechanics
$\mathbf{E}$	strain tensor $(-)$
$\mathbf{F}$	fabric tensor formed from $\bar{n}$ – the contact tensor $(-)$
$\mathbf{F_{vap}}$	fabric tensor formed from $\bar{n}_{cent}$ $(-)$
$\mathbf{F_{void}}$	fabric tensor formed from $\bar{n}_{void}$ $(-)$
$\mathbf{H}$	MIL fabric tensor (pixels, mm)
$\mathbf{K}$	general coefficient of proportionality/material parameter
$\mathbf{K}^*$	general effective coefficient of proportionality/effective material parameter
$\mathbf{L}$	orthogonal/transformation tensor $(-)$
$\mathbf{T}$	stress tensor (Pa)
$\mathbb{C}$	stiffness tensor (Pa)
γ_{ns}	microscopic shear strain component $(-)$
ϵ	porosity/void volume fraction $(-)$
ε_{nn}	microscopic axial strain component $(-)$
ζ	ratio of shear contact stiffness to axial contact siffness $(-)$
θ	absolute temperature (K)
κ, $\boldsymbol{\kappa}$	permeability (m^2)

LIST OF SYMBOLS – CONTINUED

λ	Lamé's first parameter (Pa)
μ	dynamic viscosity ($\mathrm{Pa} \cdot \mathrm{s}$)
ν	Poisson's ratio ($-$)
ϖ	tangent to the ice network skeleton at a bond site (deg)
ρ	3-D contact/bond radius (pixels, mm)
$\rho_{(2\text{-D})}$	2-D contact/bond radius (pixels, mm)
ρ_{vap}	water vapor density ($^{\mathrm{kg}}/_{\mathrm{m}^3}$)
ϱ	orientation of test lines in MIL analysis (rad, deg)
σ_{nn}	microscopic axial stress component (Pa)
τ_{ns}	microscopic shear stress component (Pa)
ϕ	solid volume fraction ($-$)
ψ	strain energy density ($^{\mathrm{J}}/_{\mathrm{m}^3} = \mathrm{Pa}$)
ω	orientation of 2-D bonds (deg)
Υ	tortuosity ($-$)
Φ	molar concentration ($^{\mathrm{mol}}/_{\mathrm{m}^3}$)
Ψ, Ψ_{ij}, Ψ_{ijkl}, etc.	coefficients of fabric tensors of the 3$^{\mathrm{rd}}$ kind from Kanatani (1984)
$\bar{\delta}$	microscopic contact displacement (pixels, mm)
$\boldsymbol{\delta}$	identity tensor ($-$)
CT	computed tomography
EHC	effective heat conductivity ($^{\mathrm{W}}/_{\mathrm{m}\cdot\mathrm{K}}$)
MIL	mean intercept length (pixels, mm)
pdf	probability density function
RVE	representative volume element

ABSTRACT

Granular materials—e.g., gravel, sand, snow, and metallic powders—are important to many engineering analysis and design problems. Such materials are not always randomly arranged, even in a natural environment. For example, applied strain can transform a randomly distributed assembly into a more regular arrangement. Deviations from random arrangements are described via material symmetry. A random collection exhibits textural isotropy whereas regular patterns are anisotropic. Among natural materials, snow is perhaps unique because thermal factors commonly induce microstructural changes, including material symmetry. This process—temperature gradient metamorphism—produces snow layers that can exhibit anisotropy.

To adequately describe the behavior of such layers, mathematical models must account for potential anisotropy. This feature is absent from models specifically developed for snow, and, in most granular models in general. Material symmetry is quantified with fabric tensors in the constitutive models proposed here. Fabric tensors statistically characterize directional features in the microstructure. For example, the collective orientation of intergranular bonds impacts processes like conduction and loading.

Anisotropic, microstructural models are analytically developed here for the conductivity, diffusivity, permeability, and stiffness of granular materials. The methodology utilizes homogenization—an algorithm linking microscopic and macroscopic scales. Idealized geometries and constitutive assumptions are also applied at the microscopic scale. Fabric tensors tying the granular arrangement to affected material properties are a natural analysis outcome.

The proposed conductivity model is compared to measured data. Dry dense snow underwent temperature gradient metamorphism in a lab. Both the measured heat transfer coefficient and a developing ice structure favored the direction of the applied gradient. Periodic tomography was used to calculate microstructural variables required by the conductivity model.

Through the fabric tensor, model evolution coincides with measured changes in the heat transfer coefficient. The model also predicts a different conductivity in directions orthogonal to the gradient due to developing anisotropy. Models that do not consider directional microstructural features cannot predict such behavior because they are strictly valid for isotropic materials. The conclusions are that anisotropy in snow can be significant, fabric tensors can characterize such symmetry, and constitutive models incorporating fabric tensors offer a more complete description of material behavior.

CHAPTER 1
INTRODUCTION AND BACKGROUND

1.1 Introduction

Snow mechanics research is relevant to a broad range of applications: analyzing avalanche risk and associated defenses, defining creep forces acting on alpine or arctic structures, understanding the contributions of seasonal and permanent snowfields to a global energy balance, and designing suitable roads and runways from snow for land and air mobility. Snow mechanics is defined in a recent U.S. Army Corps of Engineers Cold Regions Research & Engineering Laboratory (CRREL) report as "the theoretical and applied science of the mechanical behavior of snow; it is that branch of mechanics concerned with the response of snow to the force fields of its environment." (Shapiro *et al.*, 1997). And while the CRREL report focuses on the deformation and strength of snow, force fields are defined here more broadly—not only kinetic, but also thermodynamic, and even electromagnetic. The mechanical behavior of snow is taken to encompass its viscoelastic response to stresses, thermodynamic response to temperature gradients, optical response to electromagnetic radiation, and many others.

One focus area of the Subzero Science and Engineering Research Facility at Montana State University is snow mechanics. Specifically, many research projects relate to the genesis, mechanical behavior, and failure of weak layers that are known contributors to avalanches. Avalanches are costly and potentially deadly, affecting transportation, commerce and recreation in mountainous regions. For example, during the 2007-2008 winter the Colorado Department of Transportation triggered more than 500 avalanches and spent 8,406 man-hours on mitigation and cleanup efforts. Apart

from the direct costs of materiel and labor, roads were closed for a cumulative 47 days statewide as a result of avalanche mitigation and cleanup (CDOT, 2009). In terms of average annual U.S. fatalities over the thirty year period from 1979-2008, those killed by avalanches (20) are on the same order of magnitude as those killed by other natural hazards like lightning (58), tornadoes (57), earthquakes (5), floods (93) and hurricanes (48) (NWS, 2009; Vranes and Pielke Jr., 2009). It should also be noted that the gap is closing between avalanches and other natural hazards as average annual avalanche fatalities in the United States have nearly doubled since the beginning of that thirty year period and have increased fivefold since the 1950s (NWAC, 2009).

A fundamental area of ongoing snow mechanics research is developing constitutive models that capture the full range of snow's mechanical behavior. Constitutive equations are not derived from physical principles like the general balance laws of mass, momenta, energy, and entropy, but are instead mathematical models that have been validated against empirical data. In a material where the matter can be treated as a homogeneous, continuous mass, it is simplest to disregard atomic, molecular, or microstructural features and treat it as an idealized continuum. The power of this approach is that continuum mechanics is a well-established field of study dealing with the kinematics, kinetics, and general balance laws of mass, momenta, energy, and entropy. The material properties of a continuum are defined in constitutive equations that typically relate kinematic or primary field variables such as strain and temperature gradient to static or secondary field variables like stress and heat flux, respectively (Reddy, 2008).

For example, the familiar Fourier's model for heat conduction, $\bar{q} = \text{-}\mathbf{k} \cdot \nabla\theta$, relates the temperature gradient $\nabla\theta$ ($^{\text{K}}/_{\text{m}}$) and heat flux $\bar{q}$ ($^{\text{W}}/_{\text{m}^2}$). The material parameter—thermal conductivity $\mathbf{k}$ ($^{\text{W}}/_{\text{m}\cdot\text{K}}$)—is a coefficient of proportionality relating the field

variables of temperature and heat flow. There are internationally accepted testing standards for determining thermal conductivity (IEEE Std 442-1981, 1996; ASTM E1225-09, 2009), and for many materials one can simply consult reference tables to find the thermal conductivity of a material. Material parameters like thermal conductivity, diffusivity, and the elastic stiffness coefficients (e.g., the Lamé parameters for an isotropic material) are important in understanding snow's mechanical behavior because they are necessary components in constitutive models. The significance of material parameters depends upon both the process of interest and the choice of mathematical model.

Unfortunately, disregarding microstructure—the material arrangement at the microscopic level—and treating snow as a continuum is a tenuous assumption. In fact, understanding snow's microstructure is critically important because nearly all of snow's material properties are driven by microstructure (Brown *et al.*, 2001; Kachanov and Sevostianov, 2005). As an added complication, snow's microstructure changes over the course of hours, days, weeks, and months. Because snow naturally exists near its phase transition temperature, it is thermodynamically active and its microstructure is continuously changing through a process commonly called metamorphism. These changes, which can occur over time scales as short as an hour, are driven by a kinematic variable, the temperature gradient (McClung and Schaerer, 2006). In general, depending on the magnitude of the temperature gradient the snow will either coalesce into a strong, sintered material or develop weak layers that increase avalanche risk. In turn, the temperature field in the snowpack, and therefore the temperature gradient, is sensitive to variations in thermal conductivity (Slaughter and Adams, 2009). Understanding the coupled relationship between microstructure and thermal conductivity is critical in defining snowpack metamorphism.

At the other end of the time scale spectrum, creep strains affect snow's microstructure over the course of months or potentially years in the case of permanent snow fields. These changes are driven by a different kinematic variable, the strain rate. Whether the changes are thermally-induced, strain-induced, or a combination thereof, the resulting microstructure impacts snow's material properties. In addition to thermal conductivity, other material properties like diffusivity, important in mass and energy transport, and the elastic compliance coefficients, important to deformation analyses, are also affected.

1.2 Micromechanics and Constitutive Modeling

Constitutive models can be derived from a variety of approaches. As previously mentioned, continuum mechanics is a well-established branch of mechanics. Many fundamental constitutive relationships pertaining to both solids and fluids were analytically and/or empirically developed in the 19^{th} century (Reddy, 2008). For materials that can be idealized as a continuum, empirical test data validates the basic constitutive relationships, like Fourier's model above. Subsequently, references are now readily available listing the properties of many engineering materials. While these properties may vary with material density or temperature, the basic constitutive model accurately captures a broad range of behavior. Central to modeling a material as a continuum are the concepts of a representative volume element (RVE) and scale. For example, on large scales ($\geq 10^0 = 1\,\text{m}$)—the scales of the aforementioned pertinent snow mechanics problems—snow often appears to be a homogeneous, continuous mass. However, what appears to be homogeneous is actually a collection of different constituents: ice, air, water vapor, and perhaps liquid water. The problem is that the

properties that dictate the behavior of snow at larger scales are defined by elements at a much smaller scales.

The scale important to snow metamorphism, referred to as the microstructure, is not the atomic or molecular scale but the ice grain scale (Yosida, 1963; Kry, 1975b; Mellor, 1975). Microstructure is important to many other materials, from gravel to composites, and, the appropriate scales vary accordingly. For rocks or gravel, microstructure implies scales of 10^{0}–10^{-3} m whereas the microstructures of ceramics and composites indicate scales of $\leq 10^{-9}$ m (ASM Handbook, 1985). Snow falls in between; scales of 10^{-3}–10^{-6} m are appropriate. At these intermediate scales, between molecular and macroscopic, each microscopic constituent of snow can be independently treated as a continuum. The dilemma now is relating the scales of the applied problems and the microstructure; they differ by several orders of magnitude.

1.2.1 Micromechanics

One goal of granular micromechanics is to explain the observed macroscopic behavior—the equivalent continuum scale—from interactions at the grain scale of the discrete particles comprising the RVE—the microstructure scale. Defining the RVE is critical because its constitutive behavior is considered to be representative of the larger continuum. To give one example of micromechanical analysis, homogenization is a developed analytical approach often applied to granular assemblies (Cambou, 1998; Oda and Iwashita, 1999). Homogenization schemes require realistic modeling of kinematics and constitutive relations at the grain scale and analytical approximations to go between the grain and RVE scales. The approximations are reasonable so long as the requirements guiding RVE selection are satisfied, as discussed in the next section. In many homogenization algorithms, field variables at the RVE scale are defined as the volume averages of microscopic field variables. The observed relationship

between such averaged field variables defines effective material properties. And, in linking RVE behavior to the microscopic scale, homogenization schemes analytically define effective material properties in terms of microstructural parameters.

Alternatively, numerical approximations can also be used to relate grain scale kinematics and constitutive laws to the mechanical response of a larger RVE. The Discrete Element Method (DEM) is a common approach. The fundamental DEM algorithm was first proposed by Cundall and Strack (1979) and has been shown to be a mathematical extension of the Finite Element Method (FEM) (Williams *et al.*, 1985). Similar to the analytical homogenization technique, individual grains are assigned positions, initial rates, appropriate kinematic degrees of freedom and local constitutive laws governing their grain-to-grain force-displacement interactions. However, rather than applying analytical approximations to connect with the macro scale, the coupled interactions of hundreds or thousands of particles comprising an RVE are numerically solved. A variety of DEM algorithms are now available and, as with other numerical techniques, the DEM is much more accessible with advances in computing power. With the DEM, a collection of particles can be subjected to various boundary conditions and/or forcing functions and its response observed. This process defines the effective material properties of the equivalent continuum.

In summary, treating the material as a homogeneous continuum is the most common approach to constitutive modeling. However, for materials like snow where processes at the grain scale are critically important to macroscopic boundary value problems, micromechanical approaches may yield better results. Micromechanical approaches can be either analytical or numerical in nature—both use microstructural interactions to develop approximations of macroscopic behavior. The approach adopted here to the constitutive modeling of snow is the analytical technique of homogenization. The details of homogenization are outlined in the next chapter.

1.2.2 RVE Selection and Implications

The RVE is a critical component in micromechanical analysis because it links the aforementioned disparate scales. Think of the RVE as a sample from a larger body that, if tested, would exhibit thermo-mechanical behavior representative of the larger body. As a notation aside, RVE is also frequently termed the representative elementary volume. By either label, it is the smallest volume that shares bulk properties with the larger body and its behavior is therefore taken as representative of the larger body.

Selecting an RVE can be a significant process. For example, there are numerous scientific studies indicating that "larger bodies" of snow, like an entire slope, exhibit a great deal of spatial and temporal variability making it extremely difficult to identify a computationally manageable RVE (Birkeland *et al.*, 1995; Hendrikx *et al.*, 2009). For aperiodic or random microstructures, defining the RVE is a balance amongst several requirements: 1) the RVE should be statistically homogeneous, 2) boundary layer disturbances should be minimized, and 3) globally applied boundary conditions to the RVE should be realistic and representative of boundary conditions applied to the larger body.

The first requirement, statistical homogeneity, was defined by Hill (1963) in stating that the RVE should be structurally typical of the average microstructure within the larger, heterogeneous body. Hashin (1983) later added that the stress and strain fields in the RVE should be statistically homogeneous when homogeneous boundary conditions are applied to it. This condition is required except at boundary layers, which leads to the second requirement. Boundary layers necessarily exhibit different stress and strain fields in accordance with St. Venant's principle (Ugural and Fenster,

1995). While boundary layer disturbances are inevitable, the size of the RVE impacts the extent of their effect.

The preceding statements briefly address the first two factors in RVE selection. The last factor warrants a more involved explanation. The RVE should reflect the effective properties of the larger body from which it is selected. This is accomplished by applying boundary conditions to the RVE and solving a boundary value problem. The sticky wicket is that the applied boundary conditions cannot possibly represent all possible *in situ* boundary conditions to which the RVE would be subjected as part of the larger body (Hollister and Kikuehi, 1992). But, whereas the applied boundary conditions and *in situ* boundary conditions might differ, they can produce the same average fields in the RVE. Recall that in homogenization, it is the relationship between average field quantities in the RVE that defines effective properties. Thus, because of boundary condition assumptions, it is possible that the effective properties derived from homogenization differ from those of the larger continuum they are designed to represent. These points will be revisited in the next chapter when the mathematical details of homogenization are explained.

1.2.3 Constitutive Modeling of Snow

Reviews by de Quervain (1973) and Mellor (1975), and a later CRREL report (Shapiro *et al.*, 1997) serve as the foundation for this section. Hundreds of documents are referenced in these reviews. More recent micromechanical developments are also summarized here. To generalize, the rigorous study of snow mechanics began in the 1930s with Bader and other Swiss scientists. They were primarily interested in the fracture and failure of alpine snowfields. As scientific and national interests spread to the Arctic and Antarctic over the following decades, researchers also developed interest in the mechanics of snow in the context of problems involving man-made structures

and mobility. Initial experimental studies focused on defining material behavior—whether snow exhibits strain hardening or softening, whether strain rate is a function of applied stress, etc.—without proposing any particular constitutive model. Because test results in these early decades generally showed a combination of linear elastic and viscous responses, the most commonly adopted constitutive model through the 1970s was the four-parameter viscoelastic model, or Burgers model (Shapiro *et al.*, 1997).

The Burgers model is a rheological model that relates stress, strain, and their respective rates. Rheology is a branch of continuum mechanics developed to deal with materials that exhibit the properties of both a solid and fluid, in this case, elastic and viscous behavior. The Burgers model parameters represent material stiffnesses and viscosities and are derived from empirical data. Mellor (1975) reviews the Burgers model and some simpler rheological models, testing techniques, and resulting rheological parameters for snow. Shapiro *et al.* (1997) also reviews the Burgers model and related constitutive models. Unfortunately, this reasonable approach, where snow could ideally be treated as a homogeneous material and constitutive relationships would apply as in a continuum, failed to produce usable results. Rheological models were too limited in the range of problems to which they could be applied. Even when accounting for common factors like density and temperature, the scatter of empirical data in fitting the rheological parameters was too broad to be of much practical use. Still, not all interested parties have abandoned models treating snow as a homogeneous, viscoelastic material. Current efforts continue in search of useful parameters that would allow broad application of such continuum-based models (Lang and Harrison, 1995; Mishra and Mahajan, 2004; Navarre *et al.*, 2007). However, a competing approach revolving around deciphering the microstructure of snow emerged in the 1970s.

Snow "texture" was recognized as an important factor affecting the thermo-mechanical behavior of snow (Kry, 1975b; Gubler, 1978). For example, snow that has settled and sintered at nearly constant temperature consists of well-bonded, uniformly distributed, rounded grains (McClung and Schaerer, 2006). Conversely, a persistent crystal form like depth hoar is characterized by poorly-bonded, oriented, faceted grains (McClung and Schaerer, 2006). Two samples matching these descriptions could have the same density but vastly different material characteristics, contributing to the aforementioned scatter in empirical data. As a result, studies began in earnest focusing on measurable microstructural quantities and relating them to the kinematics, kinetics, and transport phenomena at the microscopic scale. Many mathematical models accounting for grain and bond size, shape, and distribution have been proposed to explain grain scale deformation and transport processes and all have their merits. While there is much in common between models there is no universally accepted set of microstructural variables and mathematical operations that lead to satisfactory constitutive explanations at the RVE scale. In part this is due to a lack of robust empirical data by which to judge the microstructural models.

The issues relating to microstructural variables and test data are addressed in the CRREL review (Shapiro *et al.*, 1997). The authors acknowledge that current continuum-based rheological models have a very limited usefulness. They hold optimism in micromechanical constitutive models but voice reservation based on the necessary image analysis required to characterize parameters at that scale. Not only is the image analysis "difficult and tedious" but they question whether it yields measurable parameters linked to the cause of mechanical behavior at the RVE scale. Instead, the authors suggest using index properties of snow as indicators or *correlation* factors. An index property might reliably predict the strength or stiffness of snow based on statistical trend analysis. But, a correlation does not imply causation.

Micromechanical approaches like homogenization seek instead to define those microstructural parameters that act as factors of *causality*. Broadly defined, causality is the study of events—the cause—and their consequences—the effect. When applied to constitutive modeling, causality sorts out variable dependence or independence and its subsequent effect on system dynamics (Karnopp *et al.*, 2000). In defining thermo-mechanical properties at the RVE scale, homogenization reveals macroscopic dependence on microstructural parameters. The primary objection of the CRREL review to such an approach relates to limitations in available image analysis techniques. However, in just the fourteen years since its publication there have been significant advances in both the hardware and software associated with microscopic image analysis (Edens, 1997; Coléou *et al.*, 2001; Lundy *et al.*, 2002; Pieritz *et al.*, 2004; Wang *et al.*, 2004; Cnudde *et al.*, 2006). In light of this fact, homogenization is applied in this research project to identify the pertinent microstructural features to a particular macroscopic constitutive relationship. Adequate algorithms already exist to identify microstructural quantities and better routines are always under development, especially once the required parameters are defined (Edens and Brown, 1995; Edens, 1997).

To illustrate, one example of a proposed index is snow hardness. Hardness is relatively easy to measure at the macroscopic scale in either the field or lab setting without requiring imagery and analysis of the microstructure. Hardness, as a measure of the connectivity or bonding in the microstructure, should correlate with stiffness and strength (Shapiro *et al.*, 1997). In contrast, coordination number is a microstructural variable that directly assesses connectivity. Coordination number is the number of bonds for a given grain and it is usually calculated as an average value within an RVE. In many analytical constitutive models, properties like conductivity and stiffness are functions of mean coordination number (Batchelor and O'Brien,

1977; Adams and Sato, 1993; Chang and Liao, 1994; Cambou *et al.*, 1995; Arons and Colbeck, 1998). Changes in mean coordination number, in concert with other appropriate microstructural variables, therefore cause changes in effective material properties. However, measuring mean coordination number requires high quality images of the microstructure and automated image analysis algorithms. This comparison of hardness and coordination number highlights the difference between correlation and causality and the proposed usage of macroscopic and microscopic measures. Although not adopted here, other research focuses on uncovering microstructural features that correlate well with thermo-mechanical properties (Agrawal and Mittal, 1995; Johnson and Schneebeli, 1999).

Regardless of if or how a classification system of micromechanical indices is established, Shapiro *et al.* (1997) propose snow mechanics research should "develop a comprehensive source of data on the mechanical properties of interest," initially through unconfined and confined uniaxial compression tests at various loading rates. In the fourteen years since the CRREL review, much analytical and numerical work has been devoted to microstructural measures and models of snow. Some empirical work usually accompanies new microstructural proposals, but experiments are limited and not devoted to building the aforementioned comprehensive data repository. The snow mechanics community has yet to agree upon a comprehensive set of microstructural parameters, and until a classification system exists empirical work will likely be limited. For review here, studies specifically developed for snow are divided into microstructural models tied to energy and mass transport and models associated with stress, strain, and strain rate. New constitutive models relating to these phenomena are developed in Chapters 3 and 4.

1.2.3.1 Transport Models—Energy: As previously mentioned, the effective thermal conductivity of a snowpack is a critical energy transport property tied to snowpack metamorphism. Several recent analytical efforts have established models relating snow microstructural parameters to macroscopic thermal conductivity (Adams and Sato, 1993; Arons and Colbeck, 1998; Satyawali and Singh, 2008). In addition to these snow-specific models, many general microstructural models can be found in the literature for discrete, granular materials (Batchelor and O'Brien, 1977; Jagota and Hui, 1990; Coelho *et al.*, 1997; Vargas and McCarthy, 2001). Each snow-specific model has its advantages and limitations.

The Adams and Sato (1993) model applies the analogy between electrical and thermal conduction through a parallel network of thermal resistors, each representing a different mechanism of energy transfer: one for conduction through the ice network, one for conduction through the air in the pore space, and one that accounts for energy transport due to vapor flux across the pore space. This model is particularly useful in its treatment of the vapor flux component, which can be a significant method of energy transfer but is often neglected. However, the Adams and Sato (1993) model is limited in that it assumes that ice grains in the RVE are uniform spherical particles in a regular packing, a known oversimplification of actual snow microstructure.

The Arons and Colbeck (1998) model also uses an electrical analogy to develop the effective thermal conductivity of the ice network. Advances in this work include the ability to incorporate distributions of grain size rather than using a mean value to represent all grains in an RVE. Additionally, it accounts for the possibility that the ice network is oriented with respect to the macroscopic temperature gradient through the t-factor. The t-factor is a weighted average of conductor elements (ice bonds) lying in a cross-section of the RVE that takes into account ice network orientation relative to the macroscopic temperature gradient. For simplicity, a regular packing of grains

is assumed in estimating the t-factor (simple cubic) in Arons and Colbeck (1998). Unfortunately, this yields a macroscopically isotropic ice structure, eliminating the dependence of conductivity on orientation. Ideally, the t-factor would be directly evaluated from the microstructure via image analysis techniques. The quantity is noteworthy because, among snow-specific analytical conductivity models, it is the only attempt to incorporate anisotropy of the microstructure. Acknowledged limitations in this model are the simplified estimates of the t-factor and that energy transfer via vapor flux is not addressed.

The most significant contribution of the Satyawali and Singh (2008) model is its incorporation of different grain shapes: spheres, cubes, or cylinders. Limitations include applying a constant value for the vapor diffusion component and assuming a regular cubic packing structure of grains.

In spite of these different approaches, several common microstructural quantities consistently appear. For example, the volume fraction of ice particles in the RVE reflects the importance of density and the connectivity of the ice network is usually quantified by the mean coordination number. Also, the ratio of bond radius to grain radius consistently appears, capturing the importance of constrictions in the ice network—bottlenecks in the transport of heat energy via conduction through the microstructure. As will be shown in Chapter 3, precisely these same quantities appear here in the derivation for thermal conductivity via homogenization. In summary, several scalar microstructural quantities prove to be important to heat transfer through the snowpack. Especially in light of continuing advances in microscopic image analysis, these quantities are—as Arons and Colbeck (1998) put it—"well-defined, physically meaningful, and, in principle, measurable."

1.2.3.2 Transport Models—Mass: Microstructural mass transport models in snow focus on vapor diffusion (Colbeck, 1993; Satyawali, 2000; Sokratov and Maeno, 2000). The difficulty of this problem in snow is compounded over that of other granular matter because snow is a multiphase material. Diffusion in many granular materials, for example gravel, is hampered by the grains that block clear paths of diffusion and restrict mass flux. In snow, as evidenced by crystal metamorphism, the grains actually participate in mass transport and do not simply serve as an impediment to diffusion. The initial model in Colbeck (1993), with some geometric assumptions, offers an analytical expression that reduces to dependence solely on the volume fraction of the pore space or porosity. With different assumptions, a derivative model shows diffusivity to vary with grain spacing rather than porosity. The Satyawali (2000) model is a hybrid analytical and empirical approach and the resulting expression is a function of porosity and an experimental constant. And, the Sokratov and Maeno (2000) model is an empirical function of porosity and microstructural indices used as experimental fit factors: tortuosity and the "gradient enhancement factor." Tortuosity is a quantification of the twisted, ill-defined diffusion path and the "gradient enhancement factor" accounts for diffusion enhancement in snow subjected to large temperature gradients.

Apart from porosity, the diffusion models do not agree on a common set of microstructural parameters. This is understandable in light of the analytical difficulties presented by diffusion through a multiphase, complex microstructure. Comparing the constitutive approaches of conduction and vapor diffusion is useful in highlighting the differences between analytical and empirical modeling. With conduction, the diffusion of heat energy through the ice network is adequately defined at the grain scale to establish reasonable assumptions that result in useful engineering approximations. However, the diffusion of water vapor between the ice network and the pore space is

such an ill-defined process at the microstructural scale that it is difficult to identify and justify simplifying assumptions. As a result, many constitutive explanations rely instead on correlations and empirical fit factors.

1.2.3.3 Deformation Models: In theory, the microstructural features that govern conduction through the ice network are often identical to those that govern deformation (Gibiansky and Torquato, 1993; Kachanov and Sevostianov, 2005; Sevostianov and Kachanov, 2008). For example, the density, connectivity, and constrictions that regulate heat flux via conduction also determine the load paths in the microstructure and the subsequent stress-strain behavior of the RVE. The first quantitative incorporation of microstructure into stress-strain relations was accomplished by Kry (1975b) where he defined chains of connected grains as the basic unit of snow structure. The review here covers analytical models that link ice network parameters at the microscopic level to the macroscopic mechanical properties of snow. Important micromechanical constitutive work since Kry's initial effort has been accomplished by Hansen and Brown (1988); Mahajan and Brown (1993); Bartelt and von Moos (2000); Nicot (2004).

Hansen and Brown (1988) introduce a micromechanical theory that treats snow as a continuum. Microstructure is incorporated by assuming the macroscopic stress, strain, and strain rate depend on a set of state variables defined at the grain scale. As will be described in Chapter 2, this approach is similar to that employed via representation theorems. Although the selection of state variables is somewhat arbitrary, the theory is significant in offering a means to link grain and bond parameters to the macroscopic properties of snow.

Mahajan and Brown (1993) offer a different model based on grains, bonds, and virtual work. The principle of virtual work is often applied to systems of interconnected bodies as it offers a way to link forces between grains to the macroscopic stress. By using virtual work, Mahajan and Brown (1993) derive important microstructural parameters rather than assume them, as was done in Hansen and Brown (1988). Mahajan and Brown (1993) also consider several deformation mechanisms at the grain scale: 1) axial straining in the bonds, 2) shear straining in the bonds, 3) superplastic straining in the bonds, and 4) intergranular slip following bond fracture. The dominant deformation mechanism depends upon the given load conditions. Local deformation mechanisms are critical to micromechanical modeling, especially in an active microstructure where bonds can deform, fracture, reorganize, and/or re-form. The Mahajan and Brown (1993) model is comprehensive but "cumbersome to implement" and has never been rigorously verified across a broad range of applied strains and strain rates.

Bartelt and von Moos (2000) apply a simplified version of the Mahajan and Brown (1993) theory by only considering the inelastic deformation mechanisms of axial and shear straining in the bonds. Their tests confirm that these dislocation strains are the dominant deformation mechanisms at relatively low strain rates (10^{-5}–10^{-7} $^{1}/_{s}$). The work of Mahajan and Brown (1993) and Bartelt and von Moos (2000), while not limited to, primarily focuses on the viscous behavior of snow. Furthermore, neither consider the directional arrangement of grains to be a critical factor; they assume the grains are randomly arranged. This assumption is offered because only medium- to high-density snow is considered. In such snow the thought is that the connectivity of grains should dominate over the effect of directional arrangement (Mahajan and Brown, 1993).

Conversely, Nicot (2004) considers the elastic, brittle behavior of low-density snow. This model also recognizes the strain-rate dependence of ice and snow, and, by only accommodating quasi-static elastic response, is limited in applicability to sufficiently large local strain rates ($\geq 10^{-3}$ $^1/_s$) (Bartelt and Christen, 1999; Bartelt and von Moos, 2000). Additionally, this theory considers only axial deformation in the bonds, neglecting shear strength as negligible in low-density snow. The model does consider directional arrangement in its development through distribution functions of bond orientation. However, in a brief comparison to previously assembled data no attempt was made to estimate these distribution functions. Instead, as is typical, an isotropic arrangement of grains was assumed so that the distribution functions simplify to a constant scalar.

1.3 Research Framework and Objectives

This project focuses on an analytical approach to micromechanics. It fits into the context of mathematically linking microstructural features to the observable macroscopic material behavior of snow. As reviewed above, much fundamental work has been done relating grain scale relations to overall heat and mass transfer and deformation behavior. However, almost invariably the models rely on an idealized microstructure of uniformly or randomly packed grains. While this may be appropriate in some cases, it is well-established that other morphologies—particularly those driven by temperature gradient metamorphism—exhibit a distinct orientation (Sturm and Johnson, 1992; Sturm *et al.*, 1997; McClung and Schaerer, 2006). The primary objective here is to quantify the thermally-induced change in the microstructure of snow and model its impact on effective material properties. Empirical evidence suggests that even current microstructural models do not accurately predict the effective prop-

erties of snow because they do not account for directional arrangement (Schneebeli and Sokratov, 2004; Satyawali *et al.*, 2008).

The purpose here is not to choose a champion among existing micromechanical models. Instead, this project intends to augment previous efforts by incorporating fabric tensors—quantities describing the directional arrangement of the microstructure—into constitutive models describing the effective material properties of a granular material. Fabric tensors account for microstructural departures from randomly distributed grains, an expected result of temperature gradient metamorphism. Expressions for important material properties like conductivity, diffusivity, and stiffness are analytically developed to incorporate fabric tensors in the subsequent chapters. In evaluating these expressions, microstructural quantities are identified using X-ray micro-tomography. The proposed material property models are compared to other models and measured values. Fabric tensors capture the directionally-dependent arrangement of the microstructure caused by temperature gradient metamorphism, a feature missing in current models.

CHAPTER 2
MICROMECHANICS AND FABRIC TENSORS

2.1 Micromechanics

Micromechanics offers an alternative to rheological modeling for materials comprised of heterogeneous constituents. A common example of a material with well-developed micromechanical relationships is a fiber-reinforced composite. In the case of a composite, the overall behavior of a lamina is governed by the contributions from both the fibers and the matrix material. The *rule of mixture* quantifies these contributions, for example, as

$$E_1 = E_f\phi + E_m(1-\phi), \tag{2.1}$$

where E_1 is the stiffness of the composite lamina in the longitudinal direction, E_f is the stiffness of the fibers (aligned in the longitudinal direction), E_m is the stiffness of the matrix and ϕ is the volume fraction of the fibers comprising the lamina (Mallick, 1993). This well-established approximation is a simple example of how an effective property (E_1) of a heterogeneous material can be analytically estimated by the properties of its constituents (E_f and E_m) and some knowledge of their apportionment (ϕ). There are a myriad of analytical approaches to micromechanics, too many to cover in detail here. The purpose of this chapter is to introduce and broadly define a few existing micromechanical quantities and methods applicable to granular media. In Chapters 3 and 4 these quantities and methods are applied to snow, resulting in general, anisotropic constitutive relationships in terms of pertinent microstructural variables.

Two general methods are illustrated in the following sections: homogenization and representation theorems. In each case the primary goal is to accurately link the microscopic and macroscopic scales. A fundamental result of this goal is defining the effective properties of the heterogeneous material in terms of measurable features of its microstructure.

2.1.1 Homogenization Schemes

A graphical representation of the general homogenization theory, concisely presented in Emeriault and Cambou (1996); Cambou (1998); Oda and Iwashita (1999), is displayed in Figure 2.1. The term homogenization seems to have been coined by Suquet (1987) as the process used to define effective material properties at the RVE scale. This overarching goal is represented by the dashed line in Figure 2.1—those constitutive relationships relating field variables at the global or macroscopic level. Homogenization techniques were initially developed for spatially periodic microstructures, like the aforementioned fiber-reinforced composite, but have been extended for randomly distributed media like granular materials (Eshelby, 1957; Christoffersen *et al.*, 1981; Cambou *et al.*, 1995; Emeriault and Cambou, 1996; Yi *et al.*, 1998; Oda and Iwashita, 1999; Kruyt and Rothenburg, 2004).

The macroscopic field variables labeled here are generic vectors $\bar{F}$ and $\bar{G}$ and their microscopic counterparts are $\bar{f}$ and $\bar{g}$. For example, in the realm of transport phenomenon $\bar{G}$ and $\bar{g}$ represent forcing gradients—temperature, concentration, pressure, etc.—while $\bar{F}$ and $\bar{f}$ are the resulting fluxes—heat, mass, volume, etc. However, the general construct is not confined to heat and mass transfer constitutive models (Nemat-Nasser and Hori, 1999). Many homogenization schemes focus on the fundamental linear elastic stress-strain relationship (Emeriault and Cambou, 1996; Cambou, 1998; Oda and Iwashita, 1999). It should be noted that in this case the

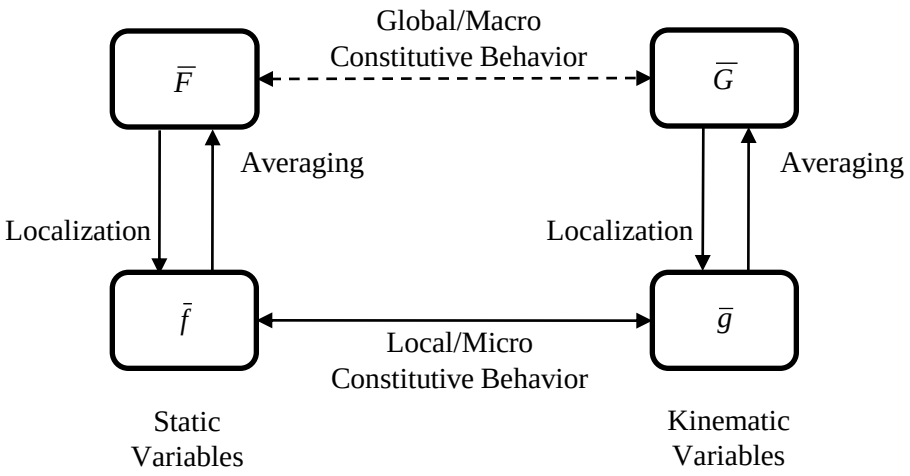


Figure 2.1: General scheme of homogenization theories.

macroscopic field variables, stress and strain, are not vector quantities but second order tensors.

Homogenization algorithms require two essential elements: 1) kinematic and constitutive assumptions at the microscopic scale, and 2) mathematical operations to relate the microscopic and macroscopic scales. In general, the notation of Emeriault and Cambou (1996); Cambou (1998) and Oda and Iwashita (1999) is used here because these references apply homogenization to granular materials rather than periodic microstructures. Consequently, their techniques are most appropriate to snow.

An additional notation point is deemed necessary here. Granular mechanists usually define the microscopic to macroscopic operation as averaging, reserving homogenization to refer to the entire process in Figure 2.1 (Emeriault and Cambou, 1996; Cambou, 1998; Oda and Iwashita, 1999). However, others refer to the averaging operation itself as homogenization (Hornung, 1997; Yi *et al.*, 1998; Hori and Nemat-Nasser, 1999; Nemat-Nasser and Hori, 1999). This is confusing when reading the body of available literature because the reader is left to consider whether homog-

enization refers to the entire algorithm or just one operation within that algorithm. The seeming discrepancy is addressed in the sections that immediately follow.

2.1.1.1 Periodic Media: Perturbation Theory: In a heterogeneous material, field quantities such as displacement, temperature, and pressure and resulting quantities such as stress, heat flux, and mass flux vary on the microscopic scale. Homogenization theory for materials with periodic microstructures, and therefore well-defined microscopic variations in field quantities, developed from studies of partial differential equations with rapidly varying coefficients (Hollister and Kikuehi, 1992; Hori and Nemat-Nasser, 1999). Relating this statement to mechanics, the partial differential equations are the general field equations in the RVE boundary value problem and the varying coefficients represent microscopic perturbations in the field quantities. Hollister and Kikuehi (1992) and Hornung (1997) offer excellent explanations and examples of this mathematical theory. In practice, this method is most frequently applied to microstructures like fiber-reinforced composites or polymers.

As mentioned in Chapter 1, the selection of the RVE is a critical concept. For periodic microstructures the natural choice is the smallest repeating unit. Because of the periodicity assumption the boundary conditions and boundary value problem are well-posed and the resulting effective properties are independent of the RVE size (Yi *et al.*, 1998; Oda and Iwashita, 1999). This is an important point and a feature from which randomly distributed microstructures do not benefit, as will be discussed in greater detail below.

To emphasize the notation, scientists and engineers who develop and apply microstructural theories for periodic microstructures usually refer to the scaling up from a periodic microstructure to the larger body as homogenization or a multi-

scale approach—what Figure 2.1 labels averaging. The lack of distinction between averaging and localization operations is again a result of the periodicity. Assumptions about the microstructural period imply that scaling down from the macro to micro level is also well-posed, rendering separate localization operations unnecessary.

2.1.1.2 Randomly Distributed Media: Mean Field Theory: In a randomly distributed heterogeneous material the fluctuations in microscopic field quantities are, in general, unknown and not necessarily well-behaved. Mean field theory establishes volume averaging methods that, when appropriately applied to such microscopic fields, yield the corresponding macroscopic fields.

Many mathematical models and a wealth of empirical evidence show that a forcing gradient $\bar{G}$ is linearly related to a resulting flux $\bar{F}$ via a coefficient of proportionality $\mathbf{K}$ as

$$\bar{F} = \text{-}\mathbf{K} \cdot \bar{G}. \tag{2.2}$$

The phenomena is so pervasive that equations relating gradients and their associated fluxes are dubbed "laws" even though they are ultimately empirical expressions and not based on general balance laws such as conservation of mass and energy. A few of these constitutive laws are listed in Table 2.1. In the cases cited in Table 2.1, $\mathbf{K}$ is in general a second order tensor because the gradient and flux are vector quantities. In the special case of homogeneous isotropic materials the coefficient $\mathbf{K}$ simplifies to a scalar value due to the material symmetry.

The form of Equation (2.2) can apply to higher order problems. For example, consider the problem of a Hookean solid in which stress is linearly related to strain through material stiffness coefficients. Stress and strain are second order tensors so the stiffness tensor is in general a fourth order tensor. The negative sign in Equation

Table 2.1: Examples of common constitutive "laws" where a gradient and flux are linearly related through a coefficient of proportionality.

Law	$\bar{G}$	$\bar{F}$	$\mathbf{K}$
Fourier's law	temperature gradient	heat (energy) flux	thermal conductivity
Ohm's law	voltage gradient	current flux	electrical resistivity
Fick's 1st law	concentration gradient	molar flux	diffusivity

(2.2) is another reminder of the empirical nature of such mathematical models. In Fourier's and Fick's laws the negative sign ensures compatibility with the 2nd law of thermodynamics. It is not present in Ohm's and Hooke's laws. The negative sign is presented here as part of the general case, but it is one aspect of Equation (2.2) that is specific to the constitutive model in question.

Many materials are neither homogeneous nor isotropic. The aforementioned microscopic fluctuations in gradients and fluxes are a consequence of microscopically heterogeneous materials. However, in a statistically homogeneous sample of such a material, the observable gradients and fluxes at the macroscopic level—$\bar{F}$ and $\bar{G}$—can be defined as the mean of the microscopic field variables—$\bar{f}$ and $\bar{g}$:

$$\bar{F} = \left\langle \bar{f} \right\rangle = \frac{1}{V} \int \bar{f} dV \qquad \bar{G} = \left\langle \bar{g} \right\rangle = \frac{1}{V} \int \bar{g} dV. \tag{2.3}$$

The angle brackets in Equation (2.3) indicate the volume average of the microscopic variables. Equation (2.3) defines the averaging processes in Figure 2.1. Now, the link between the volume averaged microscopic variables is $\mathbf{K}^*$:

$$\left\langle \bar{f} \right\rangle = \text{-}\mathbf{K}^* \cdot \left\langle \bar{g} \right\rangle . \tag{2.4}$$

The coefficient of proportionality here is marked with an asterisk to distinguish it as an effective material property. Referencing again Figure 2.1, determining $\mathbf{K}^*$ is the

overarching goal as it establishes the constitutive relationship of the heterogeneous material at the macroscopic level.

Mean field theory is sufficiently developed to be considered a classical theory in micromechanical analysis of granular materials (Eshelby, 1957; Hill, 1963; Nemat-Nasser and Hori, 1999; Oda and Iwashita, 1999). Assuming a representative macroscopic sample, volume averaging operations ensure the effective material property is consistent with experimental measurements (Nemat-Nasser and Hori, 1999). However, the accuracy of predicted effective material properties is sensitive to the RVE size, not just the averaging operations (Hill, 1963). This point will be discussed in greater detail below. Fundamentally, mean field theory executes the micro to macro transition by smoothing over microscopic field variations via operations like Equation (2.3) (Hornung, 1997). These averaging operations in Figure 2.1 define $\bar{F}$ from $\bar{f}$ and $\bar{G}$ from $\bar{g}$. Local constitutive relationships applied to the various microscopic elements define $\bar{f}$ from $\bar{g}$ (and *vice versa* in most instances), but a localization operation is required to ultimately link the macroscopic level *through* the microscopic level.

While required, localization operations are ill-defined in a randomly distributed media, unlike in a periodic microstructure. Microscopic field quantities cannot be explicitly defined with knowledge only of their volume average; some knowledge of the local variation or distribution is also required. This is a central difficulty with homogenization schemes applied to randomly distributed media (Oda and Iwashita, 1999; Cambou and Dubujet, 2001). As a consequence, localization operations are based on reasonable engineering approximations and assumptions. Much work in granular homogenization is related to developing accurate analytical localization operations (Chang and Liao, 1994; Cambou *et al.*, 1995; Emeriault and Cambou, 1996; Liao *et al.*, 1997; Chang and Hicher, 2005; Rahmoun *et al.*, 2009).

2.1.2 Localization Implications

As mentioned above, RVE selection for periodic microstructures is straightforward and the transition from macro to micro scales is well-defined due to microstructural periodicity. In granular assemblies this is not the case; there is no fundamental repeating unit on which to draw. In homogenization for a randomly distributed medium, some assumption is required in relating the microscopic and RVE scales.

The Voigt approximation (Voigt, 1889) for a heterogeneous material illustrates this through a uniform strain increment as the globally applied boundary condition. The effective stiffness in the RVE under these conditions is greater than the actual stiffness of the larger body due to the principle of minimum strain energy. If applied *in situ*, the RVE would minimize its strain energy when subject to a macroscopic strain field, but the assumption of a mean displacement field in the RVE, while mathematically admissible, produces greater energy. To generate this greater amount of energy, the average stress field in the RVE must be greater than in the larger body, resulting in an overestimate of the stiffness. Conversely, the Reuss approximation (Reuss, 1929) underestimates the actual stiffness by assuming uniform tractions within the RVE. In this case, the RVE would minimize its complementary energy when subject to a macroscopic stress field, but the assumed mean field of tractions, while admissible, produces greater energy. To generate this energy, the average strain field in the RVE must be greater than in the larger body, resulting in an overestimate of the compliance or an underestimate of the stiffness (Hollister and Kikuehi, 1992).

In summary, the accuracy of homogenization analysis for random microstructures can be significantly affected by the RVE size. For example, a relatively large RVE is probably a statistical representative of the whole and boundary layer effects are minimal. But, in a large RVE the discrepancy is potentially great between an as-

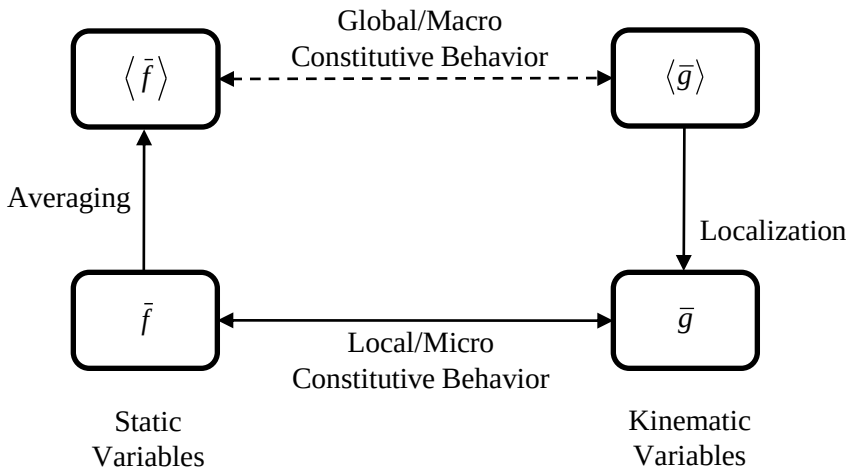


Figure 2.2: The general homogenization scheme applied here to snow as a granular material. This algorithm highlights a localization assumption in scaling the kinematic variables from the macro to micro scale, a microscopic constitutive law, and an averaging operation in scaling the static variables from the micro to macro scale.

sumed mean field in the RVE and the actual field in the larger body it is intended to represent. Shrinking the RVE improves this fit, but at the cost of more significant boundary layer disturbances and lack of statistical homogeneity. Therefore, the effective properties that result from micromechanical analyses are dependent on both RVE size and boundary condition assumptions.

In homogenization schemes applied to randomly distributed media, the latter point manifests itself in different proposed localization rules. The localization assumption consistently applied here is a Voigt-style assumption as described above. It is mathematically defined in Chapter 3. For consistency, in all the constitutive models considered here the localization approximation is applied to the primary, kinematic field variables rather than the secondary, static field variables, as pictured in Figure 2.2. This figure also reflects that in this research the macroscopic static variable is taken as the volume average of its microscopic counterparts.

2.1.3 Representation Theorems

Representation theorems are mathematical theorems that relate scalar, vector, and tensor quantities to isotropic functions. Isotropic functions play an important role in mechanics. Truesdell (1966) opens his book with two pervasive isotropic relations in mechanics, namely, generalized Hooke's law for isotropic elastic solids and its corollary for isotropic Newtonian fluids. Isotropic functions may be scalar-valued, vector-valued, or tensor-valued. The mathematical definition of an isotropic function pertains to how it transforms between orthogonal coordinate systems. The transformation is carried out by an orthogonal tensor $\mathbf{L}$. Orthogonal tensors satisfy the property

$$\mathbf{L}^{-1} = \mathbf{L}^{\mathrm{T}} \qquad \text{or} \qquad \mathbf{L}\mathbf{L}^{\mathrm{T}} = \boldsymbol{\delta}, \tag{2.5}$$

where $\boldsymbol{\delta}$ is the 2nd order identity tensor (Reddy, 2008). Orthogonal tensors are often equated with "transformation matrices" where the components of $\mathbf{L}$ are the direction cosines between a reference and alternate Cartesian coordinate system (Ugural and Fenster, 1995; Shames and Cozzarelli, 1997; Reddy, 2008). They are commonly introduced in transforming a 2nd order tensor like stress $\mathbf{T}$ to a principal orientation $\mathbf{T}'$ as

$$\mathbf{T}' = \mathbf{L}\mathbf{T}\mathbf{L}^{\mathrm{T}}. \tag{2.6}$$

The stress tensor would be labeled isotropic if $\mathbf{T}' = \mathbf{T}$. That is, $\mathbf{T}$ is isotropic if, for any orthogonal tensor $\mathbf{L}$, the result of the transformation is identical to the original tensor. Another way of describing this is that any orientation is a principal orientation.

Isotropic functions exhibit a similar property. For example, consider a scalar-valued function like a strain energy density function ψ. This is a useful function in

mechanics because the stress-strain constitutive law for a hyperelastic material can be derived from ψ (Shames and Cozzarelli, 1997). Textbooks on continuum mechanics and elasticity review this derivation (Reddy, 2008). The customary approach is to treat the strain energy density as a function of the strain tensor, $\psi = \psi(\mathbf{E})$. ψ is an isotropic function, or an invariant, if it satisfies the condition

$$\psi(\mathbf{E}) = \mathbf{L}\psi(\mathbf{E})\mathbf{L}^{\mathrm{T}} = \psi\left(\mathbf{L}\mathbf{E}\mathbf{L}^{\mathrm{T}}\right), \tag{2.7}$$

for all orthogonal tensors $\mathbf{L}$ (Wang, 1970; Boelher, 1987; Zysset and Curnier, 1995). Similar expressions for vector-valued and tensor-valued isotropic functions also exist (Wang, 1970; Cowin, 1985; Boelher, 1987).

Just as the functions can be scalar-, vector-, or tensor-valued, the arguments to the functions might be scalar, vector, and/or tensor quantities. For example, if the linear elastic behavior of a material is known through experimentation to vary with temperature θ, it is then presumed that its strain energy density is a function of both the strain tensor and temperature field as $\psi = \psi(\mathbf{E}, \theta) = \psi\left(\mathbf{L}\mathbf{E}\mathbf{L}^{\mathrm{T}}, \theta\right)$. Representation theorems create a straightforward mathematical framework for describing an isotropic function in terms of invariants of the arguments (Wang, 1970; Betten, 1986; Boelher, 1987; Betten, 2001). In this case of $\psi(\mathbf{E}, \theta)$, the result is a function of θ and the invariants of $\mathbf{E}$. Then, to derive the stress tensor, the partial derivative of this expression is taken with respect to the strain tensor.

Bone mechanics is a research field in which constitutive behavior through representation theorems is rigorously pursued. Trabecular or cancellous bone is a material whose microstructure plays a large role in governing its elastic stiffness. As it develops, trabecular bone tissue orients in the directions of applied stresses according to Wolff's law (Whitehouse, 1974; Cowin, 1986). Consider the femur as an example,

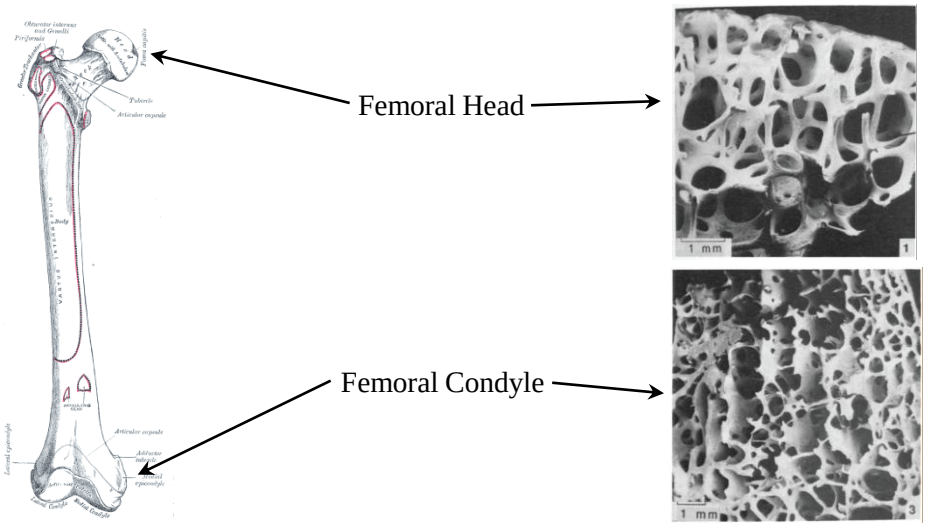


Figure 2.3: On the left, a lithograph plate from Gray's Anatomy of the anterior surface of the right femur. Modern images of the femoral head and femoral condyle microstructures are shown on the right. These images were produced with a scanning electron microscope and were taken from Gibson (1985).

pictured in Figure 2.3. In the femoral head at the hip socket, the principal stresses are practically equal and the bone tissue is distributed uniformly. Conversely, in the femoral condyle at the knee joint, the principal stresses are practically unidirectional and the bone tends to form parallel plates in the direction of the primary loading (Gibson and Ashby, 1999).

As a porous, potentially anisotropic material, biomedical engineers have presumed that solid volume fraction, ϕ, and a tensor characterizing the bone's anisotropy, $\mathbf{A}$, are the most significant microstructural variables affecting the elastic stiffness of bone (Cowin, 1985; Turner and Cowin, 1987; Turner *et al.*, 1990; Kabel *et al.*, 1999). Rather than defining stress as a function solely of strain, representation theorems provide a means to define stress as a function of strain, solid volume fraction, and anisotropy. Thus, stress is presumed a tensor-valued isotropic function of a scalar variable, ϕ, and two symmetric 2^{nd} order tensors, $\mathbf{E}$ and $\mathbf{A}$.

Cowin (1985) used the definition of isotropic functions and applied the representation theorems of Wang (1970) in defining the linear elastic stiffness coefficients in exactly this manner:

$$\begin{aligned} C_{ijkl} = {} & a_1\delta_{ij}\delta_{kl} + a_2\left(A_{ij}\delta_{kl} + \delta_{ij}A_{kl}\right) + a_3\left(\delta_{ij}A_{kq}A_{ql} + \delta_{kl}A_{iq}A_{qj}\right) \\ & + b_1A_{ij}A_{kl} + b_2\left(A_{ij}A_{kq}A_{ql} + A_{is}A_{sj}A_{kl}\right) + b_3A_{is}A_{sj}A_{kq}A_{ql} \\ & + c_1\left(\delta_{ki}\delta_{lj} + \delta_{li}\delta_{kj}\right) + c_2\left(A_{ik}\delta_{lj} + A_{kj}\delta_{li} + A_{il}\delta_{kj} + A_{lj}\delta_{ki}\right) \\ & + c_3\left(A_{ir}A_{rk}\delta_{lj} + A_{kr}A_{rj}\delta_{li} + A_{ir}A_{rl}\delta_{kj} + A_{lr}A_{rj}\delta_{ik}\right), \end{aligned} \tag{2.8}$$

where δ_{ij} are the 2^{nd} order identity tensor coefficients and a_1, a_2, a_3, b_1, b_2, b_3, c_1, c_2 and c_3 are scalar-valued isotropic functions of ϕ and the three invariants of $\mathbf{A}$. Customarily, the a_i, b_i and c_i must be experimentally determined. While Equation (2.8) is an analytical result of representation theorems, the overall approach is semi-empirical in practice due to the number of unknown coefficients that are fit to experimental data.

2.1.4 Micromechanics Summary

A few constitutive modeling approaches that incorporate relevant features of a microstructure have been introduced and defined. These are not the only micromechanical methods, but they are well-developed techniques that are explained here to illustrate the basic problem of relating micro and macro scales. Principles of homogenization for granular materials are used in Chapters 3 and 4 to develop effective material properties in terms of microstructural variables.

One alternative, the perturbation theory, is presented here first to serve as a cautionary note when using the term homogenization. Because perturbation theory is primarily intended for periodic microstructures it is not best suited for granular

materials. However, related approaches have been successfully applied to materials that lack periodicity (Mori and Tanaka, 1973; Kachanov, 1980; Mura, 1987; Lubarda and Krajcinovic, 1994). In such cases the microstructure generally arises from inclusions, cracks, pores, etc. within an otherwise homogeneous material, and therefore the deviation in the elastic properties presented by such features is treated as a perturbation. This description of microstructure is far different from observable snow microstructure. Apart from new snow, which is highly porous and comprised of dendritic crystals, most snow microstructure can be idealized as a granular material.

The mean field theory is where most work relating to granular materials has been established. Consequently, it is applied here to snow. The bottom line is that the appropriate micromechanical theory depends on the nature of the microstructure. To further emphasize that point, a number of micromechanical techniques for cellular materials—e.g., foams, cork, and wood—have also been developed but are not considered here. However, they have been applied to the aforementioned trabecular bone tissue (Gibson and Ashby, 1999).

Representation theorems are unique because they are a purely mathematical approach that are not developed with any particular microstructure in mind. The approach has been criticized because it requires *a priori* knowledge of the appropriate microstructural variables (Kachanov and Sevostianov, 2005). Conversely, homogenization schemes *reveal* the significant microstructural features through modeling at the microscopic scale and transitioning to the macroscopic scale; appropriate microstructural variables are not assumed. When used in constitutive development, representation theorems also result in a large number of unknown constants or functions, for example the a_i, b_i, and c_i in Equation (2.8).

Interestingly, because they are purely mathematical identities, representation theorems are not restricted to relating field variables in constitutive models. They have

also been used to develop localization operations in homogenization schemes (Cambou *et al.*, 1995; Emeriault and Cambou, 1996; Rahmoun *et al.*, 2009). However, even in this case, representation theorems necessarily introduce additional microstructural constants or functions that require empirical evaluation. The primary reason for introducing representation theorems is to serve as a source of comparison between models like Equation (2.8) and the models developed here in Chapters 3 and 4.

2.2 Fabric Tensors

Many scalar parameters, both macro and micro, are important in characterizing the thermo-mechanical behavior of snow: density, grain size, neck size, volume fraction of the different phases, and coordination number are commonly used. However, scalar quantities are often insufficient in describing a complex granular microstructure. An example is that two snow samples of the same density might exhibit different material properties (Sturm and Johnson, 1992; Sturm *et al.*, 1997; Schneebeli and Sokratov, 2004). Directional quantities are required to characterize any directionally-dependent arrangement of the microstructure. A commonly proposed directional quantity is termed the fabric tensor because it quantifies the alignment of the matrix and pore space—the fabric of the microstructure. The concept of fabric initially appeared in the study of granular materials (Cobbold and Gapais, 1979; Christoffersen *et al.*, 1981; Mehrabadi, 1982; Nemat-Nasser and Mehrabadi, 1983; Satake, 1983), but fabric tensors have been applied to such diverse fields as bone mechanics (Cowin, 1985, 1986; Turner and Cowin, 1987; Kabel *et al.*, 1999) and damage mechanics (Kachanov, 1980; Lubarda and Krajcinovic, 1993; Zysset and Curnier, 1995; Voyiadjis *et al.*, 2007). In bone mechanics, fabric tensors quantify the alignment of trabecular bone tissue and its directional preference according to how it is loaded. In damage mechanics, fabric

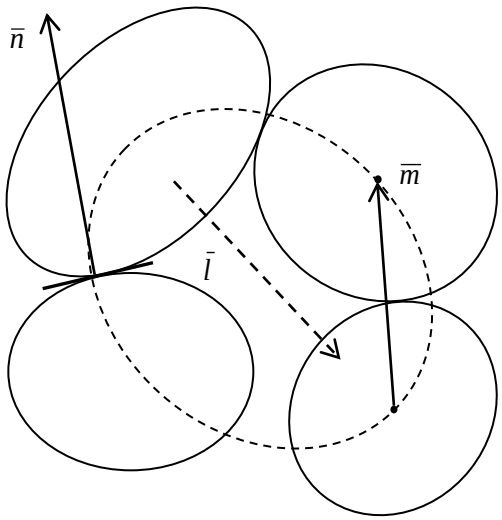


Figure 2.4: A granular assembly with example directional quantities: $\bar{l}$, a unit vector along the major axis of a void cell ellipse; $\bar{m}$, a unit vector between centers of connected grains; and $\bar{n}$, a unit vector normal to a contact plane connecting grains.

has been used to describe the geometry and arrangement of cracks, pores, or other defects in a homogeneous matrix material like rock, concrete, or metal. Any complex microstructure whose constituents could be described by directional data could be characterized by fabric tensors.

2.2.1 Directional Data

In the case of snow and other granular materials, the directional data that underpins the fabric description may arise from a myriad of sources. Figure 2.4 depicts a few such possibilities. Vectors like $\bar{l}$ might collectively govern the direction of convection or diffusion in a granular material, processes that typically occur in the void space. Conversely, vectors like $\bar{m}$ and $\bar{n}$ are commonly applied in describing the path of conduction and loading between connected grains. These vectors are introduced because they represent a few common possibilities that emerge in microscopic constitutive

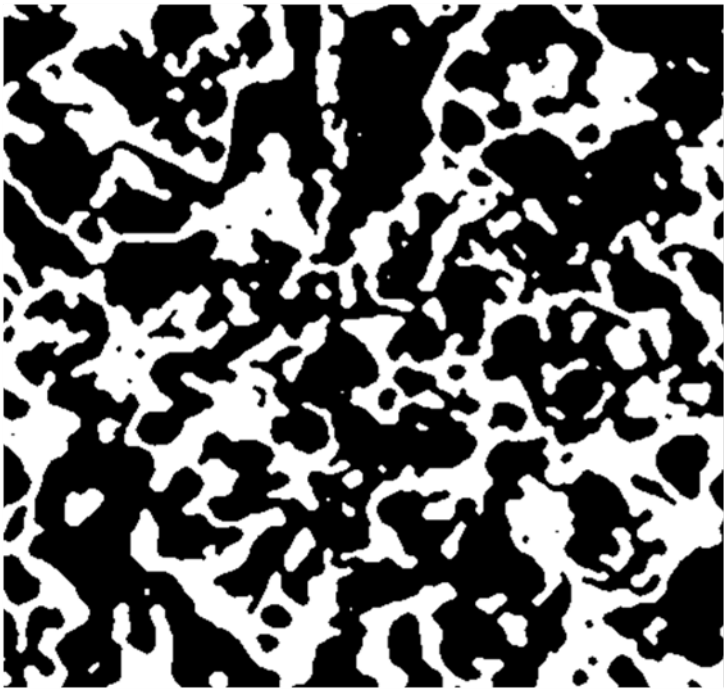


Figure 2.5: An example of snow microstructure where the ice is identified by black pixels and the void space by white.

modeling. Also, it should be apparent from Figure 2.4 that in an idealized assembly containing only circular or spherical particles, vectors $\bar{m}$ and $\bar{n}$ are coincident.

Directional quantities like those pictured in Figure 2.4 are identified in the microstructure through imaging, either by sectioning techniques or through nondestructive inspection like computed tomography (CT). Stereological algorithms (quantifying 3-D information from 2-D images) especially designed for snow have been developed at Montana State University to quantify properties of the ice grains and bonds (Edens, 1997; Lundy *et al.*, 2002). This software will be used to identify the geometric and directional features of snow's microstructure. The algorithms operate on 2-D binary images of microstructure, an example of which is depicted in Figure 2.5. A description of this software and other stereological formulae applied here in evaluating snow microstructure are presented in Chapter 6.

2.2.2 Tensors Derived from Granular Contacts

In granular assemblies, fabric characterizes the textural symmetry of the microstructure: the inherent or induced arrangement of the grains and/or voids. The objective is to determine whether the microstructure exhibits a random (isotropic) distribution or some degree of directional preference. The promise of fabric tensors is that they capture relevant microstructural information and express it in macroscopic terms. Fabric tensors are widely recognized as useful statistical characterizations of the anisotropy in a granular assembly, but tying them to constitutive models is still a developing field (Emeriault and Cambou, 1996; Cambou, 1998; Oda and Iwashita, 1999; Nemat-Nasser, 2000; Nicot, 2004; Luding, 2005; Rahmoun *et al.*, 2009). The purpose of the following sections is to define and illustrate the use of fabric tensors as a statistical characterization of directional data. The focus in Chapters 3 and 4 is applying fabric tensors to familiar constitutive models to relate textural anisotropy to the resulting anisotropy in field quantities like stress, heat flux, and mass flux. Importantly, Chapter 3 also demonstrates that fabric tensors can naturally arise in mathematical models of effective material properties through the application of homogenization techniques.

As will be analytically demonstrated later, defining unit vectors on the contact planes between connected grains as the appropriate directional quantity is useful in characterizing snow's conductive and elastic properties. A plane is defined at every contact between grains. Unit vectors $\bar{n}$ are defined here as normal to this plane, (Figures 2.4 and 2.6). This direction is intuitively appealing because, particularly in the case of idealized spherical particles, it defines the path of heat flow as well as the load path between two connected grains (Lamb, 1945; Batchelor and O'Brien, 1977; Chang and Liao, 1994). Kanatani (1984) writes a detailed treatment of fabric

tensors and how they relate to the distribution densities of directional quantities like $\bar{n}$. Much of what follows in this section is a summary of his work.

A fundamental fabric tensor, referred to here as the contact tensor $\mathbf{F}$, is the volume average of the tensor product of the contact unit normal vectors $\bar{n}$. The 2^{nd} order contact tensor in tensor and index notation, respectively, is given by

$$\mathbf{F} = \frac{1}{N}\sum_{\alpha=1}^{N} \bar{n}^{\alpha} \otimes \bar{n}^{\alpha}, \tag{2.9a}$$

$$F_{ij} = \frac{1}{N}\sum_{\alpha=1}^{N} n_i^{\alpha} n_j^{\alpha}, \tag{2.9b}$$

where the $\otimes$ operation is the dyadic product of the two vectors and N is the total number of contact normal vectors $\bar{n}$ in the representative volume. The n_i^{α} are the projections or components of the α^{th} unit vector $\bar{n}$ with respect to the x_i Cartesian coordinate.

Alternatively, if the distribution density of $\bar{n}$ can be described by a known scalar function $P(\bar{n})$ then the contact tensor in tensor and index notation, respectively, can be determined by

$$\mathbf{F} = \int_{\Omega} P\left(\bar{n}\right)\left(\bar{n} \otimes \bar{n}\right) d\Omega, \tag{2.10a}$$

$$F_{ij} = \int_{\Omega} P\left(\bar{n}\right) n_i n_j d\Omega, \tag{2.10b}$$

where Ω is the solid angle: 2π radians in 2-D and 4π steradians in 3-D.

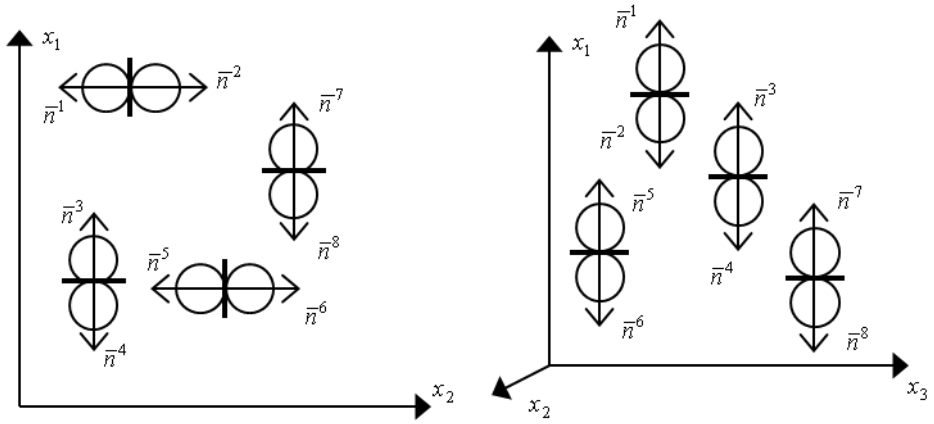
Calculating the contact tensor coefficients by Equation (2.9b) requires an image of the granular microstructure where contact normal vectors can be identified. In contrast, determining the tensor coefficients by Equation (2.10b) requires the distribution density function $P(\bar{n})$. Technically, $P(\bar{n})$ is an unknowable distribution of

a population. This distribution must either be estimated from a sufficiently large sample of normal vectors, or some assumptions must be made about its form. If the goal is to calculate the tensor coefficients from measured data, it is more direct to use Equation (2.9b), which is the approach used here.

However, if the goal is to identify $\mathbf{F}$ from a complicated mathematical expression then Equation (2.10a) or (2.10b) is of some use. In anisotropic constitutive modeling it is sometimes assumed that a microstructural quantity varies with $P(\bar{n})$ (Jagota and Hui, 1990; Chang and Liao, 1994; Chang *et al.*, 1995; Emeriault and Cambou, 1996; Nicot, 2004; Rahmoun *et al.*, 2009). This assumption, in combination with averaging operations in homogenization, paves the way for recognizing the contact tensor from an expression like Equation (2.10a) or (2.10b). This practice is referenced in Chapter 5.

Additionally, Equations (2.10a) and (2.10b) clearly define the mathematical relationship between $\mathbf{F}$ and $P(\bar{n})$ (Kanatani, 1984). This relationship will be referenced later in exploring the the link between $P(\bar{n})$ and contact tensors of 2^{nd} and higher order.

Consider the two simple granular assemblies in Figure 2.6. Recall that the summation index—the superscript in Equation (2.9b)—refers to contact normal vectors rather than planes of contact or bonds. They symmetry of contact normals that is evident in Figure 2.6 is discussed in the next section. The two-dimensional 2^{nd} order



(a) (b)

Figure 2.6: An example of two granular assemblies with N=8 contact normal vectors: (a) 2-D with half of the contact normal vectors ($\bar{n}^\alpha$) in the $\pm x_1$ direction and half in the $\pm x_2$ direction. (b) 3-D with all contact normal vectors oriented in the $\pm x_1$ direction.

contact tensor coefficients in Figure 2.6a, as defined by Equation (2.9b), are

$$\begin{aligned} F_{ij}^{(\mathrm{a})} &= \frac{1}{8}\begin{bmatrix} (n_1^1 n_1^1 + \ldots + n_1^8 n_1^8) & (n_1^1 n_2^1 + \ldots + n_1^8 n_2^8) \\ (n_2^1 n_1^1 + \ldots + n_2^8 n_1^8) & (n_2^1 n_2^1 + \ldots + n_2^8 n_2^8) \end{bmatrix}, \\ F_{ij}^{(\mathrm{a})} &= \frac{1}{8}\begin{bmatrix} (\text{-}1 \cdot \text{-}1 + \ldots + 0 \cdot 0) & (\text{-}1 \cdot 0 + \ldots + 0 \cdot \text{-}1) \\ (0 \cdot \text{-}1 + \ldots + \text{-}1 \cdot 0) & (0 \cdot 0 + \ldots + \text{-}1 \cdot \text{-}1) \end{bmatrix}, \\ F_{ij}^{(\mathrm{a})} &= \frac{1}{8}\begin{bmatrix} 4 & 0 \\ 0 & 4 \end{bmatrix} = \begin{bmatrix} 1/2 & 0 \\ 0 & 1/2 \end{bmatrix}. \end{aligned} \tag{2.11a}$$

Similarly, but considering three reference axes in Figure 2.6b, the coefficients are

$$F_{ij}^{(\mathrm{b})} = \frac{1}{8}\begin{bmatrix} 8 & 0 & 0 \\ 0 & 0 & 0 \\ 0 & 0 & 0 \end{bmatrix} = \begin{bmatrix} 1 & 0 & 0 \\ 0 & 0 & 0 \\ 0 & 0 & 0 \end{bmatrix}. \tag{2.11b}$$

2.2.3 Symmetry of Directional Data and Principal Orientation

Another important feature of the contact tensor arises due to the symmetry of a pair of contact normal vectors about the contact plane. To calculate the contact tensor coefficients of the assembly in Figure 2.6a, only a single normal vector at each contact plane is required. For example, vectors 2, 3, 6 & 7 yield

$$
\begin{aligned}
F_{ij}^{(\mathrm{a})} &= \frac{1}{4}\begin{bmatrix} (n_1^2 n_1^2 + \ldots + n_1^7 n_1^7) & (n_1^2 n_2^2 + \ldots + n_1^7 n_2^7) \\ (n_2^2 n_1^2 + \ldots + n_2^7 n_1^7) & (n_2^2 n_2^2 + \ldots + n_2^7 n_2^7) \end{bmatrix}, \\
F_{ij}^{(\mathrm{a})} &= \frac{1}{4}\begin{bmatrix} (1\cdot 1 + 0\cdot 0 + 1\cdot 1 + 0\cdot 0) & (1\cdot 0 + 0\cdot 1 + 1\cdot 0 + 0\cdot 1) \\ (0\cdot 1 + 1\cdot 0 + 0\cdot 1 + 1\cdot 0) & (0\cdot 0 + 1\cdot 1 + 0\cdot 0 + 1\cdot 1) \end{bmatrix}, \qquad (2.12) \\
F_{ij}^{(\mathrm{a})} &= \frac{1}{4}\begin{bmatrix} 2 & 0 \\ 0 & 2 \end{bmatrix} = \begin{bmatrix} 1/2 & 0 \\ 0 & 1/2 \end{bmatrix},
\end{aligned}
$$

which is identical to the result in Equation (2.11a). It is computationally less expensive to include only one normal vector per contact plane rather than two and still arrive at the same statistical measure.

The image analysis software used in this research operates on 2-D images. To take advantage of the contact tensor symmetry in practice, only contact normal vectors pointing toward the 1st and 2nd quadrants are considered. Each contact plane will have one normal vector represented in one of these two quadrants. This practice ensures that each contact plane is represented by one and only one contact normal vector.

In the simple examples of Figure 2.6, all contact normal vectors align with the reference Cartesian coordinates. Consequently, the principal directions of these contact tensors are the reference Cartesian coordinates. This is generally not the case in

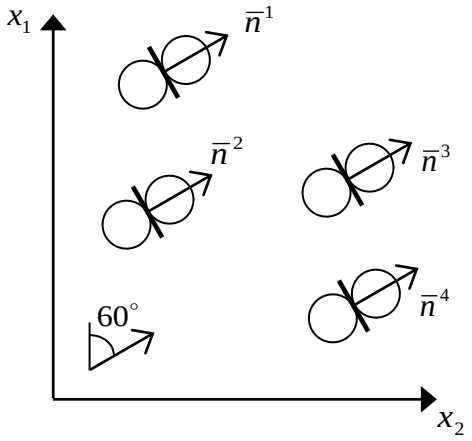


Figure 2.7: An example granular assembly with four contact planes. This example capitalizes on the symmetry of the directional data, considering only four contact normal vectors rather than eight. All contact normal vectors are oriented 60° clockwise from the $+x_1$ direction.

a statistically representative sample. A simple example where the directional data do not align with the reference coordinates is depicted in Figure 2.7. Similar to Figure 2.11b above, all contact normal vectors share a common direction. In this example that direction is obviously not a reference Cartesian coordinate.

The two-dimensional 2nd order contact tensor coefficients of the assembly in Figure 2.7, with respect to the pictured Cartesian axes, are

$$\begin{aligned} F_{ij} &= \frac{1}{4}\begin{bmatrix} (n_1^1 n_1^1 + \ldots + n_1^4 n_1^4) & (n_1^1 n_2^1 + \ldots + n_1^4 n_2^4) \\ (n_2^1 n_1^1 + \ldots + n_2^4 n_1^4) & (n_2^1 n_2^1 + \ldots + n_2^4 n_2^4) \end{bmatrix}, \\ F_{ij} &= \frac{1}{4}\begin{bmatrix} 4\left(1/2 \cdot 1/2\right) & 4\left(1/2 \cdot \sqrt{3}/2\right) \\ 4\left(\sqrt{3}/2 \cdot 1/2\right) & 4\left(\sqrt{3}/2 \cdot \sqrt{3}/2\right) \end{bmatrix}, \\ F_{ij} &= \begin{bmatrix} 1/4 & \sqrt{3}/4 \\ \sqrt{3}/4 & 3/4 \end{bmatrix}. \end{aligned} \tag{2.13}$$

The nonzero off-diagonal terms reveal that these Cartesian coordinates are not principal directions of these data. However, as with any 2nd order tensor, the principal values and directions of this system can easily be calculated through an eigenvalue problem (Reddy, 2008). The coefficients in a principal orientation—denoted with a superscript (p)—are

$$F_{ij}^{(p)} = \begin{bmatrix} 0 & 0 \\ 0 & 1 \end{bmatrix}, \tag{2.14}$$

and the principal direction of the nontrivial principal value, expressed in terms of the reference Cartesian coordinates, is

$$\bar{n}^{(p)} = \frac{1}{2}\hat{i} + \frac{\sqrt{3}}{2}\hat{j}. \tag{2.15}$$

Equation (2.14) indicates that all directional data is oriented in a single direction and Equation (2.15) identifies that direction as 60° clockwise from the $+x_1$ axis.

This example illustrates that fabric coefficients can be calculated from directional data with respect to any reference coordinates. The eigenvalues and eigenvectors of the resulting array give the principal values and directions of fabric, expressed in terms of the reference Cartesian coordinates.

2.2.4 Decomposition and Interpretation

An interesting feature of the contact tensor is evident from Equations (2.11a) and (2.11b). The first invariant or trace equals one. Now considering a general three-dimensional case, it is useful to decompose the 2nd order contact tensor into a sum of its isotropic and deviatoric parts, $\hat{F}_{ij}$ and F'_{ij}, respectively. Physically, the isotropic part represents no directional preference of contacts and the deviatoric part quantifies microstructural departures from such a random arrangement. The

mathematical decomposition illustrates the relationship between the contact tensor coefficients and the textural symmetry:

$$F_{ij} = \hat{F}_{ij} + F'_{ij} = \frac{1}{3}F_{kk}\delta_{ij} + F'_{ij} = \frac{1}{3}\delta_{ij} + F'_{ij} = f\delta_{ij} + F'_{ij}, \tag{2.16}$$

where F_{kk} is the trace of the tensor, δ_{ij} is the Kronecker delta, and f is the scalar isotropic value of the tensor. This general decomposition can apply to any 2$^{\text{nd}}$ order tensor. In the specific case of the contact tensor, F_{kk} equals one so f equals $1/3$ in three dimensions and $1/2$ in two dimensions. Applied to the example granular assemblies in Figure 2.6, the contact tensor coefficients can be written as

$$F_{ij}^{(\text{a})} = \frac{1}{2}\begin{bmatrix} 1 & 0 \\ 0 & 1 \end{bmatrix} + \begin{bmatrix} 0 & 0 \\ 0 & 0 \end{bmatrix}, \tag{2.17}$$

$$F_{ij}^{(\text{b})} = \frac{1}{3}\begin{bmatrix} 1 & 0 & 0 \\ 0 & 1 & 0 \\ 0 & 0 & 1 \end{bmatrix} + \begin{bmatrix} 2/3 & 0 & 0 \\ 0 & -1/3 & 0 \\ 0 & 0 & -1/3 \end{bmatrix}. \tag{2.18}$$

F'_{ij} contains only zeroes if the 2$^{\text{nd}}$ order contact tensor cannot identify any directional preference in the distribution of contact normals. In such cases, the distribution is considered statistically uniform/isotropic, it can be represented by the scalar value f, and the principal values of $\mathbf{F}$ are repeated. In Figure 2.6a, although the contact normals are not randomly distributed, they are divided between only two distinct directions and the second order contact tensor cannot distinguish a *preferred* direction. With only two principal directions, the 2-D 2$^{\text{nd}}$ order contact tensor lacks sufficient degrees of freedom to characterize this distribution as anything other than uniform/isotropic. This is evidenced by Equations (2.11a) and (2.17): the 2-D 2$^{\text{nd}}$

order contact tensor mathematically treats the assembly in Figure 2.6a as an example of textural isotropy.

The deviatoric part of the tensor captures any departure from textural isotropy. For example, in Figure 2.6b the contact normals exhibit a preference in only one direction, so one principal value is distinct while the other two are repeated (isotropic plane)—a transversely isotropic symmetry. In fact, Figure 2.6b is an example of the mathematical limit of transverse isotropy as *all* directional data is aligned in a single direction. Finally, if three orthogonal directions exhibit different degrees of directional preference, then the principal values are all distinct—an orthotropic symmetry.

A 2^{nd} order tensor in 3-D has only three principal values, so describing levels of symmetry above orthotropic requires the 4^{th} order contact tensor. Graphically, as will be illustrated below, this limits a 2^{nd} order tensor to distributions that are elliptical (2-D) or ellipsoidal (3-D). A 4^{th} order tensor can characterize distributions that are approximated by more complex shapes. The coefficients of the 4^{th} order contact tensor are

$$F_{ijkl} = \frac{1}{N} \sum_{\alpha=1}^{N} n_i^\alpha n_j^\alpha n_k^\alpha n_l^\alpha. \tag{2.19}$$

The granular assembly in Figure 2.6a is an example that is adequately described by the 4^{th} order contact tensor but not the 2^{nd}. In 3-D, this collection of contact normal vectors is equivalent to a simple cubic packing structure. It was shown above that the 2^{nd} order contact tensor, for lack of sufficient degrees of freedom, considers this regular arrangement of directional data to be uniform/random. Conversely, the 4^{th} order contact tensor can sufficiently characterize a cubic symmetry and does not simplify it to a case of textural isotropy (Cowin, 1985). This is not to imply that the 2^{nd} order coefficients are calculated incorrectly, it simply highlights the limitation of a 2^{nd} order tensor in describing higher levels of material symmetry.

Figure 2.6a depicts a case where it is clear whether a 2^{nd} or 4^{th} order contact tensor is required in quantifying the textural symmetry. With measured data, the distribution of the directional quantity $\bar{n}$ will likely not be as straightforward as any of the offered examples. Quantitatively, choosing whether to incorporate the 2^{nd}, 4^{th}, or higher order tensors is a convergence issue in estimating the probability density of $\bar{n}$.

A common way to arrange observed data is on a histogram, and, the probability density function (pdf) of a variable can be estimated from histograms. A pdf of a directional quantity is also a statistical characterization—it is a different way of characterizing the directional arrangement of the contact normal vectors. Kanatani (1984) was the first to articulate that, in the case of observed directional data like contact normal vectors, contact tensors and the pdf of $\bar{n}$ are related.

The underlying problem in creating the pdf of $\bar{n}$ is one of density estimation: calculating the pdf of a population from a disjointed empirical density distribution. Kanatani (1984) reviews how the pdf of $\bar{n}$, $P(\bar{n})$, can be estimated using what he terms fabric tensors of the second and third kind. The most accessible statistical model is derived using his fabric tensors of the third kind of various order with coefficients Ψ, Ψ_{ij}, etc. $P(\bar{n})$ can be expressed as an infinite series expansion (Kanatani, 1984):

$$P(\bar{n}) = \frac{1}{\Omega}\left\{\Psi + \Psi_{ij}n_i n_j + \Psi_{ijkl}n_i n_j n_k n_l + \ldots\right\}, \tag{2.20}$$

where Ω is 2π radians in 2-D and 4π steradians in 3-D and Ψ is the cumulative value of the pdf which by definition is one (cumulative probability cannot exceed 100%). Others (Lubarda and Krajcinovic, 1993; Voyiadjis *et al.*, 2007) have used the same formulation in estimating distribution functions that are not *density* functions. In these cases Ψ, a scalar value, is not necessarily equal to one.

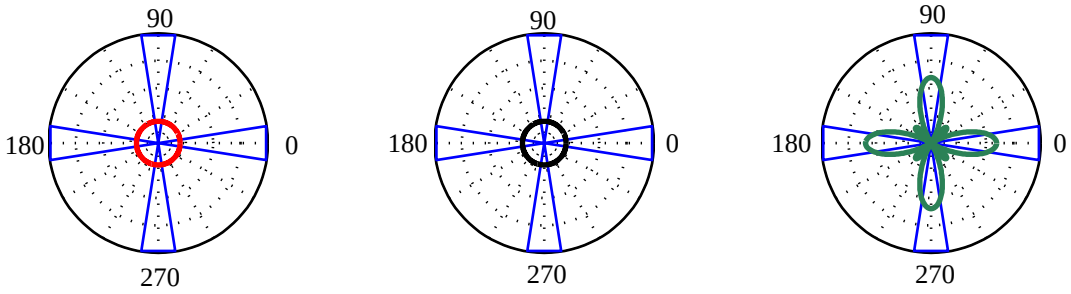
The higher order tensors of the third kind are deviatoric and are related to the deviatoric part of the contact tensor. For simplicity and succinctness, only the 2^{nd} order case is shown here:

$$\Psi_{ij} = zF'_{ij}, \tag{2.21}$$

where z is 4 in 2-D and $^{15}/_{2}$ in 3-D. It is important to note that Ψ_{ij} differs from F'_{ij} by a scalar factor—the difference depends on the basis of functions spanning the unit circle or unit sphere (Kanatani, 1984). Expressions for Ψ_{ij}, Ψ_{ijkl}, and Ψ_{ijklmn} appropriate for both 2-D and 3-D distributions can be found in Kanatani (1984). Also, due to the symmetry of the directional data, odd ordered tensors do not contribute to the series solution.

In order to follow every discontinuity of an empirical data distribution, the estimated pdf must potentially include an infinite number of higher order tensors. This is obviously unrealistic and statistically unnecessary. In application, a hypothesis test should be used to determine whether 2^{nd}, 4^{th} or even higher order tensors are statistically appropriate in characterizing the distribution of contact normals. For example, there is nothing to be gained by including Ψ_{ijkl} in the estimation of $P(\bar{n})$ if the series solution has converged with Ψ_{ij}—a hypothesis test quantifies this convergence. With any hypothesis test, the conclusion is sensitive to sample size and significance level. The reason the model in Equation (2.20) is so accessible is because the hypothesis test permits an objective manner in determining the appropriate number of terms in estimating $P(\bar{n})$.

Figure 2.8 is an initial illustration of empirical data and functions used to approximate their distribution. In this example, the empirical data are drawn from Figure 2.6a and are represented here on 2-D angle histograms or rose diagrams. Recall that the contact normals are equally distributed between the vertical and horizontal



(a) Scalar approx. (b) 2^{nd} order tensor approx. (c) 4^{th} order tensor approx.

Figure 2.8: A regular empirical distribution density of $\bar{n}$ and the various functions to approximate $P(\bar{n})$ using a series solution comprised of Cartesian tensors. The empirical data were drawn from the example assembly in Figure 2.6a.

directions. This histogram requires only four buckets or bins (blue wedges) and the distribution density is equal for each bin in this very regular arrangement. The smooth functions in (a)–(c) are different approximations to this empirical data distribution using Equation (2.20). By definition, the cumulative probability—the area enclosed by the various shapes—equals one for the empirical distribution and the pdf approximations.

The smooth function in (a) is the pdf approximation using only a mean scalar value: $P(\bar{n}) \approx {}^{1}/_{2\pi}$. The smooth function in (b) is the 2^{nd} order tensor approximation: $P(\bar{n}) \approx {}^{1}/_{2\pi}\{1 + \Psi_{ij} n_i n_j\}$. The smooth function in (c) is the 4^{th} order tensor approximation: $P(\bar{n}) \approx {}^{1}/_{2\pi}\{1 + \Psi_{ij} n_i n_j + \Psi_{ijkl} n_i n_j n_k n_l\}$. The functions in (a) and (b) are obviously both circles. Recall from Equations (2.11a) and (2.17), that the 2^{nd} order tensor cannot distinguish this case from textural isotropy: $\Psi_{ij} = \begin{bmatrix} 0 & 0 \\ 0 & 0 \end{bmatrix}$. Graphically, an ellipse fits this empirical data no better than a circle. The pdf approximation in (b) is therefore equivalent to (a). With so few samples—only eight contact normal vectors considered—the difference between the various pdf approximations is statistically insignificant. However, this example qualitatively illustrates an empirical

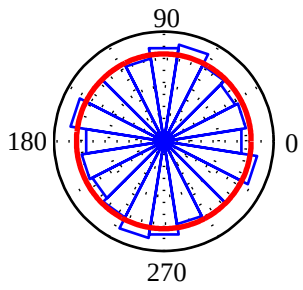
arrangement where the 4^{th} order tensor obviously contributes useful information in estimating $P(\bar{n})$.

Figure 2.9 further illustrates the interpretation of contact tensors and $P(\bar{n})$. These scenarios utilize a statistically significant sample size—the total number of contact normal vectors is one thousand—and more closely represent a randomly distributed granular material. The distribution of these vectors is divided between twenty buckets on the 2-D rose diagrams in Figure 2.9. The empirical distribution is identical in (a)–(c). It was drawn from a uniform population. As before, the cumulative probability—the area enclosed by the various shapes—equals one for both the empirical distribution and the pdf approximations.

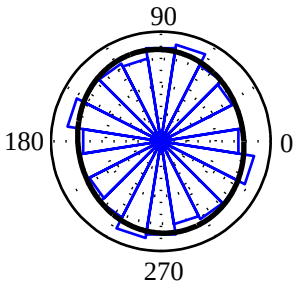
Again, the circle in (a) is the approximation of the pdf using only a mean scalar value—the function that assumes the data show no directional preference. The ellipse in (b) is the 2^{nd} order tensor approximation—the smooth function of best fit assuming the deviatoric part in Equation (2.16) is significant. Finally, the shape in (c) is the 4^{th} order tensor approximation. Qualitatively, the 4^{th} order approximation appears better than the scalar approximation, as would be expected in a series solution—including a greater number of terms improves the accuracy of the solution. However, recall that the true population from which the empirical data are drawn is random—there is no directional preference in the underlying population.

The hypothesis test reflects this truth. To a significance of 0.005, the 2^{nd} order tensor solution in (b) offers no improvement over the scalar approximation in (a) in estimating the pdf. Of course, the 4^{th} order solution then offers no significant improvement to the fit in (b) as well. The conclusion drawn from the first row is that the data are randomly distributed and the isotropic solution in (a) is an adequate approximation to the true population distribution density. The 2^{nd} and 4^{th}

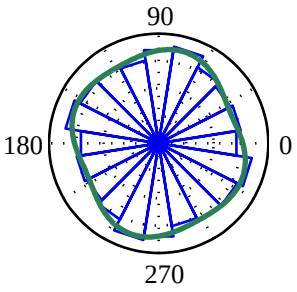
order solutions offer a more accurate fit to the available empirical data, but they are unnecessary in characterizing the pdf of $\bar{n}$.



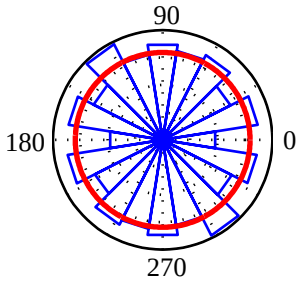
(a) Scalar approx.



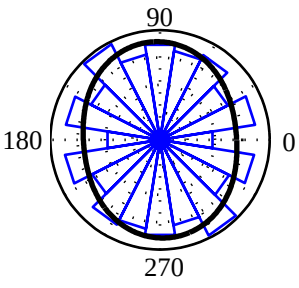
(b) 2^{nd} order tensor approx.



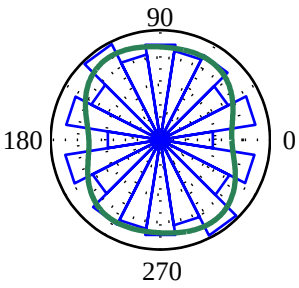
(c) 4^{th} order tensor approx.



(d) Scalar approx.



(e) 2^{nd} order tensor approx.



(f) 4^{th} order tensor approx.

Figure 2.9: Empirical distribution densities of $\bar{n}$ and the various functions to approximate $P(\bar{n})$ using a series solution comprised of Cartesian tensors. The empirical data in (a)–(c) were drawn from an isotropic population while the data in (d)–(f) were drawn from an anisotropic population.

Moving to the second row of Figure 2.9, the empirical distribution density in (d)–(f) was skewed to pull fewer samples around 0° and 180°, effectively creating anisotropy. Similar to the first row, from left to right are the pdf approximations based on including: a scalar; a scalar and 2^{nd} order tensor; and a scalar, 2^{nd} order, and 4^{th} order tensor. For these data, with the same significance of 0.005, the 2^{nd} order tensor offers a statistically better approximation to the underlying population distribution than the scalar solution. However, the 4^{th} order solution is not significantly different from the 2^{nd} order approximation. The conclusion based on the second row is that

the data are anisotropic and that the anisotropy is adequately captured by $P(\bar{n}) \approx {}^{1}/_{2\pi}\{1 + \Psi_{ij} n_i n_j\}$. The figures are used to illustrate the objectivity of the test as opposed to relying on a qualitative evaluation of the sample empirical data.

The purposes of introducing and reviewing all these examples are several:

- To offer a visual, realistic rendering of empirical data and the various approximations to the underlying pdf,
- To illustrate the pdf of $\bar{n}$ as a truncated series solution derived from Cartesian tensors,
- To introduce a hypothesis test as a means to test the convergence of the series,
- To highlight that a fabric tensor is not a precise measurement of microstructure but a statistical characterization of a microstructural feature,
- To highlight that "fabric" is a generic term—different fabric tensors characterize different phenomena.

To further emphasize the final bullet consider the difference between the 2$^{\text{nd}}$ order contact tensor in Equation (2.9a) and the 2$^{\text{nd}}$ order tensor approximation to the pdf of $\bar{n}$: $P(\bar{n}) \approx {}^{1}/_{2\pi}\{1 + \Psi_{ij} n_i n_j\}$. This expression can be written differently for direct comparison to the contact tensor as $P(\bar{n}) \approx {}^{1}/_{2\pi}\left\{\delta_{ij} + \Psi_{ij}\right\} n_i n_j = {}^{1}/_{2\pi}\left\{\delta_{ij} + z F'_{ij}\right\} n_i n_j$. Now, a comparison of the two tensors yields:

$$\delta_{ij} + z F'_{ij} \tag{2.22a}$$

$$f\delta_{ij} + F'_{ij}. \tag{2.22b}$$

Equation (2.22a) is the 2$^{\text{nd}}$ order tensor approximation to the pdf of $\bar{n}$, while Equation (2.22b) is the 2$^{\text{nd}}$ order contact tensor decomposed into its mean and deviatoric parts.

Both are "fabric" tensors in that they characterize the directional arrangement of contact normal vectors. However, the top expression has an isotropic value of 1 and modifies deviations from that through z. The bottom expression has an isotropic value of f and does not modify the deviatoric component.

As with any 2nd order tensor, the components of either expression can describe an ellipse or ellipsoid, as in Figure 2.9. The shape created by Equation (2.22a) corresponds to the pdf of $\bar{n}$ and the shape created by Equation (2.22b), while qualitatively very similar (especially with small deviations from isotropy), represents the distribution of the volume average of the tensor product of contact unit normal vectors. As Kanatani (1984) points out in this latter case, "it is not easy to understand the intuitive meaning of this tensor," which is exactly the motivation for his development of expressions for the pdf of $\bar{n}$, a function with broad statistical appeal and potential application.

The point of emphasizing these differences is that many analytical models relating fabric to constitutive behavior neglect the details of such definitions (Cowin, 1986; Zysset and Curnier, 1995). Their broad aim is to mathematically incorporate a 2nd order fabric tensor in constitutive models. However, for a specific application such as proposed here, the details of that fabric tensor are important. First, the selection of the directional quantity is the most fundamental distinction between fabric tensors. Second, and more subtly, Equations (2.22a) and (2.22b) illustrate that tensors derived from the same directional quantity characterize different phenomena. These points will be revisited in Chapters 4 and 5.

There is ample qualitative and quantitative evidence to suggest that the thermally-induced fabric changes in snow that occur during temperature gradient metamorphism result in a transversely isotropic symmetry (Kry, 1975a; Sturm *et al.*, 1997; Schneebeli and Sokratov, 2004; Srivastava *et al.*, 2010). The direction with the unique principal

value of fabric is coincident with the applied unidirectional temperature gradient. Therefore, a 2^{nd} order fabric tensor should offer a sufficient characterization of the anisotropy in snow. The anisotropic micromechanical constitutive models developed in Chapters 3 and 4 incorporate a 2^{nd} order fabric tensor. Not only should it be sufficient, but a 2^{nd} order tensor is simply easier to visualize and mathematically manipulate. Still, the 4^{th} order tensor will be calculated and the hypothesis test determining its significance will be executed in order to quantify the level of anisotropy. Even if the 4^{th} order solution proves to be a significantly better statistical characterization, the 2^{nd} order tensor still provides a good approximation of textural anisotropy whereas the scalar solution provides none.

2.2.5 Tensors Derived from Mean Intercept Length

Another stereological technique used to characterize microstructural fabric is mean intercept length (MIL) analysis. Similar to the approach using unit vectors, MIL analysis relies on images of the microstructure where the constituents can be clearly identified. However, MIL analysis does not require the identification of any of the directional data pictured in Figure 2.4. MIL analysis instead uses a test line superimposed on the microstructural image. A test line is usually implemented as a family of parallel line segments in order to collect a larger sample of data. MIL is determined via a point counting technique: the number of intersections between the test line and the two-constituent interface is tallied as I, and directional dependence is introduced by calculating I for test lines of varying orientation angle ϱ (Underwood, 1970; Whitehouse, 1974; Harrigan and Mann, 1984; Odgaard, 1997). MIL is calculated as

$$\mathrm{MIL}\left(\varrho\right) = \frac{\text{Total Test Line Length}}{I\left(\varrho\right)}. \tag{2.23}$$

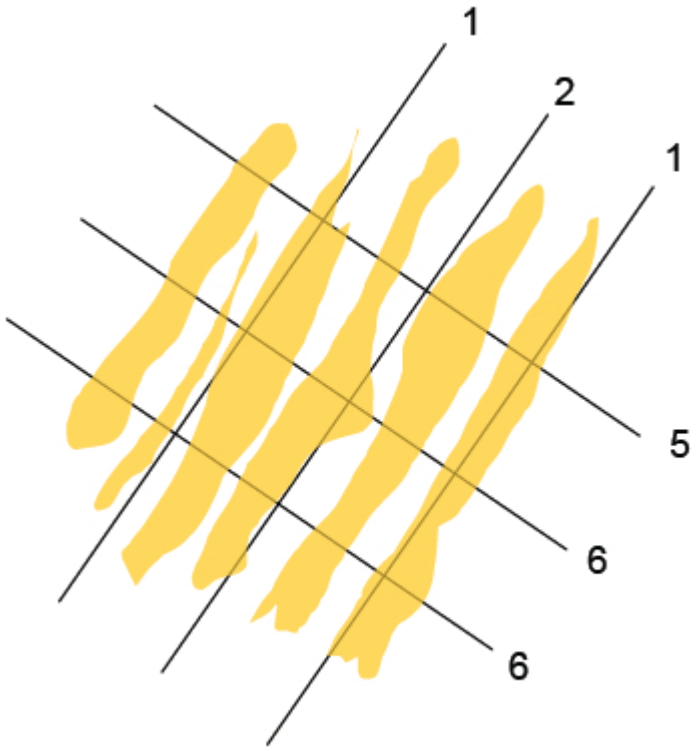


Figure 2.10: An example image of an anisotropic microstructure with test line segments at two different orientations. The number of intersections with the solid constituent is labeled with the corresponding test line segment. The graphic was taken from SkyScan (2009).

For illustration, Figure 2.10 depicts test lines consisting of three segments each at two different orientations. The total test line length is the sum of the three segments sharing a given orientation. The number of intersections with the solid constituent in the image is listed with each segment. In this implementation, a single intersection is tallied as an entrance *and* exit with the solid constituent (SkyScan, 2009). Other algorithms count an intersection with each entrance or exit. The scalar difference between these methods does not affect the anisotropy (Odgaard, 1997). The number of

intersections, and therefore MIL, varies with orientation for this obviously anisotropic example.

When accomplished for a large number of angles ϱ, the resulting distribution of mean intercept lengths can be plotted on a polar or spherical diagram, similar to the plots in Figure 2.9. However, a fundamental difference between MIL analysis and the approach relying on directional data is emphasized here. With directional data, the empirical observations are arranged in a histogram, tallying the contact normal vector frequency of occurrence over all considered directions. That frequency histogram is then considered relative to the total number of observations, creating the empirical distribution density represented by the blue wedges in Figure 2.9. Finally, the density estimation technique outlined by Kanatani (1984) calculates the pdf of the contact normal vectors from this empirical data.

With MIL analysis, the distribution of mean intercept lengths, while dependent on orientation, is not represented by a histogram. The method does not tally MIL frequency of occurrence over different orientations, but rather a MIL value is calculated for many different orientations. Consequently, plotting the distribution of mean intercept lengths on a polar or spherical diagram results in a "pin cushion" rather than a histogram (Harrigan and Mann, 1984; SkyScan, 2009). The pin cushion consists of a single vector at each considered orientation, whose magnitude corresponds to the mean intercept length at that orientation.

Although the underlying data is different in nature, an ellipse (in 2-D) or ellipsoid (in 3-D) can be statistically fit to a "pin cushion" of data using a least squares error method, similar to the method outlined by Kanatani (1984). Whitehouse (1974) observed that MIL data from trabecular bone tissue produced ellipses on 2-D polar diagrams, and Harrigan and Mann (1984) noted that the equation for an ellipse or ellipsoid can be expressed as the quadratic form of a 2^{nd} order tensor. Specifically,

Harrigan and Mann (1984) articulated the approximate relationship between the distribution function of MIL and a 2nd order "anisotropy tensor", $\mathbf{M}$, as

$$\frac{1}{(\mathrm{MIL}(\bar{m}))^2} \approx \bar{m} \cdot \mathbf{M} \cdot \bar{m} = M_{ij} m_i m_j, \tag{2.24}$$

where $\bar{m}$ is a unit vector in the direction of the test line. Equation (2.24) clearly shows that this anisotropy tensor is proportional to the inverse of mean intercept length squared, meaning that larger MIL measurements will result in smaller coefficients in the tensor $\mathbf{M}$. Figure 2.10 illustrates that it is *larger* MIL measurements that coincide with preferred microstructural orientation. Consequently, it is customary to adopt

$$\mathbf{H} = \mathbf{M}^{-1/2} \tag{2.25}$$

as the MIL fabric tensor (Cowin, 1985, 1986; Odgaard *et al.*, 1997; Srivastava *et al.*, 2010). Tensor $\mathbf{H}$ is proportional to mean intercept length rather than the inverse of mean intercept length squared. Its principal directions are coincident with directions of preferred microstructural orientation, similar to $\mathbf{F}$.

While there is no established analytical connection between contact normal vectors and mean intercept length, the tensors derived from either technique, $\mathbf{F}$ and $\mathbf{H}$, statistically characterize microstructural arrangement and identify any preferred orientation. For a granular material, the contact between grains has obvious and significant analytical implications for thermo-mechanical behavior. However, it can be difficult and tedious to identify such directional quantities in microstructural images. Furthermore, contact planes are irrelevant and unidentifiable features in many microstructures. For example, the aforementioned trabecular bone tissue can show distinct anisotropy but is certainly not a granular material. MIL analysis avoids

the requirement of identifying directional data by using an alternative stereological technique. Both approaches fundamentally quantify the same thing—microstructural anisotropy—but there are important differences.

H has dimensions of length while **F** is dimensionless. Also, because **F** is derived from unit vectors, its first invariant is a constant value of one. Conversely, the first invariant of **H** varies as the microstructure coarsens or thins. Consider an image oriented like Figure 2.10 that contains twice as many solid constituent pieces that are each half as thick. The anisotropy of this microstructure is the same as in Figure 2.10, but the measured MIL values are different. Consequently, it is also customary to normalize **H** so that its first invariant is equal to one (Cowin, 1985, 1986; Odgaard *et al.*, 1997; Srivastava *et al.*, 2010). This further increases the similarities with **F** because now their traces are both equal to one and normalizing **H** also renders it dimensionless.

MIL analysis is now a standard component of CT scanner software because it is commonly used to characterize bone anisotropy (SkyScan, 2009). While CT was initially developed for medical applications, it is increasingly used in the study of snow microstructure (Coléou *et al.*, 2001; Lundy *et al.*, 2002; Schneebeli and Sokratov, 2004; Satyawali *et al.*, 2008; Srivastava *et al.*, 2010). As a result, MIL fabric tensors describing snow microstructure are readily accessible in many scenarios. A goal of this research effort is to illustrate how different fabric tensors, whether derived from commercially available CT software or from algorithms especially suited for snow, can be used to improve constitutive modeling in anisotropic media.

2.2.6 Tensors Derived from Void Parameters

Fabric tensors are not restricted to the contact tensor. The underlying directional data defines the resulting fabric tensor. To reiterate, the contact plane or bond be-

tween grains is an important geometric feature to intergranular heat flow and loading. Consequently, the direction describing that plane—the contact normal vector—is critical in formulating local/microscopic constitutive laws for these phenomena. However, contact planes and contact normal vectors have little or nothing to do with fluid flow through the pore space in a granular material. As a void space process, fluid flow should be better described by a different choice of directional data. For example, a model developed in the next chapter adopts a vector that marks connections between void cells in formulating a fabric tensor for effective permeability. Importantly, this microstructural direction is not assumed. Instead, the balance of energy, mass, and momenta at the microscopic scale; idealized microstructural geometry; and constitutive assumptions reveal the appropriate directional quantities.

2.3 Summary

Several micromechanical approaches to constitutive modeling were introduced in this chapter. They all relate features of the microstructure to material behavior at the macroscopic level. Of these, a homogenization scheme will be applied in subsequent chapters in deriving constitutive relationships and expressions for effective material properties. The homogenization scheme consists of : 1) a localization assumption in scaling the kinematic variables from the macro to micro scale, 2) a microscopic constitutive law, and 3) a volume averaging operation in scaling the static variables from the micro to macro scale.

The application of volume averaging techniques presents a natural avenue for fabric tensors to surface in the expressions for effective material properties. Fabric tensors were defined and illustrated in this chapter. They are built from vectors that

define constitutive processes at the microscopic scale. MIL fabric tensors were also introduced as a source of comparison to fabric tensors derived from directional data.

CHAPTER 3

EFFECTIVE PROPERTIES: ENERGY AND MASS TRANSPORT

3.1 Transport Properties

When evaluating the effective heat transfer coefficient of a material in a laboratory or field setting, it is difficult to separate the contributions of different energy transfer modes. The standard modes of sensible heat transfer must be considered: conduction, convection and radiation. Also, because snow is a multiphase material, a temperature gradient also establishes an H_2O concentration gradient that drives water vapor through the snowpack. This diffusion can lead to crystal metamorphism due to sublimation and deposition as the water vapor migrates in the direction of the temperature gradient. For such diffusion that involves phase change, the bulk mass flux is associated with an additional energy flux due to the "latent heat" of phase change. This brief qualitative description is reviewed in quantitative detail in Appendix A.

Fortunately, some of these modes of energy transfer can be neglected. While radiation is a dominant mechanism of energy exchange near the surface of the snowpack in a natural environment, radiation effects within the snowpack can be justifiably ignored (Adams and Sato, 1993; Arons and Colbeck, 1998). Additionally, convection might also be quite significant in a natural environment but can be minimized in a well-controlled laboratory experiment (Sturm and Johnson, 1991). Consequently, neither radiation nor convection are considered in this analytical development. This is consistent with many mathematical models addressing heat and mass transfer in snow (Colbeck, 1983b; Adams and Sato, 1993; Lehning *et al.*, 2002; Miller *et al.*, 2003; Bartelt *et al.*, 2004; Satyawali and Singh, 2008). For dry snow, this leaves

conduction—both through the ice network and the pore space—and energy transfer via the combined effect of vapor diffusion and phase change. What follows is a common constitutive approach to energy transfer in a dry snowpack, identifying the pertinent transport properties.

Many basic constitutive models are useful building blocks in mathematically describing the behavior of snow. One such model is Fourier's model for heat conduction, generally stated as

$$\bar{q}_c = \text{-}\mathbf{k}^* \cdot \nabla\theta, \tag{3.1}$$

where the heat flux vector due to conduction $\bar{q}_c$ ($^{\text{W}}/_{\text{m}^2}$) is related to the temperature gradient $\nabla\theta$ ($^{\text{K}}/_{\text{m}}$) through the material's thermal conductivity $\mathbf{k}^*$ ($^{\text{W}}/_{\text{m}\cdot\text{K}}$). Thermal conductivity is a symmetric 2^{nd} order tensor in the general case. Because constitutive relationships are applied here to snow, a microscopically heterogeneous material, the asterisk is used to denote the property as an effective material property. The effective thermal conductivity of snow should address conduction through both the solid ice network and the gaseous pore space, as outlined above.

Similarly, the basic constitutive relationship often used to describe molar flux, $\overline{J}$ ($^{\text{mol}}/_{\text{m}^2\cdot\text{s}}$) , due to a concentration gradient, $\nabla\Phi$ ($^{\text{mol}}/_{\text{m}^4}$), is given by Fick's 1^{st} law:

$$\overline{J} = \text{-}\mathbf{D}^* \cdot \nabla\mathbf{\Phi}, \tag{3.2}$$

where $\mathbf{D}^*$ ($^{\text{m}^2}/_{\text{s}}$) is a second order tensor characterizing the effective diffusivity of water vapor through snow. For gaseous species that follow the ideal gas model, it is usual to express Fick's law using density or partial pressure. Specifically for water vapor, this relates a mass flux ($^{\text{kg}}/_{\text{m}^2\cdot\text{s}}$) and a gradient of density, ρ_{vap}, or partial pressure,

p_{vap}:

$$\overline{J} = -\mathbf{D}^* \cdot \nabla \rho_{vap} = -\frac{1}{R_{vap}\theta}\mathbf{D}^* \cdot \nabla p_{vap}, \tag{3.3}$$

where R_{vap} is the gas constant for water vapor ($^{\mathrm{J}}/_{\mathrm{kg \cdot K}}$) and θ is absolute temperature (K).

Application of the chain rule and the Clausius-Clapeyron relationship establishes vapor flux as a function of the temperature gradient (de Quervain, 1973; Colbeck, 1983b). Fick's 1st law can now be written as

$$\overline{J} = -\frac{1}{R_{vap}\theta}\mathbf{D}^* \cdot \frac{dp_{sat}}{d\theta}\nabla\theta = -\frac{L_s p_{sat}}{R_{vap}^2\theta^3}\mathbf{D}^* \cdot \nabla\theta, \tag{3.4}$$

where L_s is the latent heat of sublimation ($^{\mathrm{J}}/_{\mathrm{kg}}$) and p_{sat} is the saturation vapor pressure of water vapor with respect to a planar ice surface at a given temperature (Pa). The principles, assumptions and simplifications in deriving Equation (3.4) from Equation (3.2) are well-established. They are the subject of Appendix A.

Equation (3.4) is particularly useful because the temperature gradient is now linked to both heat and mass flux. Lastly, because the mass flux is assumed to be associated with phase change, the energy flux due to the combination of mass flux and phase change is taken to be

$$\bar{q}_{vap} = L_s\overline{J} = -\frac{L_s^2 p_{sat}}{R_{vap}^2\theta^3}\mathbf{D}^* \cdot \nabla\theta. \tag{3.5}$$

Consequently, the dominant modes of energy transfer in the snowpack can be combined as:

$$\bar{q} \;=\; \bar{q}_c + \bar{q}_{vap} = -\left\{\mathbf{k}^* + \frac{L_s^2 p_{sat}}{R_{vap}^2\theta^3}\mathbf{D}^*\right\} \cdot \nabla\theta. \tag{3.6}$$

Because Equation (3.6) represents energy flux caused by a temperature gradient, it is common to refer to the bracketed expression as the effective thermal conductivity or effective heat transfer coefficient. Here, the bracketed expression will be referred to as the effective heat transfer coefficient so as not to confuse it with the thermal conductivity tensor. The effective heat transfer coefficient is taken as the sum of true thermal conductivity and the apparent conductivity due to the combined effect of phase change and vapor flux. Equation (3.6) indicates that thermal conductivity and diffusivity are the effective material properties of snow that contribute to the overall effective heat transfer coefficient. The following sections address the development of mathematical models that express $\mathbf{k}^*$ and $\mathbf{D}^*$ in terms of microstructural variables.

Effective permeability $\boldsymbol{\kappa}^*$ is also considered. It is addressed in part to extend the presented technique, but also because permeability is one important factor in calculating advective fluid flow in a porous medium. The Rayleigh number is a dimensionless quantity in the study of free convection: bulk fluid motion due to density/temperature differences within the fluid. In a fluid, whether gaseous or liquid, the Rayleigh number is a ratio where the numerator is the product of buoyancy forces and advection and the denominator is a product of viscous forces and conduction (Nield and Bejan, 2006). A critical Rayleigh number characterizes the point at which buoyancy forces overcome viscous forces, representing the onset of free convection. Quantifying the critical Rayleigh number depends on the effective permeability of the porous medium. Although not considered a significant mode of heat transfer in most snow studies—including here—the offered microstructural approach may encourage future researchers to reevaluate assumptions surrounding advection and convection in the snowpack.

3.2 Mean Field Theory and Two-Constituent Microstructures

Now that the effective material properties of interest have been established, this section builds upon the homogenization scheme in Chapter 2 to derive a general approach to effective material properties. Recall the volume averaging operations in mean field theory:

$$\bar{F} = \langle \bar{f} \rangle = \frac{1}{V} \int \bar{f} dV \qquad \bar{G} = \langle \bar{g} \rangle = \frac{1}{V} \int \bar{g} dV. \tag{3.7}$$

The effective material property is defined by linking the macroscopic variables, $\langle \bar{f} \rangle$ and $\langle \bar{g} \rangle$, through the microscopic level. The following development is succinctly laid out in Batchelor (1974).

In a microstructure consisting of two constituents, the RVE volume V can be divided into two regions. These are labeled *Pore* and *Grains*:

$$\langle \bar{f} \rangle = \frac{1}{V} \int_{Pore} \bar{f} dV + \frac{1}{V} \int_{Grains} \bar{f} dV, \tag{3.8a}$$

$$\langle \bar{g} \rangle = \frac{1}{V} \int_{Pore} \bar{g} dV + \frac{1}{V} \int_{Grains} \bar{g} dV. \tag{3.8b}$$

Locally, applying the familiar linear constitutive law to relate $\bar{f}$ and $\bar{g}$, but recognizing that the two constituents have different coefficients of proportionality, results in

$$\begin{aligned} \bar{f} &= -K_{Pore} \bar{g}, \\ \bar{f} &= -K_{Grains} \bar{g}, \end{aligned} \tag{3.9}$$

where the constituents are assumed to be isotropic materials such that their coefficients of proportionality reduce to scalar values. Substituting Equations (3.9) into

Equation (3.8a) results in

$$\left\langle \bar{f} \right\rangle = -\frac{1}{V} \int_{Pore} K_{Pore} \bar{g} dV - \frac{1}{V} \int_{Grains} K_{Grains} \bar{g} dV. \tag{3.10}$$

Solving Equation (3.8b) for $^1/_V \int_{Pore} \bar{g} dV$ and substituting into Equation (3.10) yields

$$\left\langle \bar{f} \right\rangle = -K_{Pore} \left\langle \bar{g} \right\rangle + \frac{1}{V} \int_{Grains} (K_{Pore} - K_{Grains}) \bar{g} dV. \tag{3.11}$$

The first term in Equation (3.11) is the pore space contribution; it achieves the goal of relating the macroscopic flux and macroscopic gradient. However, the grain space term is still a function of the microscopic gradient. Further manipulation and substitution of Equation (3.8b) does not alleviate this condition. This is indicative that at some point in the development a localization assumption is required that will derive $\bar{g}$ from $\langle \bar{g} \rangle$.

Rather than integrate $\bar{g}$, a function of position within the RVE volume, over a complicated function defining the entire grain space, this expression is divided into an integration over one discrete particle ($Grain$) with a summation over P particles in the RVE as

$$\left\langle \bar{f} \right\rangle = -K_{Pore} \left\langle \bar{g} \right\rangle + \frac{1}{V} \sum_{p=1}^{P} \int_{Grain_p} (K_{Pore} - K_{Grains}) \bar{g} dV. \tag{3.12}$$

Multiplying by $^P/_P$ and recognizing that $^1/_P \sum_{p=1}^{P} x^p$ is the discrete notation for the volume average of quantity x, and, that $^P/_V$ is the number density of grains m,

Equation (3.12) is recast as

$$\left\langle \bar{f} \right\rangle = \text{-}K_{Pore} \left\langle \bar{g} \right\rangle + m \left\langle \bar{S} \right\rangle, \text{ with} \tag{3.13}$$

$$\bar{S} = \int_{Grain_p} (K_{Pore} - K_{Grains}) \bar{g} dV. \tag{3.14}$$

Equation (3.13) reflects that the macroscopic flux is affected by the pore space and by the inclusion of grains that supplant pore space in the RVE. The vector quantity $\bar{S}$ is a grain or particle parameter that captures the "dipole strength of the particle" above and beyond that of pore material occupying the same volume (Batchelor and O'Brien, 1977). This expression for the macroscopic flux is "exact for any shape, orientation, concentration and spatial arrangement of the particles" (Batchelor and O'Brien, 1977).

A few cases of K_{Pore} versus K_{Grains} are illustrative of useful applications of Equations (3.13) and (3.14). First, if $K_{Pore} = K_{Grains}$ it implies that the two microscopic constituents are indistinguishable in terms of material behavior. $\bar{S}$ equals zero and the macroscopic flux and gradient are simply linked through $K_{Pore} (= K_{Grains})$. This is equivalent to rendering microstructure irrelevant to the constitutive process in question and treating the RVE as a single constituent—a homogeneous material. Second, if $K_{Pore} \ll K_{Grains}$ then the macroscopic flux is dominated by the contribution of the grains and Equations (3.13) and (3.14) can be approximated as

$$\left\langle \bar{f} \right\rangle \approx m \left\langle \bar{S} \right\rangle, \text{ with} \tag{3.15}$$

$$\bar{S} \approx \int_{Grain_p} \text{-}K_{Grains} \bar{g} dV. \tag{3.16}$$

This approximation is applied below to the problem of heat conduction in the snow, where generic K corresponds to thermal conductivity k. It is justified on the basis that the thermal conductivity of ice (k_{Grains}) is approximately two orders of magnitude greater than that of air (k_{Pore}).

Similarly, the elastic behavior of snow—presented in the next chapter—is also treated as solely a grain space phenomenon. In this case it is technically not that K_{Pore} (a stiffness coefficient like Young's modulus) is small compared to K_{Grains}, but rather that K_{Pore} is undefined. A microscopic elastic constitutive relationship does not apply to the fluid-filled pore space—there is no empirical basis for treating the pore material like an elastic material where stress is a function of strain. Taking Equations (3.15) and (3.16) as identically true (defining K_{Pore} as zero) accomplishes the effect of rendering the pore space irrelevant to elastic response.

The development of Batchelor (1974) revolves around the notion expressed in Equation (3.13) that replacing pore space with grains will increase the flux, that is, $K_{Pore} < K_{Grains}$. This ensures that dipole strength $\bar{S}$ is always a grain parameter. However, for transport processes and properties that obviously pertain to the voids, the approach will be extended here in applying the concept of dipole strength to a void cell.

Take for example a constitutive model like Darcy's law that describes bulk fluid flow through a permeable material caused by a pressure gradient. The coefficient of proportionality in Darcy's model is $\mathbf{K}^* = {}^1\!/_{\mu}\boldsymbol{\kappa}^*$ where μ is the fluid dynamic viscosity and $\boldsymbol{\kappa}^*$ is the permeability of the porous medium. For a given fluid pressure gradient the flow obviously *decreases* with a greater number of grains, i.e., an increasing m. This contradicts the idea that the grain dipole strength enhances flux. It seems more appropriate to define instead a pore space parameter.

As with elasticity in the pore space, the concept of permeability does not exist for a solid grain material. It follows that K_{Grains} should equal zero here because a solid grain is impermeable to fluid flow. Applying this simplification to Equations (3.13) and (3.14) results in

$$\left\langle \bar{f} \right\rangle = -K_{Pore} \left\langle \bar{g} \right\rangle + m \left\langle \bar{S} \right\rangle, \text{ with} \tag{3.17}$$

$$\bar{S} = \int_{Grain_p} K_{Pore} \bar{g} dV. \tag{3.18}$$

In this example, the constitutive behavior exclusively occurs through the voids or pore space. Consequently, Equation (3.18), where dipole strength is defined as a grain parameter, yields some mathematical contradictions. First, the quantity $K_{Pore}\bar{g}$ is fluid flux in the pore space, yet it appears in an integral across a grain volume. Second, the field variable $\bar{g}$—fluid pressure gradient—cannot even be defined within the boundaries of a grain volume.

These contradictions are remedied by returning to Equation (3.10) and substituting instead the expression for $^1/_V \int_{Grains} \bar{g} dV$ from Equation (3.8b). After some algebraic simplification, the expression for macroscopic flux is

$$\left\langle \bar{f} \right\rangle = t \left\langle \bar{R} \right\rangle - K_{Grains} \left\langle \bar{g} \right\rangle, \text{ with} \tag{3.19}$$

$$\bar{R} = \int_{Void_p} (K_{Grains} - K_{Pore}) \bar{g} dV, \tag{3.20}$$

where t is the number density of void cells in the RVE and $\bar{R}$ is the dipole strength of a single void cell beyond that of grain material occupying the same volume. Finally, for situations where the contribution of the grains to the flux is undefined, the above

expressions reduce to

$$\left\langle \bar{f} \right\rangle = t \left\langle \bar{R} \right\rangle, \text{ with} \tag{3.21}$$

$$\bar{R} = \int_{Void_p} -K_{Pore} \bar{g} dV. \tag{3.22}$$

When it is reasonable to assume that $K_{Grains} = 0$, then the flux is driven solely through the pore space and it follows that a quantity like $\bar{R}$ should be defined as a void parameter.

To summarize, for the constitutive laws considered here, both conduction and elasticity are treated as grain space phenomena according to Equations (3.15) and (3.16). Here, the key is to define the *grain* parameter of dipole strength in terms of microstructural parameters. Conversely, fluid advection is treated as void space phenomena according to Equations (3.21) and (3.22). In this case, estimating the macroscopic flux depends on a *void* parameter instead. Vapor diffusion and phase change is a hybrid approach. The apparent conductivity of these phenomena is tied to both the void and grain space. In building upon previous particle-to-particle models, the approach here adopts the notion that the inclusion of ice grains enhances this overall energy transfer mode (Yosida, 1963; Colbeck, 1983b, 1993). Therefore, similar to pure conduction, dipole strength for apparent conductivity is defined as a grain parameter.

3.3 Thermal Conductivity

For homogeneous, isotropic materials the thermal conductivity tensor reduces to a scalar value. However, for a heterogeneous, two-constituent material like dry snow, the challenge is to define an effective thermal conductivity $\mathbf{k}^*$ that represents the

equivalent continuum. Batchelor and O'Brien (1977) applied the aforementioned mean field theory to derive the effective conductivity of a granular assembly. First, Fourier's law is written as

$$\langle \bar{q}_c \rangle = \text{-}k_{air} \langle \nabla\theta \rangle + m \left\langle \bar{S}_c \right\rangle. \tag{3.23}$$

Compared to Equation (3.13), the generic flux and gradient have been replaced by heat flux due to conduction $\bar{q}_c$ ($\mathrm{W/m^2}$) and the temperature gradient $\nabla\theta$ ($\mathrm{K/m}$), respectively. The mean heat flux of the equivalent continuum $\langle \bar{q}_c \rangle$ equals the sum of contributions from the pore space, $\text{-}k_{air} \langle \nabla\theta \rangle$, and the solid network of grains. Conduction through the grains equals the product of m, the number density of grains, and the volume averaged thermal dipole strength $\bar{S}_c$.

As an initial simplification, it is customary to assume that heat transfer primarily occurs through the grains and their connections. Adams and Sato (1993) and Kaempfer *et al.* (2005) also determined that the network of ice grains represents the most significant mechanism in determining snow's effective thermal conductivity. This simplification is reasonable if the ratio of the grain to pore conductivities is much larger than one (Vargas-Escobar, 2002). This is the case with snow where the conductivity of ice is approximately two orders of magnitude greater than that of air. Now, as in Equations (3.15) and (3.16), the mean heat flux of the equivalent continuum is approximated by

$$\langle \bar{q}_c \rangle \approx m \left\langle \bar{S}_c \right\rangle, \tag{3.24}$$

and the thermal dipole strength of a particle is taken as

$$\bar{S}_c \approx \text{-}k_{ice} \int_{V_p} \nabla\theta \mathrm{d}V, \tag{3.25}$$

where k_{ice} is the scalar thermal conductivity of the grain material, in this case ice, and V_p is the volume of a particle within a large volume V of the granular assembly. By application of Stoke's theorem, the volume integral in Equation (3.25) can be expressed as a surface integral:

$$\bar{S}_c \approx \int_{V_p} \bar{q}_c \mathrm{d}V = \int_{A_p} \bar{x}\bar{q}_c \cdot \hat{n} \mathrm{d}A, \tag{3.26}$$

where A_p is the surface of a particle, $\hat{n}$ is a unit outward normal vector to surface A_p, and $\bar{x}$ is a position vector to a point on A_p (Batchelor and O'Brien, 1977).

The simplification of neglecting pore conductivity has other important implications for analysis. If the grain conductivity is relatively large, then temperature gradients within individual particles are relatively small. The temperature within one grain is therefore approximately uniform and, in general, different from the temperature of neighboring grains. The temperature differences between neighboring grains establish the gradients that lead to heat flux. And, because conductivity across the pore space is so poor, heat flux is concentrated at points where neighboring grains are connected. Importantly, this establishes the fundamental microscopic unit of heat conduction as a grain and its connections with neighboring grains.

Because there are a finite number of contact points for a given grain, Equation (3.26) can be approximated as a discrete summation over i such intergranular con-

tacts:

$$\bar{S}_c \approx \sum_i \bar{x}^i H^i, \tag{3.27}$$

where H^i is the magnitude of the outward heat flow ($^{\mathrm{J}}/_{\mathrm{s}} = \mathrm{W}$) across A_p in the neighborhood of the i^{th} contact.

The problem now reduces to solving for microscopic heat flow at or near a point of contact. The bulk of the work in Batchelor and O'Brien (1977) is devoted to developing useful solutions for H for three different intergranular geometries: grains nearly in contact, grains with a point contact, and grains with a circular area of contact. With these varying geometries, Batchelor and O'Brien's primary result is an expression that describes how a single grain and its connectivity with other grains establish the conduction of the equivalent continuum.

Because it most closely approximates bonded ice grains, the geometry of circular contact areas is adopted here. Batchelor and O'Brien (1977) report that this microscopic heat flow was investigated by Lamb (1945) for relatively large bonds. This solution is

$$H = 2k_{ice}\rho\left(\theta_0 - \theta\right), \tag{3.28}$$

where ρ is the contact radius, θ_0 is taken as the temperature at the center of the isothermal reference grain and θ is the temperature at the center of the neighboring isothermal grain (see Figure 3.1). Batchelor and O'Brien (1977) also investigated the geometry of particles with circular areas of contact and offer a more general heat flow solution, also appropriate for relatively small bonds. Their numerical solution estimates that—for the conductivities of ice and air—"relatively large" bonds equates to $\rho \geq {}^1/_{10}R$, where R is the grain radius (Batchelor and O'Brien, 1977).

In addition to the heat flow through both large and small bonds, Batchelor and O'Brien (1977) also offer a solution for heat flow through the air immediately sur-

rounding a circular bond. For both simplicity and for later comparison with existing micromechanical models, Equation (3.28) is taken here to sufficiently characterize heat flow between bonded ice grains. Substituting Equation (3.28) into Equation (3.27) results in an approximation of the thermal dipole strength of a single particle in the granular assembly with i circular contacts with other particles:

$$\bar{S}_c \approx 2k_{ice} \sum_i \bar{x}^i \rho^i \left(\theta_0 - \theta^i\right). \tag{3.29}$$

Both ρ and θ carry the superscript in recognition that, with respect to the reference grain, these quantities may vary from contact point to contact point (see Figure 3.1).

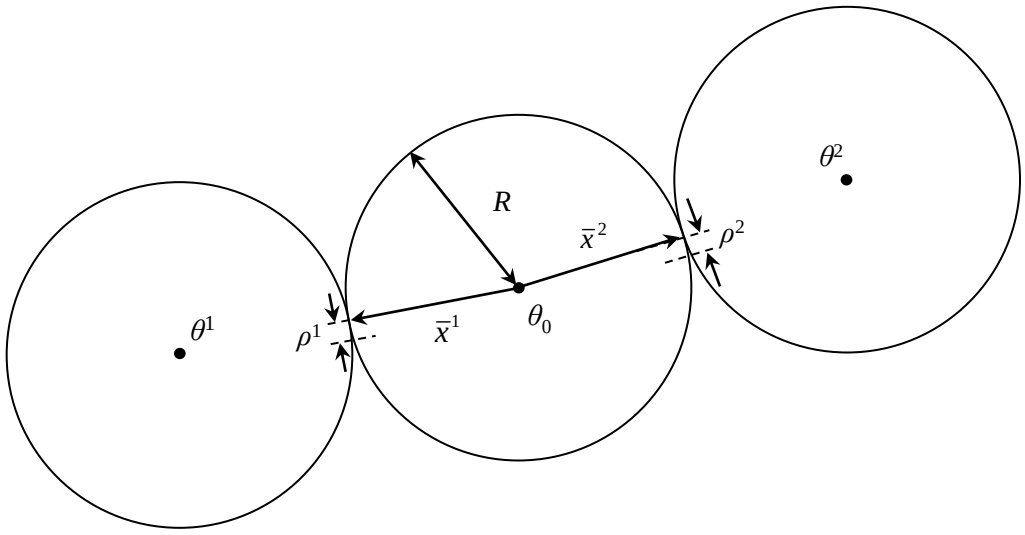


Figure 3.1: An idealized granular assembly and associated quantities for calculating effective thermal conductivity, as applied in Equation 3.29.

Batchelor and O'Brien (1977) were interested only in an effective scalar conductivity so they eventually drop the directionality in Equation (3.29). However, if starting with this definition of $\bar{S}_c$ and following through with the vector notation,

their approach yields the effective thermal conductivity $\mathbf{k}^*$ in terms of the contact tensor.

The volume average of $\bar{S}_c$, required in Equation (3.24), involves summing over P particles:

$$\left\langle \bar{S}_c \right\rangle = \frac{1}{P}\sum_{p=1}^{P} \bar{S}_c^p = \frac{1}{P}\sum_{p=1}^{P}\left\{ 2k_{ice}\sum_i \bar{x}^i\rho^i\left(\theta_0-\theta^i\right)\right\}^p = \frac{2k_{ice}}{P}\sum_{\alpha=1}^{N}\bar{x}^\alpha\rho^\alpha\left(\theta_0-\theta^\alpha\right), \tag{3.30}$$

where summing over P particles, each with i contacts, is the same as executing one summation over N total contact normals. The following simplifications are then applied to $\left\langle \bar{S}_c \right\rangle$ (Batchelor and O'Brien, 1977):

- Each particle can be represented by an average radius $\hat{R}$ such that $\bar{x}^\alpha = \hat{R}\bar{n}^\alpha$,
- Likewise, each contact can be represented by an average contact radius $\hat{\rho}$,
- The temperature difference is given by

$$\left(\theta_0-\theta^\alpha\right) = 2\bar{x}^\alpha\cdot\left\langle\nabla\theta\right\rangle, \tag{3.31}$$

and the heat flux of the equivalent continuum becomes:

$$\left\langle \bar{q}_c \right\rangle \approx m\left\langle \bar{S}_c \right\rangle = \frac{4\hat{R}^2 m k_{ice}\hat{\rho}}{P}\sum_{\alpha=1}^{N}\bar{n}^\alpha\otimes\bar{n}^\alpha\cdot\left\langle\nabla\theta\right\rangle. \tag{3.32}$$

The final simplification in the list above warrants further explanation. Equation (3.31) is the required localization operation, deriving local temperature differences from the macroscopic temperature gradient. The assumption is that the temperature difference between two spherical grains is everywhere linear with the global temper-

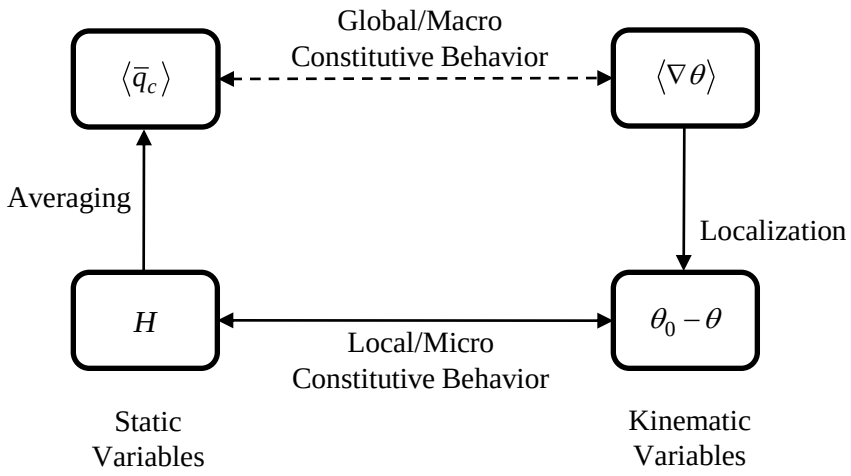


Figure 3.2: Homogenization Scheme for Thermal Conductivity

ature gradient. Equation (3.31) is the final element in the homogenization scheme, summarized in Figure 3.2. It is useful at this point to review the components:

- *Localization:* Equation (3.31),
- *Local/Micro Constitutive Behavior:* Equation (3.28) ,
- *Averaging:* Equation (3.24).

Equation (3.32) is the global constitutive behavior, linking the macroscopic field variables through the microscopic scale.

Accordingly, the effective thermal conductivity of the equivalent continuum is identified from Equation (3.32) as

$$\mathbf{k}^* = \frac{4\hat{R}^2 m k_{ice} \hat{\rho} N}{P} \left(\frac{1}{N} \sum_{\alpha=1}^{N} \bar{n}^\alpha \otimes \bar{n}^\alpha \right). \tag{3.33}$$

Recognizing the following geometric groups greatly simplifies this expression:

- The volume fraction of spherical ice particles: $\phi = \frac{4}{3}\pi \hat{R}^3 m$,

- The average number of contacts per particle, or coordination number: $\mathcal{N} = \frac{N}{P}$,
- The discrete form of the contact tensor (Equation (2.9a)): $\mathbf{F} = \frac{1}{N}\sum_{\alpha=1}^{N} \bar{n}^{\alpha} \otimes \bar{n}^{\alpha}$,
- The isotropic value of the 3-D contact tensor: $f = \frac{1}{3}$.

The effective thermal conductivity tensor is now written as

$$\boxed{\mathbf{k}^{*} = \frac{1}{\pi}\phi\mathcal{N}k_{ice}\frac{\hat{\rho}}{\hat{R}}\frac{1}{f}\mathbf{F}.} \tag{3.34}$$

The incorporation of the contact tensor $\mathbf{F}$ accounts for the textural anisotropy of the granular assembly. So, this effective material property depends upon pertinent microstructural scalar quantities and the directional distribution of the contacts.

To demonstrate that this derivation is consistent with Batchelor and O'Brien's work, consider their scalar isotropic result:

$$\boxed{k^{*}_{B\&O} = \frac{1}{\pi}\phi\mathcal{N}k_{ice}\frac{\hat{\rho}}{\hat{R}}.} \tag{3.35}$$

This expression is the effective scalar conductivity when the arrangement of ice grains is statistically isotropic. Now recall Equation (2.16), where in the isotropic case the contact tensor reduces to $f\boldsymbol{\delta}$. Then, Equation (3.34) becomes

$$\mathbf{k}^{*} = \frac{1}{\pi}\phi\mathcal{N}k_{ice}\frac{\hat{\rho}}{\hat{R}}\boldsymbol{\delta}, \tag{3.36}$$

and each component of this tensor matches Batchelor and O'Brien's scalar result in Equation (3.35). Equivalently, Equation (3.34) can be written in the principal orientation of the contact tensor as

$$\mathbf{k}^* = k^*_{B\&O}\frac{1}{f}\mathbf{F} = k^*_{B\&O}\begin{bmatrix} \frac{F_{11}}{f} & 0 & 0 \\ 0 & \frac{F_{22}}{f} & 0 \\ 0 & 0 & \frac{F_{33}}{f} \end{bmatrix}. \tag{3.37}$$

The scalar effective thermal conductivity, $k^*_{B\&O}$, incorporates pertinent scalar microstructural quantities for any textural symmetry. The quantity $(1/f)\,\mathbf{F}$ reduces to the identity tensor for an isotropic arrangement, and the contact tensor $\mathbf{F}$ drives any directional variation in $\mathbf{k}^*$ for textural departures from isotropy. This derivation demonstrates how the contact tensor can describe an effective material property with directional dependence. Equation (3.37) will also be useful in drawing parallels between between the effect of fabric on this simpler 2^{nd} order transport property and the more complex 4^{th} order linear elastic stiffness tensor.

Equation (3.34) is the simplest expression of anisotropic effective conductivity. The only quantity that varies with direction is $\bar{n}$. However, the derivation is not so rigid that other parameters cannot vary with direction. Equation (3.34) neatly yields the contact tensor as first presented in Chapter 2. In contrast, a tensor that accommodates variables other than dimensionless unit vectors is still a fabric tensor—just a perturbation of the fundamentals reviewed in Chapter 2.

For example, instead of using an average bond radius in an RVE, permit bond radius to vary across α contacts. The effective conductivity tensor is now

$$\boxed{\mathbf{k}^* = \frac{3}{\pi}\phi\mathcal{N}k_{ice}\frac{1}{\hat{R}}\left(\frac{1}{N}\sum_{\alpha=1}^{N}\rho^{\alpha}\bar{n}^{\alpha}\otimes\bar{n}^{\alpha}\right).} \tag{3.38}$$

Compare this result to Equation (3.34). Here, the parenthetical expression does not reduce to $\mathbf{F}$. The coefficients of this tensor carry the magnitude and units of bond radius and the isotropic value of this tensor does not equal f. So, while the anisotropic

tensor in Equation (3.38) is not as mathematically elegant, if bond radius also exhibits anisotropy, it should be more accurate and is not computationally more difficult.

3.4 Diffusivity

Appendix A outlines the qualitative and quantitative principles behind vapor diffusion, phase change, and energy flux in a porous snowpack. They are briefly addressed here for the purpose of setting the stage for an effective diffusivity tensor. The fundamental microscopic unit of vapor diffusion is an individual void cell and the ice grains that surround it. Water vapor diffuses across the pore space driven by regions of relatively higher or lower vapor pressure at the interface of the pore space and adjacent ice grains. Vapor pressure differences are driven by temperature variations in the adjacent ice grains. This idea meshes with the idealizations of pure conduction, where each ice grain is assumed to be isothermal and at a different temperature than its neighboring grains.

The energy transfer due to the processes of phase change and vapor flux also fits into the same context as conductivity. The specific aim of the developments at the outset of this chapter and in Appendix A is to couch these processes as a "heat" flux. It follows then that Equation (3.23) is tailored for this apparent heat flux $\langle \bar{q}_{vap} \rangle$ ($\mathrm{W/m^2}$) as

$$\langle \bar{q}_{vap} \rangle = -k'_{air} \langle \nabla \theta \rangle + m \left\langle \bar{S}_{vap} \right\rangle. \tag{3.39}$$

k'_{air} ($\mathrm{W/m \cdot K}$), the apparent conductivity of the pore space contributing to this flux (see Appendix A) is

$$k'_{air} = \frac{L_s^2 p_{sat} D_{vap}}{R_{vap}^2 \theta^3}, \tag{3.40}$$

where D_{vap} is the diffusivity of water vapor in the air-filled pore space. In the problem of pure conduction the thermal conductivity of air was neglected. The pore space contribution to the overall flux in Equation (3.39) is retained.

The grain parameter $\bar{S}_{vap}$ is again approximated by a discrete summation, similar to Equation (3.27) in the case of pure conduction:

$$\bar{S}_{vap} \approx L_s \sum_i \bar{x}^i M^i. \tag{3.41}$$

In this case i corresponds to points of concentrated phase change L_s ($^{\mathrm{J}}/_{\mathrm{kg}}$) and mass flow rate M ($^{\mathrm{kg}}/_{\mathrm{s}}$) at the surface of a given ice particle either from sublimation or deposition. The idea expressed by Equation (3.39) is that the apparent heat flux exists in the absence of grains ($m = 0$) through k'_{air}, but that the overall flux is enhanced by supplanting pore space with ice particles. Because the particles are the same substance as water vapor, just a different phase, they act as microscopic sources and sinks of water vapor, decrease microscopic paths of diffusion, and improve the macroscopic energy flux. This concept is consistent with previous analytical approaches and supported by empirical data (Yosida, 1963; Colbeck, 1993).

Equation (3.41) represents the contribution of a single ice grain to the overall flux. Applying this expression requires that the phase change and mass flow at the surface of an ice particle can be captured by a discrete number of points where this phenomenon is concentrated. The position vectors $\bar{x}^i$ in Equation (3.41) identify such points. With conductivity, the intergranular contacts are the physical conduits for heat diffusion; they represent obvious points around the surface of a particle across which heat energy is transferred. Identifying points of concentrated phase change and mass flow around the surface of a particle is more challenging.

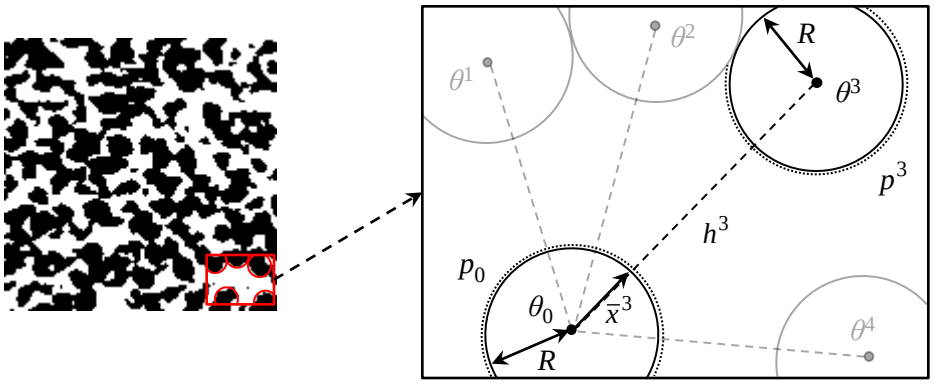


Figure 3.3: A void cell with idealized grains and associated quantities for calculating apparent conductivity, as applied in Equation (3.47)

Figure 3.3 illustrates a void cell with a reference grain at temperature θ_0 and adjacent grains at temperatures θ^i. As a consequence of temperatures θ^i, water vapor pressures p^i exist at the available surface area of particles at temperatures θ^i. Because each ice grain is assumed isothermal, there are no variations in p^i for a given particle due to temperature variations. Additionally, because the grains are idealized as spheres of uniform radius, there are no variations for a given particle in p^i due to surface curvature effects. Therefore, for a pair of grains with vapor pressures p^i immediately adjacent to their surfaces, the largest one-dimensional pressure gradient corresponds to the shortest distance between them. This minimum path of diffusion is a line connecting their centroids. Such lines h^i are included in Figure 3.3 for the reference grain. Vectors $\bar{x}^i$ are defined by the points where h^i intersect the surface of a given particle. Vectors $\bar{x}^i$ identify points of concentrated phase change and mass flow at the surface of a given ice grain.

This idealization is supported by empirical evidence (Akitaya, 1985). In this study, laboratory experiments using ice hemispheres were used to record recrystallization.

The experimental geometry closely approximates the idealized geometry in Figure 3.3. Five grains in contact were arranged horizontally on the cold side of a temperature-controlled microscope stage. Likewise, five grains in contact were arranged on the warm side. These two rows of grains were separated by void space. The temperature gradient across the stage was $520\,{}^{\mathrm{K}}/_{\mathrm{m}}$. The resulting time-lapse images are depicted in Figure 3.4. These images support using vectors $\bar{x}^i$ (see Figure 3.3) to identify points of concentrated phase change and mass flow at the surface of a spherical ice grain. In particular, grain pairs with shorter diffusion paths highlight the vapor diffusion and phase change process: a–f, c–h, d–h, d–i, and e–i.

The remaining quantity required to evaluate Equation (3.41) is M^i: the microscopic mass flow rate at or near a point i. The expression presented in Colbeck (1983a,b, 1993) for mass flow rate is adopted here:

$$M = 4\pi C D_{vap} \left(\rho_0 - \rho\right), \tag{3.42}$$

where D_{vap} $({}^{\mathrm{m}^2}/_{\mathrm{s}})$ is again the diffusivity of water vapor in air, ρ_0 and ρ $({}^{\mathrm{kg}}/_{\mathrm{m}^3})$ are the vapor densities adjacent to the reference grain and neighboring grain, respectively, and $4\pi C$ (m) is an electrostatic analogy quantifying the capacitance for neighboring particles of opposite charge. Colbeck (1983b) empirically approximates C:

$$C = 1.65\hat{R}\left(\frac{\hat{R}}{h}\right)^{0.52}, \tag{3.43}$$

where $\hat{R}$ is again the uniform particle radius and h is the center-to-center particle spacing. For simplicity, Equation (3.43) is used here as

$$C = 1.65\hat{R}\left(\frac{\hat{R}}{h}\right)^{1/2}. \tag{3.44}$$

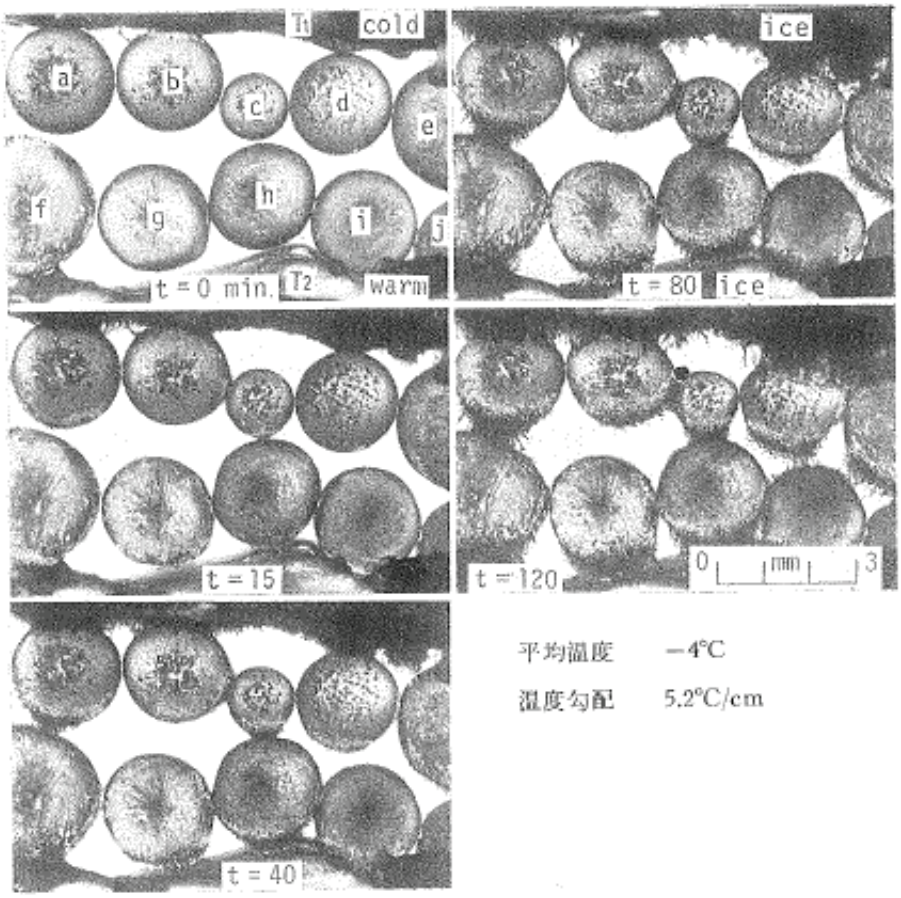


Figure 3.4: Time-lapse microscopic photography of the recrystallization of ice hemispheres subject to a $520\,^{\mathrm{K}}/_{\mathrm{m}}$ temperature gradient. These images are taken from Akitaya (1985), Figure 5.

The driving vapor density difference in Equation (3.42) can be related to vapor pressures using the ideal gas law, $\rho = {}^{p}/_{R_{vap}\theta}$. This, combined with Equation (3.44), results in a mass flow rate expression of

$$M = 4\pi \left(1.65\hat{R} \left(\frac{\hat{R}}{h} \right)^{1/2} \right) \frac{D_{vap}}{R_{vap}\theta} \left(p_0 - p \right). \tag{3.45}$$

The equation for $\bar{S}_{vap}$ is now

$$\bar{S}_{vap} \approx \frac{L_s D_{vap}}{R_{vap}\theta} 6.6\pi \hat{R}^{3/2} \sum_i \bar{x}^i \left(h^{-1/2} \right)^i \left(p_0 - p^i \right). \tag{3.46}$$

Both h and p carry the superscript because these quantities may vary from point to point whereas $\hat{R}$ does not.

As with $\bar{S}_c$, the volume average of $\bar{S}_{vap}$ involves summing over P particles:

$$\begin{aligned} \left\langle \bar{S}_{vap} \right\rangle &= \frac{1}{P} \sum_{p=1}^{P} \bar{S}_{vap}^{p} = \frac{1}{P} \sum_{p=1}^{P} \left\{ \frac{L_s D_{vap}}{R_{vap}\theta} 6.6\pi \hat{R}^{3/2} \sum_i \bar{x}^i \left(h^{-1/2} \right)^i \left(p_0 - p^i \right) \right\}^p, \\ &= \frac{L_s D_{vap}}{R_{vap}\theta} 6.6\pi \hat{R}^{3/2} \frac{1}{P} \sum_{\beta=1}^{N} \bar{x}^\beta \left(h^{-1/2} \right)^\beta \left(p_0 - p^\beta \right), \end{aligned} \tag{3.47}$$

where summing over P particles, each with i points of concentrated apparent heat flux, is the same as executing one summation over N total "centroid normal" vectors $\bar{n}_{cent}$. The following assumptions are then applied to $\left\langle \bar{S}_{vap} \right\rangle$:

- For spherical particles of uniform radius: $\bar{x}^\beta = \hat{R}\bar{n}_{cent}^{\beta}$,
- The vapor pressure difference is given by

$$\left(p_0 - p^\beta \right) = h^\beta \bar{n}_{cent}^{\beta} \cdot \left\langle \nabla p \right\rangle. \tag{3.48}$$

As with pure conduction, this last simplification is the localization assumption—deriving local vapor pressure differences from the macroscopic vapor pressure gradient. The same kinematic assumption is applied here: local pressure differences are everywhere linear with the global pressure gradient. Center-to-center grain spacing is also used here, the difference being that the grains are not connected but separated by a void cell. Interestingly, this is the exact geometry that Colbeck (1983b, 1993) applies in relating local vapor density/temperature fields to global vapor density/temperature gradients. It is referred to in these papers as a "geometrical enhancement factor".

By the arguments in Appendix A, the pressure gradient can be cast in terms of the temperature gradient via the chain rule and Clausius-Clapeyron relationship as

$$\left(p_0 - p^\beta\right) = h^\beta \bar{n}^\beta_{cent} \cdot \frac{dp_{vap}}{d\theta} \langle \nabla\theta \rangle = \frac{L_s p_{sat}}{R_{vap}\theta^2} h^\beta \bar{n}^\beta_{cent} \cdot \langle \nabla\theta \rangle \,. \tag{3.49}$$

Incorporating the bulleted assumptions into Equation (3.47) yields

$$\left\langle \bar{S}_{vap} \right\rangle = \frac{L_s^2 p_{sat} D_{vap}}{R_{vap}^2 \theta^3} 6.6\pi \hat{R}^{5/2} \frac{1}{P} \sum_{\beta=1}^{N} \left(h^{1/2}\right)^\beta \bar{n}^\beta_{cent} \otimes \bar{n}^\beta_{cent} \cdot \langle \nabla\theta \rangle \,. \tag{3.50}$$

Finally, returning to the expression for the overall apparent flux results in

$$\begin{aligned} \langle \bar{q}_{vap} \rangle &= \text{-}k'_{air} \langle \nabla\theta \rangle + m \left\langle \bar{S}_{vap} \right\rangle, \\ &= \text{-}\frac{L_s^2 p_{sat}}{R_{vap}^2 \theta^3} \left\{ D_{vap} + m D_{vap} 6.6\pi \hat{R}^{5/2} \frac{1}{P} \sum_{\beta=1}^{N} \left(h^{1/2}\right)^\beta \bar{n}^\beta_{cent} \otimes \bar{n}^\beta_{cent} \right\} \cdot \langle \nabla\theta \rangle \,. \end{aligned} \tag{3.51}$$

This completes the homogenization algorithm for the energy transfer due to phase change and vapor flux:

- *Localization:* Equations (3.48) and (3.49),

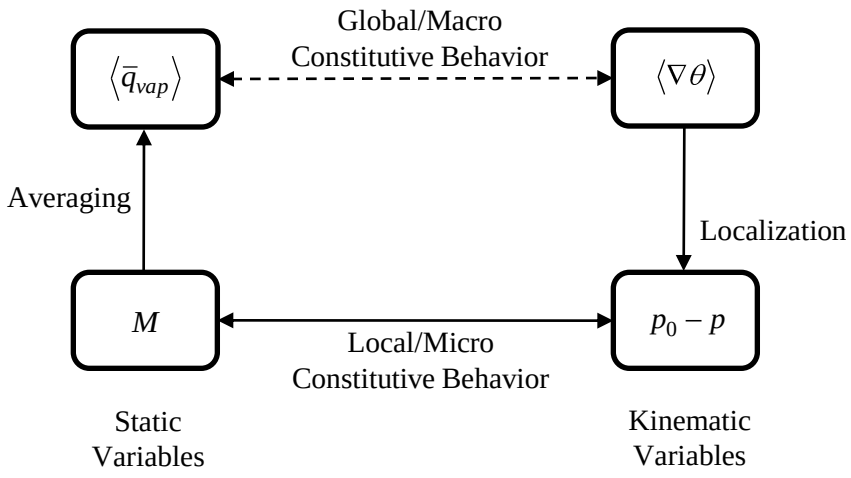


Figure 3.5: Homogenization Scheme for Apparent Conductivity

- *Local/Micro Constitutive Behavior:* Equation (3.45) ,
- *Averaging:* Equation (3.39).

This is also depicted in Figure 3.5.

The effective diffusivity tensor of the equivalent continuum is the bracketed expression in the above equation:

$$\mathbf{D}^* = D_{vap}\left(\boldsymbol{\delta} + m6.6\pi\hat{R}^{5/2}\frac{1}{P}\sum_{\beta=1}^{N}\left(h^{1/2}\right)^{\beta}\bar{n}_{cent}^{\beta}\otimes\bar{n}_{cent}^{\beta}\right). \tag{3.52}$$

Defining a few terms can tidy this expression:

- The volume fraction of spherical ice particles: $\phi = \frac{4}{3}\pi\hat{R}^3 m$,
- The average number of "centroid normal" vectors $\bar{n}_{cent}$ per particle: $\mathcal{Q} = \frac{N}{P}$.

The effective diffusivity tensor is now written as

$$\boxed{\mathbf{D}^* = D_{vap}\left(\boldsymbol{\delta} + 4.95\phi\mathcal{Q}\hat{R}^{-1/2}\frac{1}{N}\sum_{\beta=1}^{N}\left(h^{1/2}\right)^{\beta}\bar{n}_{cent}^{\beta}\otimes\bar{n}_{cent}^{\beta}\right).} \tag{3.53}$$

Additional assumptions further reduce the anisotropic tensor:

- An average quantity $\hat{h}$ characterizes the center-to-center grain spacing,
- The discrete notation of a fabric tensor formed from "centroid normal" vectors: $\mathbf{F_{vap}} = \frac{1}{N}\sum_{\beta=1}^{N} \bar{n}_{cent}^{\beta} \otimes \bar{n}_{cent}^{\beta}$,
- The isotropic value of this 3-D fabric tensor: $f_{vap} = \frac{1}{3}$.

Now, in its simplest anisotropic form, the diffusivity tensor is:

$$\boxed{\mathbf{D}^* = D_{vap}\left(\boldsymbol{\delta} + \frac{5}{3}\phi\mathcal{Q}\left(\frac{\hat{h}}{\hat{R}}\right)^{1/2}\frac{1}{f_{vap}}\mathbf{F_{vap}}\right).} \tag{3.54}$$

If the distribution of "centroid normal" vectors is uniform or random then the quantity $(1/f_{vap})\,\mathbf{F_{vap}}$ reduces to the identity tensor, indicating an isotropic effective diffusivity:

$$\boxed{D^* = D_{vap}\left(1 + \frac{5}{3}\phi\mathcal{Q}\left(\frac{\hat{h}}{\hat{R}}\right)^{1/2}\right).} \tag{3.55}$$

While Equation (3.54) is the simplest form of the anisotropic diffusivity tensor, Equation (3.53) is more general without levying any assumptions on void space geometry. The primary assumption in deriving Equation (3.54) from Equation (3.53) is that h, the center-to-center particle spacing, does not vary with index β. For grains of uniform radius $\hat{R}$, this is tantamount to declaring that the path of diffusion between neighboring ice particles is also uniform. If this quantity varies significantly with orientation, then Equation (3.53) should yield more accurate results.

3.5 Permeability

Permeability $\boldsymbol{\kappa}^*$ (m^2) and dynamic viscosity μ ($\mathrm{Pa} \cdot \mathrm{s}$) are two material properties that relate a fluid pressure gradient ∇P ($^{\mathrm{Pa}}/_{\mathrm{m}}$) to the Darcy flux or superficial flow velocity $\bar{\mathrm{d}}$ ($^{\mathrm{m}}/_{\mathrm{s}}$) in a porous medium through Darcy's law:

$$\bar{\mathrm{d}} = \frac{1}{\mu} \boldsymbol{\kappa}^* \cdot \nabla P. \tag{3.56}$$

Darcy flux or superficial flow velocity is the velocity of the fluid if it occupied the entirety of the RVE. To solve for an average advective velocity $\bar{u}$ in the pore space, one must account for the presence of impermeable matter like grains. This is usually accomplished with the following relationship between void volume fraction or porosity ϵ, $\bar{\mathrm{d}}$, and $\bar{u}$ (Dullien, 1992; Nield and Bejan, 2006):

$$\bar{\mathrm{d}} = \epsilon \bar{u}. \tag{3.57}$$

Darcy's law applies to laminar flows in a fluid-saturated pore space. Darcy's law may apply to either liquid and gaseous flows. For snow with liquid water content the pore space is far from saturated. Therefore, other constitutive formulations are applied in describing liquid water flow through snow. In dry snow the pore space is necessarily saturated with air. Darcy's law can describe such a flow.

In snow, it is usually estimated that both permeability and the pressure gradient are too low to result in bulk fluid motion through the pore space. Nevertheless, permeability is pursued here for three reasons: 1) it is illustrative of how mean field theory can apply to an exclusively pore space phenomenon, 2) the effective material properties developed here are generally applicable to a broader range of granular

materials, and 3) the potential anisotropy of permeability in snow has never been considered.

Besides impacting fluid flow, permeability is important to energy analysis in determining the onset and extent of free and forced convection. Anisotropic snow morphologies like near-surface facets and surface hoar form at or near the snow surface and are subject to forced convection. Until the anisotropic material properties of such anisotropic snow layers are considered, the balance of mass and energy cannot fully be characterized.

The arguments for effective permeability stem directly from the assumptions applied to the vapor diffusion problem. The rationale for treating an individual pore or void cell as isobaric and isothermal—a system in quasistatic equilibrium—is outlined in Appendix A. The coupled interactions of a network of pores, each at a slightly different total pressure and temperature, dictate any bulk fluid flow through snow. This is analogous to the idea in pure conduction that the connections between ice grains, each at a different temperature, determine heat flow in the snow.

Because the gradient of total gaseous pressure can only be defined in the void space, Equation (3.21) is the appropriate form of the mean field theory. Specifically for this constitutive relationship the expression becomes

$$\langle \bar{\mathrm{d}} \rangle \;=\; t \langle \bar{R} \rangle \,, \tag{3.58a}$$

where t is the number density of void cells and the pore parameter $\bar{R}$ is approximated as a discrete summation, here as

$$\bar{R} \approx \sum_i \bar{x}^i Q^i, \tag{3.58b}$$

where Q^i ($^{m^3}/_s$) is the volume flow rate across the surface of a void cell at the i^{th} point where it is connected to another void cell. Again, the position vectors $\bar{x}^i$ identify the points i of connectivity between a given void cell and its neighbors. The summation approximation is certainly justified here, as fluid flow between pores must occur through their connections—there is no potential for fluid flow through the grain space.

In many capillary-type porosity models the classic Hagen-Poiseuille flow solution to the momentum equation is used to characterize the flow through the pore space. This closed-form solution is applicable to a fully developed laminar flow through a cylindrical pipe of radius r. The channels that connect void cells are the points through which Q must be characterized. It is assumed here that such flow conditions exist inside these channels. The Hagen-Poiseuille solution yields a volume flow rate of

$$Q = \frac{\pi r^4}{8\mu}\left(-\frac{dP}{dx}\right), \tag{3.59}$$

where $^{dP}/_{dx}$ is the unidirectional pressure gradient along the longitudinal axis of the channel.

Substituting Equation (3.59) into Equation (3.58b) yields the pore parameter for a single pore:

$$\bar{R} \approx \frac{\pi}{8\mu}\sum_i \bar{x}^i \left(r^4\right)^i \left(-\frac{dP}{dx}\right)^i. \tag{3.60}$$

The derivative of a continuous total pressure field presents a mathematical challenge given the microstructural assumptions. Each void cell is assumed an isobaric space where pressure is defined at a given pore centroid. Similar to the assumed temperature field in the conduction problem, this requires a jump discontinuity in pressure at the boundary between void cells where the derivative is undefined. Consequently, a finite

difference quotient is used instead:

$$\left(-\frac{dP}{dx}\right)^i \approx \left(-\frac{\triangle P}{\triangle x}\right)^i \approx \frac{(P_0 - P^i)}{2\hat{R}_{void}}, \tag{3.61}$$

where, for mathematical simplicity, analogy to the grain space problems, and for stereological constraints, void cells will also be assumed spheres of uniform radius $\hat{R}_{void}$. The following assumptions are also applied to $t\left\langle \bar{R} \right\rangle$:

- Position vectors $\bar{x}^i$ are related to average cell radius as $\bar{x}^i = \hat{R}_{void}\bar{n}^i_{void}$,
- Every channel connecting void cells can be represented by an average radius $\hat{r}$,
- The total pressure difference is given by

$$\left(P_0 - P^i\right) = 2\hat{R}_{void}\bar{n}^i_{void} \cdot \left\langle P \right\rangle, \tag{3.62}$$

where $\bar{n}^i_{void}$ is an outward unit normal vector to the surface of the void cell at its i^{th} connection with a neighboring void.

Applying these assumptions to the expression for macroscopic Darcy flux and simplifying yields

$$\left\langle \bar{\mathrm{d}} \right\rangle = t\left\langle \bar{R} \right\rangle = \frac{1}{\mu}\left\{ \frac{\pi t \hat{R}_{void}\hat{r}^4 N}{8C} \frac{1}{N}\sum_{\gamma=1}^{N} \bar{n}^\gamma_{void} \otimes \bar{n}^\gamma_{void} \right\} \cdot \left\langle P \right\rangle, \tag{3.63}$$

where C is the total number of void cells and N is the total number of "void normal" vectors $\bar{n}_{void}$ in the RVE. The bracketed expression in Equation (3.63) is the permeability tensor. Recognizing some geometric quantities further simplifies this expression:

- The volume fraction of void cells or porosity: $\epsilon = \frac{4}{3}\pi\hat{R}^3_{void}t$,

- The average number of "void normal" vectors $\bar{n}_{void}$ per cell: $\mathcal{C} = \frac{N}{C}$,
- The discrete notation of a fabric tensor formed from "void normal" vectors: $\mathbf{F_{void}} = \frac{1}{N}\sum_{\gamma=1}^{N} \bar{n}^{\gamma}_{void} \otimes \bar{n}^{\gamma}_{void}$,
- The isotropic value of this 3-D fabric tensor: $f_{void} = \frac{1}{3}$.

The permeability tensor can now be written as

$$\boxed{\boldsymbol{\kappa}^* = \frac{1}{32}\epsilon\mathcal{C}\left(\frac{\hat{r}^2}{\hat{R}_{void}}\right)^2 \frac{1}{f_{void}}\mathbf{F_{void}}.} \tag{3.64}$$

This is the most general anisotropic form of the tensor. Again, if the distribution of the directional quantity $\bar{n}_{void}$ is statistically random/uniform then the isotropic microstructural permeability is

$$\boxed{\kappa^* = \frac{1}{32}\epsilon\mathcal{C}\left(\frac{\hat{r}^2}{\hat{R}_{void}}\right)^2.} \tag{3.65}$$

As before, if some other microstructural quantity varies significantly with orientation, then a more general form of the anisotropic tensor than Equation (3.64) is required.

To summarize, the list below and Figure 3.6 review the homogenization algorithm for permeability.

- *Localization:* Equation (3.62)
- *Local/Micro Constitutive Behavior:* Equations (3.59) and (3.61),
- *Averaging:* Equation (3.58a).

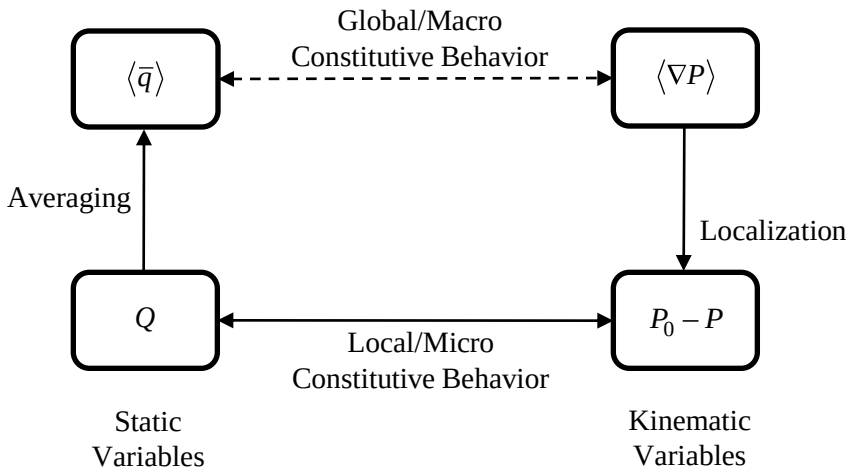


Figure 3.6: Homogenization Scheme for Permeability

3.6 Summary

Expressions for general anisotropic material property tensors were developed in this chapter based on homogenization techniques for granular materials. In every case, volume averaging techniques were applied to relate microscopic flows to macroscopic fluxes. Relating such macroscopic fluxes and gradients identifies effective material properties, expressed in terms of microstructural variables. Also, in every case the localization assumption—deriving microscopic primary field variables (here, temperature and pressure) from macroscopically applied gradients—was based on mean field theory. Mean field theory restricts differences in local field variables to be everywhere linear with their macroscopic counterpart.

Once the localization and averaging operations are established, the fundamental problem is to describe the microscopic constitutive relationship. This involves: 1) identifying the fundamental microstructural unit, and 2) describing the microscopic flow at this level. For the problem of conduction, this pair is heat flow between

connected ice grains. For the apparent conduction due to phase change and vapor diffusion, the analysis involves the mass flow of water vapor across a void between neighboring grains. For permeability, the problem is volume flow between connected void cells.

The derivations highlight the flexibility of the theory, applied here to a two-constituent microstructure: grain and void. The first two properties presented, conductivity and diffusivity, are widely recognized as important contributors to energy transfer within seasonal snowpacks. Energy transfer is framed here as a grain space problem and the grain dipole strength is a fundamental quantity. Grain dipole strength requires defining idealized points on the particle surface where energy is transferred and determining whether that transfer is due to conduction or phase change/vapor diffusion (Figure 3.7). The microscopic geometry and flow solution are both important. The microscopic heat flow used here (Equation (3.28)) is an approximate solution of the heat equation, while the adopted microscopic mass flow (Equation (3.42)) is a semi-empirical solution of the continuity equation. Different geometric assumptions and flow solutions may be explored.

Permeability is treated here as an exclusive function of the pore space and the dipole strength is a void parameter. The microstructural geometry describes the void space and the microscopic flow (Equation (3.59)) is a closed-form solution of the momentum equation. Permeability within a snowpack is generally viewed as being many orders of magnitude too small to permit advective gaseous flow and promote the onset of natural convection (Jordan *et al.*, 1999). However, different boundary conditions at the snow surface indicate that forced convection due to wind is an important mechanism of surface energy exchange and externally applied flows permeate the snowpack to some extent. Anisotropic snow morphologies like surface

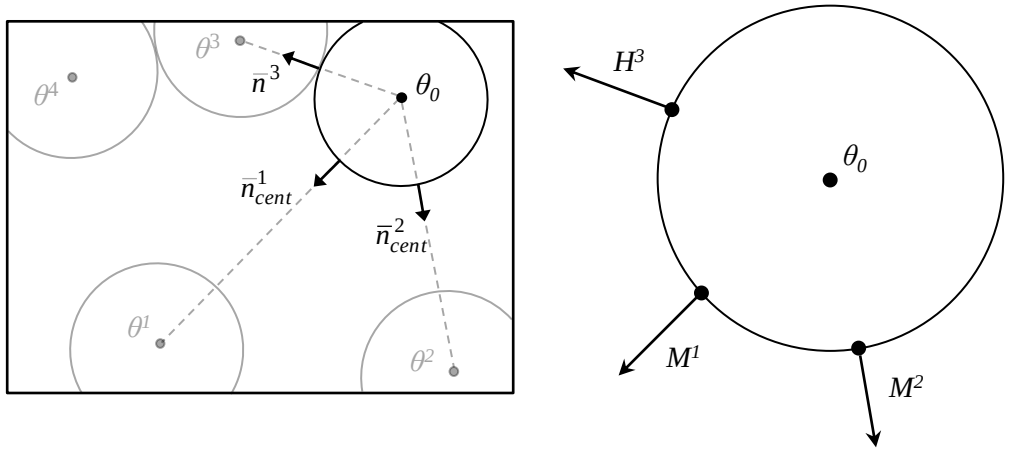


Figure 3.7: On the left is an idealized microstructure and directional data for a reference grain exchanging energy with three neighboring grains: with 1 and 2 via phase change/vapor diffusion and with 3 via conduction. The sketch on the right shows the simplified points on the surface of the reference grain where these exchanges occur. Also displayed are the microscopic heat (H) and mass (M) flows at these points that contribute to the macroscopic energy flux.

hoar exist at the snow surface, so the anisotropic permeability tensor presented here may be useful to such applied problems.

The models developed here for conductivity and permeability are generally applicable to any granular material and need not be restricted to snow. The diffusivity model, because it is linked to phase change, is not generally applicable to a two-constituent microstructure. It is presented specifically for snow but might apply to other *two-phase* microstructures. In Chapter 4, the principles of homogenization will be applied to the problem of elasticity. In Chapter 5, both the transport models developed here and the elasticity model from Chapter 4 will be compared to existing models and available data to assess their validity.

CHAPTER 4

EFFECTIVE PROPERTIES: ELASTIC STIFFNESS

4.1 Elastic Stiffness Coefficients

The elastic properties of snow are important to understanding the quasi-static mechanical behavior of a granular material and serve as a gateway to more complicated deformation analysis. Confronting the 4^{th} order stiffness tensor $\mathbb{C}$ adds complication in deriving effective material properties. Consider even the simplest case of an isotropic microstructure: grains and voids impact only one material constant in the case of the transport properties but two independent constants in elasticity. As a result, analytical and numerical analyses indicate that transport properties are robust to deviations from the idealized microstructural geometry of spherical grains whereas elastic properties are not (Kachanov and Sevostianov, 2005). That is, a quantity like $\hat{\rho}/\hat{R}$ can be defined to yield an accurate prediction of a property like k^* even if circular bonds and spherical grains are difficult to identify in the microstructure. This might not be the case with the coefficients of $\mathbb{C}$.

The independent elastic engineering constants used here are effective Lamé's parameters, λ^* and G^*. Atypically, the second parameter is not referred to as μ^* because μ is reserved for dynamic viscosity. The properties are again considered effective because they are expressed in terms of microstructural variables, but valid for the heterogeneous material at the macroscopic scale. They can be related to other constants like Young's modulus E^* or Poisson's ratio ν^* through common identities (Shames and Cozzarelli, 1997). Much recent analytical work in granular mechanics has been devoted to developing homogenization schemes to accurately predict macroscopic stress-strain behavior (Chang and Ma, 1992; Chang and Liao, 1994; Cambou

et al., 1995; Emeriault and Cambou, 1996; Liao *et al.*, 1997; Rahmoun *et al.*, 2009). Because of its broad application and relative simplicity, the case of linear elasticity where strain is related to stress via the 4^{th} order stiffness tensor $\mathbb{C}$ is usually tackled first. The following sections address the development of a common model that expresses $\mathbb{C}$ in terms of microstructural variables for the case of randomly arranged microstructures.

4.1.1 Kinematic Localization: Voigt's Hypothesis

The homogenization assumption again lies with the kinematic localization process: the process by which local contact displacements $\bar{\delta}^{\alpha}$ are defined by the macroscopic state of strain $\mathbf{E}$. According to the Voigt hypothesis, the kinematic assumption is that the movement of a particle in a granular assembly follows the mean displacement field (Voigt, 1889; Liao *et al.*, 1997). When an incremental macroscopic strain $\boldsymbol{\Delta}\mathbf{E}$ is applied to the granular assembly, the mean incremental displacement field is

$$\Delta\bar{u}^{a} = \bar{x}^{a} \cdot \Delta\mathbf{E}, \tag{4.1}$$

where $\Delta\bar{u}^{a}$ is the displacement and $\bar{x}^{a}$ is the position vector of the centroid of particle a. However, in an assembly of particles, the displacement of primary interest is the *relative* displacement of two centroids of grains connected at contact α. Chang and Ma (1992) and others show this to be

$$\Delta\bar{\delta}^{\alpha} = \bar{L}^{\alpha} \cdot \Delta\mathbf{E}, \tag{4.2}$$

where $\Delta\bar{\delta}^{\alpha}$ is the relative displacement of two centroids and $\bar{L}^{\alpha}$ is the position vector connecting the centroids of the two particles, commonly called the branch vector.

Another way of describing the kinematic assumption resulting in Equation (4.2) is that the local displacement field is exactly linear everywhere with the macroscopic strain field. The Voigt model is highlighted here because the assumption relating local displacements and the macroscopic strain field is analogous to the localization assumptions applied in Chapter 3 to the effective transport properties. Finally, if it is assumed that strain is concentrated in the bonds, then the grains can be considered rigid and deformation is allowed only in the bonds connecting grains. Therefore, the quantity $\Delta\bar{\delta}^{\alpha}$ will be referred to as the incremental contact displacement. Equation (4.2) defines the localization operation in this homogenization scheme.

Permitting axial deformation or "necking" is physically inconsistent with the idealization of a contact plane with no axial dimension, but it presents no analytical difficulties. A small neck is admitted in this chapter to accommodate the assumption of rigid grains and aid in visualizing axial deformation. The contact plane or bond is the critical plane of minimum diameter in a neck connecting two grains (Alley, 1986; Edens and Brown, 1995; Nicot, 2004).

4.1.2 Static Averaging: Love Operation

In a well-established operation, global stress equals the volume average of local stresses. This is commonly expressed not in terms of local stress fields but rather contact forces between connected grains as

$$\Delta\mathbf{T} = \left\langle \Delta\bar{\mathrm{f}}^{\alpha} \otimes \bar{L}^{\alpha} \right\rangle, \tag{4.3}$$

where an increment in global stress $\Delta\mathbf{T}$ equals the volume average across α contacts of the dyadic product of incremental contact forces $\Delta\bar{\mathrm{f}}^{\alpha}$ and branch vectors $\bar{L}^{\alpha}$. This formula was first developed by Love (1927) and often bears his name. It

is treated as a fundamental relationship in granular mechanics (Christoffersen *et al.*, 1981; Mehrabadi, 1982; Cambou, 1998; Oda and Iwashita, 1999). Equation (4.3) is the averaging operation in this homogenization scheme.

One proof of the Love operation is based on the principle of virtual work. The principle of virtual work is useful for systems with many degrees of freedom, as is the case with a collection of interconnected grains. Here, the work done by α virtual incremental displacements at the microscopic level is equal to the macroscopic strain energy per unit volume, or strain energy density, by

$$\mathbf{T} : \Delta\mathbf{E} = \left\langle \bar{\mathrm{f}}^{\alpha} \cdot \Delta\bar{\delta}^{\alpha} \right\rangle . \tag{4.4}$$

Substituting the kinematic assumption, Equation (4.2), into Equation (4.4) results in

$$\mathbf{T} : \Delta\mathbf{E} = \left\langle \bar{\mathrm{f}}^{\alpha} \cdot \bar{L}^{\alpha} \cdot \Delta\mathbf{E} \right\rangle . \tag{4.5}$$

Through a tensor identity (Venkataraman, 2004) the scalar products of the two vectors and 2$^{\mathrm{nd}}$ order tensor can be written as

$$\mathbf{T} : \Delta\mathbf{E} = \left\langle \bar{\mathrm{f}}^{\alpha} \otimes \bar{L}^{\alpha} : \Delta\mathbf{E} \right\rangle = \left\langle \bar{\mathrm{f}}^{\alpha} \otimes \bar{L}^{\alpha} \right\rangle : \Delta\mathbf{E}. \tag{4.6}$$

The : operation is the scalar or double-dot product of the two 2$^{\mathrm{nd}}$ order tensors. For two 2$^{\mathrm{nd}}$ order Cartesian tensors—like $\mathbf{T}$ and $\triangle\mathbf{E}$ above—the operation results in a scalar:

$$\mathbf{T} : \Delta\mathbf{E} = T_{ij} \triangle E_{ji}. \tag{4.7}$$

The incremental macroscopic strain is moved outside the volume average summation because it is not a function of the α contacts. Also, by the above definition,

the double-dot product of two 2nd order tensors is commutative and distributive over addition. Rearranging yields

$$\left(\mathbf{T} - \left\langle \bar{\mathrm{f}}^{\alpha} \otimes \bar{L}^{\alpha} \right\rangle\right) : \Delta\mathbf{E} = 0. \tag{4.8}$$

For Equation (4.8) to be satisfied for any arbitrary increment of macroscopic strain, $\mathbf{T} = \left\langle \bar{\mathrm{f}}^{\alpha} \otimes \bar{L}^{\alpha} \right\rangle$, which is the Love operation for deriving macroscopic stress from microscopic contact forces.

4.1.3 Contact Law

The final piece of the homogenization algorithm is the local constitutive relationship or contact law. The contact law adopted here is a simple one of linear elasticity. Because the local variables are force and displacement at a given contact, it is common to view the linear elastic intergranular model as one of springs connecting rigid grains:

$$\Delta\bar{\mathrm{f}}^{\alpha} = \text{-}\mathbf{K} \cdot \Delta\bar{\delta}^{\alpha}, \tag{4.9a}$$

where the coefficient of proportionality $\mathbf{K}$ is comprised of contact "spring" stiffnesses. In local Cartesian coordinates, unit vector $\bar{n}$ defines the direction normal to a contact plane connecting grains (see Figure 4.1). The other vectors forming the Cartesian basis, $\bar{s}$ and $\bar{t}$, are on the contact plane. Figure 4.1 depicts the $\bar{n}$ and $\bar{s}$ directions and $\bar{t}$ points into the page, forming an orthogonal basis.

Because the idealized bond is a circular plane it is axisymmetric about $\bar{n}$. Two stiffnesses are then required: k_n representing resistance to axial deformation, and k_s representing resistance to shear deformation or sliding of two grains relative to one

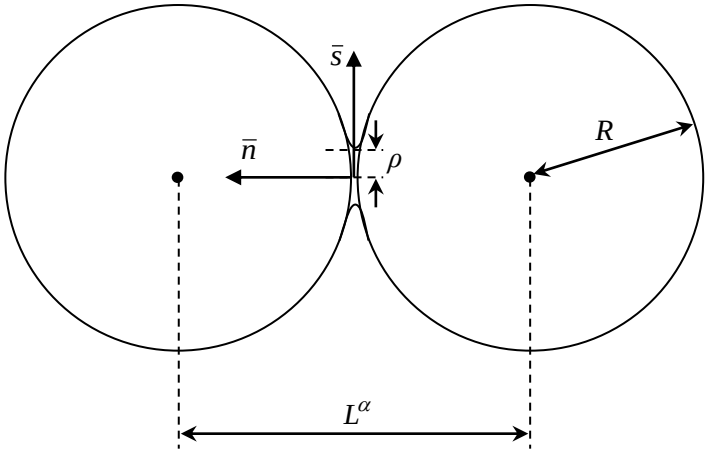


Figure 4.1: Undeformed contact geometry identifying the local Cartesian coordinates on the contact plane and the undeformed branch vector.

another. In a decoupled linear elastic contact law the coefficients of $\mathbf{K}$ are

$$K_{ij} = \begin{bmatrix} k_n & 0 & 0 \\ 0 & k_s & 0 \\ 0 & 0 & k_s \end{bmatrix}. \tag{4.9b}$$

Many studies have applied this contact law based on contact stiffnesses with the Voigt hypothesis and Love formula to derive a linear elastic macroscopic constitutive relationship (Walton, 1987; Chang and Liao, 1994; Cambou *et al.*, 1995; Chang *et al.*, 1995). The extension here is to express the spring stiffnesses in terms of microstructural geometry and grain material properties using an idealized geometry.

4.1.3.1 Axial Stiffness: Consider a decoupled linear elastic contact law written instead in terms of local incremental axial stress $\Delta\sigma_{nn}$ and strain $\Delta\varepsilon_{nn}$ in the bond. For a cohesive bond that resists both tensile and compressive loads in the axial

direction, such a contact law is simply one-dimensional Hooke's law:

$$\Delta\sigma_{nn} = E_{ice}\Delta\varepsilon_{nn}, \tag{4.10}$$

where E_{ice} is the modulus of elasticity or Young's modulus of the bond material, in this case ice. Assuming the local incremental stress is an average axial stress, $\Delta\sigma_{nn}$ can be written as ${}^{\Delta \mathrm{f}_n^\alpha}/_{A_c^\alpha}$ where A_c^α is the minimum cross-sectional area—at the bond—supporting the local axial stress. Similarly, expressing the local incremental strain in terms of contact displacement results in $\triangle\varepsilon_{nn} = {}^{\Delta\delta_n^\alpha}/_{L^\alpha}$. The contact displacement $\Delta\delta_n^\alpha$ is the axial deformation and the branch length L^α represents the original undeformed length.

In this idealized geometry, every bond is considered to be a circular cross-section of mean radius $\hat{\rho}$ such that A_c^α equals $\pi\hat{\rho}^2$. And, to a first order approximation valid for small bonds relative to grains, every branch length L^α can be approximated by $2\hat{R}$ where $\hat{R}$ is the mean grain radius. Combining terms in Equation (4.10) yields

$$\Delta \mathrm{f}_n^\alpha = \left(\frac{\pi\hat{\rho}^2 E_{ice}}{2\hat{R}}\right)\Delta\delta_n^\alpha, \tag{4.11}$$

where the parenthetical term is the normal spring stiffness k_n, relating the incremental contact normal displacement at any bond to the resulting incremental axial force. It is now expressed in terms of contact geometry and the solid constituent material property.

Lending support to the assumption of local average stresses and strains, Nicot (2004) develops a macroscopic constitutive law for cohesive snow and identifies a

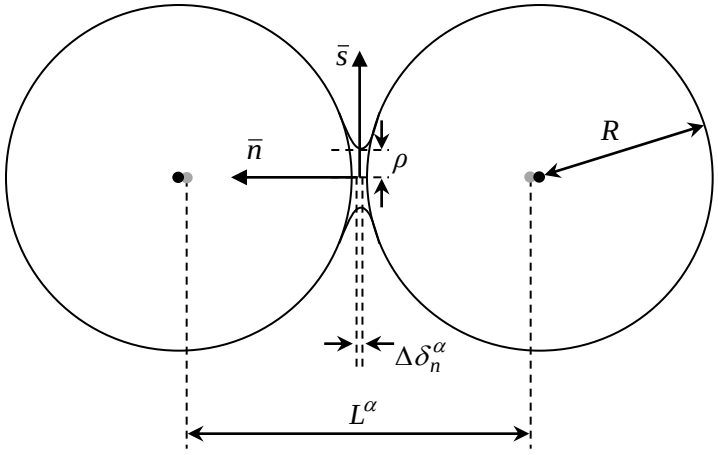


Figure 4.2: Contact geometry as a result of a hypothetical axial load. The schematic highlights the undeformed branch vector and the axial contact displacement.

similar k_n. In the notation used here, his expression is

$$k_n = \frac{\pi \hat{\rho}^2 E_{ice}}{2\hat{R}\sqrt{1 - \left(\hat{\rho}/\hat{R}\right)^2}}. \tag{4.12}$$

The difference between Equations (4.11) and (4.12) is the approximation of branch length.

Nicot (2004) defines this axial spring stiffness in order to write his macroscopic results in terms of k_n, facilitating a direct comparison with other models (Walton, 1987; Chang and Liao, 1994; Cambou *et al.*, 1995; Chang *et al.*, 1995). As a first order approximation, Nicot (2004) neglects k_s, employing a one-dimensional local constitutive law. The assumed axisymmetric contact law here requires the shear component. This development follows.

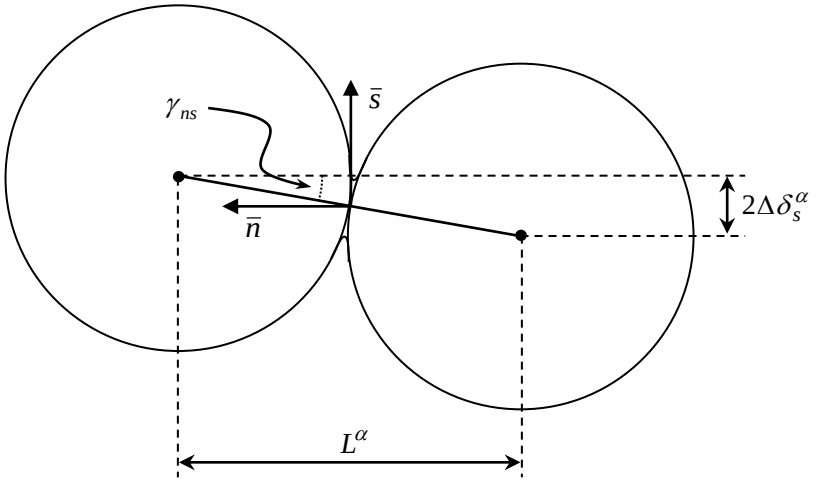


Figure 4.3: Contact geometry as a result of a hypothetical shearing load. The schematic highlights the shearing strain and deformation.

4.1.3.2 Shear Stiffness: Similar to above, consider a local stress-strain contact law in a sliding or shear direction ($\bar{s}$ or $\bar{t}$):

$$\Delta\tau_{ns} = G_{ice}\Delta\gamma_{ns}, \tag{4.13}$$

where G_{ice} is the shear modulus of ice. Again, assume an average state of shear stress and $\Delta\tau_{ns} = {}^{\Delta \mathrm{f}_s^\alpha}/_{A_c}$. For small strain the average shearing strain is related to shear deformation by $\Delta\gamma_{ns} = {}^{2\Delta\delta_s^\alpha}/_{L^\alpha}$, as illustrated in Figure 4.3. Now Equation (4.13) can be written as

$$\Delta \mathrm{f}_s^\alpha = \left(\frac{\pi\hat{\rho}^2 G_{ice}}{2\hat{R}}\right) 2\Delta\delta_s^\alpha, \tag{4.14}$$

where the "spring stretch" is $2\Delta\delta_s^\alpha$. The parenthetical term here is the shear spring stiffness k_s in terms of contact geometry and a material property of ice.

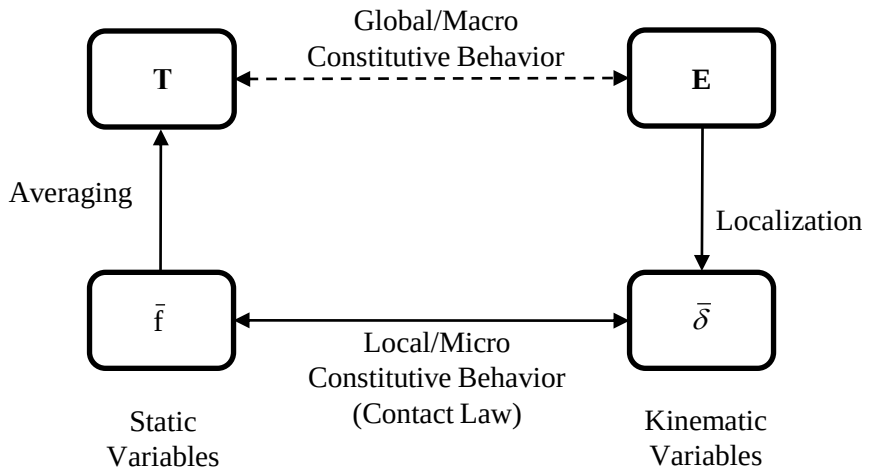


Figure 4.4: Homogenization Scheme for Linear Elastic Stiffness

4.1.4 Isotropic Elastic Stiffness Coefficients

The homogenization scheme is complete and the global constitutive tensor can be derived from the following relationships, as depicted in Figure 4.4:

- *Localization:* Equation (4.2),
- *Local/Micro Constitutive Behavior:* Equations (4.9a) and (4.9b),
- *Averaging:* Equation (4.3).

Several studies have accomplished this derivation for a randomly packed microstructure comprised of uniformly sized spheres and contact areas (Walton, 1987; Chang and Liao, 1994; Cambou *et al.*, 1995; Chang *et al.*, 1995). As is the case for a homogeneous isotropic material, the global constitutive tensor for this heterogeneous isotropic assembly reduces to two independent elastic coefficients. A few of these

coefficients are

$$\begin{aligned} E^* &= \frac{4k_n N_{cp}\hat{R}^2}{3V}\left(\frac{2+3\zeta}{4+\zeta}\right), \\ \nu^* &= \frac{1-\zeta}{4+\zeta}, \\ \lambda^* &= \frac{4k_n N_{cp}\hat{R}^2}{15V}\left(1-\zeta\right), \\ G^* &= \frac{2k_n N_{cp}\hat{R}^2}{15V}\left(2+3\zeta\right), \end{aligned} \tag{4.15}$$

where N_{cp} is the total number of contact planes or bonds in the representative volume V and $\zeta = {}^{k_s}/_{k_n} = {}^{G_{ice}}/_{E_{ice}}$.

With the expression developed above for the contact stiffnesses k_n, the elastic coefficients can be written in terms of microstructure and grain material as

$$\boxed{\begin{aligned} E^* &= \frac{1}{4}\left(\frac{\hat{\rho}}{\hat{R}}\right)^2 \phi\mathcal{N}E_{ice}\left(\frac{2+3\zeta}{4+\zeta}\right), \\ \nu^* &= \frac{1-\zeta}{4+\zeta}, \\ \lambda^* &= \frac{1}{20}\left(\frac{\hat{\rho}}{\hat{R}}\right)^2 \phi\mathcal{N}E_{ice}\left(1-\zeta\right), \\ G^* &= \frac{1}{40}\left(\frac{\hat{\rho}}{\hat{R}}\right)^2 \phi\mathcal{N}E_{ice}\left(2+3\zeta\right). \end{aligned}} \tag{4.16}$$

This section outlines how the independent elastic coefficients are determined for a random granular microstructure, borrowing from a derivation presented in many other sources (Walton, 1987; Chang and Liao, 1994; Cambou *et al.*, 1995; Chang *et al.*, 1995). In every study that presents this development the assumption is that the contacts are distributed uniformly/randomly. Therefore, a general anisotropic material tensor is never included at any point during the derivation. This differs from the approach taken in the derivation of the transport properties in Chapter 3.

There, the anisotropic result is delivered first and then simplified for the case of a uniform/random distribution of directional data.

4.2 Elastic Stiffness Coefficients: Anisotropy

In this section, anisotropy is incorporated into the effective material property by assuming that, in the simplest case, the 2^{nd} order contact tensor dictates departures from isotropy. This is driven by the conductivity results from Chapter 3. The aim here is to use a 2^{nd} order fabric tensor because: 1) as mentioned in Chapter 2, such MIL fabric tensors are widely available through CT software, and 2) a 2^{nd} order fabric tensor should be sufficient to characterize the textural anisotropy encountered in snow as a result of temperature gradient metamorphism. This does not imply that stiffness will be reduced to a 2^{nd} order tensor. As will be shown below, tensor products between two 2^{nd} order fabric tensors mathematically ensure that stiffness is a 4^{th} order tensor. A model relating a 4^{th} order fabric tensor to stiffness anisotropy has been proposed (Rahmoun *et al.*, 2009), and is still a topic of ongoing research.

Recall that in the case of the thermal conductivity tensor, the simplest anisotropic expression includes: 1) a scalar isotropic conductivity expression, and 2) the contact tensor normalized by its isotropic value (Equations (3.34) or (3.37)). The same fundamental approach is applied here using the previously defined isotropic stiffness parameters (Equation (4.16)) and the contact tensor to derive a microstructural anisotropic expression for elastic stiffness. The key is mathematically incorporating the 2^{nd} order contact tensor into the 4^{th} order stiffness tensor.

Consider generalized Hooke's law in tensor notation:

$$\mathbf{T} = \mathbb{C} : \mathbf{E}, \tag{4.17a}$$

where $\mathbf{T}$ is the 2^{nd} order macroscopic stress tensor, $\mathbb{C}$ is the 4^{th} order stiffness tensor, and $\mathbf{E}$ is the 2^{nd} order strain tensor. Following the definition of the double-dot product given in Equation (4.7) and recognizing the symmetry of the strain tensor ($E_{lk} = E_{kl}$) leads to Hooke's law in index notation:

$$T_{ij} = C_{ijkl} E_{kl}. \tag{4.17b}$$

In this most general form, the three-dimensional stiffness tensor has 81 coefficients. However, because both stress and strain tensors are symmetric, the stiffness tensor also exhibits symmetries

$$C_{ijkl} = C_{jikl}, \text{ and} \tag{4.18a}$$

$$C_{ijkl} = C_{ijlk}. \tag{4.18b}$$

This reduces the 81 coefficients C_{ijkl} to 36 different constants. It is possible to write this simplified tensor as a square matrix

$$[C] = \begin{bmatrix} C_{1111} & C_{1122} & C_{1133} & C_{1123} & C_{1131} & C_{1112} \\ C_{2211} & C_{2222} & C_{2233} & C_{2223} & C_{2231} & C_{2212} \\ C_{3311} & C_{3322} & C_{3333} & C_{3323} & C_{3331} & C_{3312} \\ C_{2311} & C_{2322} & C_{2333} & C_{2323} & C_{2331} & C_{2312} \\ C_{3111} & C_{3122} & C_{3133} & C_{3123} & C_{3131} & C_{3112} \\ C_{1211} & C_{1222} & C_{1233} & C_{1223} & C_{1231} & C_{1212} \end{bmatrix}, \tag{4.19}$$

relating a strain vector $\{E\}$ to a stress vector $\{T\}$. Through a series of rotations and reflections about the reference Cartesian coordinates it is possible to further reduce the number of independent stiffness constants based on whether the material

exhibits symmetry about a given plane or axis (Ugural and Fenster, 1995; Shames and Cozzarelli, 1997). In the simplest case of isotropy, where the stiffness coefficients do not vary with any rotation or reflection about any axis, the number of independent coefficients reduces to two and the stiffness matrix becomes

$$[C] = \begin{bmatrix} (\lambda+2G) & \lambda & \lambda & 0 & 0 & 0 \\ \lambda & (\lambda+2G) & \lambda & 0 & 0 & 0 \\ \lambda & \lambda & (\lambda+2G) & 0 & 0 & 0 \\ 0 & 0 & 0 & 2G & 0 & 0 \\ 0 & 0 & 0 & 0 & 2G & 0 \\ 0 & 0 & 0 & 0 & 0 & 2G \end{bmatrix}, \tag{4.20}$$

or more succinctly in index notation as

$$C_{ijkl} = \lambda\delta_{ij}\delta_{kl} + 2G\delta_{ik}\delta_{jl}. \tag{4.21}$$

Equation (4.21) is now modified for a heterogeneous, multi-constituent material, drawing parallels to the thermal conductivity problem. First, the Lamé parameters are identified as λ^* and G^*, defining them as *effective* constants as in Equation (4.16)—much like the isotropic $k^*_{B\&O}$ in the thermal conductivity problem. Second, introducing the 2^{nd} order contact tensor as the microstructural variable that characterizes changes in textural symmetry requires the following substitution:

$$\delta_{ij} \Leftrightarrow \frac{1}{f}F_{ij}. \tag{4.22}$$

F_{ij} are the contact tensor coefficients and f is its isotropic value. Equation (4.22) is a reminder of developments in Chapter 3 for thermal conductivity. The quantity

$(1/f)\, F_{ij}$ simplifies to the identity tensor for an isotropic microstructure and captures changes in textural symmetry through F_{ij}. The same relationship is assumed here, and Equation (4.21) takes the form

$$\boxed{C^*_{ijkl} = \frac{1}{f^2}\left(\lambda^* F_{ij}F_{kl} + 2G^* F_{ik}F_{jl}\right).} \tag{4.23}$$

The tensor products in Equation (4.23) are carried out in the principal orientation of **F**:

$$F_{ij} = \begin{bmatrix} F_{11} & 0 & 0 \\ 0 & F_{22} & 0 \\ 0 & 0 & F_{33} \end{bmatrix}.$$

This dictates that the material symmetry of the resulting stiffness matrix will follow the textural symmetry reflected in the fabric tensor. There is analytical and empirical evidence supporting this assumption (Odgaard *et al.*, 1997; Satyawali *et al.*, 2008; Srivastava *et al.*, 2010). Following this, Equation (4.23) in matrix form is

$$[C^*] = \ldots$$

$$\begin{bmatrix} (\lambda^*+2G^*)\left(\frac{F_{11}}{f}\right)^2 & \lambda^*\frac{F_{11}F_{22}}{f^2} & \lambda^*\frac{F_{11}F_{33}}{f^2} & 0 & 0 & 0 \\ \lambda^*\frac{F_{22}F_{11}}{f^2} & (\lambda^*+2G^*)\left(\frac{F_{22}}{f}\right)^2 & \lambda^*\frac{F_{22}F_{33}}{f^2} & 0 & 0 & 0 \\ \lambda^*\frac{F_{33}F_{11}}{f^2} & \lambda^*\frac{F_{33}F_{22}}{f^2} & (\lambda^*+2G^*)\left(\frac{F_{33}}{f}\right)^2 & 0 & 0 & 0 \\ 0 & 0 & 0 & 2G^*\frac{F_{22}F_{33}}{f^2} & 0 & 0 \\ 0 & 0 & 0 & 0 & 2G^*\frac{F_{33}F_{11}}{f^2} & 0 \\ 0 & 0 & 0 & 0 & 0 & 2G^*\frac{F_{11}F_{22}}{f^2} \end{bmatrix}. \tag{4.24}$$

If all principal values of F_{ij} are equal, indicating an isotropic textural arrangement, then $F_{11} = F_{22} = F_{33} = f$, and Equation (4.24) reduces to an isotropic stiffness matrix with dependence only on λ^* and G^*. Likewise, if two of the fabric principal values are equal (transversely isotropic textural symmetry) then the stiffness matrix has five independent coefficients, and if all of the fabric principal values are distinct (orthotropic textural symmetry) then nine of the stiffness coefficients are independent. This result is consistent with the substitution represented by Equation (4.22). This substitution guarantees that any anisotropy in the stiffness matrix is a result of textural anisotropy, quantified by the contact tensor. Equation (4.22) is critical to this derivation. It mathematically captures how a normalized contact tensor both: 1) simplifies to the identity tensor in the case of a uniform/random distribution of contacts, and 2) drives departures from the identity tensor for cases of textural anisotropy.

A substitution like Equation (4.22) was first proposed by Zysset and Curnier (1995). However, in their work they propose a different fabric tensor in the substitution. They instead use the tensor in Equation (2.22a)—the 2^{nd} order tensor approximation to the pdf of contact normal vectors $\bar{n}$. In contrast, the substitution used here draws on a tensor like Equation (2.22b) normalized by f. The mathematical differences are subtle but important. The approach taken here adopts the spirit of the work of Zysset and Curnier (1995), but modifies the details based on the developments of Chapter 3.

There is no physical reason to suggest that the tensor form of a pdf approximation should naturally arise in a microstructural derivation. Zysset and Curnier (1995) offer no justification for their particular substitution choice. However, the results in Chapter 3 indicate that volume averaging can naturally produce the substitution tensor applied here when directional data are carefully considered. Drawing on evidence

supporting ties between conductive and elastic properties, the normalized contact tensor is applied here in exactly the same manner as it was derived in Chapter 3 in the case of thermal conductivity (Gibiansky and Torquato, 1993; Kachanov and Sevostianov, 2005; Sevostianov and Kachanov, 2008).

The model of Zysset and Curnier (1995) additionally introduces an exponent dubbed the homogeneity property. It expresses that the stiffness anisotropy is "independent of the size or physical units of the [fabric tensor]." This research does not dispute that claim: both the pdf of $\bar{n}$ and fabric tensors derived from $\bar{n}$ are built from dimensionless unit vectors. Also, the substitution proposed here—even if using a normalized MIL fabric tensor—always lacks physical units and always reduces to the identity tensor in the absence of textural anisotropy. The assertion is that the homogeneity property is unnecessary. It is a parameter tied to a model that is too easily used as an empirical fit factor in practice.

4.3 Summary

A common Voigt-style homogenization was summarized for a granular material. The result was two independent elastic coefficients expressed in terms of generic spring stiffnesses (Equation (4.15)). The local constitutive law was extended here beyond spring stiffnesses to draw in geometry and material properties specific to an idealized snow microstructure. A comparison between these isotropic effective elastic coefficients (Equation (4.16)) and the isotropic effective conductivity (Equation (3.35)) highlights several identical variables or groups: $\hat{\rho}/\hat{R}$, ϕ, and $\mathcal{N}$. This contributes to the argument that the conductive and elastic behavior of a granular assembly are governed by many of the same microstructural features.

Building on this connection, anisotropy is introduced to the linear elastic model in exactly the same manner as it affects the conduction model. The results of the effective conductivity derivation in Chapter 3 indicate that the tensor $(1/f)\,\mathbf{F}$ drives potential anisotropy in $\mathbf{k}^*$; the contact tensor was applied here to drive anisotropy in $\mathbb{C}^*$. The result is a global linear elastic anisotropic constitutive model, expressed in terms of microstructural features of a granular material.

CHAPTER 5

EFFECTIVE PROPERTIES: COMPARISON TO EXISTING MODELS & DATA

5.1 Thermal Conductivity

The microstructural thermal conductivity tensor developed in Chapter 3 compares favorably to other analytical models and empirical data. Recall the simplest expression of anisotropic effective conductivity:

$$\boxed{\mathbf{k}^* = \frac{1}{\pi}\phi\mathcal{N}k_{ice}\frac{\hat{\rho}}{\hat{R}}\frac{1}{f}\mathbf{F},} \tag{5.1a}$$

and its isotropic counterpart:

$$\boxed{k^*_{B\&O} = \frac{1}{\pi}\phi\mathcal{N}k_{ice}\frac{\hat{\rho}}{\hat{R}},} \tag{5.1b}$$

where ϕ is the volume fraction of spherical ice particles, $\mathcal{N}$ is the average number of contacts per particle, k_{ice} is the scalar thermal conductivity of polycrystalline ice, $\hat{\rho}$ is the mean bond or contact radius, and $\hat{R}$ is the mean grain radius. Equation (5.1a) incorporates anisotropy through the quantity $(1/f)\,\mathbf{F}$: the contact tensor normalized by its isotropic value.

First, a derivation of an effective thermal conductivity tensor by Jagota and Hui (1990) results in *exactly* the same expression as Equation (5.1a). The difference in their approach is that the macroscopic flux is assumed to depend upon contact orientation via a distribution density function $P(\bar{n})$, as described in Chapter 2. They assume all microstructural quantities besides $\bar{n}$ do not vary with orientation and the effective conductivity is left as a function of scalar variables and Equation (2.10b), the continuous form of the contact tensor. Jagota and Hui (1990) do not consider in-

finitesimally small bonds, nor do they consider additional enhanced flux in the region immediately surrounding a bond—as Batchelor and O'Brien (1977) do—but their result reinforces the analytical arguments for a microstructural anisotropic conductivity model like Equation (5.1a).

Next, while anisotropic conductivity models have not yet been applied to snow, Equation (5.1b) can be compared to isotropic conductivity models developed for snow. The conductivity model proposed by Adams and Sato (1993) results in a similar expression to Equation (5.1b). An adaptation of their derivation is currently incorporated into the Swiss SNOWPACK model (Lehning *et al.*, 2002). SNOWPACK is a numerical model used by operational avalanche forecasters as part of the Swiss federal avalanche warning system, so the Adams and Sato (1993) conductivity is an appropriate standard of comparison (Bartelt and Lehning, 2002).

As mentioned in the introduction, an advantage of the Adams and Sato (1993) model is its comprehensive treatment of different modes of energy transfer. However, for the direct comparison with $k^*_{B\&O}$, their conductivity through the ice network in a unit volume ($1\,\mathrm{m}^3$) can be isolated as

$$k^*_{A\&S} = \frac{\pi^2}{32}\mathcal{N}k_{ice}\hat{\rho}\frac{n_{cA}}{n_{cl}}. \tag{5.2}$$

The parameters n_{cA} and n_{cl} are the number of spherical grains in the cross section of the unit volume and number of spherical grains in the length of the unit volume, respectively. This ratio reduces to $n_c^{1/3}$, where n_c is the number of spherical ice particles in the sample volume (Adams and Sato, 1993):

$$k^*_{A\&S} = \frac{\pi^2}{32}\mathcal{N}k_{ice}\hat{\rho}n_c^{1/3}. \tag{5.3}$$

For a unit sample volume, n_c is equivalent to Batchelor and O'Brien's m; either can be related to the volume fraction of spherical ice grains as:

$$\phi = \frac{4}{3}\pi\hat{R}^3 m = \frac{4}{3}\pi\hat{R}^3 n_c.$$

Substituting this expression into Equation (5.3) yields the Adams and Sato (1993) effective scalar conductivity in terms of the same variables as Equation (5.1b):

$$k^*_{A\&S} = 0.0284\pi^{5/3}\phi^{1/3}\mathcal{N}k_{ice}\frac{\hat{\rho}}{\hat{R}}. \tag{5.4}$$

Precisely the same scalar microstructural variables appear in both expressions, albeit in a slightly different arrangement.

Lastly, both $k^*_{B\&O}$ and $k^*_{A\&S}$ compare favorably to empirical data. Many properties of snow have been parameterized by density—effective thermal conductivity is among them. Sturm *et al.* (1997) developed a widely cited empirical expression that can be applied to a broad range of densities of the form

$$k^*_{Sturm} = 0.138 - 1.01\rho_s + 3.233\rho_s^2, \tag{5.5}$$

where ρ_s is snow density measured in $^{g}/_{cm^3}$. Sturm *et al.* (1997) suggests that the valid density range of Equation (5.5) is $\{0.156 \leq \rho_s \leq 0.6\}$.

Figure 5.1 compares Equation (5.5) to the analytical developments of Batchelor and O'Brien (1977) and Adams and Sato (1993). The relationships in Table 5.1 were applied to Equations (5.1b) and (5.4) in order to investigate their density dependence. Additionally, the contact radius to grain radius ratio ($^{\hat{\rho}}/_{\hat{R}}$) was varied in the micromechanical models to illustrate their sensitivity to this quantity.

Table 5.1: Parameter definitions used in calculating the density dependence of the scalar thermal conductivity models in Equations (5.1b) and (5.4).

Variable		Function/Parameterization	Reference
ϕ		ρ_s/ρ_{ice} ($\rho_{ice} = 920\,\mathrm{kg/m^3}$)	Adams and Sato (1993)
$\mathcal{N}$		$3.565 - 7.435\phi + 24.825\phi^2$	Adams and Sato (1993)
k_{ice}		$\frac{651}{\theta}$ (W/m·K)	Petrenko and Whitworth (1999)
θ		268 K (-5°C)	

The qualitative agreement in Figure 5.1a is uncanny, but bear in mind that Equation (5.5) is a quadratic regression of a data set with significant scatter ($R^2 = 0.79$). Additionally, there is no empirical basis in selecting $\hat{\rho}/\hat{R}$ here; it represents a proposed microstructural parameter that potentially explains such scatter in experimental data. The comparison primarily serves to assess the feasibility of the microstructural models. The general agreement of the analytical models with the empirical equation lends credence to the micromechanical approach.

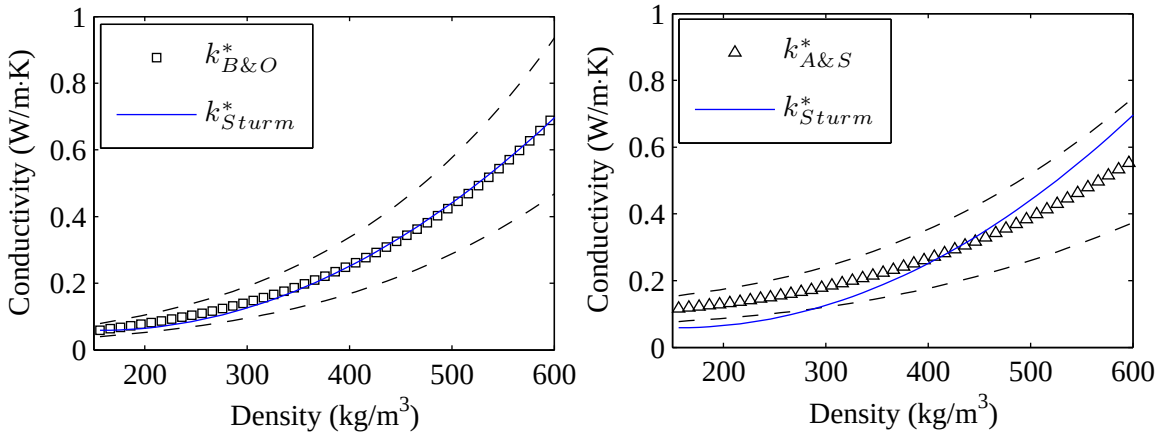


Figure 5.1: Density dependence of effective thermal conductivity comparing (a) the analytical approach of Batchelor and O'Brien (1977), and (b) the analytical approach of Adams and Sato (1993) to the empirical relation of Sturm *et al.* (1997). The dashed envelope represents the ±33% variation of $\hat{\rho}/\hat{R} = 0.15$ applied to the micromechanical models.

The proposed model, at least in its reduced isotropic form, compares well to established analytical and empirical snow conductivity models. And, with imagery and stereology, evaluating quantities like $\hat{\rho}/\hat{R}$ and $\mathbf{F}$ should lend precision and permit evaluation of anisotropic snow morphologies like depth hoar and near surface facets. Current scalar models like Equations (5.2) and (5.5) cannot account for variations in conductivity caused by textural anisotropy.

5.2 Diffusivity

The effective diffusivity of water vapor in snow, D^*, is a difficult property to evaluate (Yosida, 1963; Colbeck, 1993). In snow, most experiments derive diffusivity by either 1) attempting to measure very slight values of mass loss/redistribution, or 2) measuring an effective heat transfer coefficient and separating the apparent conductivity of vapor diffusion/phase change from other energy transfer modes (Satyawali, 2000; Sokratov and Maeno, 2000). The impediments involved with either of these approaches predominantly explain why much uncertainty still surrounds this property.

To summarize two recent experimental endeavors, Satyawali (2000) and Sokratov and Maeno (2000) measured the effective diffusivity of water vapor in snow. The eight Sokratov and Maeno (2000) samples were high density: 400–500 $^{kg}/_{m^3}$. The Satyawali (2000) samples could roughly be divided into two groups: fourteen in the 200–300 $^{kg}/_{m^3}$ range and twelve in the 400–500 $^{kg}/_{m^3}$ range. The ratio of D^* to the diffusivity of water vapor in air, D_{vap}, is reported in generalizing their results. The $^{D^*}/_{D_{vap}}$ of most lower density samples from Satyawali (2000) was $2^1/_2$–5. In both studies, the higher density samples yielded $^{D^*}/_{D_{vap}}$ of $^1/_2$–2.

Additionally, Sokratov and Maeno (2000) neatly summarize other experimental measurements of D^* in their Table 1. The results vary significantly, but most labo-

ratory research indicates that, in lower density snow, $^{D^*}/_{D_{vap}}$ is significantly greater than one, probably in the range reported by Satyawali (2000). In higher density snow, $^{D^*}/_{D_{vap}}$ diminishes to approximately one or even a fraction. Satyawali (2000) states that "evidence from the field and laboratory confirms that diffusion mass transfer should decrease with an increase in snow density."

Empirical models are offered in both Satyawali (2000) and Sokratov and Maeno (2000), in each case derived specifically from their data. Unlike the Sturm *et al.* (1997) conductivity parameterization, these diffusivity models include experimental constants and do not reduce to a simple density-dependence. In terms of analytical models, apart from the the particle-to-particle diffusion model developed in Colbeck (1993), the diffusivity model developed here is the only one that considers microstructural details—like grain spacing—beyond density/porosity. It is not possible to conduct a simplified density-dependence comparison between these various models. This is due to both the empirical constants and unknown microstructural relationships to density, if any, in the analytical model parameters. For this reason, a summary of the Colbeck (1993) model and qualitative evaluation of the diffusivity model presented in Chapter 3 ensues.

The model initially proposed in Colbeck (1993) shows a continual increase in $^{D^*}/_{D_{vap}}$ with increasing snow density. He points out that this result "seems to contradict the common observation," and attributes it to the assumed simple cubic packing structure of ice particles. This assumption artificially restricts the spacing between particles. He then applies a log-normal distribution of interparticle spacings, defining the geometric mean and geometric standard deviation as parameters of the statistical distribution. The primary outcome of this alternate geometry is that $^{D^*}/_{D_{vap}}$ decreases with increasing particle spacing. Colbeck (1993) presents this as the fundamental conclusion: $^{D^*}/_{D_{vap}}$ is 4–7 and that it slowly decreases as the mean pore size increases.

He emphasizes that particle spacing—defined by the parameters of the log-normal distribution—is not strictly tied to density; the two can vary independently.

The diffusivity model developed in Chapter 3 is also a function of density and other microstructural features. Recall that the simplest anisotropic expression is

$$\boxed{\mathbf{D}^* = D_{vap}\left(\boldsymbol{\delta} + \frac{5}{3}\phi\mathcal{Q}\left(\frac{\hat{h}}{\hat{R}}\right)^{1/2}\frac{1}{f_{vap}}\mathbf{F_{vap}}\right),} \tag{5.6}$$

which reduces in the case of an isotropic arrangement of grains to

$$\boxed{D^* = D_{vap}\left(1 + \frac{5}{3}\phi\mathcal{Q}\left(\frac{\hat{h}}{\hat{R}}\right)^{1/2}\right).} \tag{5.7}$$

ϕ is the volume fraction of spherical ice particles, $\hat{h}$ is an average center-to-center grain separation across the pore space, and $\hat{R}$ is the mean grain radius. $\mathcal{Q}$ is a measure of connectivity; it refers to the average number of grains a reference grain can "see" across the pore space. These grains represent potential partners in the vapor diffusion/phase change process. Equation (5.6) accounts for potential anisotropy in the arrangement of these partners through the quantity $(1/f_{vap})\,\mathbf{F_{vap}}$: a fabric tensor normalized by its isotropic value.

The variables in Equation (5.6) are explicitly tied to the microstructure. However, current stereological software—even that designed for snow microstructure—is not yet capable of evaluating all of these parameters; this is a topic of ongoing work. Useful quantitative comparison to a microstructural model like that proposed in Colbeck (1993) and to available experimental data currently requires too much speculation. Instead, what follows is a term-by-term discussion of the various features of the model proposed here.

In the low density limit where $\phi = 0$, Equation (5.6) reduces to D_{vap}. This is correct for a volume containing only air-filled pore space. The Colbeck (1993) model achieves this requirement with the *ad hoc* addition of a "vapor bypass" term. It is a natural result of the derivation in Chapter 3.

This model cannot predict fractional ${}^{D^*}/_{D_{vap}}$. At a minimum ${}^{D^*}/_{D_{vap}} = 1$; the product of microstructural quantities in Equation (5.7) cannot be negative. With all other variables fixed, D^* increases linearly with an increasing ϕ.

A useful minimum value of $\hat{h}$ is $2\hat{R}$, representing the case where—on average—a reference grain is in contact with all neighboring grains. This implies a large ϕ but a defined empirical or analytical relationship between $\hat{h}$ and ϕ is unknown. Discounting such a relationship, D^* increases as $\hat{h}^{1/2}$ with an increasing $\hat{h}$. Interestingly, this result is opposite the conclusion drawn by Colbeck (1993).

The fabric tensor effect on Equation (5.6) is difficult to estimate. With potentially a broad directional distribution of data contributing to the coefficients, speculation is that the result is likely an isotropic or nearly isotropic result. As an initial estimate it is always simpler to assume isotropy.

$\mathcal{Q}$ is likely the driving feature in variations in D^*. Consider that ϕ potentially varies from 0–0.7405. This maximum ϕ corresponds to the theoretical upper limit for a regular packing of spheres, above which the microstructural model loses any physical significance (Dullien, 1992). Also consider a large $\hat{h}$—$\hat{h} = 8\hat{R}$—for low density snow and the aforementioned $2\hat{R}$ as a small $\hat{h}$ in high density snow. This variation results in a range of 2.83–1.41 for $\left({}^{\hat{h}}/_{\hat{R}}\right)^{1/2}$. However, $\mathcal{Q}$ should vary over a much broader range of values.

In the model, $\mathcal{Q}$ is defined as the average number of grains to which a reference grain is linked via h^β (see Figure 3.3). This definition excludes grains to which the reference grain is bonded. For low density, poorly connected snow with a low $\mathcal{N}$, it

is deduced that any given grain can "see" many grains across the relatively open pore space. Manual estimates from 2-D images of low density snow are $\mathcal{Q} = 7 - 9$. And, as $\mathcal{N}$ increases $\mathcal{Q}$ will decrease. In high density, well-connected snow with a high $\mathcal{N}$, $\mathcal{Q}$ should be vanishingly small. In this scenario, a reference grain is connected to each of its neighbors and essentially has no adjacent pore space. Therefore, $\mathcal{Q}$ should generally force the largest swings in magnitude in D^*.

The proposed microstructural diffusivity model is a combination of grain and pore parameters. Many of these parameters are likely coupled but the exact relationships are undefined. The model exhibits several appealing features but many others that are difficult to evaluate. Recall that the foundation of the model is that the addition of grains from a low density limit should enhance the resulting mass flux. This is consistent with the idea in snow that grains do not impede the diffusion process but rather serve as local sources and sinks (Yosida, 1963; Colbeck, 1993). However, inserting ever more grains adversely affects pore parameters that are also critical to the process. The result is a coupled grain-pore microstructural model that seems to exhibit no simple trend.

The assertion here is that D^* increases rapidly as the number of grains rises from the low density limit. A maximum D^* is reached where $\mathcal{Q}$ is maximized. Snow in this state is porous and poorly connected with a low conductivity but contains enough grains to act as local vapor sources and sinks. This affords ample void space for recrystallization and energy transfer via the apparent conductivity of vapor diffusion/phase change. If available experimental data is any indication, this is generally in snow around $100\,{}^{\mathrm{kg}}/_{\mathrm{m}^3}$. Then, with the inclusion of more and more grains, the snow becomes better connected and $\mathcal{Q}$ tends toward zero. In terms of energy, this snow is dominated by conduction and the apparent conductivity is a less significant mode

of energy transfer. While the described scenario is speculation based on inconclusive experimental data, Equation (5.6) is a model that potentially reflects this behavior.

5.3 Permeability

The permeability model developed in Chapter 3 is based on capillary-type assumptions where the volume flow rate through the channels connecting void cells is assumed to behave as a Hagen-Poiseuille flow. To review, the simplest anisotropic and isotropic permeability models from Chapter 3 are repeated here:

$$\boxed{\boldsymbol{\kappa}^* = \frac{1}{32}\epsilon\mathcal{C}\left(\frac{\hat{r}^2}{\hat{R}_{void}}\right)^2 \frac{1}{f_{void}}\mathbf{F_{void}},} \tag{5.8a}$$

$$\boxed{\kappa^* = \frac{1}{32}\epsilon\mathcal{C}\left(\frac{\hat{r}^2}{\hat{R}_{void}}\right)^2,} \tag{5.8b}$$

where ϵ is porosity, $\mathcal{C}$ is connectivity of the pores—average number of connections per void cell, $\hat{r}$ is the mean radius of a cylindrical channel connecting pores, and $\hat{R}_{void}$ is the mean radius of an assumed spherical void cell. Equation (5.8a) accounts for anisotropy through the quantity $(1/f_{void})\,\mathbf{F_{void}}$: a void fabric tensor normalized by its isotropic value.

The most pervasive simple permeability model is the Kozeny-Carman correlation (Nield and Bejan, 2006). It is a semi-empirical scalar equation developed for 1-D flow. Therefore, it is a suitable source of comparison for Equation (5.8b). While not a rigorous derivation, it is useful to briefly present the development of the Kozeny-Carman equation.

Kozeny essentially adopted the Hagen-Poiseuille solution to the momentum equation and attenuated it by porosity. This is accomplished to account for the fact

that flow through a porous medium (e.g., Darcy's law, the Ergun equation, etc.) is expressed in terms of superficial velocity and it differs from advective flow through a pipe (see Equation (3.57)). In taking such an approach, Kozeny treats the porous medium as an impermeable matrix punctuated by capillary tubes representing the voids. This modified Hagen-Poiseuille solution is

$$\bar{\mathrm{d}} = \epsilon\bar{u} = \frac{1}{\mu}\frac{\epsilon r^2}{8}\left(\frac{dp}{dx}\right), \tag{5.9}$$

where r is the capillary or pipe radius and $^{dp}/_{dx}$ is the 1-D pressure gradient. Permeability in this expression is

$$\kappa_{Kozeny} = \frac{\epsilon r^2}{8}. \tag{5.10}$$

The contribution of Carman was recognizing that the mean path of the capillary tubes l' is necessarily longer than the size of the porous sample l, i.e., capillary tubes are not straight (Dullien, 1992). This is analogous to the concept of tortuosity Υ where the maze of interconnected pores is a twisting path through the complex microstructure. With this addition, the semi-empirical Kozeny-Carman equation is

$$\kappa_{K-C} = \frac{\epsilon r^2}{8\left(^{l'}/_{l}\right)}. \tag{5.11}$$

It is customary to see the Kozeny-Carman equation expressed in terms of grain radius or hydraulic radius rather than pore/capillary radius. This is accomplished by equating the surface areas of the void and grain space. However, for direct comparison with Equation (5.8b), Equation (5.11) will suffice.

Experimentation with granular media comprised of uniform spherical particles yields an empirical value of $\iota'/\iota = 2.5$ and Equation (5.11) becomes

$$\kappa_{K-C} = \frac{\epsilon r^2}{20}. \tag{5.12}$$

Equation (5.12) is consistent with the geometric assumptions applied here of spherical particles of uniform size. This expression has been found to agree well with experimental results in the porosity range of 0.26–0.8 (Li and Park, 2000). The equation is often not valid for cases where the grains deviate strongly from the spherical assumption or their size distribution exhibits a large variance (Dullien, 1992; Nield and Bejan, 2006). Various adaptations of the essential Kozeny-Carman equation exist in an attempt to account for such variations in grain size and shape (Coelho *et al.*, 1997; Carrier, 2003; Wong, 2003).

A more robust capillary-type model incorporates bundles of periodically constricted tubes in a serial-parallel arrangement (Dullien, 1992). While still a 1-D model, this approach accommodates variable pore size and connectivity to some extent. In this model, permeability reduces to

$$\kappa_{bundle} = \frac{\epsilon \bar{r}^2}{8\Upsilon}, \tag{5.13}$$

where $\bar{r}$ is the mean pore radius and Υ is the tortuosity of the pore network. In theory, $\Upsilon = 3$ because the capillaries are arranged with equal probability in three directions. However, experiment has shown that this model fits best with $\Upsilon = 1.725$, resulting in a permeability of

$$\kappa_{bundle} = \frac{\epsilon \bar{r}^2}{13.8}. \tag{5.14}$$

For comparison, Equation (5.8b) must be simplified to a form like Equations (5.12) and (5.14). First, in a 1-D capillary tube, a given void cell is connected as in a chain to two other void cells: $\mathcal{C} \approx 2$ (cells at the RVE boundary have only one connection). Then, render any geometric difference between void cells and connecting channels moot by letting $\hat{r} \to \hat{R}_{void}$ (or $\hat{R}_{void} \to \hat{r}$) so that the pore is characterized by a single radius r. This leaves Equation (5.8b) as

$$\kappa^* = \frac{\epsilon r^2}{16}, \tag{5.15}$$

predicting a permeability 20% greater than Equation (5.12) and 16% less than Equation (5.14).

Most capillary-type models reduce to dependence on porosity and the pore radius squared. Empiricism is drawn into the expression in whether ϵr^2 is related to κ by a factor of 13.8, 20, or something different. Simplifying Equation (5.8b) reveals this factor to be approximately 16—squarely in the range of feasible values. Where other capillary models rely on empiricism for accuracy, Equation (5.8b) relies on detailed microstructural information.

A fundamental criticism of the Kozeny-Carman correlation and other capillary models are their inability to address the coupled interactions of pores in more than one direction. Capillary models attempt to account for multidimensional coupling through some measure of tortuosity. Dullien (1992) offers some sharp words regarding tortuosity, even when used in his own developments. Although some attempts are made to measure tortuosity from microstructure, in most applications it is a feature of the *model* rather than the *porous medium*. Dullien (1992) further states "...Υ is simply interpreted as a "fudge factor" for any permeability model (i.e., $\Upsilon \equiv {}^{\kappa_{model}}/_{\kappa_{measured}}$). It is important to stress the point that the very concept of Υ

is limited to one-dimensional models because the tortuosness of the pore network is intrinsically incorporated into three-dimensional models."

As a philosophical aside, this is precisely the intent of developing fully anisotropic 3-D models in this research. Three-dimensional connectivity and directionality are inherent features of Equation (5.8a) through the variables $\mathcal{C}$ and $(1/f_{void})\,\mathbf{F_{void}}$. A quantity like tortuosity is too often presented as a microstructural measure, but more often in practice it is simply used as an empirical fit factor. Three-dimensional microstructural models preclude the need or urge to incorporate such quantities in mathematical models.

Dullien (1992) reviews many other permeability models: statistical, empirical, network, and deterministic. Due to the complexity of the full momentum equations, empirical models often offer the best result across a broad range of flow regimes. A general model like Equation (5.8a) also has its restrictions. Because it was developed from Darcy's law, the permeability model presented here is specific to linear Darcy flows at very low Reynold's Numbers ($Re_r \leq 1$). At higher flow rates in nonlinear and potentially turbulent flow regimes, constitutive formulations like the Forchheimer equation or Ergun equation are better suited. Additional material properties are introduced in these constitutive models (Dullien, 1992; Wang, 1999; Nield and Bejan, 2006).

Outside the isotropic 1-D capillary-type models it is difficult to directly compare other permeability expressions to an analytical expression like Equation (5.8a). Because the fundamental difference between Equations (5.8a) and (5.8b) is potential anisotropy, other models that address this are of interest. Anisotropic permeability has been observed in geologic materials and mathematical models follow (Clavaud *et al.*, 2008). Wong (2003) investigates strain-induced changes in quantities comprising the semi-empirical Kozeny-Carman correlation. Specifically, he ties the evolution

of parameters like hydraulic radius and tortuosity to shearing strain, linearly relating principal values of a permeability tensor to the principal values of strain. His results exhibit anisotropic permeability, but a microstructural expression for the permeability tensor is not specifically developed.

Several network modeling efforts have investigated anisotropic pore structure (Bear *et al.*, 1987; Friedman and Seaton, 1996; Wang, 1999; Ursino *et al.*, 2000; Helmig *et al.*, 2006). Network models represent a complicated pore structure with a lattice of interconnected nodes and branches. Physically, the nodes represent the void cells and the bonds represent the channels connecting voids. Capillary networks imply numerical simulation. To generalize, anisotropic studies in such networks involve a sensitivity analysis of sorts. Means of inducing anisotropy in such networks are: varying the connectivity by direction (removing branches in the network) (Friedman and Seaton, 1996; Wang, 1999), varying void or channel size by direction (Bear *et al.*, 1987; Friedman and Seaton, 1996; Wang, 1999), and varying the spatial-correlation of void cells by direction (Wang, 1999; Helmig *et al.*, 2006). For example, the channels are increased in size in a given direction and the subsequent effect on network permeability is observed. In doing so the effect of pore-scale geometry is related to macroscopic permeability and anisotropy factors can be calculated. These methods do not produce analytical expressions.

Despite a lack of direct comparison, features of the network models lend credence to the assumptions taken here. First, the networks of Wang (1999) and Martins *et al.* (2007) assign spherical shape to void cells and cylindrical shape to channels, as was assumed in deriving Equation (5.8a). Helmig *et al.* (2006) uses cubic void cells and square channels. Second, Wang (1999) applies an identical microscopic constitutive law between centers of two connected pores, as was applied here. He also treats the pressure drop within a void cell as negligible and inertial terms in a channel

are neglected with the assumption of Stokes' flow (low Reynold's Number)—both assumptions also applied here.

Qualitatively, accurately describing a complicated pore structure requires three essential features: connectivity, the converging-diverging nature of pore segments, and the distribution of pore sizes (Wang, 1999). In the limits of slow, low Reynold's Number flow, a permeability model like Equation (5.8a)—or even more generalized to also let $\hat{r}$ or even $\hat{R}_{void}$ vary with orientation—captures all of these features in a tractable, analytical expression.

5.4 Elastic Stiffness

The proposed linear elastic stiffness model in Chapter 4, repeated here for ease of reference, is

$$\boxed{C^*_{ijkl} = \frac{1}{f^2}\left(\lambda^* F_{ij}F_{kl} + 2G^* F_{ik}F_{jl}\right),} \tag{5.16}$$

with effective isotropic stiffness coefficients

$$\boxed{\begin{aligned} \lambda^* &= \frac{1}{20}\left(\frac{\hat{\rho}}{\hat{R}}\right)^2 \phi\mathcal{N}E_{ice}\left(1-\zeta\right) \\ G^* &= \frac{1}{40}\left(\frac{\hat{\rho}}{\hat{R}}\right)^2 \phi\mathcal{N}E_{ice}\left(2+3\zeta\right) \end{aligned}}, \tag{5.17}$$

where F_{ij} are the coefficients of the contact tensor and $f = 1/3$ is the contact tensor's isotropic value in 3-D.

5.4.1 Other Analytical Models

There are two other models in the literature that use the 2nd order contact tensor with the 4th order elasticity tensor to incorporate granular anisotropy into the micromechanical description: Chang *et al.* (1995) and Rahmoun *et al.* (2009). A brief interpretation of these approaches is listed here:

- Both use the Voigt homogenization algorithm presented in Chapter 4.
- Rather than assume a random/uniform distribution of contacts, both incorporate a distribution density function $P(\bar{n})$ into the averaging operation. This permits the averaged local contact quantities to vary with orientation.
- Both assume $P(\bar{n}) = {}^{1}/_{4\pi}\{1 + \Psi_{ij}n_in_j\}$ as presented in Chapter 2. That is, they estimate the smooth scalar 3-D pdf as a series solution truncated at two terms: the scalar isotropic value and deviations from that given by a 2nd order fabric tensor. Recall that $\Psi_{ij} = {}^{15}/_{2}F'_{ij}$ in 3-D, where F'_{ij} are the coefficients of the deviatoric part of the 2nd order contact tensor Kanatani (1984).
- Both then derive expressions for the elastic stiffness coefficients in terms of microstructural geometry, spring stiffnesses, and contact tensor coefficients.

Comparing these models to Equation (4.24) is pertinent to the current research. Chang *et al.* (1995) and Rahmoun *et al.* (2009) take essentially identical analytical approaches and their results are also identical in how the coefficients of $\mathbf{F}$ relate to the coefficients of $[C^*]$. This conclusion is not immediately obvious as their results are written in terms of different variables. Appendix B demonstrates that the Chang *et al.* (1995) and Rahmoun *et al.* (2009) models are equivalent with two examples. The model will be referred to as the Chang *et al.* (1995) model from this point forward

as this represents the first publication of these results. There are other significant conclusions in Rahmoun *et al.* (2009) apart from incorporating $\mathbf{F}$ into $\mathbb{C}$.

The effective stiffness tensor developed in Chapter 4, the Chang *et al.* (1995) model, and the result of representation theorems are presented here in terms of common variables. The expressions are written in index notation for succinctness. First, Equation (5.17) is taken as Equation (4.15) so that λ^* and G^* are written as functions of: 1) normal and shear spring stiffnesses k_n and k_s, respectively, 2) the total number of contact planes or bonds N_{cp}, 3) the representative volume V, and 4) mean spherical grain radius $\hat{R}$. Applying $f = 1/3$ and Equation (5.16) becomes

$$C^*_{ijkl} = \frac{12N_{cp}\hat{R}^2}{5V}\left\{(k_n - k_s)\,F_{ij}F_{kl} + (2k_n + 3k_s)\,F_{ik}F_{jl}\right\}. \tag{5.18a}$$

Next the Chang *et al.* (1995) model is written in terms of the same variables. This expression was taken from Rahmoun *et al.* (2009), Equation (24):

$$\begin{aligned} C^{hom}_{ijkl} = \frac{4N_{cp}\hat{R}^2}{7V}\Bigg\{ & k_n\left[-\frac{1}{5}\left(\delta_{ij}\delta_{kl} + 2\delta_{ik}\delta_{jl}\right) + \left(F_{ij}\delta_{kl} + \delta_{ij}F_{kl}\right) + 2\left(F_{ik}\delta_{jl} + \delta_{ik}F_{jl}\right)\right] \\ & -k_s\left[-\frac{1}{5}\left(\delta_{ij}\delta_{kl} + 2\delta_{ik}\delta_{jl}\right) + \left(F_{ij}\delta_{kl} + \delta_{ij}F_{kl}\right) - \frac{3}{2}\left(F_{ik}\delta_{jl} + \delta_{ik}F_{jl}\right)\right]\Bigg\}. \end{aligned} \tag{5.18b}$$

Finally, the result of representation theorems—Equation (2.8)—is repeated here:

$$\begin{aligned} C_{ijkl} = {} & a_1\delta_{ij}\delta_{kl} + a_2\left(F_{ij}\delta_{kl} + \delta_{ij}F_{kl}\right) + a_3\left(\delta_{ij}F_{kq}F_{ql} + \delta_{kl}F_{iq}F_{qj}\right) \\ & + b_1F_{ij}F_{kl} + b_2\left(F_{ij}F_{kq}F_{ql} + F_{is}F_{sj}F_{kl}\right) + b_3F_{is}F_{sj}F_{kq}F_{ql} \\ & + c_1\left(\delta_{ki}\delta_{lj} + \delta_{li}\delta_{kj}\right) + c_2\left(F_{ik}\delta_{lj} + F_{kj}\delta_{li} + F_{il}\delta_{kj} + F_{lj}\delta_{ki}\right) \\ & + c_3\left(F_{ir}F_{rk}\delta_{lj} + F_{kr}F_{rj}\delta_{li} + F_{ir}F_{rl}\delta_{kj} + F_{lr}F_{rj}\delta_{ik}\right). \end{aligned} \tag{5.18c}$$

The anisotropy tensor coefficients are changed to F_{ij} from A_{ij} for consistency. Recall that a_1, a_2, a_3, b_1, b_2, b_3, c_1, c_2 and c_3 are scalar-valued isotropic functions of ϕ and the three invariants of $\mathbf{F}$. Because these coefficients are typically defined by fitting to experimental data, this model is considered a semi-empirical approach to anisotropic stiffness.

As an initial check, the Chang *et al.* (1995) model (Equation (5.18b)) reduces to dependence on only two coefficients—Equation (4.15)—in the isotropic case, consistent with an isotropic Voigt homogenization. The model proposed here—Equation (5.16) or Equation (5.18a)—also correctly reduces to an isotropic Voigt homogenization. Likewise, Equation (5.18c) reduces to two independent coefficients in the case of an isotropic microstructure. This case is reviewed in Cowin (1985) where he defines the Lamé parameters as

$$\begin{aligned} \lambda &= a_1 + 2a_2F_{11} + (2a_3 + b_1)F_{11}^2 + 2b_2F_{11}^3 + b_3F_{11}^4, \\ \mu &= c_1 + 2c_2F_{11} + 2c_3F_{11}^2. \end{aligned} \tag{5.19}$$

In general, all three models correctly reflect the number of independent elastic stiffness coefficients for the isotropic, transversely isotropic, and orthotropic cases: two, five, and nine, respectively. The models cannot capture levels of symmetry in C_{ijkl} above orthotropic due to the limitations of the 2$^{\text{nd}}$ order anisotropy tensor (see Chapter 2).

For a wholly oriented microstructure—all contacts aligned in a single direction—the Chang *et al.* (1995) model results in numerically significant negative stiffness values (see Appendix B). This occurs for common values of $\zeta = {}^{k_s}/_{k_n} = {}^{G_{ice}}/_{E_{ice}}$. For most engineering materials, Young's modulus is more than double the shear modulus (Ugural and Fenster, 1995). With a contact tensor reflecting the extreme limit of transverse isotropy, the Chang *et al.* (1995) model yields negative stiffnesses unless

$\zeta \geq 1$. The other models do not share this characteristic. While such an extreme textural arrangement is not anticipated in practice, Equations (5.18a) and (5.18c) deliver physically meaningful outputs for even the limiting case of anisotropy.

Representation theorems indicate that to sufficiently describe up to orthotropic stiffness behavior with a 2^{nd} order fabric tensor, terms up to and including squared terms of that fabric tensor must be included (Cowin, 1985). Equation (5.18c) contains terms of order one, two, three and four in $\mathbf{F}$. It is customary to neglect terms of order higher than two (Cowin, 1985; Turner *et al.*, 1990; Odgaard, 1997), in which case $b_2 = b_3 = 0$. This simplifies Equation (5.18c) without restricting possible material symmetry. Representation theorems have drawbacks, chiefly the number of unknown constants/functions that must be empirically determined. However, they are useful for identifying the functional relationship between two tensors like contact and stiffness. Equation (5.18a) neatly incorporates squared fabric terms, consistent with the prediction of representation theorems. Equation (5.18b) model uses only linear fabric terms.

5.4.2 A Numerical Model and CT Data

Srivastava *et al.* (2010) conducted a temperature-gradient metamorphism experiment to quantify thermally-induced changes in the microstructure of snow. They accomplished this by imaging samples via X-ray computed tomography (CT) during the experiment. CT software was used to evaluate several microstructural parameters and indices, including density and a MIL fabric tensor. Additionally, CT images were used to directly create a mesh for a finite element model that numerically simulated the linear elastic properties of the snow. They concluded that $\sim 90\%$ of the variation they observed in the simulated stiffness coefficients could be attributed to changes in density and fabric.

The measured changes in density and fabric permit a unique opportunity to evaluate and compare mathematical models. Additionally, Srivastava *et al.* (2010) calculated the unknown a_i, b_i and c_i for Equation (5.18c) by "using non-linear multiple regression analysis." Therefore, this data set permits an initial comparison of two different analytical models, the semi-empirical model, and the numerically modeled finite element results.

The spring stiffness expressions developed in Chapter 4 are applied to Equations (5.18a) and (5.18b):

$$k_n = \frac{\pi \hat{\rho}^2 E_{ice}}{2\hat{R}} \qquad k_s = \frac{\pi \hat{\rho}^2 G_{ice}}{2\hat{R}}. \tag{5.20}$$

Apart from $\hat{\rho}/\hat{R}$, the variables in Equations (5.18a) and (5.18b): 1) can be parameterized by density (see Table 5.1), 2) are material properties of ice, or 3) are measured fabric tensor coefficients. The stiffness properties of isotropic polycrystalline ice are taken from Petrenko and Whitworth (1999): $E_{ice} = 9,330$ MPa and $G_{ice} = 3,520$ MPa.

The reported evolution in density and fabric from Figure 4a. and Figure 4d. in Srivastava *et al.* (2010) are reproduced here in Figure 5.2. The reported density in Srivastava *et al.* (2010) was derived both from direct mass and volume measurements, and from CT images. Only the CT-based density is reproduced here because the numerically simulated stiffness coefficients are a direct byproduct of the CT images. Also, no attempt is made here to reproduce the error bars in Figure 4d. of Srivastava *et al.* (2010). It is noteworthy that within statistical uncertainty: 1) the reported MIL fabric coefficients are the principal values, 2) the principal direction of MIL_1 is coincident with the direction of the applied temperature gradient, and 3) magnitude differences between MIL_2 and MIL_3 are negligible (Srivastava *et al.*, 2010). These

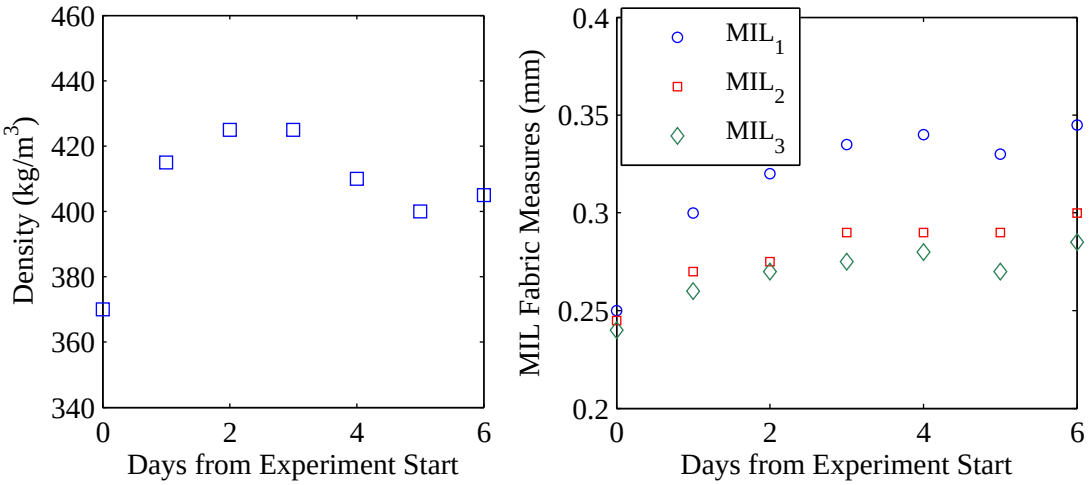


Figure 5.2: Evolution of density and MIL fabric tensor coefficients during temperature gradient experiment of Srivastava *et al.* (2010). The figures are reproduced from Figure 4a. and Figure 4d. in Srivastava *et al.* (2010).

observations indicate a developing transversely isotropic microstructure where the ice structure is exhibiting a preference for the "1" direction—the direction of the applied gradient—and the "2-3" plane is isotropic.

The microstructural analytical models rigorously require a contact tensor, but the available data are MIL fabric tensor coefficients. The arguments in Chapter 2 indicate that a normalized MIL fabric tensor should be an appropriate surrogate for the contact tensor. These normalized MIL fabric coefficients are pictured in Figure 5.3. These data are used as the contact tensor coefficients in Equations (5.18a) and (5.18b) as

$$\begin{bmatrix} F_{11} & 0 & 0 \\ 0 & F_{22} & 0 \\ 0 & 0 & F_{33} \end{bmatrix}. \tag{5.21}$$

Srivastava *et al.* (2010) notes that density varies in a complicated manner. There is an initial increase followed by a slight decrease. It is speculation, but these effects

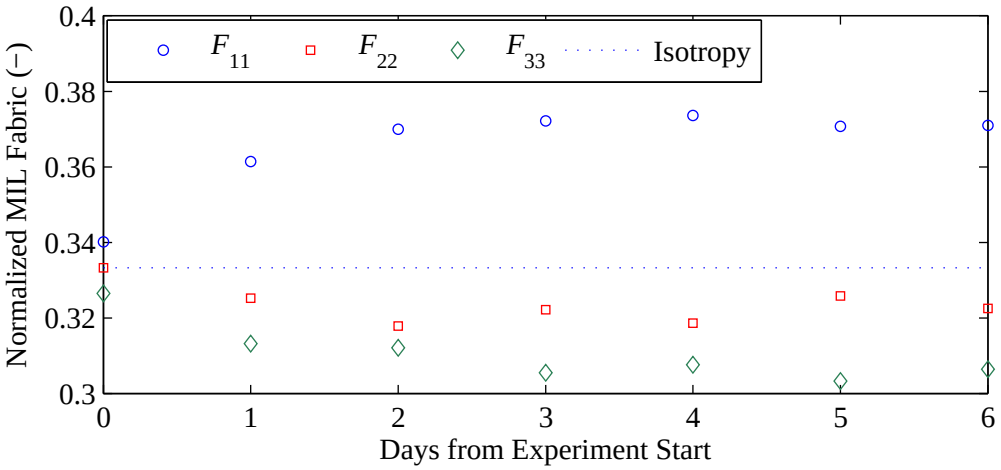


Figure 5.3: Normalized MIL fabric tensor coefficients. Each coefficient is normalized by the trace of the measured MIL fabric tensor coefficients in Figure 5.2b: $\mathrm{MIL}_1 + \mathrm{MIL}_2 + \mathrm{MIL}_3$.

might be due to an initial settling and subsequent mass loss. The test apparatus is open on the top and the large temperature gradient would force sublimation and vapor diffusion over time. The normalized MIL fabric coefficients exhibit approximately a 10% increase in the direction of the applied gradient and a corresponding 5% decrease in each of the orthogonal directions defining the isotropic plane. Figures 5.2a and 5.3 portray the inputs to the analytical models.

The numerically simulated linear elastic stiffness coefficients are plotted in Figure 5.4. Again, these values are reproduced from Figure 5a. and Figure 5b. in Srivastava *et al.* (2010). Results from the analytical models are plotted in Figures 5.5 and 5.6. Figure 5.7 shows the semi-empirical results. Identical axis limits are used for ease of comparison. In the analytical microstructural models, $\hat{\rho}/\hat{R}$ was fixed to a constant 0.36, also for ease of comparison. This value virtually matched the initial stiffness coefficients of the analytical models to the numerical results.

The maximum percent increase in any stiffness moduli is C_{1111}. Not surprisingly, an increase in stiffness follows the preferential direction of ice structure. Comparing

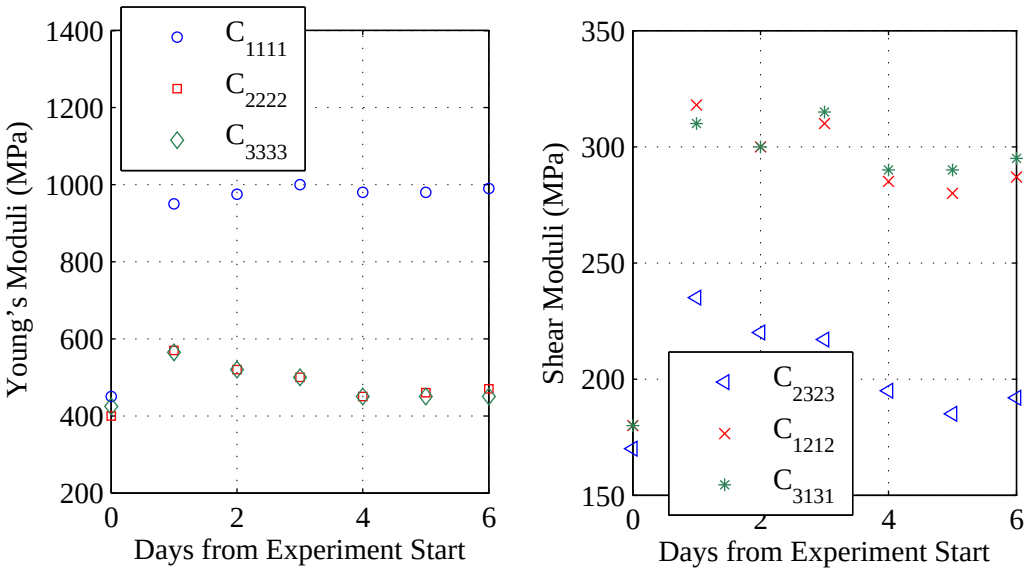


Figure 5.4: Evolution of elastic stiffness coefficients during temperature gradient experiment of Srivastava *et al.* (2010). The moduli were numerically simulated with a finite element model. The figures are reproduced from Figure 5a. and Figure 5b. in Srivastava *et al.* (2010).

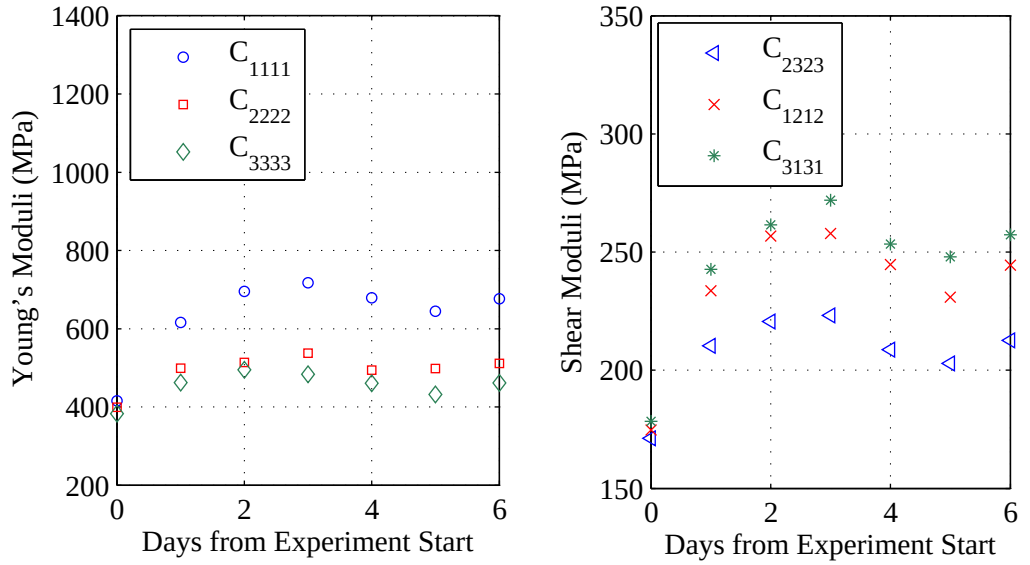


Figure 5.5: Evolution of stiffness coefficients predicted by Equation (5.18a) based on density and fabric changes with $\hat{\rho}/\hat{R} = 0.36$: this ratio was fixed to mimic the numerical results in Figure 5.4 on Day 0.

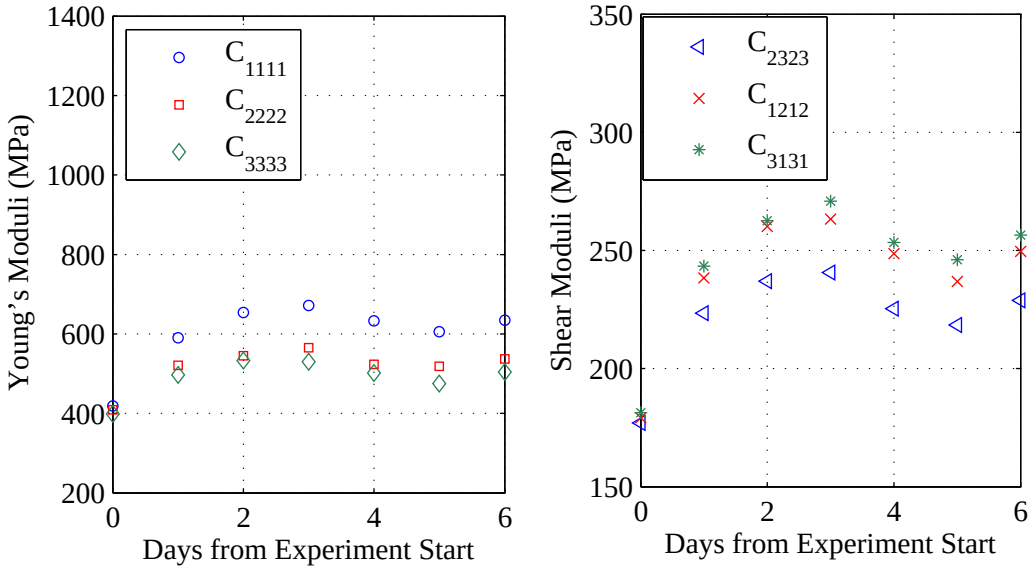


Figure 5.6: Evolution of stiffness coefficients predicted by Equation (5.18b) based on density and fabric changes. As above, $\hat{\rho}/\hat{R}$ was fixed at 0.36.

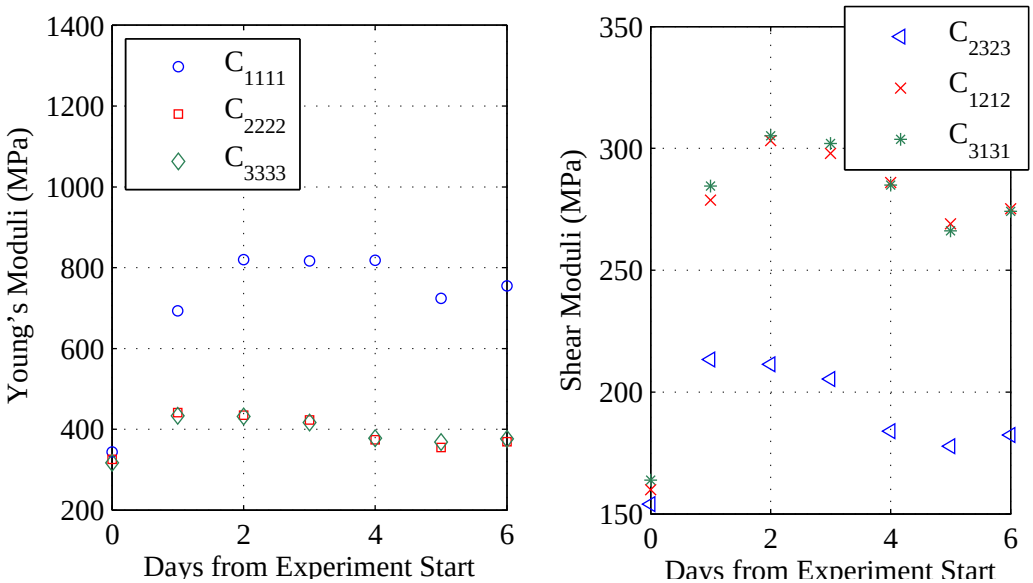


Figure 5.7: Evolution of stiffness coefficients predicted by Equation (5.18c) based on density and fabric changes. In this model there are no other microstructural variables. The empirically determined coefficients were taken from Srivastava *et al.* (2010), Table 4. They were determined as the best fit to the data in Figure 5.4.

Day 3 versus Day 0 for the Srivastava *et al.* (2010) numerically modeled data shows an increase of 119%. Between the same two days, Equation (5.18a) predicts an increase of 73%, Equation (5.18b) predicts a 60% increase, and Equation (5.18c) predicts a 137% increase. This coefficient is also the greatest discrepancy between the numerical and analytical models. The percent difference between the different models for other moduli is not as great.

In terms of anisotropy, the numerical results indicate a difference of approximately 520 MPa between C_{1111} and C_{2222}–C_{3333} and 100 MPa between C_{1212}–C_{3131} and C_{2323}. These same comparisons from the other models are approximately: 200 MPa and 45 MPa from the model developed here, 120 MPa and 25 MPa from the Chang *et al.* (1995) model, and 400 MPa and 100 MPa from the representation theorem model.

With no validation data it is difficult to draw conclusions regarding accuracy of the various methods. The FEM has an advantage of drawing directly on the microstructural geometry delivered by CT scans. However, a complicated geometry creates difficulties in element selection and meshing, both of which impact the results. The coefficients of the representation theorem model were tailored to the FEM results. The number of coefficients in this model permits the greatest flexibility in fitting to experimental data at the cost of limited ties to the microstructure. The analytical microstructural models are restricted because they spring from an idealized geometry of uniform spheres. Also, anisotropic effects on the analytical models due to bond radius cannot be investigated with these data.

In terms of absolute numbers, the stiffness values predicted here are high. Summarizing many sources, Shapiro *et al.* (1997) reports that for snow of this density—approximately $400\,^{\mathrm{kg}}/_{\mathrm{m}^3}$—Young's modulus usually falls in the range 150-300 MPa. The numerical model predicts stiffer than this for even the isotropic initial condition. Srivastava *et al.* (2010) points out that most experimental results come from quasi-

static compression tests that assume an isotropic microstructure. Such tests might obscure the true elastic response of the test material and reduce the measured effective stiffness. In short, the linear elastic response of snow is a difficult behavior to simulate and measure.

In conclusion, all the models predict that a change in density and a relatively modest reorientation of the ice structure have a significant effect on the macroscopic stiffness. Highlighting C_{1111} again, the models predict anywhere from a 60–137% increase in this coefficient due to a 14% increase in density and a 10% increase in the fabric coefficient. Density has long been recognized as an important parameter in predicting snow's thermo-mechanical properties. Anisotropy is also evident in these data, a behavior that density cannot characterize. The measured MIL fabric tensor quantifies the anisotropy and the analytical and semi-empirical models each incorporate fabric in a different manner. The analytical model proposed here compares well to these other models in this initial assessment.

5.5 Summary

The anisotropic microstructural constitutive models developed in Chapters 3 and 4 were compared here to other models and published experimental data. The conclusion is that the models are feasible and deserving of additional investigation. The effective diffusivity model is the least tested as there is little conclusive data and very few other mathematical models targeted at two-phase microstructures. The reduced isotropic permeability model compares well to the Kozeny-Carman correlation. Qualitatively, the anisotropic and connectivity features of the general permeability model mesh with other network/numerical approaches that quantify these effects.

This chapter marks the extent of this investigation into these models. Current stereological algorithms cannot calculate many of the diffusivity parameters. Despite its recognized impact on energy transfer, evaluating this model is left to future work. The permeability model, while of potential widespread application to general granular materials, is not a focus of this research. This project is more interested anisotropic effects on energy transport and stiffness properties.

The effective conductivity model is well-supported. Assuming isotropy, the model developed here compares well to other analytical microstructural and empirical models. The use of the contact tensor to account for anisotropy is also backed by another analytical derivation. The elastic stiffness model uniquely benefits here from a study that measured anisotropy. The method of relating a 2^{nd} order fabric tensor and the 4^{th} order stiffness tensor is different from other approaches, but initial results indicate it compares favorably to other mathematical models.

This also marks the end of the discussion of the elastic stiffness model. Creating anisotropic snow layers and testing and modeling their mechanical behavior is a topic of ongoing research in the Subzero Science and Engineering Research Facility at Montana State University. The anisotropic linear elastic microstructural model proposed here is included in this effort.

CHAPTER 6
EXPERIMENTS AND METHODS

6.1 Microstructural Experiments and Data

Schneebeli and Sokratov (2004) describe a series of temperature gradient experiments in which a novel apparatus dubbed the snow breeder simultaneously: 1) applied a temperature gradient to a snow sample, 2) measured the temperature boundary conditions and energy flux in the direction of the applied gradient, and 3) recorded CT images of the evolving microstructure. The snow breeder consisted of a cylindrical sample chamber of 48 mm diameter and 25 mm height surrounded by an insulating foam ring of the same height and an 18 mm thickness. The foam ring is included to minimize heat flow in the radial direction. The top and bottom of the sample chamber were closed. Instrumentation at each end consisted of a disk-type heat flux sensor and thermocouple. A film heater applied heat at the bottom and a passive heat exchanger removed heat at the top.

6.1.1 EHC: Effective Heat Conductivity

Heat was applied to the snow breeder over the course of approximately one week, resulting in temperature gradient metamorphism. Measuring the one-dimensional temperature gradient and energy flux enabled calculation of the scalar material property relating theses two variables:

$$q = \text{-EHC}\frac{\triangle\theta}{l}, \tag{6.1}$$

where q ($\mathrm{W/m^2}$) is the average of the measured energy fluxes, $\triangle\theta$ (K) is the measured temperature difference in the direction of the applied gradient, and l (m) is the height

of the snow column in the sample chamber. They labeled the material property as effective heat conductivity—EHC ($^{W}/_{m \cdot K}$)—to reflect that it is the aggregate of many different processes and not limited to pure conduction. The EHC data were recorded in a table of time (sec) and EHC. An EHC calculation was performed every 5 minutes from averages of recorded energy flux and temperature data.

6.1.2 CT Images

CT images provided a nondestructive means to capture changes in microstructure over the course of an experiment. The CT images were assembled as reconstructed volumes from a sequence of 200 planar images or slices. Each 200 image sequence required 7.5 hours to execute and the process was repeated every 8 hours. Subsequently, three volumes were produced every 24 hour period. The nominal resolution was 36 μm and the images were segmented by threshold prior to this analysis. The threshold converted grayscale pixels to black or white pixels so that ice and pore are easily differentiated. The reconstructed volume in Figure 6.1 consists of grayscale pixels prior to binary conversion. The binary values yield black ice particles and white void space. The threshold was selected to match the porosity of the reconstructed volume to the porosity determined by the weight and volume of the snow sample. In the reference frame of Figure 6.1, the arrays of CT data provided for analysis were 135 x 204 x 204 pixels^3 in dimension. The reader is referred to Schneebeli and Sokratov (2004) for more details regarding the test apparatus, instrumentation, and CT scanner.

6.1.3 Other Microstructural Data

The derived EHC values and CT images provide both an affected material property and evolving microstructural imagery—a combination required to initially test the

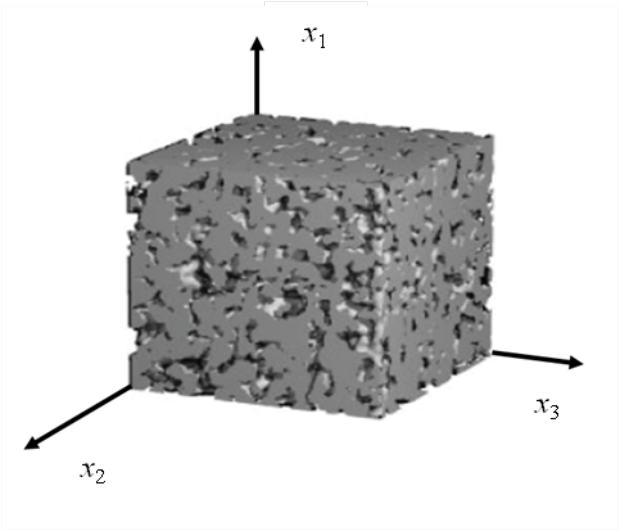


Figure 6.1: Example of a grayscale reconstructed volume of high density snow (490 $^{kg}/_{m^3}$) with reference axes. $+x_1$ is the direction of heat flow given the idealized applied unidirectional temperature gradient. The physical dimensions of the pictured volume are 5 x 5 x 4.85 mm^3.

validity of constitutive models like those proposed in Chapters 3 and 4. Additional stereological parameters of the microstructure were also calculated by CT scanner companion software. These data are presented in Schneebeli and Sokratov (2004) and a few of these measures were useful in comparing to the stereological analysis presented here.

Specifically, the CT companion software estimates ice structure size, pore size, and degree of anisotropy (DA). Both ice structure and pore size were presented in Figure 3 and Table IV in Schneebeli and Sokratov (2004). These parameters correspond to the physical ice grain and pore cell diameters (μm). DA is the ratio between the largest and smallest principal values of a MIL fabric tensor, as described in Chapter 2. Unfortunately, the coefficients of the actual tensor were not available for comparison, but the reported DA values yield some insight into any anisotropy of the microstructure. A DA of one equates to an isotropic microstructure, while DA $\rightarrow \infty$ for a wholly anisotropic arrangement. It was also reported whether the largest principal value

favored a horizontal direction (orthogonal to the applied temperature gradient) or the vertical direction (parallel to the applied temperature gradient).

6.1.4 Experimental Samples

The stated aim of the experiments was to simultaneously observe structural changes in snow during temperature gradient metamorphism and to measure the changes in EHC of the same snow. The results from six different samples were reported in Schneebeli and Sokratov (2004). Samples 1–3 were lower density snow and samples 4–6 were high density snow. The high density samples were requested for this analysis. They were favored for two reasons. First, the reported ice structure size for the high density samples was 1.5–2 times that of the low density snow. The analysis required here depends on identifying both grains and bonds, and bonds are a fraction of the size of grains. The lower density samples might present numerical difficulties in defining such tiny grains and bonds.

Second, the derived EHC values from the high density experiments indicated, inasmuch as only three samples can reveal, a well-defined and repeatable behavior. These samples exhibited no appreciable change in density but measured significant increases in EHC in the direction of the temperature gradient. With negligible changes in density, current conductivity models parameterized by density cannot predict such a pronounced change in thermal conductivity. This opens a door for introducing anisotropic models like Equation (3.34) to explain such observed changes.

Unfortunately, CT images were not available for sample 5 due to equipment problems. However, the available data from samples 4 and 6 were provided in support of this research. Test characteristics for each of these samples is summarized in Table 6.1. Unfortunately, no heat flux data was recorded after day 1 of the sample 6 run. The reconstructed CT volumes were still analyzed.

Table 6.1: Characteristics of the high density snow samples in Schneebeli and Sokratov (2004).

Sample Number	Density ($^{kg}/_{m^3}$)	Temperature Gradient ($^{K}/_{m}$)	Preparation
4	490	100	0.711 mm sieve
6	514	50	0.711 mm sieve

6.1.5 Modeling Changes in EHC

Both the conduction and vapor diffusion/phase change models from Chapter 3 should be evaluated to compare to the reported EHC. Unfortunately, available image analysis software is not yet equipped to measure the microstructural quantities of the vapor diffusion/phase change model. However, with slight modification, the algorithms developed in Edens (1997) are capable of evaluating the microstructural quantities in the simpler conductivity model. Especially when considering that the experimental data are a product of temperature gradient metamorphism, not including the vapor diffusion/phase change model—one of the dominant modes of energy transfer—is dissatisfying.

Still, the provided CT images offer a unique opportunity to evaluate the proposed anisotropic microstructural conductivity model. This is an important contribution and the first occasion to link a measured contact tensor to a measured material property in snow. Although the conductivity model does not incorporate all energy transfer modes captured by EHC, it is still undoubtedly a critical contributor. The following sections address the analysis techniques used to evaluate each of the quantities in the conductivity model from the provided CT images.

6.2 Stereological Analysis

Edens (1997) describes algorithms developed specifically to identify grains, necks, and bonds in snow microstructure from planar sections. The primary advantage of this approach is its ability to distinguish bonds from grains. Standard stereology methods can distinguish a solid constituent from void, but estimating quantities such as bond size and bond orientation demands the specific features described in Edens and Brown (1995) and Edens (1997). One current limitation of the software is that it operates only on 2-D images. Estimating associated 3-D quantities from such surface measurements is the realm of stereology, requiring probability and assumptions regarding distributions of grain and bond size and shape.

The stereology software operates on white ice particles rather than black. This requires a simple binary inversion but it is an important step that cannot be omitted. The algorithms rely on the "skeletonization" of the white ice structure. Skeletonization applies a thinning filter that erodes the white pixels to a connected backbone that is everywhere one pixel thick. Figure 6.2 portrays excerpts from a typical image processing sequence. Figure 6.2a is a binary image where pixels representing ice are white. Figure 6.2b is the skeletonization of Figure 6.2a.

The size or thickness of the original ice structure normal to the skeleton is associated with each point along the skeleton. Bonds are delineated based on a combination of this thickness data and changes in slope/concavity of the skeleton. To further illustrate, Edens and Brown (1995) draw a useful analogy—repeated here—between the skeleton and a ridge line connecting mountain peaks. Mountain peaks represent thicker points in the ice structure, and saddles connecting peaks (points of changing concavity) represent thinner points. If the height of the lowest saddle relative to the height of the lowest connected peak falls below a user-defined threshold, then



(a) Binary image (b) Skeleton of the binary image (c) Segmented binary image

Figure 6.2: A sample image processing chronology: (a) a binary microstructural image of snow where white pixels represent ice, (b) the skeletonization of (a), and (c) the final, segmented image where the lines overlaid on (a) represent the 2-D bonds.

that point on the skeleton is defined as a bond. Pixelated line segments that span the ice structure are defined normal to the skeleton at such bond sites. These line segments represent constrictions in the planar ice network: 2-D bonds. The result is a segmented ice network, pictured in Figure 6.2c.

The preceding paragraphs succinctly summarize the bond-specific points of Edens (1997). One additional detail pertinent to this analysis is that 2-D grains are defined as circular disks that fit inside the white pixels at points on the skeleton identified as grain centers. This necessarily underestimates the 2-D grain radius, a point that is revisited in the next chapter when estimating 3-D grain radius. The reader is referred to Edens and Brown (1995) and Edens (1997) for further details regarding the applied stereological techniques.

The software produces three output files for every 2-D image analyzed. In the first file, each 2-D bond generates a row of data. The data used in this analysis are:

- 2-D bond radius, $\rho_{(2-\mathrm{D})}$ (pixels), and orientation, ω (deg), with respect to the reference Cartesian coordinates,

- 2-D radii, $R_{(2\text{-D})}$ (pixels), and centroid coordinates (pixels) of the grains the bond connects, and
- The tangent to the ice network skeleton, ϖ (deg), at the bond site.

The second file addresses connectivity. The total number of 2-D grains are binned according to whether they have zero, one, two, etc. bonds. From these data it is simple to calculate a mean 2-D coordination number, $\mathcal{N}_{(2\text{-D})}$. For example, consider five grains: one with zero bonds, two with one bond, and two with two bonds. Via a weighted average, the mean 2-D coordination number is $(1/5)\,0 + (2/5)\,1 + (2/5)\,2 = 6/5$. This is the average number of bonds per grain.

The third file contains results from test line analyses. The quantities used here are total test line length (pixels) and total intercept length (pixels). The concept of test lines was introduced in Chapter 2. Many parallel lines superimposed across a 2-D image comprise a test line. The total intercept length is the number of pixels along that line that correspond to a particular constituent. The intercept of interest here is with the white pixels representing ice, so, the total intercept length is the number of pixels along the total test line length that are also white. This is not to be confused with mean intercept length (MIL) presented in Chapter 2. MIL denotes *points* of intersection along the test line while Total Intercept Length represents *lines* of overlap with the test line.

Lastly, stereological data must be collected from all three orthogonal reference planes. 2-D images were created by "slicing" the 3-D reconstructed array along a reference axis. For example, Figure 6.3 depicts 2-D binary images in the $x_1 - x_3$ plane extracted from the volume at different points along the x_2 axis. Ten 2-D images were saved at each planar orientation. Each image was assumed representative of the microstructure at that orientation, so the data in each output file was concatenated

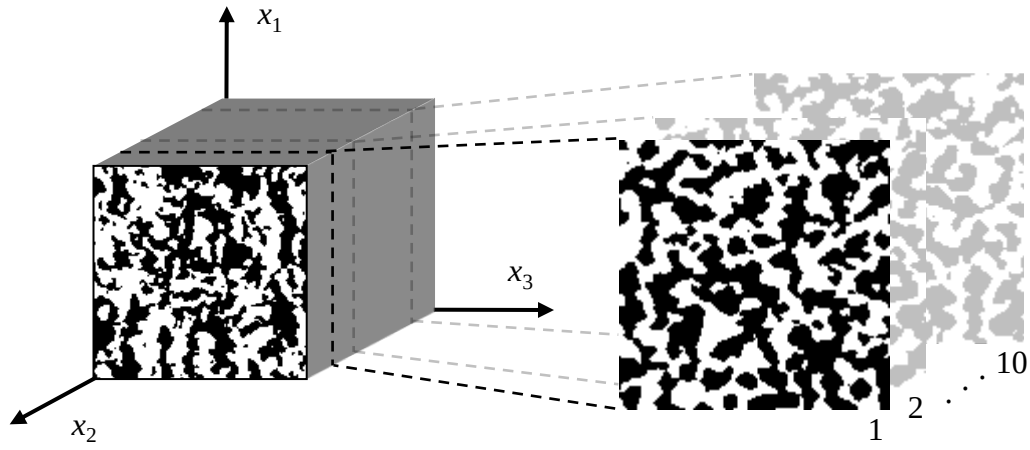


Figure 6.3: Examples of 2-D images or slices extracted from the 3-D reconstructed volume. Ten slices at each planar orientation are used for stereological analysis. This figure uses the $x_1 - x_3$ plane to illustrate the sampling technique.

into a single file. Using multiple images yields more representative samples in calculating the stereological measures required in the conductivity model. Examples of the concatenated files can be found in Appendix C, along with an explanation of the available stereological quantities.

6.3 Conductivity Model Parameters

6.3.1 k: Grain Conductivity

The only term that gives the units of conductivity to Equation 3.34 is k. In treating snow as a granular material, this is the scalar conductivity of the grain material: ice. Following Petrenko and Whitworth (1999), k_{ice} is taken as $^{651}/_{\theta}$, where θ is absolute temperature (K). The mean temperature of all snow samples in the experiments of Schneebeli and Sokratov (2004) was reported as -8°C $\approx$ 265 K, resulting in a k_{ice} of 2.46 $^{\mathrm{W}}/_{\mathrm{m \cdot K}}$. This is the only parameter in the conductivity model that is not derived from the CT images via stereology.

6.3.2 $(1/f)\,\mathbf{F}$: Normalized Contact Tensor

A primary objective of this research is to evaluate anisotropy and its effect on material properties. Consequently, the bulk of the development in this chapter is devoted to the contact tensor term. By definition, the isotropic value of the 3-D contact tensor is $f = 1/3$ (see Chapter 2). Given directional data in three dimensions, the components of $\mathbf{F}$ are calculated directly from Equation (2.9b). However, as described above, the stereological software delivers only 2-D directional data so only the 2-D fabric tensors are readily calculated. First, descriptions of this underlying directional data and associated 2-D fabric tensors are presented. Then, a technique is developed to define the coefficients of a 3-D fabric tensor from 2-D tensors measured on three orthogonal planes.

6.3.2.1 2-D Directional Data and Tensors: This section describes the task of defining directional data from the stereological output files and using it to calculate 2-D tensor coefficients. Three sources of directional data are available: 1) $\omega \pm 90°$—directions normal to 2-D bond segments, 2) ϖ—the skeleton tangent at bond sites, and 3) the angles of line segments connecting centers of bonded grains. The first of these was discarded due to image resolution. Approximately 46% of all identified 2-D bonds were the minimum resolvable radius of a single pixel. With a diameter of only two pixels, these bonds were limited in direction to 0°, 45°, or 90°. With nearly half of the bonds subject to this artificial restriction, the analysis focused on the other two sources of directional data. The 2-D tensor coefficients are then calculated by Equation (2.9b). The differences that arise from using different source data are compared in the next chapter.

6.3.2.2 3-D Tensor from 2-D Data: There is a central difficulty in using 2-D unit vectors to reconstruct a tensor that is rigorously derived from 3-D unit vectors. Figure 6.4 shows an idealized 3-D bonded grain system and an example 2-D rendering that results from an $x_1 - x_3$ plane of section through the 3-D system. $\bar{n}^{(3\text{-D})}$ is the contact normal vector in 3-D, and if available, the contact tensor would be calculated directly from its components. However, $\bar{n}^{(2\text{-D})}$ is typical of what the stereological software delivers. Note that the projection of $\bar{n}^{(3\text{-D})}$ onto the $x_1 - x_3$ plane and $\bar{n}^{(2\text{-D})}$ share direction, preserving this critical information. Put another way, this means that the two components of $\bar{n}^{(2\text{-D})}$ are weighted properly with respect to each other.

Concerning magnitude, with 2-D images the assumption is that the contact normal vectors are of magnitude one: unit vectors. The magnitude of the projection of $\bar{n}^{(3\text{-D})}$ onto the $x_1 - x_3$ plane—the truth data in this example—is clearly less than one. While planar vectors share direction with the 3-D projections, the fact that each planar vector is assumed to be of magnitude one presents the problem. The result is that the absolute values of the 2-D tensor coefficients are meaningless when comparing orthogonal planes. The coefficients only carry meaning relative to the other 2-D coefficients in their plane. Appendix D illustrates this point with a numerical example.

The coefficients of the 2-D contact tensors are labeled $F_{ij}^{(1-2)}$, $F_{ij}^{(1-3)}$, and $F_{ij}^{(2-3)}$ where the superscript defines the 2-D plane on which the tensor was calculated: the $x_1 - x_2$, $x_1 - x_3$ and $x_2 - x_3$ planes, respectively. To further illustrate, consider for example the coefficients $F_{11}^{(1-2)}$ and $F_{11}^{(1-3)}$. Both refer to tensor products of the x_1 components of directional data. However, the first of these coefficients considers x_1 relative to the x_2 direction while the second considers x_1 relative to x_3. The result of averaging within a plane is a quantity that differs in magnitude from plane to plane, even though it refers to the same reference direction. The absolute values of 2-D

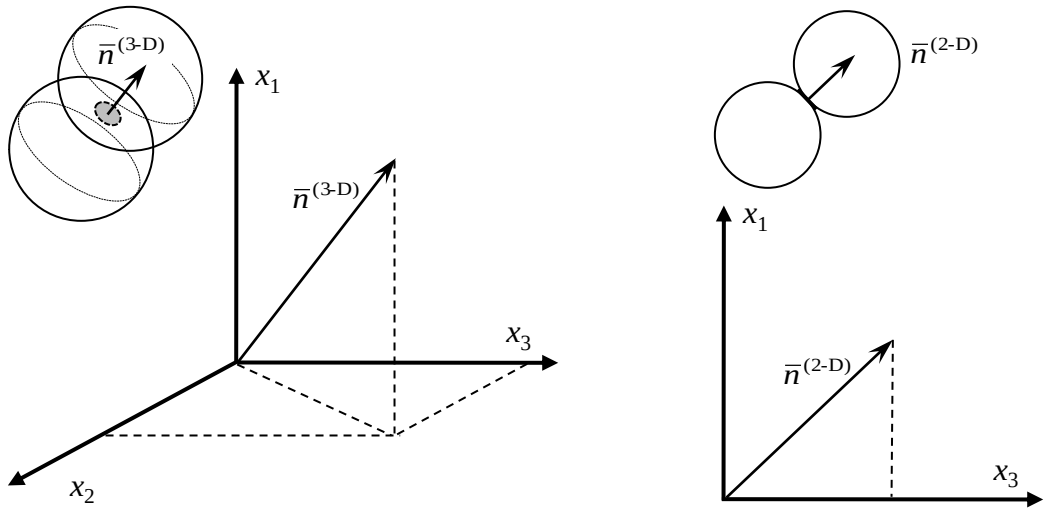


Figure 6.4: On the left, a 3-D bonded grain system with shaded circular bond and contact normal vector. An example of an $x_1 - x_3$ plane of section through the 3-D system is on the right. The 2-D image illustrates that planes of section through spherical grains and circular bonds are circles and lines, respectively. $\bar{n}^{(2\text{-D})}$ shares direction with the projection of $\bar{n}^{(3\text{-D})}$ onto the $x_1 - x_3$ plane. However, $\left|\bar{n}^{(2\text{-D})}\right|$ equals one whereas the magnitude of the projection of $\bar{n}^{(3\text{-D})}$ onto the $x_1 - x_3$ plane is less than one.

fabric coefficients cannot translate between orthogonal planes. However, their relative values—the ratios of 2-D fabric coefficients—offer a connection to three dimensions.

The goal is to construct a 3-D tensor with coefficients $F_{ij}^{(3-\mathrm{D})}$. The constraints on the 2-D tensors from which it is constructed are: 1) they must be calculated on orthogonal planes, and 2) they must "fit" together. This last point is akin to the idea that a value of stress or strain should be a fixed quantity, independent of an observer's position with respect to the reference coordinates. The first constraint is satisfied by the stereological sampling techniques described above. The second constraint is assumed satisfied in the development immediately following. The concept of "fit" is discussed in the next section.

The unknown 3-D coefficients are

$$F_{ij}^{(3\text{-D})} = \begin{bmatrix} F_{11} & F_{12} & F_{13} \\ F_{21} & F_{22} & F_{23} \\ F_{31} & F_{32} & F_{33} \end{bmatrix}^{(3\text{-D})} . \tag{6.2a}$$

Due to the symmetry of the 3-D fabric tensor, this involves six unknown coefficients. The known 2-D coefficients are

$$F_{ij}^{(1-2)} = \begin{bmatrix} F_{11} & F_{12} \\ F_{21} & F_{22} \end{bmatrix}^{(1-2)} \quad F_{ij}^{(1-3)} = \begin{bmatrix} F_{11} & F_{13} \\ F_{31} & F_{33} \end{bmatrix}^{(1-3)} \quad F_{ij}^{(2-3)} = \begin{bmatrix} F_{22} & F_{23} \\ F_{32} & F_{33} \end{bmatrix}^{(2-3)} . \tag{6.2b}$$

Here, the subscripts do not refer to the usual row, column location in the array but rather the reference axis with respect to which the tensor product is taken.

The following relationships are applied to solve for the three diagonal unknowns:

$$\begin{aligned}
\left(\frac{F_{11}}{F_{22}}\right)^{(3-\mathrm{D})} &= \left(\frac{F_{11}}{F_{22}}\right)^{(1-2)} = \widetilde{R}_{12}, \\
\left(\frac{F_{11}}{F_{33}}\right)^{(3-\mathrm{D})} &= \left(\frac{F_{11}}{F_{33}}\right)^{(1-3)} = \widetilde{R}_{13}, \\
\left(\frac{F_{22}}{F_{33}}\right)^{(3-\mathrm{D})} &= \left(\frac{F_{22}}{F_{33}}\right)^{(2-3)} = \widetilde{R}_{23}. \\
\left(\frac{F_{12}}{F_{11}}\right)^{(3-\mathrm{D})} &= \left(\frac{F_{12}}{F_{11}}\right)^{(1-2)} = \widetilde{R}_{21}, \\
\left(\frac{F_{13}}{F_{11}}\right)^{(3-\mathrm{D})} &= \left(\frac{F_{13}}{F_{11}}\right)^{(1-3)} = \widetilde{R}_{31}, \\
\left(\frac{F_{23}}{F_{22}}\right)^{(3-\mathrm{D})} &= \left(\frac{F_{23}}{F_{22}}\right)^{(2-3)} = \widetilde{R}_{32}.
\end{aligned} \tag{6.3}$$

Equations (6.3) communicate the fact that the known ratios of coefficients from any 2-D tensor equal the unknown ratios of their counterparts in the 3-D tensor. Please see Appendix D for further background, development, and example calculations.

Assuming the 2-D tensors "fit" together well, Equations (6.3) are linearly dependent and therefore reduce to a case of degeneracy or singularity. Consequently, a seventh equation is required:

$$F_{11}^{(3-\mathrm{D})} + F_{22}^{(3-\mathrm{D})} + F_{33}^{(3-\mathrm{D})} = 1. \tag{6.4}$$

This condition placed on the first invariant is a property of any fabric tensor rigorously calculated from 3-D unit vectors (see Chapter 2). Equation (6.4) could replace any one of the six Equations (6.3) to form a square system of six equations for six unknowns.

In practice, Equation (6.4) supplements Equations (6.3) to form a linear system from which the six unknown 3-D coefficients are solved:

$$\begin{bmatrix} 1 & -\widetilde{R}_{12} & 0 & 0 & 0 & 0 \\ 1 & 0 & -\widetilde{R}_{13} & 0 & 0 & 0 \\ 0 & 1 & -\widetilde{R}_{23} & 0 & 0 & 0 \\ -\widetilde{R}_{21} & 0 & 0 & 1 & 0 & 0 \\ -\widetilde{R}_{31} & 0 & 0 & 0 & 1 & 0 \\ 0 & -\widetilde{R}_{32} & 0 & 0 & 0 & 1 \\ 1 & 1 & 1 & 0 & 0 & 0 \end{bmatrix} \begin{Bmatrix} F_{11}^{(3-\mathrm{D})} \\ F_{22}^{(3-\mathrm{D})} \\ F_{33}^{(3-\mathrm{D})} \\ F_{12}^{(3-\mathrm{D})} \\ F_{13}^{(3-\mathrm{D})} \\ F_{23}^{(3-\mathrm{D})} \end{Bmatrix} = \begin{Bmatrix} 0 \\ 0 \\ 0 \\ 0 \\ 0 \\ 0 \\ 1 \end{Bmatrix}. \tag{6.5}$$

This is accomplished because the 2-D tensor coefficients do not necessarily "fit" within numerical working precision so the linear dependence of Equations (6.3) is not guaranteed. The iterative operations involved in solving Equation (6.5) are not computationally difficult for modern computers. Appendix D applies this system of equations in two examples in order to illustrate the operations.

6.3.2.3 Experimental Considerations: The check on the "fit" constraint also involves comparing the ratios of diagonal values of fabric. For example, from Equations (6.2b) and (6.3), $(F_{11}/F_{22})^{(1-2)}$ is calculated on the $x_1 - x_2$ plane and $(F_{22}/F_{33})^{(2-3)}$ from the $x_2 - x_3$ plane. These measurements also fix (F_{11}/F_{33}). That is, two orthogonal planes—in this example $x_1 - x_2$ and $x_2 - x_3$—establish the values of fabric in all three reference Cartesian coordinates. This example also illustrates why Equations (6.3) are insufficient in establishing a linearly independent set of equations.

The check is to determine if the (F_{11}/F_{33}) suggested by the combination of the $x_1 - x_2$ and $x_2 - x_3$ planes matches the $(F_{11}/F_{33})^{(1-3)}$ calculated directly from $x_1 - x_3$

data:

$$\left(\frac{F_{11}}{F_{22}}\right)^{(1-2)} \cdot \left(\frac{F_{22}}{F_{33}}\right)^{(2-3)} \equiv \left(\frac{F_{11}}{F_{33}}\right)^{(1-3)}, \tag{6.6}$$

where $\equiv$ denotes equivalency.

The expected developing symmetry of transverse isotropy is useful in illustrating Equation (6.6). Take for example the following three 2-D contact tensors:

$$\begin{aligned} F_{ij}^{(1-2)} &= \begin{bmatrix} 2/3 & 0 \\ 0 & 1/3 \end{bmatrix}^{(1-2)}, \\ F_{ij}^{(1-3)} &= \begin{bmatrix} 2/3 & 0 \\ 0 & 1/3 \end{bmatrix}^{(1-3)}, \\ F_{ij}^{(2-3)} &= \begin{bmatrix} 1/2 & 0 \\ 0 & 1/2 \end{bmatrix}^{(2-3)}. \end{aligned} \tag{6.7}$$

These data indicates that $x_2 - x_3$ is an isotropic plane and that 2-D bonds favor x_1 twice as frequently as either x_2 or x_3. Equation (6.6) looks like this:

$$\left(\frac{2/3}{1/3}\right)^{(1-2)} \cdot \left(\frac{1/2}{1/2}\right)^{(2-3)} \equiv \left(\frac{2/3}{1/3}\right)^{(1-3)}. \tag{6.8}$$

In this contrived case it is easy to see that the equivalency holds true. To emphasize, this is *not* due to simply canceling a coefficient like F_{22}: $F_{22} = 1/3$ on the $x_1 - x_2$ plane and $F_{22} = 1/2$ on the $x_2 - x_3$ plane. The value of a 2-D fabric tensor diagonal only carries meaning with respect to its planar pair.

With experimental data it is virtually impossible to generate 2-D contact tensors as neat as those in Equation (6.7). This might be due to microstructural artificialities introduced in creating the binary images, sampling variation of the reconstructed

microstructure, or analysis errors in identifying directional data from the images. Although working with 2-D mean intercept length measurements, Harrigan and Mann (1984) also recognized the constraint of Equation (6.6). Rearranging Equation (6.6) as

$$\left(\frac{F_{11}}{F_{22}}\right)^{(1-2)} \cdot \left(\frac{F_{22}}{F_{33}}\right)^{(2-3)} \cdot \left(\frac{F_{33}}{F_{11}}\right)^{(1-3)} = \text{fit}, \tag{6.9}$$

and the result is a simple algebraic check to perform on the quantity "fit". It should equal one, but considering the statistical uncertainty in the 2-D tensor coefficients, "fit" likely is not identically equal to one. In this scenario, the following steps may be taken.

Following Harrigan and Mann (1984), small distortions—$d_1 - d_6$—can be applied to the coordinate axes in each plane. The distortions modify the six tensor coefficients in Equation (6.9), enabling equivalency. The d_i factors stretch or shrink a coordinate axis as

$$\begin{aligned}
x_1^{'} &= d_1 x_1, \quad x_2^{'} = d_2 x_2 && \text{in the } x_1 - x_2 \text{ plane,} \\
x_2^{'} &= d_3 x_2, \quad x_3^{'} = d_4 x_3 && \text{in the } x_2 - x_3 \text{ plane, and} \\
x_1^{'} &= d_5 x_1, \quad x_3^{'} = d_6 x_3 && \text{in the } x_1 - x_3 \text{ plane.}
\end{aligned}$$

The 2-D tensors in the primed or stretched reference frame are

$$F_{ij}^{\prime(1-2)} = \begin{bmatrix} d_1^2 F_{11} & d_1 d_2 F_{12} \\ d_2 d_1 F_{21} & d_2^2 F_{22} \end{bmatrix}^{(1-2)},$$
$$F_{ij}^{\prime(1-3)} = \begin{bmatrix} d_5^2 F_{11} & d_5 d_6 F_{13} \\ d_6 d_5 F_{31} & d_6^2 F_{33} \end{bmatrix}^{(1-3)}, \tag{6.10}$$
$$F_{ij}^{\prime(2-3)} = \begin{bmatrix} d_3^2 F_{22} & d_3 d_4 F_{23} \\ d_4 d_3 F_{32} & d_4^2 F_{33} \end{bmatrix}^{(2-3)},$$

and Equation (6.9) in the primed frame is

$$\left(\frac{d_1^2 d_3^2 d_6^2}{d_2^2 d_4^2 d_5^2}\right) \cdot \left(\frac{F_{11}}{F_{22}}\right)^{(1-2)} \cdot \left(\frac{F_{22}}{F_{33}}\right)^{(2-3)} \cdot \left(\frac{F_{33}}{F_{11}}\right)^{(1-3)} = 1. \tag{6.11}$$

The use of distortions permits the equivalency. Equation (6.11) is rearranged as

$$\left(\frac{d_1^2 d_3^2 d_6^2}{d_2^2 d_4^2 d_5^2}\right) = \left(\frac{F_{22}}{F_{11}}\right)^{(1-2)} \cdot \left(\frac{F_{33}}{F_{22}}\right)^{(2-3)} \cdot \left(\frac{F_{11}}{F_{33}}\right)^{(1-3)} = X. \tag{6.12}$$

Following Harrigan and Mann (1984), the distortions applied to each face are required to be equal so that no single plane bears all the distortion:

$$\left(\frac{d_1^2}{d_2^2}\right) = \left(\frac{d_3^2}{d_4^2}\right) = \left(\frac{d_6^2}{d_5^2}\right). \tag{6.13}$$

Inserting Equation (6.13) into Equation (6.12) yields

$$\left(\frac{d_1^2}{d_2^2}\right) = \left(\frac{d_3^2}{d_4^2}\right) = \left(\frac{d_6^2}{d_5^2}\right) = X^{1/3}. \tag{6.14}$$

Equations (6.14) provide three equations in solving for the unknown d_i. The other three come from Equations (6.10)—the trace of each of these 2-D tensors is set equal to one. This establishes six independent equations used to solve for the six distortion factors:

$$\begin{bmatrix} F_{11}^{(1-2)} & F_{22}^{(1-2)} & 0 & 0 & 0 & 0 \\ 0 & 0 & F_{22}^{(2-3)} & F_{33}^{(2-3)} & 0 & 0 \\ 0 & 0 & 0 & 0 & F_{11}^{(1-3)} & F_{33}^{(1-3)} \\ 1 & -X^{1/3} & 0 & 0 & 0 & 0 \\ 0 & 0 & 1 & -X^{1/3} & 0 & 0 \\ 0 & 0 & 0 & 0 & -X^{1/3} & 1 \end{bmatrix} \begin{Bmatrix} d_1^2 \\ d_2^2 \\ d_3^2 \\ d_4^2 \\ d_5^2 \\ d_6^2 \end{Bmatrix} = \begin{Bmatrix} 1 \\ 1 \\ 1 \\ 0 \\ 0 \\ 0 \end{Bmatrix}. \quad (6.15)$$

Note that enforcing Equations (6.13) decouples the three orthogonal planes. That is, Equations (6.15) are an assembly of three decoupled systems of two equations for two unknowns. Each plane shares the common quantity X, but the equivalency of Equation (6.11) is not strictly enforced. Equations (6.15) instead solve for distortion factors that *nudge* the system towards equivalency. This has proved adequate thus far considering statistical uncertainty. Perhaps developing an objective function from the d_i or d_i^2 to be minimized via linear or quadratic programming techniques would be a more rigorous approach that forces Equation (6.11) to equal one.

The preceding sections addressed the derivation of 3-D fabric tensor coefficients from 2-D data. The algorithm requires that the 2-D planes are orthogonal and that the 2-D tensor coefficients "fit" together well. If they do not fit together within an acceptable level of statistical uncertainty, the coordinate axes are stretched using distortion factors until their relative values match.

6.3.3 ϕ: Solid Volume Fraction

The simplest stereological estimate is solid volume fraction. In an isotropic microstructure, test lines and intercept data at any orientation yield this parameter. According to Underwood (1970), the formulation is

$$\phi = \frac{\text{Total Intercept Length}}{\text{Total Test Line Length}}. \tag{6.16}$$

In execution, the contact tensors were calculated first. The $x_2 - x_3$ plane consistently proved to be isotropic. Consequently, only the output files from these planes were used to estimate solid volume fraction.

6.3.4 $\hat{\rho}/\hat{R}$: Mean 3-D Bond and Grain Radii

Where a bond intersects a planar section it appears as a line. Probabilistic stereological techniques estimate the size of idealized circular bonds from such lines. Fullman (1953) developed an oft-cited formula for 3-D bond radius, valid for circular bonds of varying size:

$$\hat{\rho} = \frac{\pi}{4\Pi}. \tag{6.17}$$

Π is the harmonic mean of the measured bond segments on the plane, defined as

$$\Pi = \frac{1}{N} \sum_{\alpha=1}^{N} \frac{1}{D_\alpha}, \tag{6.18}$$

where N is the total number of observed 2-D bond segments and D_α is the length of the line at the α contact/bond. In the first output file, N corresponds to the number of rows. In each row, D equals two times the given $\rho_{(2\text{-D})}$.

Where a grain intersects a planar section it appears as an area. This area is a circle in the case of idealized spherical grains. A simple expression, valid for 3-D

spherical grains of uniform size, is

$$\hat{R} = \frac{4R_{(2\text{-D})}}{\pi}, \tag{6.19}$$

where $R_{(2\text{-D})}$ is the arithmetic mean of 2-D circular grains identified on the planar section (Alley, 1986). Estimating a spherical radius from an observed area is a more complicated probabilistic topic than the case of bonds. Formulae abound to account for different grain size and shape distributions, at the cost of complexity and including various empirical fit and shape factors (Underwood, 1970; Alley, 1986; Edens and Brown, 1995).

The actual 3-D geometry of snow microstructure most assuredly does not match the assumptions of Equations (6.17) and (6.19). However, the idealized microstructure used to develop the thermal conductivity model does, so these expressions should be reasonable links between the measured 2-D microstructural features and the modeled geometry.

6.3.5 $\mathcal{N}$: 3-D Coordination Number

Like 3-D bond radius, mean 3-D coordination number is another difficult stereological problem (Underwood, 1970; Alley, 1986). Many approaches rely on estimating the number of grains per unit volume, which can vary by an order of magnitude depending on the assumptions. Case in point, one such approach was initially attempted in this analysis and the result was an $\mathcal{N}$ in the twenties. For comparison, Dullien (1992) reports that the densest possible packing of spheres has a mean 3-D coordination number of twelve. Twenty is obviously an unrealistic conclusion, so approaches based on number density were discarded.

Alley (1986) developed a formula that relies only on $\mathcal{N}_{(2\text{-D})}$ and $\hat{\rho}/\hat{R}$. Both of these quantities are measured or estimated for this project. The expression is

$$\mathcal{N} = \frac{\mathcal{N}_{(2\text{-D})}}{\Gamma\left(\frac{\hat{\rho}}{\hat{R}}\right)}, \tag{6.20}$$

where Γ is a probabilistic function of the mean 3-D bond-to-grain radii ratio. It estimates the average fraction of bonds intersected by a planar section cut through a spherical grain. The best approximation for Γ, valid except at large bond-to-grain ratios ($\hat{\rho}/\hat{R} > 0.8$), is

$$\Gamma \approx \frac{\pi}{4}\frac{\hat{\rho}}{\hat{R}}\left[\frac{1+\left\{1+\left(\frac{\hat{\rho}}{\hat{R}}\right)^2\right\}^{-1/2}}{2}\right]. \tag{6.21}$$

As will be shown in the next chapter, this combination resulted in reasonable estimates of $\mathcal{N}$.

6.4 Summary

Schneebeli and Sokratov (2004) measured the effective heat conductivity (EHC) of laboratory snow samples undergoing temperature gradient metamorphism over a period of one week. Their high density samples indicated no appreciable change in density, but still measured a significant increase in EHC in the direction of the temperature gradient. Current density-based or even microstructural models cannot predict such density-independent, directionally-dependent behavior. Schneebeli and Sokratov (2004) also recorded the microstructural evolution of the samples with CT scans. Analyzing these CT scans with stereological software specifically designed

for snow quantifies microstructural features such as grain size, bond size, and bond orientation.

This chapter reviewed how available stereological outputs estimate each of the parameters contributing to the thermal conductivity model proposed in Chapter 3. Ideally, the modeled data should also include the apparent conductivity due to vapor diffusion/phase change. However, the stereological software is not yet equipped to evaluate many parameters required by this model.

The anisotropic thermal conductivity model will be compared to the measured EHC in the next chapter. Conductivity does not capture all energy measured by EHC, but it is still a major contributor. The combination of CT images and measured EHC presents a unique occasion to couple a measured directional microstructural feature—the contact tensor—to a measured material property in snow.

CHAPTER 7
RESULTS AND DISCUSSION

This chapter presents the results of the microstructural analysis of samples 4 and 6 from Schneebeli and Sokratov (2004). The parameters required by the proposed anisotropic thermal conductivity model are evaluated and the evolution in this material property is calculated. The model is compared to the derived EHC from Schneebeli and Sokratov (2004).

7.1 Sample 4

Sample 4 was high density snow subject to a $100\,^{\mathrm{K}}/_{\mathrm{m}}$ temperature gradient for approximately eight days. See Table 6.1 for sample characteristics. The EHC was derived every five minutes during the experiment and reconstructed volumes of CT images were accomplished every eight hours. There were 23 volumes of CT data to analyze—three each of the first seven days and two on day eight.

7.1.1 Scalar Conductivity Model Parameters

The conductivity of ice was taken as $2.46\,^{\mathrm{W}}/_{\mathrm{m\cdot K}}$ (see Chapter 6). The remaining scalar parameters in Equation (3.34)—ϕ, $\mathcal{N}$, $\hat{\rho}$, and $\hat{R}$—were evaluated first in order to calculate a scalar, isotropic effective conductivity (Equation (3.35)). The methods outlined in Chapter 6 were applied in calculating these parameters for each of the 23 reconstructed volumes of snow. Figure 7.1 shows these results. There is practically no variation in ϕ and $\mathcal{N}$. There is approximately a 7% variation in both $\hat{\rho}$ and $\hat{R}$. Interestingly, these variations are "in phase" and the resulting bond-to-grain ratio exhibits practically no variation.

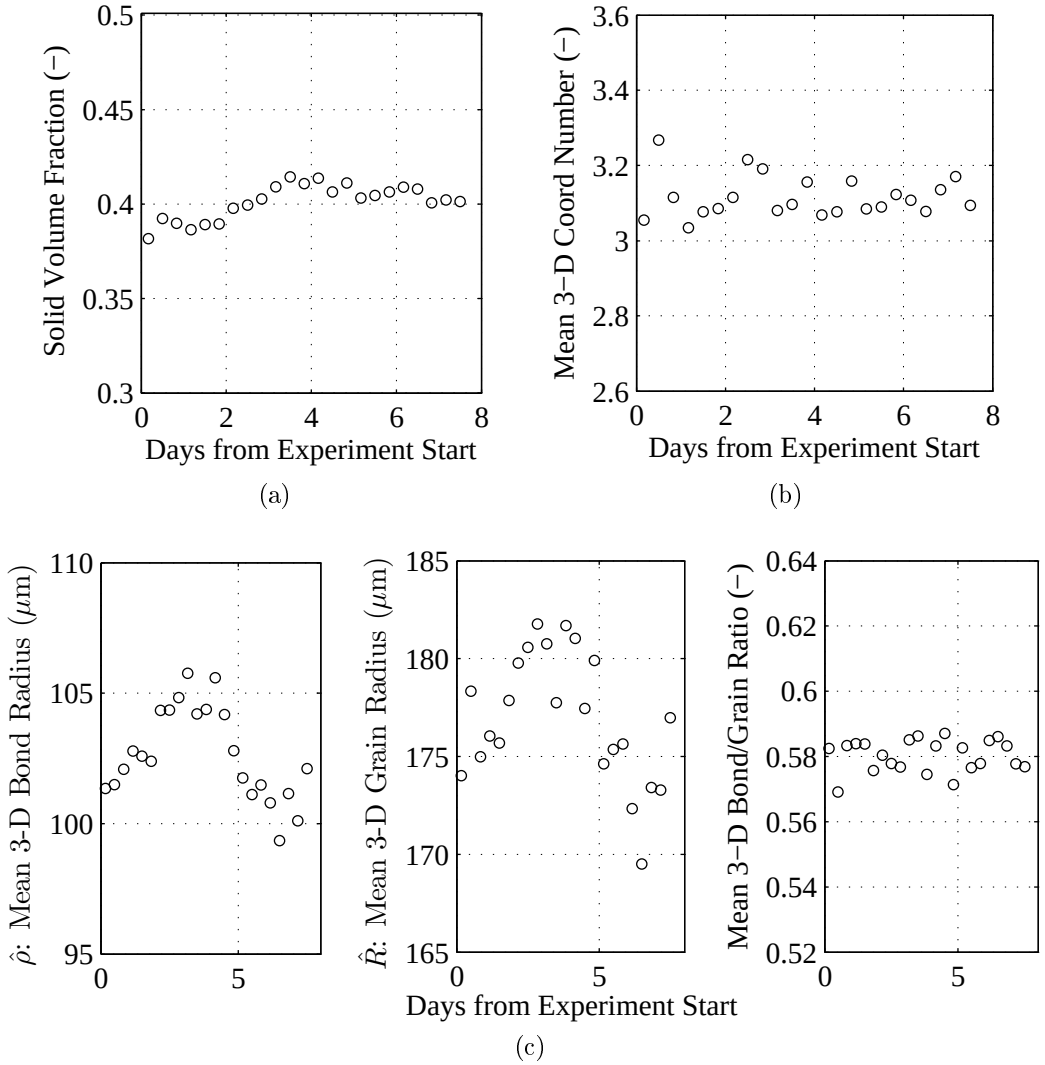


Figure 7.1: The scalar conductivity model parameters evaluated from sample 4 microstructural images.

The calculated ϕ is approximately 0.40. Assuming an ice density of $920\,{}^{\mathrm{kg}}/_{\mathrm{m}^3}$, the ϕ of this sample based on the measured density should be 0.53. For comparison, the calculated ϕ corresponds to a snow density of $368\,{}^{\mathrm{kg}}/_{\mathrm{m}^3}$. The calculated $\mathcal{N}$ is approximately 3.1. For comparison, the parameterization used in Chapter 5 (Table 5.1) in evaluating the conductivity and elastic stiffness models results in $\mathcal{N} = 4.6$ based on the calculated ϕ of 0.40.

There is little basis of comparison for the measured $\hat{\rho}$ and $\hat{R}$ as most image analysis software does not divide the solid constituent into grains and bonds. Schneebeli and Sokratov (2004) estimate ice structure size in their Figure 3 and Table IV: ice structure size is physically tied to both $\hat{\rho}$ and $\hat{R}$. They report a slight variation in ice structure size between 180 and 184 μm for this sample. The measured mean grain radius here varies between roughly 170 and 182 μm . Although difficult to quantify, the measured 3-D grain size here must underestimate the true radius because it is based on a stereological technique that uses *inscribed* disks to represent 2-D grains. The measured result is feasible, but the grain-to-bond ratio is likely overestimated.

Figure 7.2 displays the result of using these scalar parameters in Equation (3.35). Although somewhat speculative, the comparisons above suggest that ${}^{\hat{\rho}}/_{\hat{R}}$ might be an overestimate, while ϕ and $\mathcal{N}$ are underestimated. Still, the magnitude of the modeled effective conductivity is feasible when compared to EHC.

More importantly, the modeled data do not replicate the changes evident in EHC. These changes are not density-driven as the experimental apparatus was a closed system, preventing mass loss and associated changes in density. To reiterate, the hypothesis is that the changes are due to: 1) the onset of apparent conductivity due to vapor diffusion/phase change, and 2) reorientation where ice structure favors the direction of the temperature gradient. As mentioned in Chapter 6, apparent

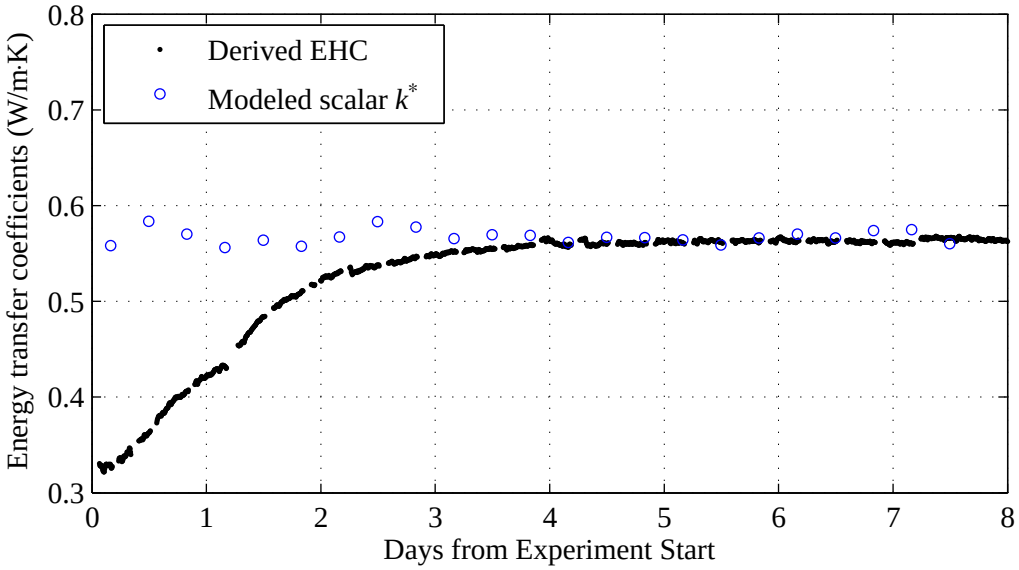
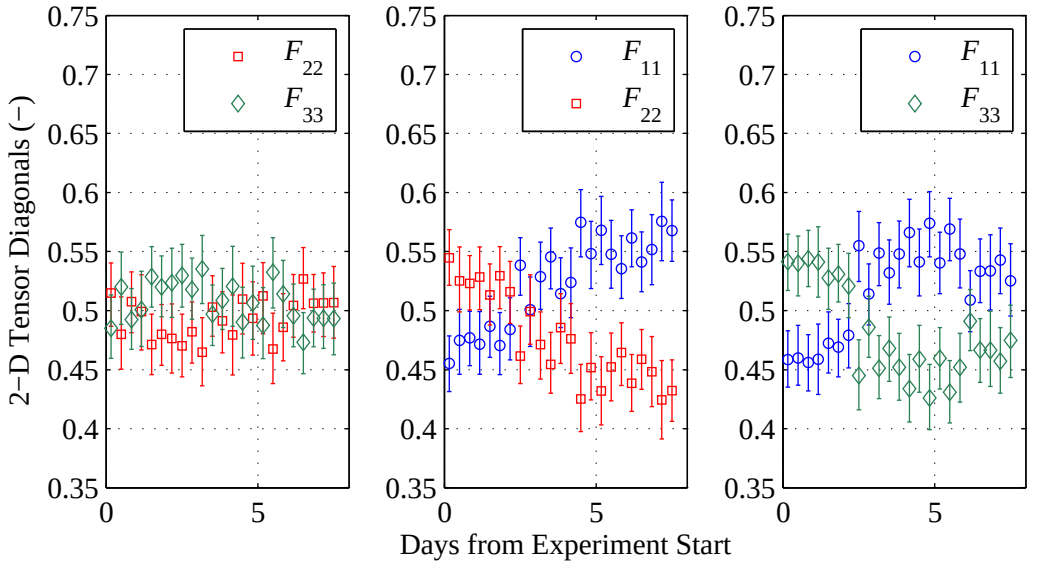


Figure 7.2: The scalar conductivity model $k^* = k^*_{B\&O}$ based on stereologically determined parameters from sample 4 images compared to EHC derived from experimental data.

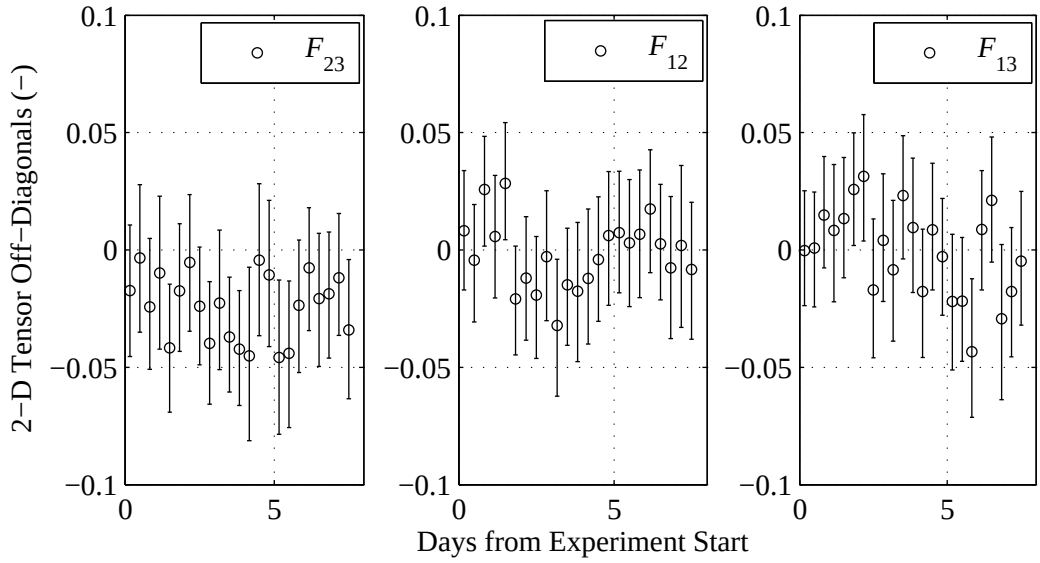
conductivity is not modeled here. Also, the modeled scalar conductivity presented here cannot reflect directionally-dependent behavior.

7.1.2 Contact Tensor: Center-to-Center Orientation

The 2-D 2nd order contact tensor coefficients are calculated by the methods outlined in Chapter 6. The directional data used here are the orientations of line segments between centers of connected grains. The error bars represent the 95% confidence intervals on the calculated coefficient. These are calculated by resampling the directional data with a technique called the bootstrap method (Efron and Tibshirani, 1994). Figure 7.3b shows that, with a few exceptions, the off-diagonal coefficients are zero within statistical uncertainty. This indicates that the reference Cartesian coordinate system is coincident with the principal directions of fabric. Figure 7.3a addresses these diagonal/principal coefficients.



(a)



(b)

Figure 7.3: The 2-D contact tensor coefficients calculated from sample 4 images using grain center-to-grain center orientation as the source of directional data: (a) the diagonal components, and (b) the off-diagonal component of the three planar tensors.

The statistical significance of the 2-D 2^{nd} order contact tensor coefficients is pictorially evident in Figure 7.3. Planar coefficients with overlap in their 95% confidence intervals indicate planar isotropy to a statistical significance of 0.05. The x_2-x_3 plane generally exemplifies this. Conversely, pairs that have no overlap denote statistically significant anisotropy. This is evident in both the x_1-x_2 and x_1-x_3 planes. Together, these data indicate an evolving transversely isotropic microstructure.

To determine the significance of even higher order terms, the 2-D 4^{th} order contact tensor coefficients are also calculated from the directional data. The hypothesis test in Kanatani (1984) is applied with a significance of 0.05. These coefficients are not displayed pictorially because each 2-D 4^{th} order tensor has ten independent coefficients.

The 4^{th} order coefficients are statistically unnecessary for 67 out of 69 planes. The exceptions are the $x_1 - x_3$ plane on Day 4–Vol 1 and the $x_1 - x_2$ plane on Day 4–Vol 2. The general conclusion is that the 2-D distribution density of directional data is adequately described without including the 4^{th} order tensor terms. The 3-D distribution density cannot be evaluated without 3-D directional data, a stereological limitation. Still, this analysis suggests that the thermally-induced changes in snow microstructure result in a statistically significant anisotropy, specifically, a transversely isotropic symmetry that is sufficiently characterized by a 2^{nd} order fabric tensor.

As described in Chapter 6, the "fit" of the planar tensors is evaluated. These results are presented in Figure 7.4. Within statistical uncertainty, these 23 planar sets fit well together. A few points do not include the ideal fit, however, no stretching of the coordinate axes is accomplished here—the fit is judged acceptable.

The last three data points in Figure 7.3a illustrate perfectly the concept of fit. The $x_2 - x_3$ plane indicates that the expected values of fabric are essentially equal. The $x_1 - x_2$ and $x_1 - x_3$ planes indicate different relative weighting. If bonding in

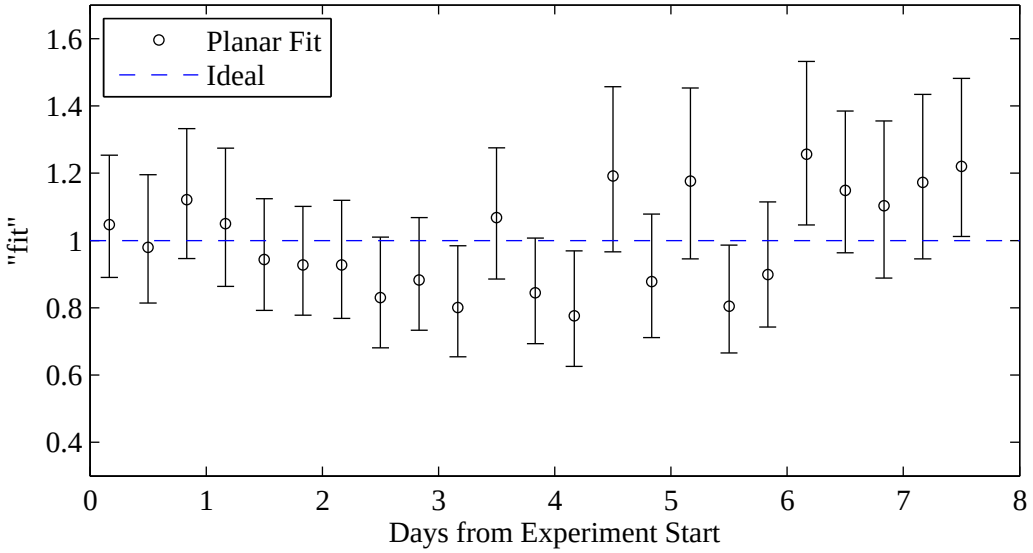
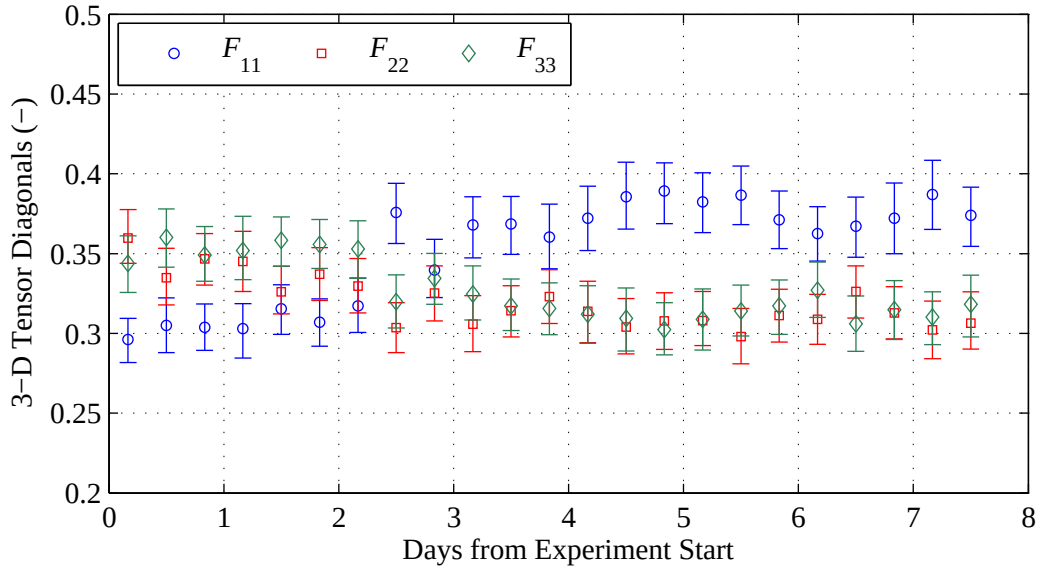


Figure 7.4: The "fit" of the sample 4 planar contact tensors calculated from center-to-center data. The fit parameter is defined by Equation (6.9).

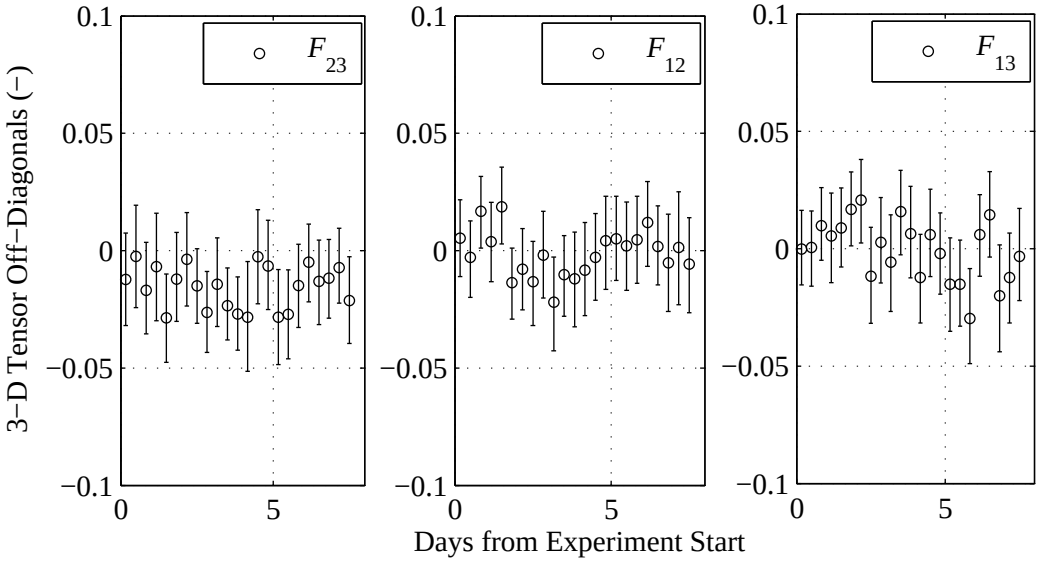
the x_2 and x_3 directions is interchangeable, then one of these two must be incorrect. The stretching factors in Chapter 6 achieve a better fit, but without guidance from a truth value. There is no way to know if an independent planar evaluation is correct or incorrect. This experimental consideration would be unnecessary with 3-D image analysis techniques.

The 3-D contact tensor coefficients are shown in Figure 7.5. As suggested by the 2-D coefficients from which they are derived, the 3-D coefficients indicate a transversely isotropic microstructure. Bonds initially prefer the isotropic $x_2 - x_3$ plane. As the microstructure reorients, the symmetry passes through 3-D isotropy on about Day 2 and eventually exhibits a preference for the x_1 direction.

For comparison, Figure 7.6 plots the degree of anisotropy (DA) from both Schneebeli and Sokratov (2004) and as calculated from the 3-D contact tensor coefficients. Recall from Chapter 6 that DA is the ratio of the largest and smallest principal values. The percent difference of the contact tensor DA from the Schneebeli and Sokratov



(a)



(b)

Figure 7.5: The 3-D contact tensor coefficients calculated from sample 4 images using grain center-to-grain center orientation as the source of directional data: (a) the diagonal components, and (b) the off-diagonal components.

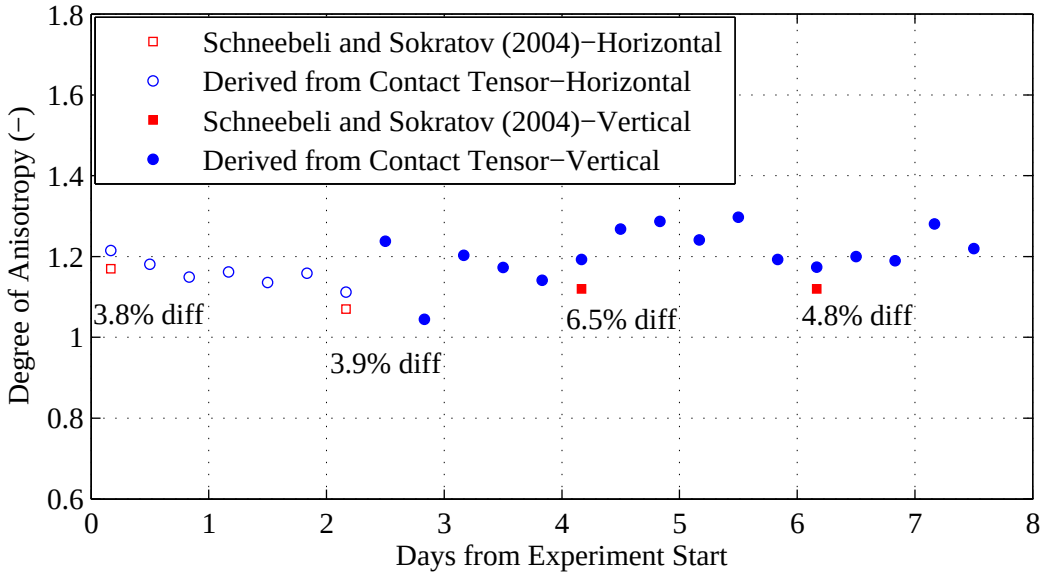
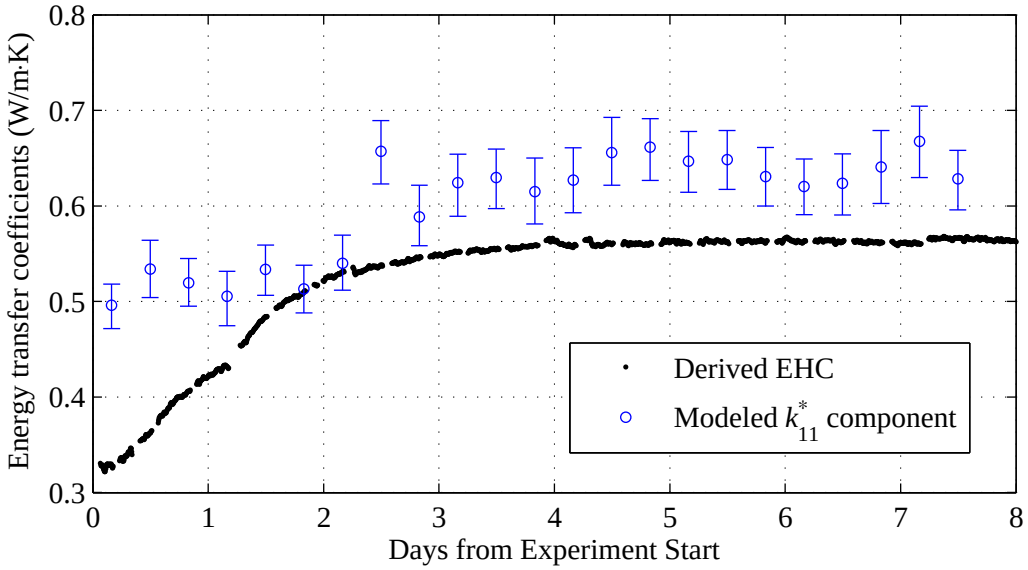


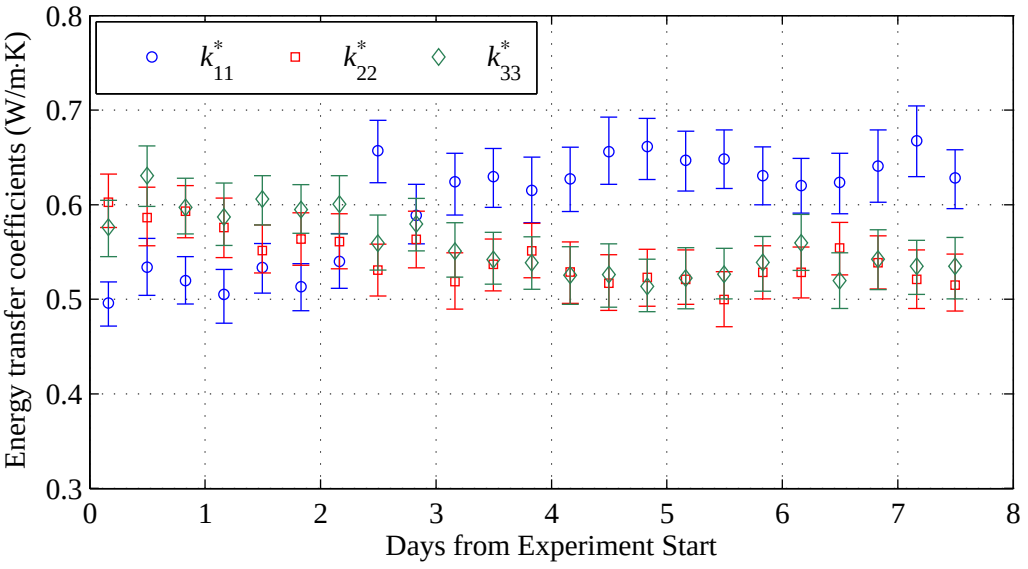
Figure 7.6: DA from Schneebeli and Sokratov (2004) compared to the DA calculated from sample 4 center-to-center 3-D contact tensor coefficients. Hollow markers indicate that either F_{22} or F_{33} was the largest magnitude principal value. Solid markers indicate that F_{11} was the greatest principal value.

(2004) DA is also listed in Figure 7.6. Although only four DA values are reported in Schneebeli and Sokratov (2004), they still offer some measure of comparison in quantifying the evolving anisotropy. The calculated DA also indicate an initial preference for ice structure in a horizontal direction with a transition to the vertical direction.

Finally, the component of the modeled conductivity tensor that shares direction with the derived EHC is presented in Figure 7.7. In terms of absolute values the fit is imperfect. However, with the addition of the contact tensor, the conductivity model shows similar change over the duration of the test. The EHC exhibits a 70% increase in this direction. The expected value of the conductivity model shows a 32% increase, potentially accounting for about 45% of the observed increase in EHC. While not measured in the experiments, the tensor model also predicts conductivity in other directions. This is also shown in Figure 7.7.



(a)



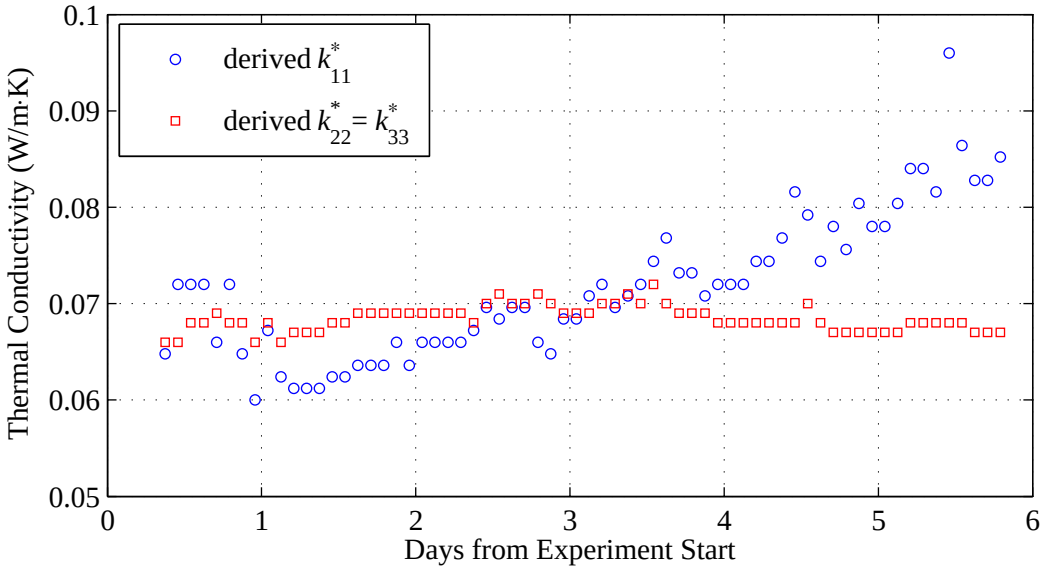
(b)

Figure 7.7: The modeled conductivity tensor $\mathbf{k}^*$ based on stereologically determined parameters from sample 4 images: (a) k_{11}^* component compared to EHC derived from experimental data, and (b) the diagonal/principal components. The contact tensor is calculated from center-to-center directional data.

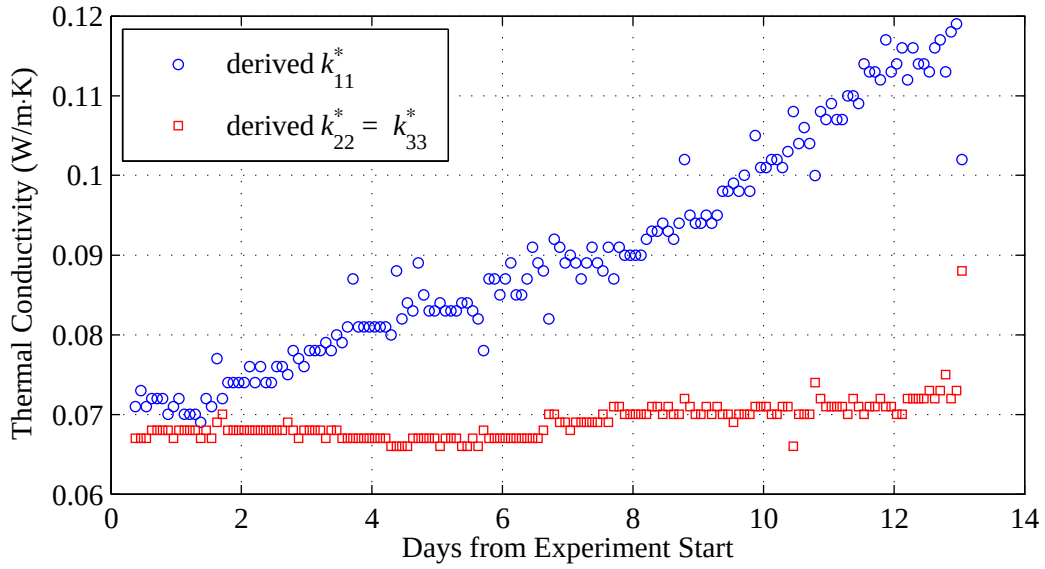
The anisotropy in modeled conductivity that is evident in Figure 7.7b obviously arises from the measured contact tensor. This general behavior—different parameter values in different directions—has been documented in the Subzero Science and Engineering Research Facility at Montana State University (MSU). Most experimental apparatus, similar to that in the Schneebeli and Sokratov (2004) study, are instrumented to measure conductivity in only one direction. With a focus on potential anisotropy, an experimental apparatus for temperature gradient metamorphism developed at MSU incorporates two heated probe conductivity instruments (Decagon Devices KD2 Pro instruments with KS-1 sensors). The *in situ* probes are fixed at orthogonal orientations, and, with multiple probes, conductivity is measured in multiple directions. The only assumption is that the $x_2 - x_3$ plane is isotropic, an assumption supported by the measured contact tensor coefficients here (see Figure 7.3).

Figure 7.8 depicts conductivity evolution for two temperature gradient metamorphism experiments conducted in the Subzero Science and Engineering Research Facility at MSU. The conductivity values are labeled "derived" because of the aforementioned analysis assumption. Three probes are required to unambiguously calculate three orthogonal directions.

To reiterate, these data should not be compared directly to the modeled conductivity in Figure 7.7b—they are not derived from the same snow samples. These measurements are included here because, for the first time, the measured conductivity of a morphology like depth hoar is shown to exhibit anisotropy: different values in different directions. The manner in which these observations develop is generally consistent with the model predictions.



(a)



(b)

Figure 7.8: The evolution in thermal conductivity for two different temperature gradient metamorphism experiments. The conductivity is measured by multiple heated probe instruments: (a) snow density of 130 $^{\mathrm{kg}}/_{\mathrm{m}^3}$ subject to 200 $^{\mathrm{K}}/_{\mathrm{m}}$ temperature gradient, (b) snow density of 240 $^{\mathrm{kg}}/_{\mathrm{m}^3}$ subject to a 100 $^{\mathrm{K}}/_{\mathrm{m}}$ temperature gradient.

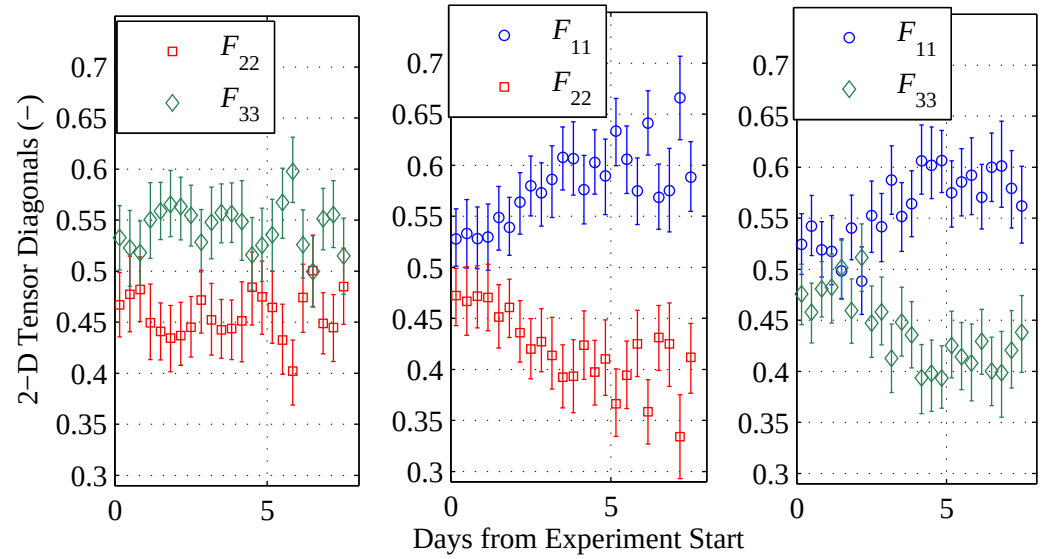
7.1.3 Contact Tensor: Skeleton Tangent Orientation

The only analysis difference in this section is the source of directional data used to calculated the 2-D contact tensor coefficients. The directional data used here are tangents to the skeleton in the neighborhood of identified bond sites. As with the center-to-center directional data, Figure 7.9b shows that, in most cases, the off-diagonal coefficients are zero within statistical uncertainty. The broader error bars indicate that statistical uncertainty is greater in Figure 7.9 than in Figure 7.3.

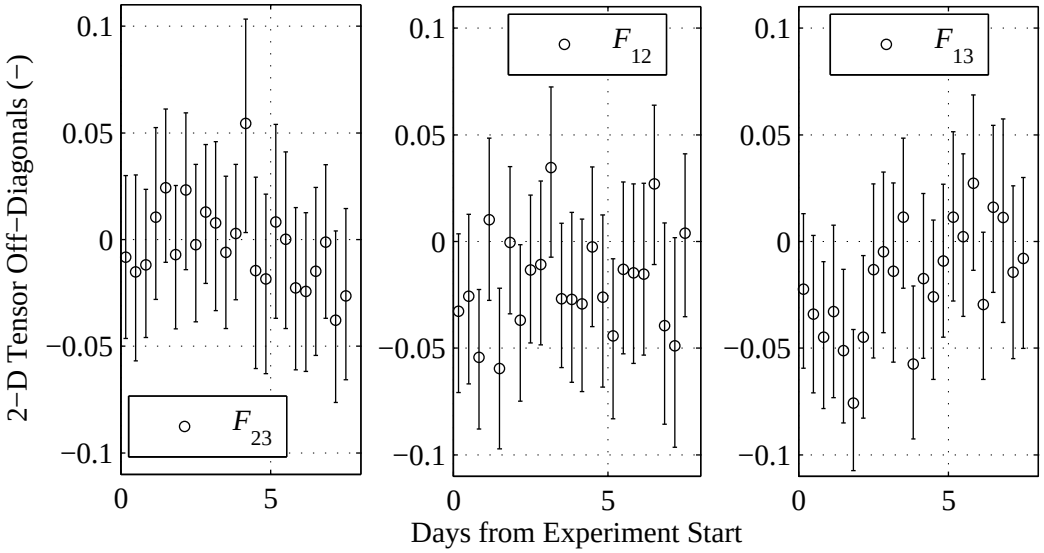
The 2-D diagonal/principal coefficients in Figure 7.9a and their derived 3-D counterparts in Figure 7.11 tell a slightly different story with these directional data. The data in Figure 7.11 exhibit an initial isotropic symmetry and a departure from that as the experiment develops. While the developing symmetry in Figure 7.11 looks qualitatively similar to that in Figure 7.5, the transverse isotropy is not as convincing. This is not for lack of fit; Figure 7.10 indicates as good a fit with this choice of directional data as before. The cause is the statistical uncertainty.

In fact, the hypothesis tests indicate that—with this directional data—in *every* instance where anisotropy is statistically significant both the 2-D 2^{nd} and 4^{th} order contact tensor contributions are significant on one or more planes. This indicates either: 1) the sampling technique does not deliver enough data to draw significant conclusions, or 2) the nature of the anisotropy of these directional data is inconclusive. The same sampling technique is applied to these data as above, so the latter is more likely the cause.

Figure 7.12 plots the DA from Schneebeli and Sokratov (2004) and these 3-D contact tensor coefficients. Unlike both the Schneebeli and Sokratov (2004) and center-to-center DA, these exhibit a consistent weighting toward the x_1 direction and a much larger magnitude. The components of the modeled conductivity tensor



(a)



(b)

Figure 7.9: The 2-D contact tensor coefficients calculated from sample 4 images using the tangent to the skeleton as the source of directional data: (a) the diagonal components, and (b) the off-diagonal component of the three planar tensors.

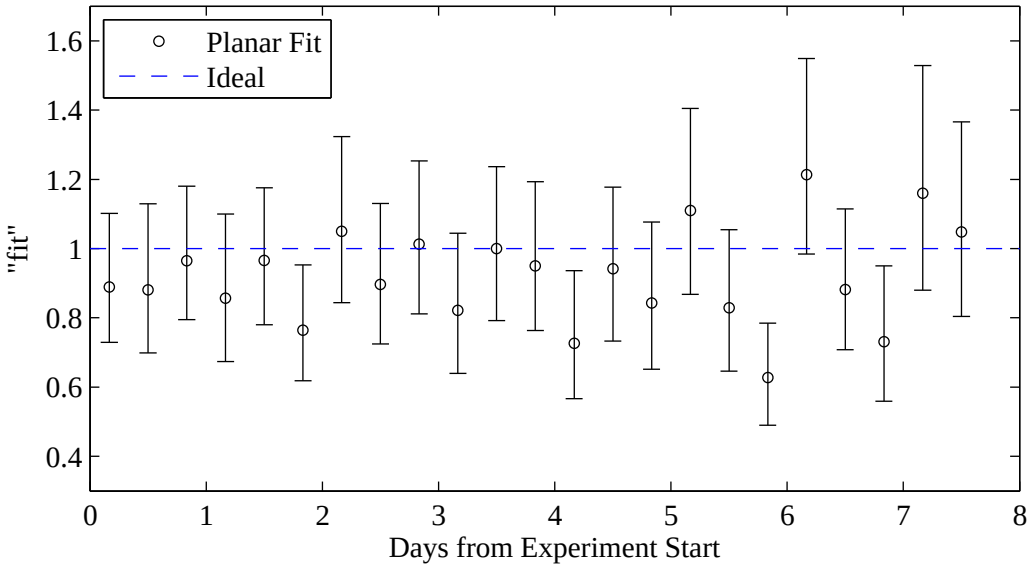


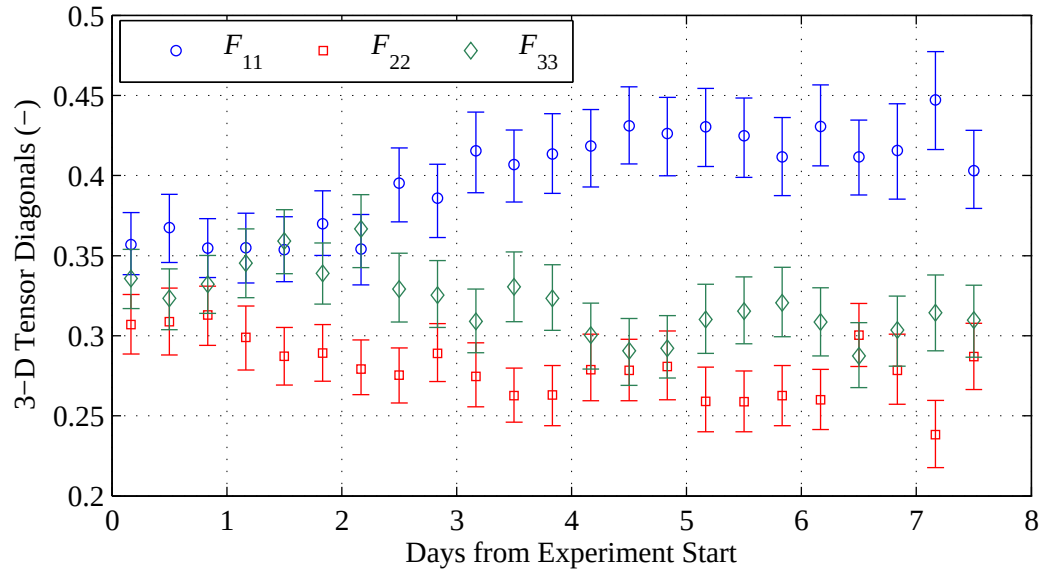
Figure 7.10: The "fit" of the sample 4 planar contact tensors calculated from skeleton tangent data. The fit parameter is defined by Equation(6.9).

and EHC are shown in Figure 7.13. In the x_1 direction, the expected value of the conductivity model based on these data shows a more modest 25% increase with a corresponding decrease in the orthogonal directions.

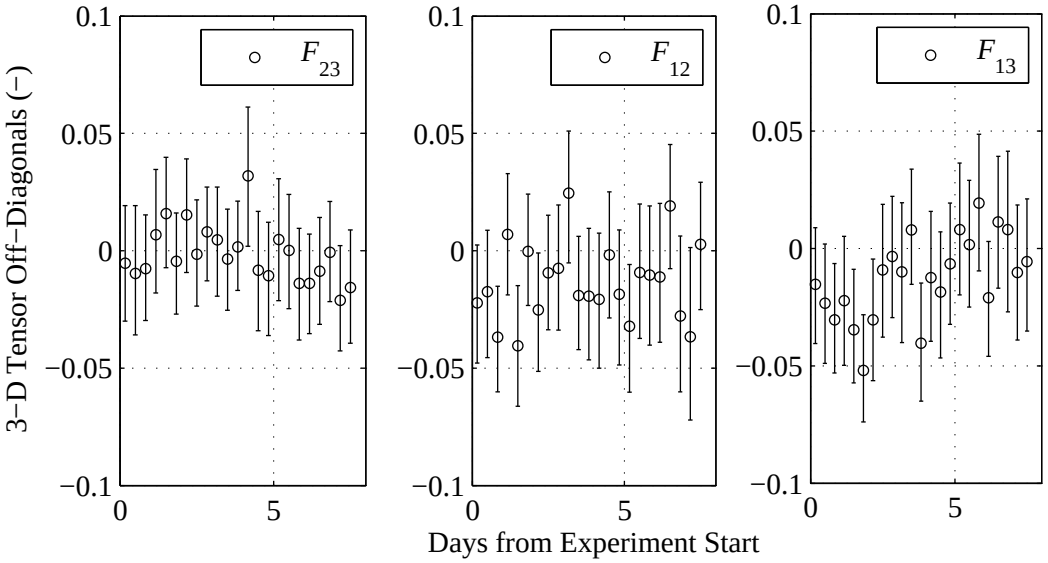
7.1.4 Discussion

The parameters in the microstructural conductivity model are derived from sample 4 images via stereology. The scalar parameters yield a reasonable conductivity value, but the fundamental point is that this value does not vary over the course of the experiment. Similar to conductivity models parameterized by density, the scalar microstructural model does not mimic the observed EHC.

To account for directionality, the anisotropic conductivity model includes a contact tensor. The model requires a 2^{nd} order contact tensor, which was evaluated using two different sources of directional data. With either source, the contact tensor is the only term in the conductivity model that varies over the course the experiment. This



(a)



(b)

Figure 7.11: The 3-D contact tensor coefficients calculated from sample 4 images using the tangent to the skeleton as the source of directional data: (a) the diagonal components, and (b) the off-diagonal components.

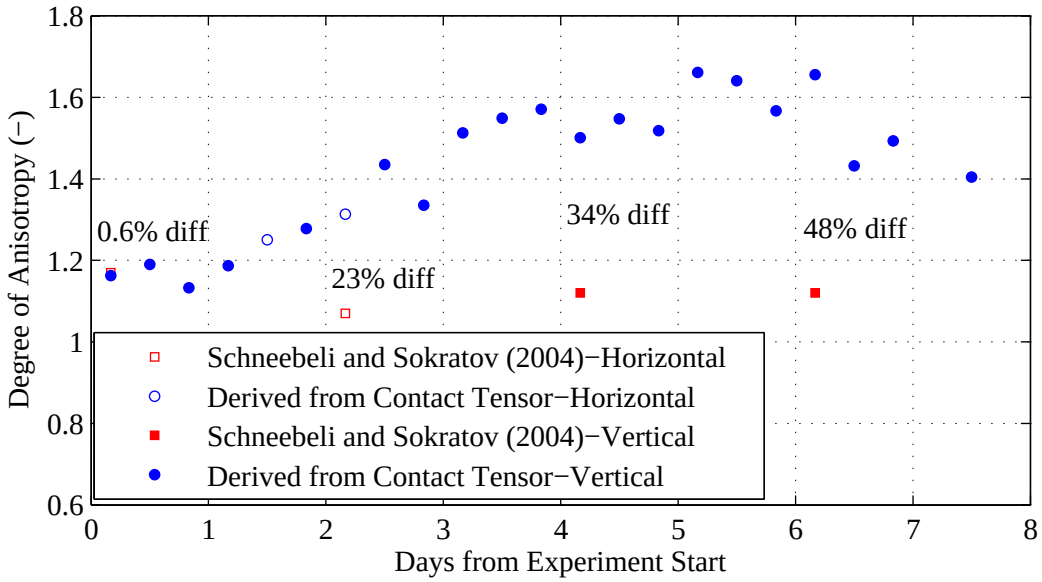
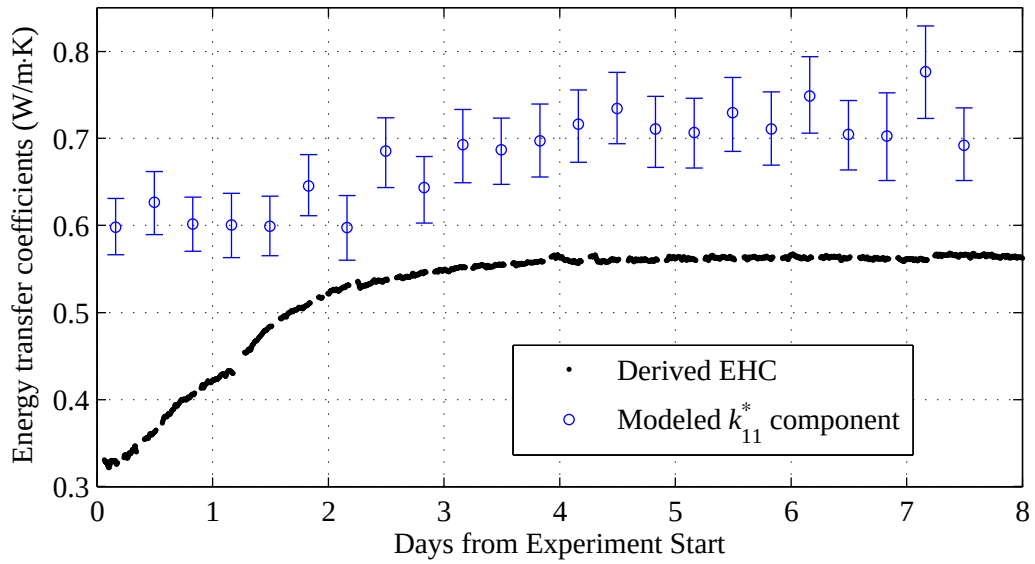


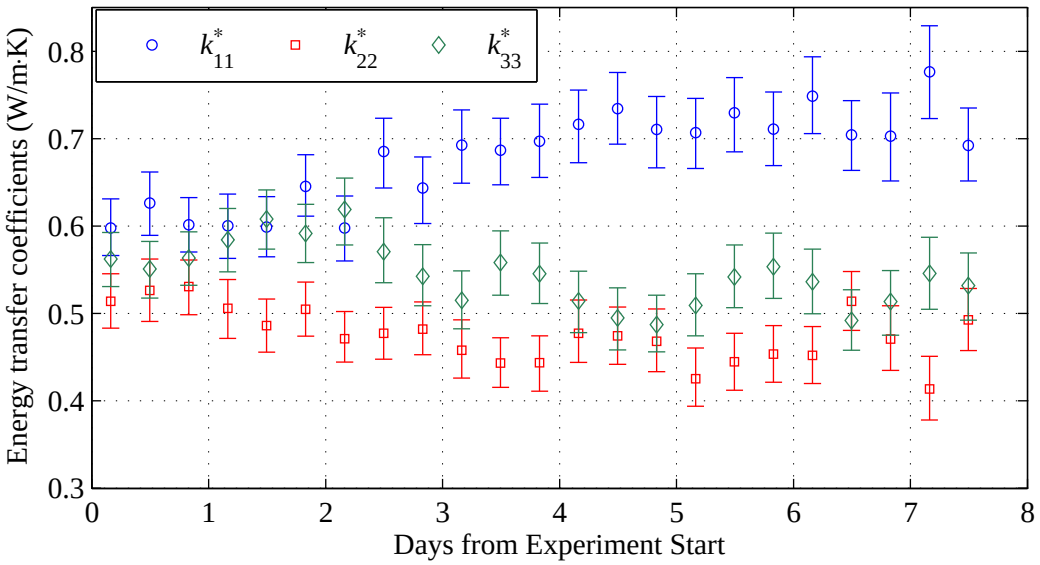
Figure 7.12: DA from Schneebeli and Sokratov (2004) compared to the DA calculated from sample 4 skeleton tangent 3-D contact tensor coefficients. Hollow markers indicate that either F_{22} or F_{33} was the largest magnitude principal value. Solid markers indicate that F_{11} was the greatest principal value.

variance is statistically significant and in general consistent with the expected result of a transversely isotropic symmetry.

The modeled conductivity tensor component in the direction of the applied gradient increases by 25-32%, depending on the choice of directional data. This accounts for 35-45% of the observed change in EHC. The model was not expected to account for the entirety of EHC because the apparent conductivity due to vapor diffusion/phase change is not included. It is difficult to quantitatively judge the accuracy of the conductivity model with a direct comparison to EHC because of this, but the observed EHC and modeled conductivity share a qualitative trend.



(a)



(b)

Figure 7.13: The modeled conductivity tensor $\mathbf{k}^*$ based on stereologically determined parameters from sample 4 images: (a) k^*_{11} component compared to EHC derived from experimental data, and (b) the diagonal/principal components. The contact tensor is calculated from skeleton tangent directional data.

7.2 Sample 6

Sample 6 was prepared similar to sample 4 but subject to a $50\,^{\mathrm{K}}/_{\mathrm{m}}$ temperature gradient (Table 6.1). There were five days worth of CT data to analyze. On Day 2–Vol 3 there was no available reconstructed volume of CT images. Unfortunately, derived EHC data was not available past the second day for this experiment.

7.2.1 Scalar Conductivity Model Parameters

Samples 4 and 6 share a common preparation and are nearly the same density. Figure 7.14 indicates they also share similar scalar conductivity parameters as calculated by the stereological algorithms. Like Figure 7.2, Figure 7.15 shows that the modeled effective conductivity does not vary significantly with these scalar parameters. Although the EHC data are cut short, the modeled data do not mimic the changes evident in EHC.

7.2.2 Contact Tensor: Center-to-Center Orientation

As before, the orientations of line segments between centers of connected grains are used to calculate the 2-D 2^{nd} order contact tensor coefficients. Figure 7.16 shows the 2-D diagonal and off-diagonal tensor components. Figure 7.17 shows the "fit" of these planar tensors. As before, no stretching of the coordinate axes is performed.

The 2-D 4^{th} order contact tensor coefficients are also calculated to assess their significance. As was the case in sample 4, the conclusion is that the 2-D density distribution of these directional data is adequately described without including the 4^{th} order tensor terms. As is evident in Figure 7.16a, most of these data point to isotropy, so not even the 2^{nd} order contributions are required. However, in those

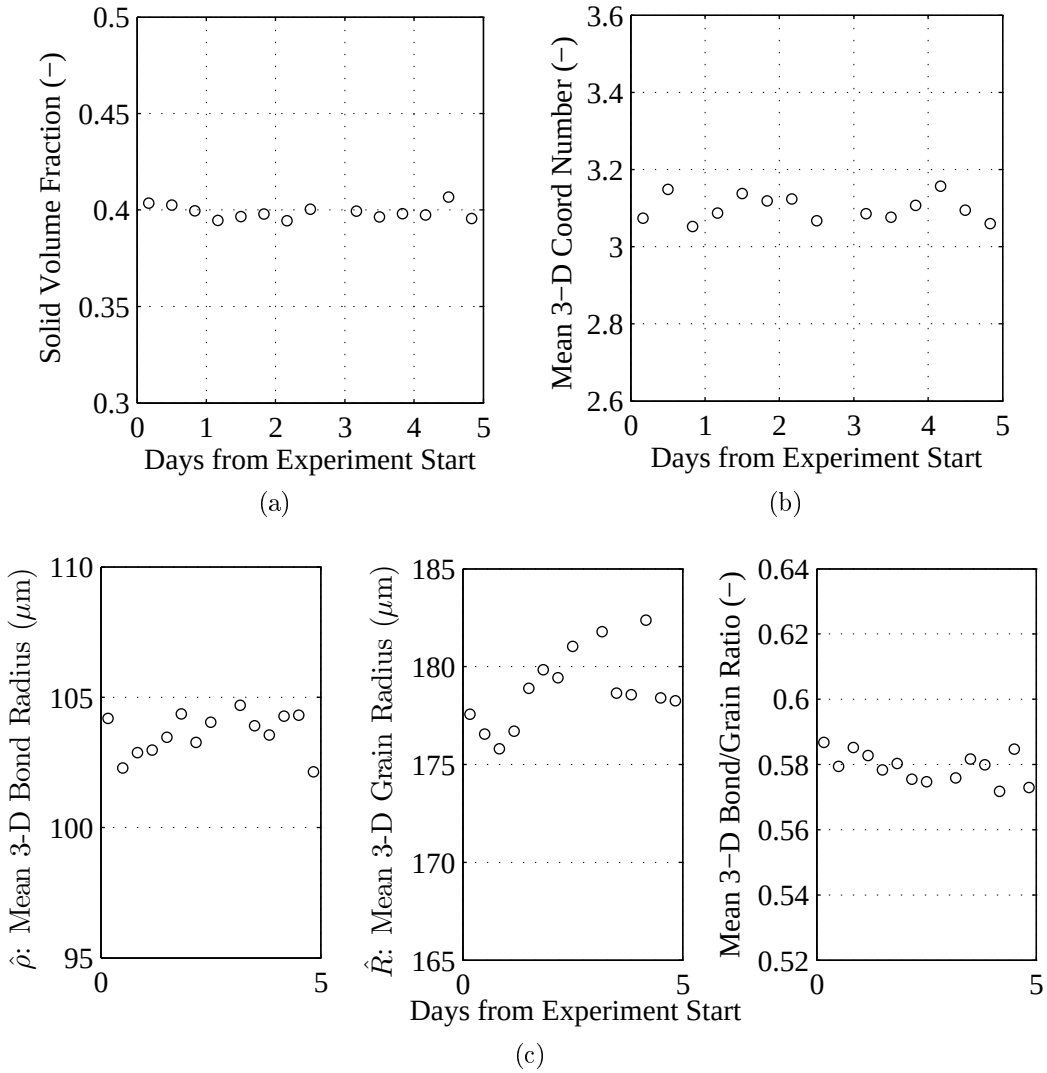


Figure 7.14: The scalar conductivity model parameters evaluated from sample 6 microstructural images.

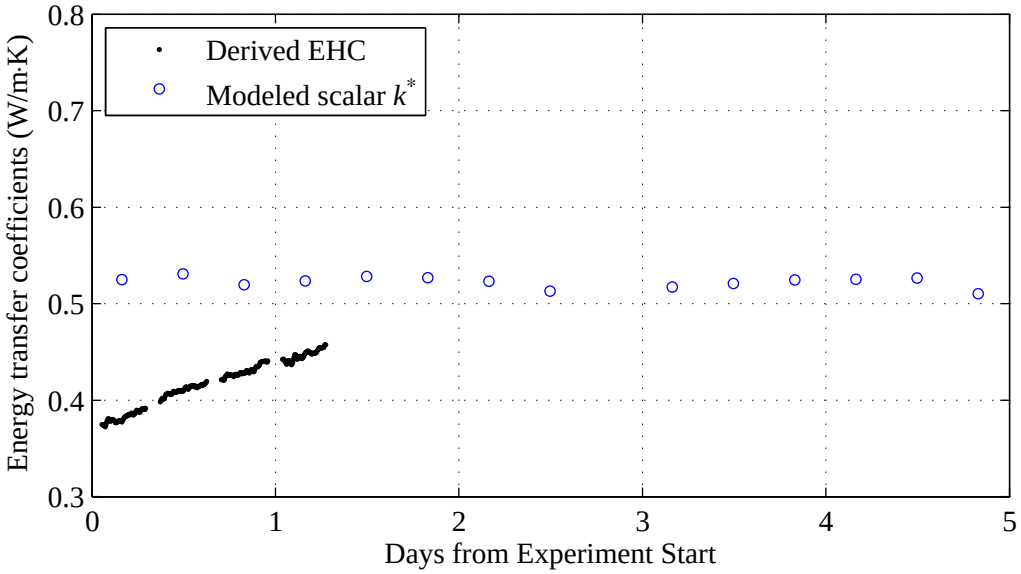
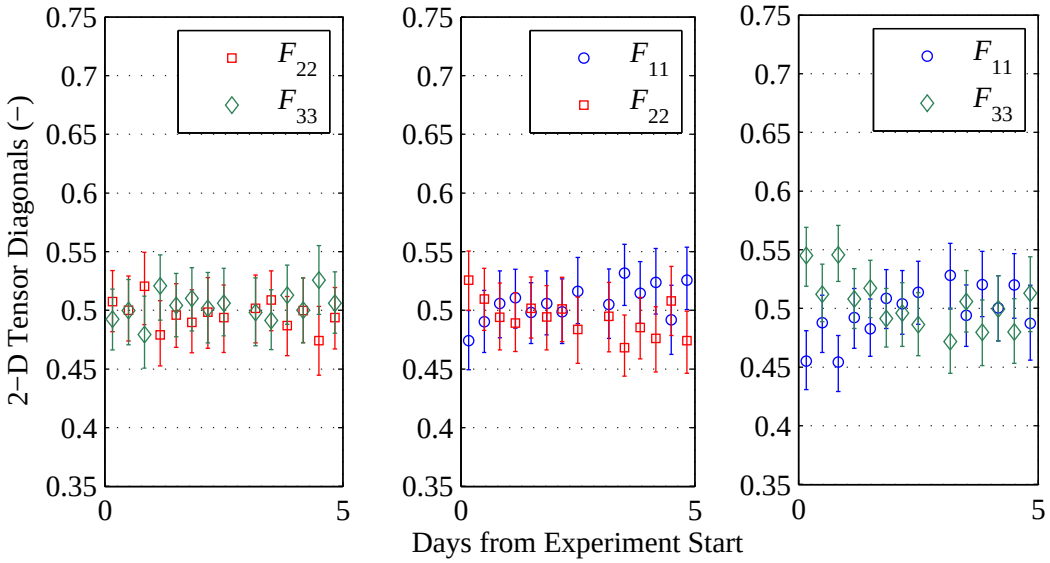


Figure 7.15: The scalar conductivity model $k^* = k^*_{B\&O}$ based on stereologically determined parameters from sample 6 images compared to EHC derived from experimental data.

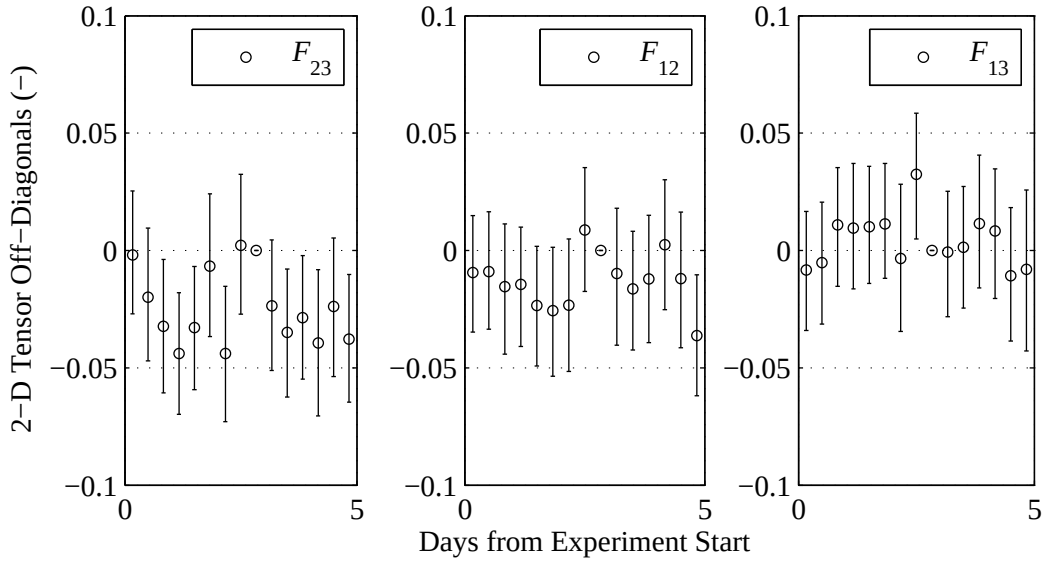
instances where the anisotropy is significant, none of them indicated the 4^{th} order tensor terms are significant.

The 3-D contact tensor coefficients are shown in Figure 7.18. Like sample 4, bonds initially prefer the $x_2 - x_3$ plane. 3-D isotropy is reached on about Day 1. The expected values of the 3-D coefficients evolve, but a statistical evaluation concludes this change is potentially insignificant. The initial anisotropy and ensuing migration to isotropy are statistically significant. These data never yield a preference for ice structure in the direction of the applied temperature gradient. Speculation is that the smaller magnitude gradient and shorter test duration result in this observation. There is no DA data from Schneebeli and Sokratov (2004) for this sample.

The components of the modeled conductivity tensor are presented in Figure 7.7. The abbreviated EHC exhibits approximately a 20% increase in the x_1 direction in



(a)



(b)

Figure 7.16: The 2-D contact tensor coefficients calculated from sample 6 images using grain center-to-grain center orientation as the source of directional data: (a) the diagonal components, and (b) the off-diagonal component of the three planar tensors.

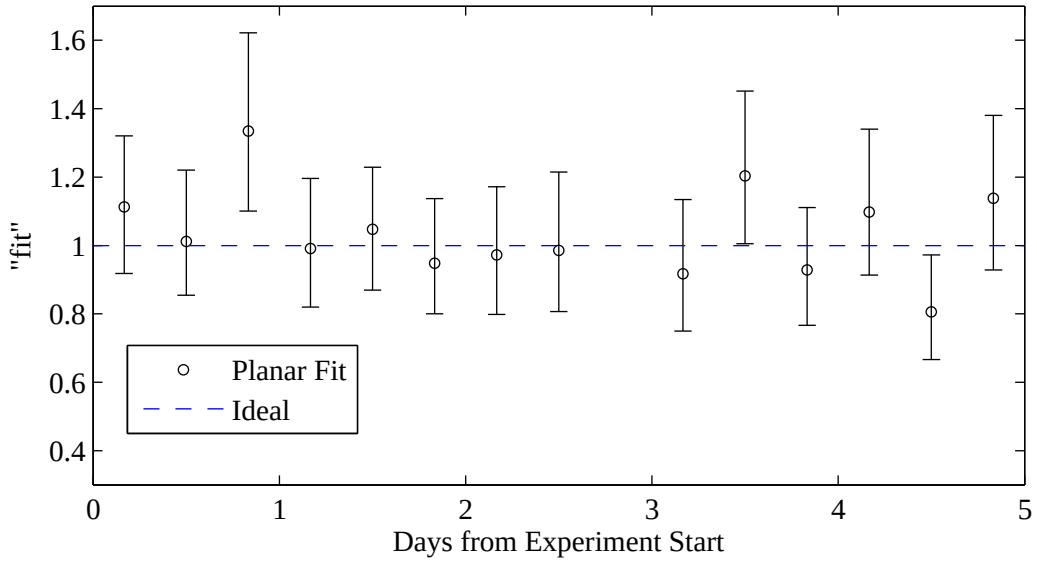


Figure 7.17: The "fit" of the sample 6 planar contact tensors calculated from center-to-center data. The fit parameter is defined by Equation (6.9).

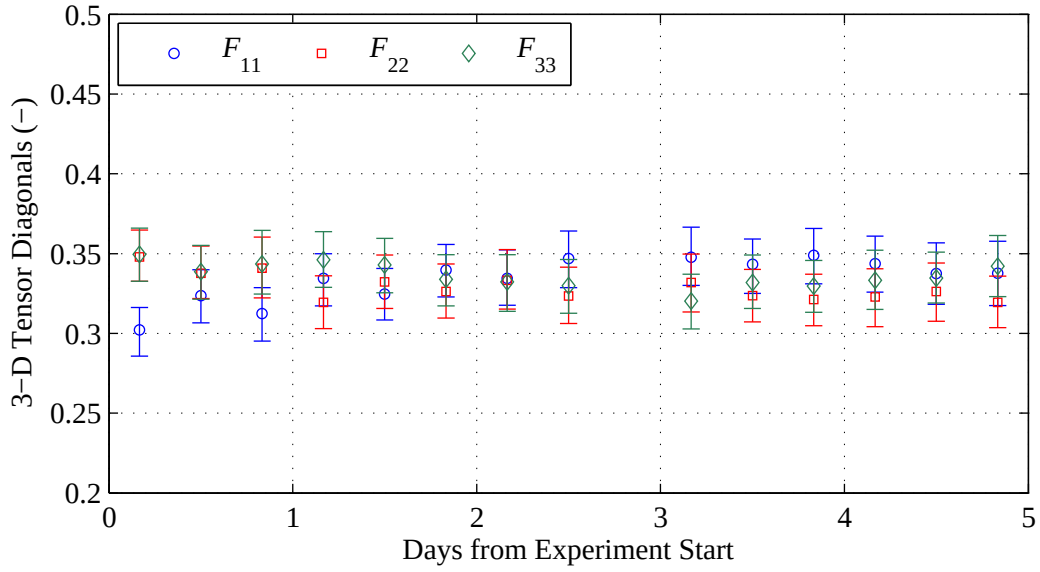
the first $1\frac{1}{3}$ days. The expected value of the conductivity model shows a 14% increase over 5 days.

7.2.3 Contact Tensor: Skeleton Tangent Orientation

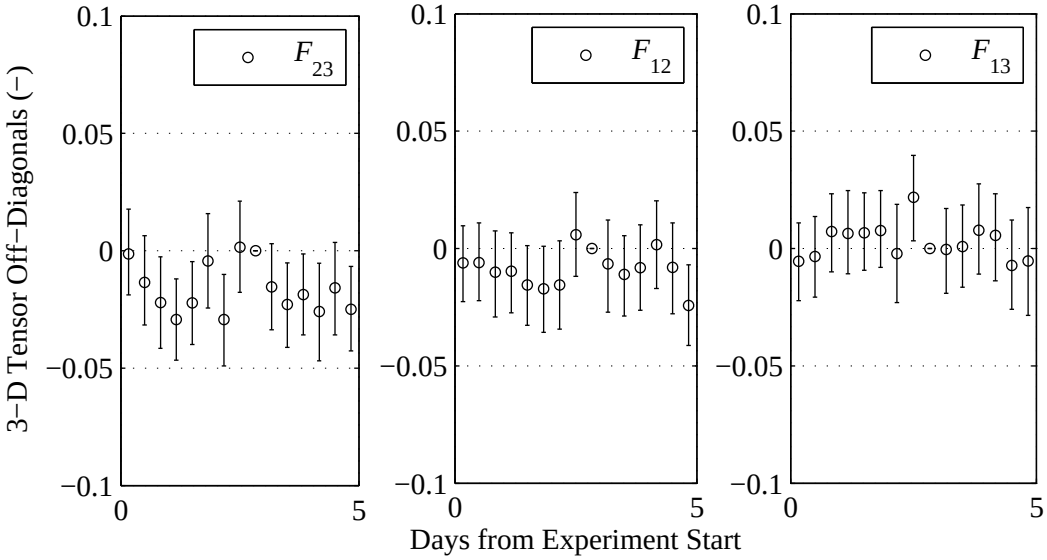
The sample 6 analysis is accomplished in this section using tangents to the skeleton in the neighborhood of identified bond sites as the source of directional data. Figure 7.20 displays the 2-D tensor coefficients and Figure 7.21 shows their planar "fit".

The 2-D 4^{th} order contact tensor coefficients are also calculated. Similar to this choice of directional data in sample 4, when the anisotropy is significant the hypothesis test indicates that both the 2^{nd} and 4^{th} order contact tensor coefficients are required to accurately describe their distribution density. The only exception is Day 3–Vol 1. In this case only the 2^{nd} order coefficients were required.

Figure 7.22 exhibits the 3-D tensor coefficients. Differing from the previous directional data, the initial microstructure is isotropic with a transition to transversely

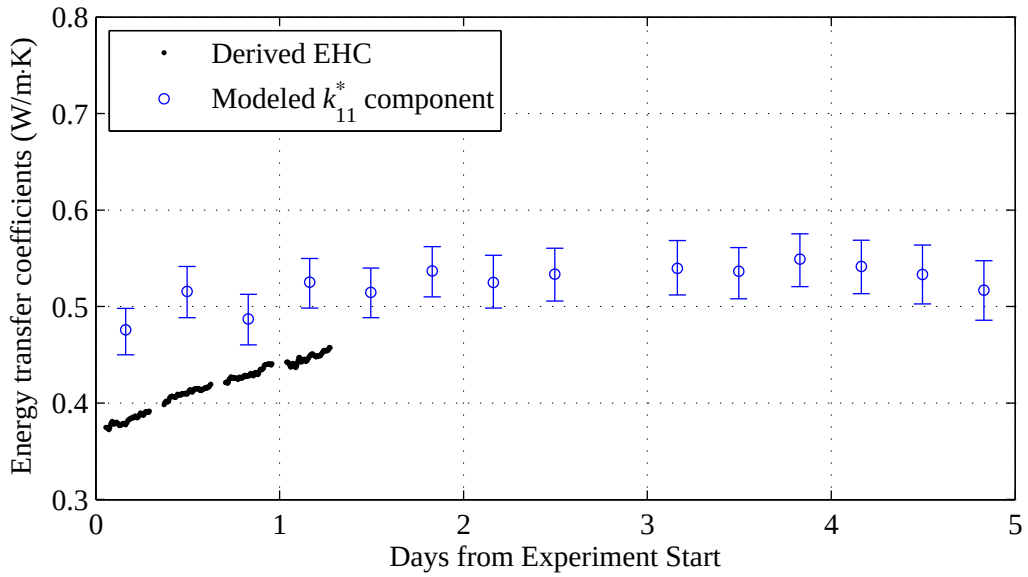


(a)

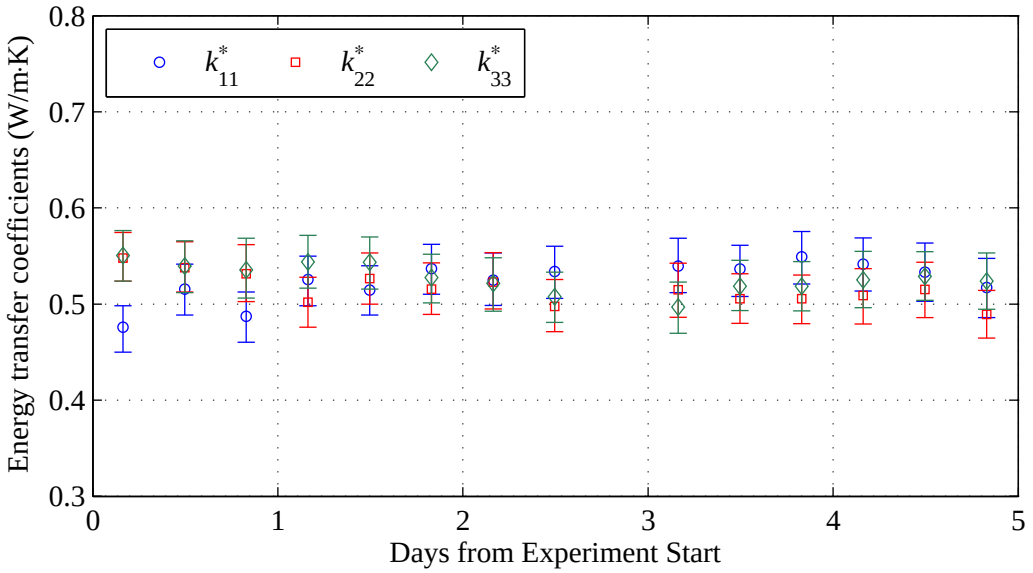


(b)

Figure 7.18: The 3-D contact tensor coefficients calculated from sample 6 images using grain center-to-grain center orientation as the source of directional data: (a) the diagonal components, and (b) the off-diagonal components.

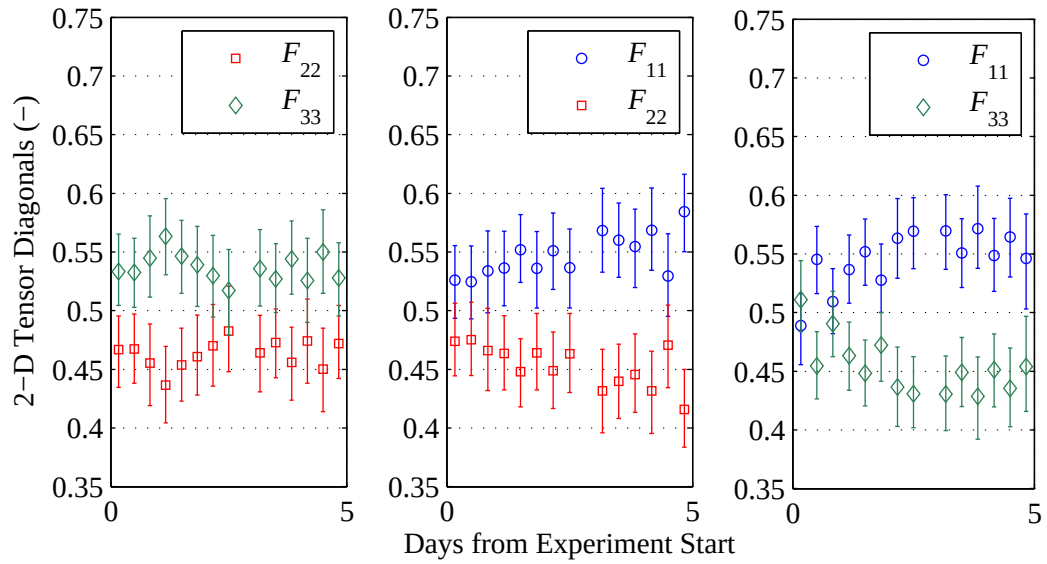


(a)

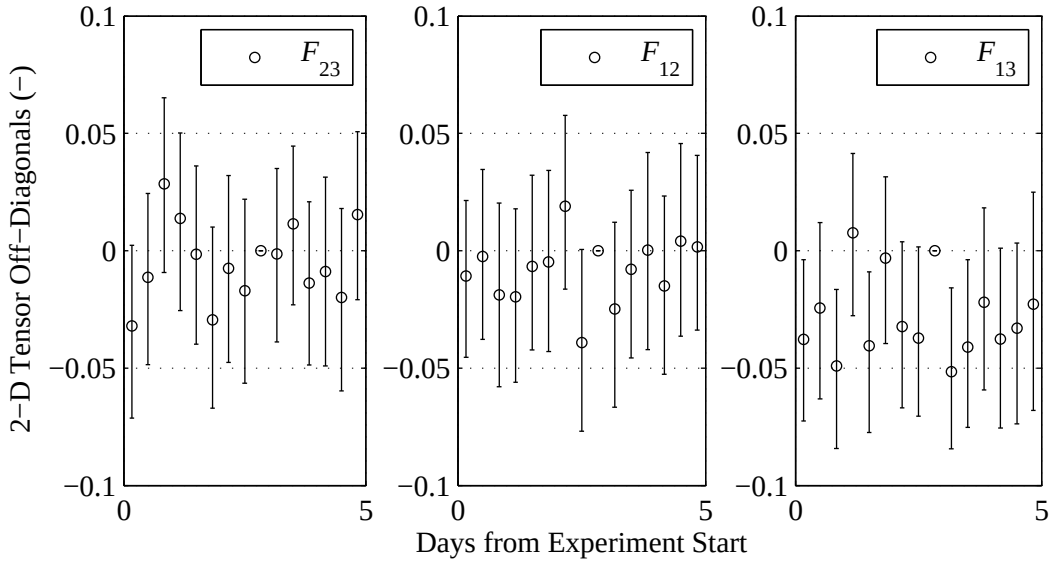


(b)

Figure 7.19: The modeled conductivity tensor $\mathbf{k}^*$ based on stereologically determined parameters from sample 6 images: (a) k^*_{11} component compared to EHC derived from experimental data, and (b) the diagonal/principal components. The contact tensor is calculated from center-to-center directional data.



(a)



(b)

Figure 7.20: The 2-D contact tensor coefficients calculated from sample 6 images using the tangent to the skeleton as the source of directional data: (a) the diagonal components, and (b) the off-diagonal component of the three planar tensors.

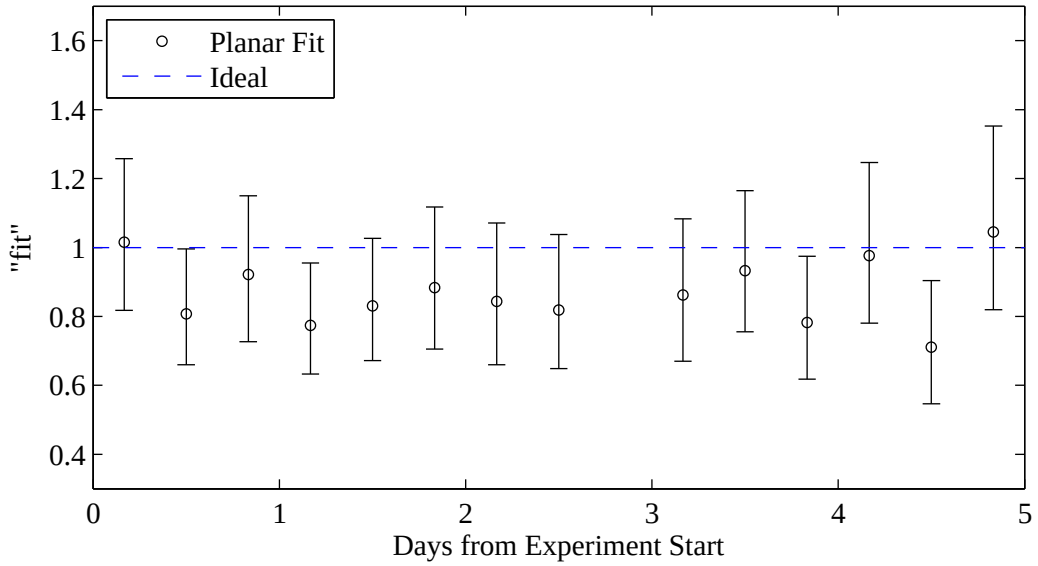


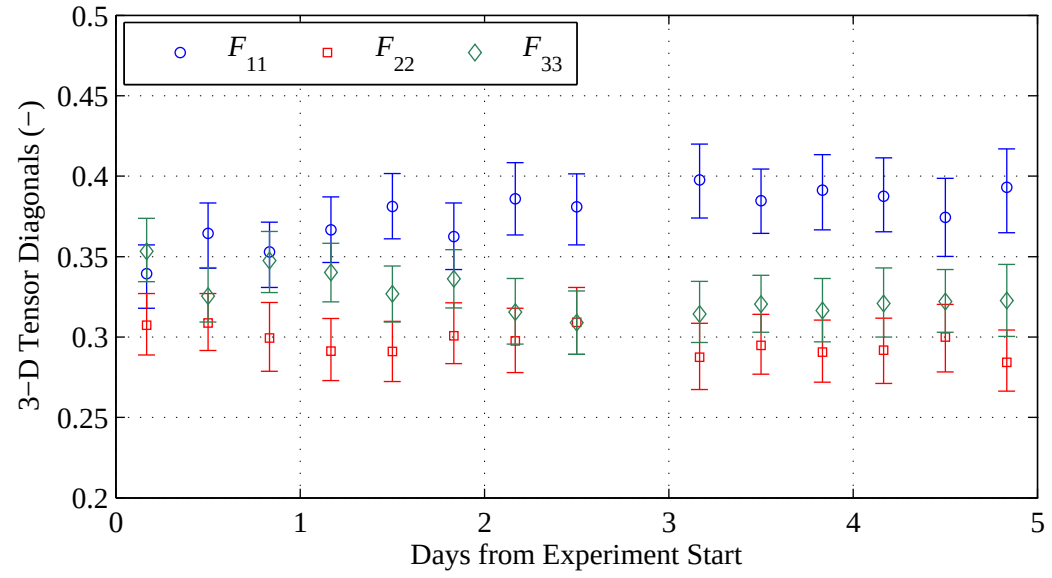
Figure 7.21: The "fit" of the sample 6 planar contact tensors calculated from skeleton tangent data. The fit parameter is defined by Equation(6.9).

isotropic on or about Day 1. As was the case in sample 4, the eventual preferred direction of bonding is clearly x_1 and the orthogonal $x_2 - x_3$ plane is consistently isotropic. The developing anisotropy is statistically significant but the changes in individual coefficients over the course of the test are not as dramatic as with sample 4. Again, this is presumably due to a smaller gradient and shorter test duration.

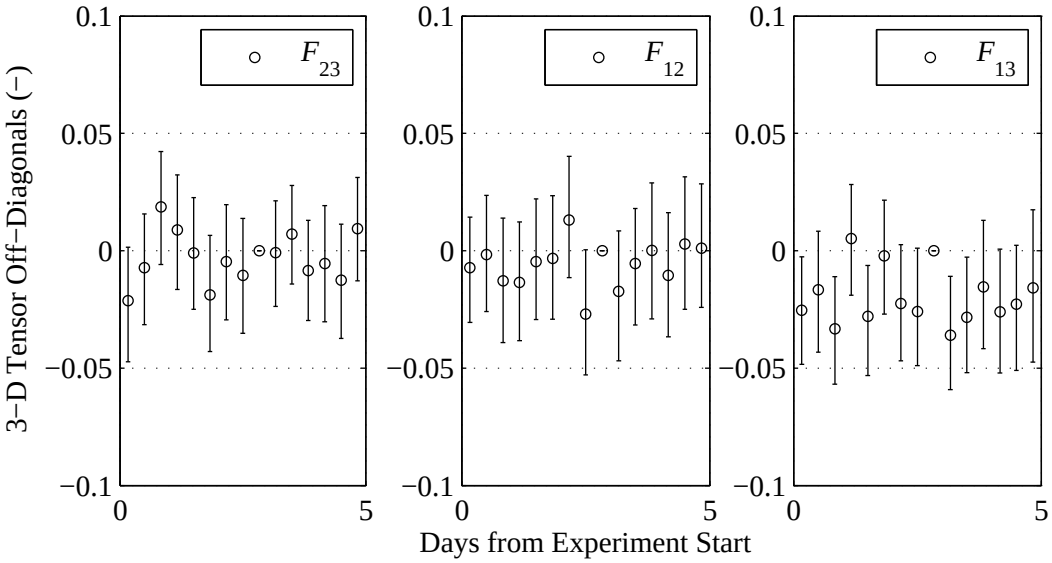
The modeled conductivity tensor coefficients are shown in Figure 7.7. The expected value of this conductivity model shows an approximate 20% increase.

7.2.4 Discussion

Sample 6 images yield similar qualitative results to sample 4. The EHC data to which to compare in this experiment is incomplete, but that which was recorded shows an approximately 20% increase over the first 1⅓ days. This indicates an expected significant change. However, while the scalar parameters calculate a reasonable conductivity value, it does not vary over the course of the test.

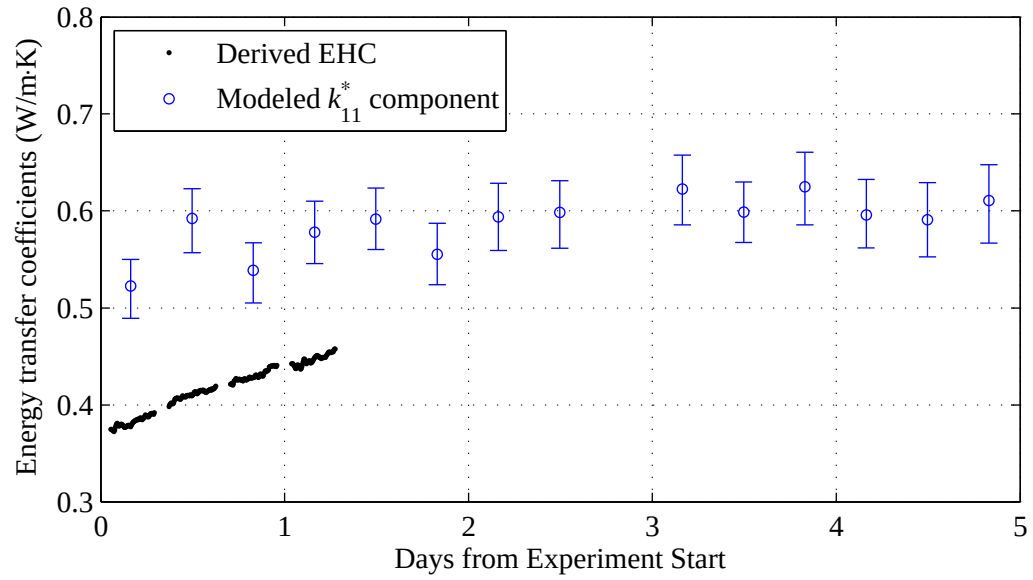


(a)

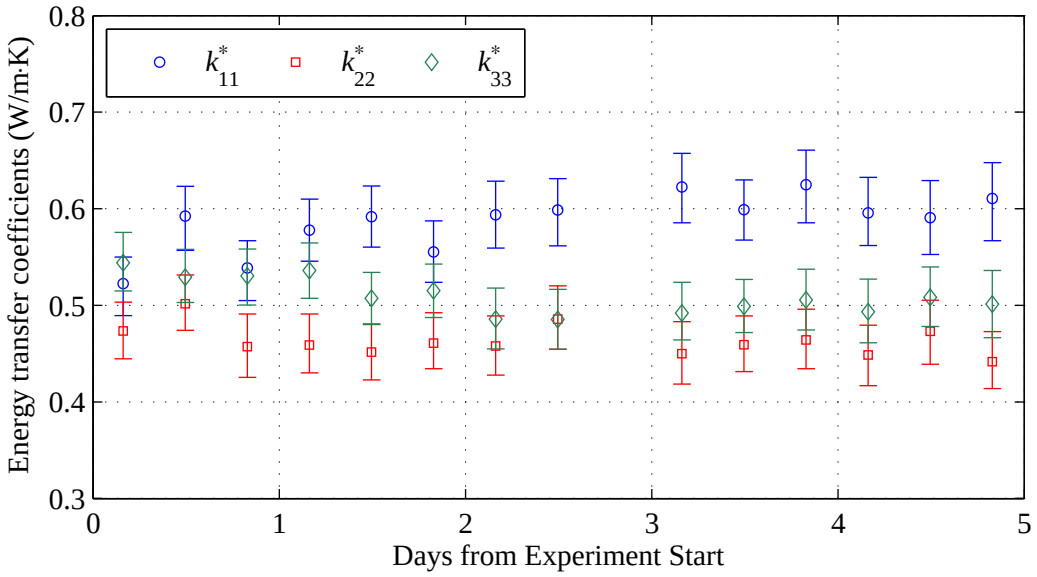


(b)

Figure 7.22: The 3-D contact tensor coefficients calculated from sample 6 images using the tangent to the skeleton as the source of directional data: (a) the diagonal components, and (b) the off-diagonal components.



(a)



(b)

Figure 7.23: The modeled conductivity tensor $\mathbf{k}^*$ based on stereologically determined parameters from sample 6 images: (a) k^*_{11} component compared to EHC derived from experimental data, and (b) the diagonal/principal components. The contact tensor is calculated from skeleton tangent directional data.

As before, the only parameter in the conductivity model that varies is the contact tensor. The measured changes are not as significant as with sample 4, but the applied gradient here is only half as great and the test duration is five rather than eight days. The changes in textural symmetry are statistically significant and qualitatively similar to both the sample 4 tensor evolution and the expected result of a developing transversely isotropic microstructure. The modeled conductivity tensor component in the x_1 direction increases by approximately 14-20%, depending on the choice of directional data.

7.3 Summary

Two experiments consisting of 37 reconstructed volumes of CT images were analyzed in order to evaluate the parameters comprising the proposed conductivity model. None of the scalar variables showed convincing change over the course of the experiments. Of the model parameters, only the contact tensor varied during the tests. The conclusion is that anisotropy is statistically significant.

The accuracy of the overall model and its incorporation of anisotropy through the contact tensor is more difficult to ascertain. A comparison to the derived EHC is useful but incomplete as conductivity is but one component of EHC. The results of the conductivity analysis are feasible and deserve further investigation. Of particular interest is developing stereological algorithms that will enable evaluation of the apparent conductivity of vapor diffusion/phase change.

In each experiment, the contact tensor was calculated using two different sources of directional data. In general, each showed the expected result of—relative to the initial symmetry—an increasing fraction of bonds in the direction of the applied gradient as the tests progressed. Each 3-D 2^{nd} order tensor, required by the model, also generally

exhibited either an isotropic or transversely isotropic symmetry. With the center-to-center data this evaluation was statistically conclusive. With the skeleton tangent data it was not. Concerning the available directional data, the center-to-center is judged the better choice because:

- It matches the directional quantity derived from the idealized geometry of spherical grains,
- The hypothesis test concludes that the material is either isotropic or transversely isotropic. These symmetries are also documented by the Srivastava *et al.* (2010) study cited in Chapter 5 as the observed initial state and end result of temperature gradient metamorphism,
- The comparison with available DA data is significantly better than the alternative.

This does not imply the skeleton tangent data is incorrect; it just yields greater statistical ambiguity. Comparisons of available directional data are a topic of ongoing research.

CHAPTER 8
CONCLUSIONS AND RECOMMENDATIONS

8.1 Research Summary and Conclusions

Snow is a complex material whose microstructure and material properties are constantly changing. Quantifying these properties is difficult but nonetheless important. The interaction between environment, microstructure, and material properties drives snow metamorphism and dictates whether weak layers develop. This is of obvious significance to avalanche research, but there are many other applications. For example, seasonal snow greatly impacts water supplies so hydrologists and water resource managers need to understand snow's transport properties. Climatologists are concerned with the optical properties of snow because they impact how much energy it reflects and absorbs. Snow's material properties are required in evaluating the avalanche risk of a particular slope or evaluating a global energy balance.

This research proposed an analytical microstructural approach utilizing fabric tensors in order to better quantify effective material properties. The benefit of fabric tensors is two-fold. First, fabric quantifies directional-dependence of the microstructure; scalar quantities simply cannot capture this information. Second, fabric is explicitly tied to statistical distributions of the constituents in the microstructure—ice grains and pore space. Fabric tensors are calculated from measurable directional data identified in the microstructure. This stands in contrast to empirically derived factors often used to account for microstructural directionality. With temperature gradient metamorphism, a directionally-dependent arrangement of the microstructure is expected because the forcing gradient is a directional quantity. This phenomenon

has been observed and documented in several temperature gradient metamorphism experiments cited here.

A summary of the research contributions follows. A granular homogenization algorithm was extended to include both grain and pore space phenomena. It was proposed and demonstrated how a more common anisotropy measure—a MIL fabric tensor—might serve as a substitute for the analytically rigorous contact tensor when normalized by its isotropic value. Four anisotropic microstructural constitutive models were developed that are generally applicable to granular materials. These models demonstrated that fabric tensors calculated from different directional quantities can naturally arise in the derivation of effective properties of granular materials. The conductivity and elastic stiffness models arise from a grain-space focus while permeability is treated as strictly a pore-space problem. Because snow is a multi-phase material, diffusivity is a combined grain- and pore-space problem.

The feasibility of all four models was addressed using available data and comparisons to other mathematical models. In particular, the elastic stiffness model benefited from the anisotropy measurements of Srivastava *et al.* (2010). This evaluation not only demonstrated the model anisotropy, but also the proposed usage of a MIL fabric tensor. The conductivity model was evaluated in detail using CT images and stereological algorithms specifically designed for snow microstructure. Temperature gradient metamorphism experiments produced the CT images so they were well-suited to evaluate potential anisotropy. In fact, the only significant changes in the conductivity model were a result of changes in the contact tensor.

The conclusion is that anisotropy is measurable and statistically significant in these samples. It is more difficult to judge the manner in which this anisotropy is accounted for in the overall model. The modeled conductivity is compared to

a measured effective heat transfer coefficient (EHC). This comparison is useful but incomplete as conductivity is only one energy contributor to the measured property.

The derived EHC values in these experiments indicate an increase in the direction of the applied gradient. These changes occur independent of density. The hypothesis of Schneebeli and Sokratov (2004) is that other factors—shape, orientation, etc.—relate to the observed changes in EHC. Scalar conductivity models also bear this out: none of the scalar parameters—commonly parameterized by density—echoes the EHC behavior.

Sturm and Johnson (1992) and Sturm *et al.* (1997) address the thermal conductivity of depth hoar—a natural product of temperature gradient metamorphism similar to the experimental setup here. They also conclude that it shows density-independent behavior. However, they note a *decrease* in thermal conductivity as the gradient persists. Recently, Morin *et al.* (2010) also report a decrease in thermal conductivity in potentially similar snow layers. The critical distinction between these observations is that Schneebeli and Sokratov (2004) measure EHC in the direction of the gradient, while Sturm and Johnson (1992) and Morin *et al.* (2010) measure the property in planes approximately orthogonal to the gradient. These independent experiments suggest that snow subject to temperature gradient metamorphism might exhibit density-independent, directionally-dependent characteristics. The laboratory experiments at Montana State University, cited in Chapter 7, reinforce this supposition.

Sturm and Johnson (1992) recognize the importance of the fabric of the microstructure, but lament that its effect has not yet been quantified. The models developed here address this through fabric tensors. The models account for density-dependence, directional-dependence, and other microstructural features. They rely on idealized microstructural geometries, identifying directional quantities pertinent

to microscopic processes, and the principles of homogenization. The microstructural analysis here demonstrates how the textural anisotropy affects conductivity, improving it in one direction while diminishing it in others. This analysis also quantifies how modest changes in fabric result in more dramatic changes in an effective material property.

8.2 Recommendations for Future Work

As with any research project, new challenges are equally as numerous as those addressed. Microstructural models demand much of available stereological capabilities. Microstructural parameters, including the different sources of directional data, should continue to be investigated in order to establish techniques that yield the most accurate estimates. Stereological methods should be extended to enable evaluation of the effective diffusivity model. In general, because 3-D imagery is available via the reconstructed volumes of CT data, 3-D image analysis algorithms are preferred to planar analysis.

Different averaging and localization operations could be applied in the homogenization algorithm. The models developed here consistently applied only one such combination. Different idealized geometries and local constitutive laws could also be applied. In particular, the contact law applied in the elastic stiffness homogenization is a simplification. Rotational degrees of freedom and the resulting force-couples could be added at the cost of greater model complexity. Also, a linear elastic model for snow—while a contributor to overall mechanical response—is limited as snow additionally exhibits a significant viscous response. A local viscoelastic constitutive law—similar to that proposed in Nicot (2004)—could produce this response.

Adapting to different geometries is potentially very complex. This is one limitation of models derived from a relatively simple geometry—they do not account for changes in grain or pore shape. Such changes are also measurable and potentially impact the effective material properties. For example, both Schneebeli and Sokratov (2004) and Srivastava *et al.* (2010) independently report that the structure model index (SMI) also varies significantly for their high density samples. SMI estimates the convexity/curvature of the ice structure and is therefore a quantification of shape changes. A parameter like this is absent from the models proposed here and analytical connections are difficult. This might be an appropriate scenario for empiricism in the form of "shape factors": commonly incorporated parameters to account for aspherical grains.

Another limitation of the proposed models is that they describe an effective property at a snapshot in time. The microstructural parameters change, but these constitutive models do not explain microstructure evolution. This limits the applicability of these models in dynamic constitutive modeling. Mixture theory is currently used to predict grain, neck, and bond growth (Lehning *et al.*, 2002; Bartelt *et al.*, 2004). A 3-D extension of such techniques might provide an analytical avenue for calculating the microstructural parameters required here, but these developments are probably distant.

Fabric evolution might be another scenario for potential empiricism. For example, the independent experiments of Schneebeli and Sokratov (2004) and Srivastava *et al.* (2010) indicate that high density snow subject to a $100\,\mathrm{K/m}$ temperature gradient for one week results in an approximately 10% increase in the fabric coefficient in the direction of the applied gradient. While only based on a few samples, these observations potentially point to a relationship between fabric evolution and the initial snow state, magnitude of the applied gradient, and persistence of the applied gradient.

Snow is unique in that natural thermal conditions result in significant material changes. A change in textural symmetry is one of the significant changes. Fabric tensors quantify this change and its effect on material properties. This research verifies that this effect is measurable and significant. Constitutive models for snow should reflect its microstructural dependence and potential anisotropy; those proposed here provide such a means.

REFERENCES CITED

Adams, E. E. and Sato, A. (1993). Model for effective thermal conductivity of a dry snow cover composed of uniform ice spheres. *Annals Of Glaciology*, **18**, 300–304.

Agrawal, K. C. and Mittal, R. K. (1995). Influence of microstructure on mechanical properties of snow. *Defence Science Journal*, **45**(2), 93–105.

Akitaya, E. (1985). Quick hardening of snow under a strong temperature gradient. *Low Temperature Science, Series A*, **44**, 27–35.

Alley, R. B. (1986). Three-dimensional coordination number from two-dimensional measurements: a new method. *Journal of Glaciology*, **32**(112), 391–396.

Arons, E. M. and Colbeck, S. C. (1998). Effective medium approximation for the conductivity of sensible heat in dry snow. *International Journal of Heat and Mass Transfer*, **41**(17), 2653–2666.

ASM Handbook (1985). *ASM metals handbook*. American Society for Metals, Metals Park, OH, 9th edition.

ASTM E1225-09 (2009). *Standard test method for thermal conductivity of solids by means of the guarded-comparative-longitudinal heat flow technique*. ASTM International, West Conshohocken, PA.

Bartelt, P. and Christen, M. (1999). *Advances in cold-region thermal engineering and sciences*, volume 533 of *Lecture Notes in Physics*. Springer Berlin / Heidelberg, Berlin.

Bartelt, P. and Lehning, M. (2002). A physical SNOWPACK model for the Swiss avalanche warning Part I: numerical model. *Cold Regions Science and Technology*, **35**(3), 123–145.

Bartelt, P. and von Moos, M. (2000). Triaxial tests to determine a microstructure-based snow viscosity law. *Annals of Glaciology*, **31**, 457–462.

Bartelt, P., Buser, O., and Sokratov, S. A. (2004). A nonequilibrium treatment of heat and mass transfer in alpine snowcovers. *Cold Regions Science and Technology*, **39**, 219–242.

Batchelor, G. K. (1974). Transport properties of two-phase materials with random structure. *Annual Review of Fluid Mechanics*, **6**(1), 227–255.

Batchelor, G. K. and O'Brien, R. W. (1977). Thermal and electrical conduction through a granular material. *Proc. R. Soc. London*, **A-355**, 313–333.

Bear, J., Braester, C., and Menier, P. (1987). Effective and relative permeabilities of anisotropic porous media. *Transport in Porous Media*, **2**(3), 301–316.

Betten, J. (1986). Applications of tensor functions to the formulation of constitutive equations involving damage and initial anisotropy. *Engineering Fracture Mechanics*, **25**(5-6), 573–584.

Betten, J. (2001). Recent advances in applications of tensor functions in continuum mechanics. *Advances in Applied Mechanics*, **37**, 277–364.

Birkeland, K. W., Hansen, K. J., and Brown, R. L. (1995). The spatial variability of snow resistance on potential avalanche slopes. *Journal of Glaciology*, **41**(137), 183–190.

Boelher, J. P., editor (1987). *CISM courses and lectures #292: applications of tensor functions in solid mechanics*. Springer-Verlag, New York.

Brown, R. L., Satyawali, P. K., Lehning, M., and Bartelt, P. (2001). Modeling the changes in microstructure of snow during metamorphism. *Cold Regions Science and Technology*, **33**(2-3), 91–101.

Cambou, B., editor (1998). *CISM courses and lectures #385: behaviour of granular materials*. Springer-Verlag, New York.

Cambou, B. and Dubujet, P. (2001). Difficulties and limitation of statistical homogenization in granular materials. *Lecture Notes in Physics*, **568**, 205–214.

Cambou, B., Dubujet, P., Emeriault, F., and Sidoroff, F. (1995). Homogenization for granular materials. *European Journal of Mechanics, A/Solids*, **14**(2), 255–276.

Carrier, W. D. (2003). Goodbye, Hazen; Hello, Kozeny-Carman. *Journal of Geotechnical and Geoenvironmental Engineering*, **129**(11), 1054.

Chang, C. and Hicher, P. (2005). An elasto-plastic model for granular materials with microstructural consideration. *Int. J. Solids Structures*, **42**(14), 4258–4277.

Chang, C. S. and Liao, C. L. (1994). Estimates of elastic modulus for media of randomly packed granules. *Applied Mechanics Reviews*, **47**(1), 197–206.

Chang, C. S. and Ma, L. (1992). Elastic material constants for isotropic granular solids with particle rotation. *Int. J. Solids Structures*, **29**(8), 1001–1018.

Chang, C. S., Chao, S. J., and Chang, Y. (1995). Estimates of elastic moduli for granular material with anisotropic random packing structure. *Int. J. Solids Structures*, **32**(14), 1989–2008.

Christoffersen, J., Mehrabadi, M. M., and Nemat-Nasser, S. (1981). A micromechanical description of granular material behavior. *Journal of Applied Mechanics*, **48**(2), 339–344.

Clavaud, J.-B., Maineult, A., Zamora, M., Rasolofosaon, P., and Schlitter, C. (2008). Permeability anisotropy and its relations with porous medium structure. *Journal of Geophysical Research*, **113**(B1), 1–10.

Cnudde, V., Masschaele, B., Dierick, M., Vlassenbroeck, J., Hoorebeke, L., and Jacobs, P. (2006). Recent progress in X-ray CT as a geosciences tool. *Applied Geochemistry*, **21**(5), 826–832.

Cobbold, P. R. and Gapais, D. (1979). Specification of fabric shapes using an eigenvalue method: discussion. *Geological Society of America Bulletin*, **90**(3), 310–312.

Coelho, D., Thovert, J.-F., and Adler, P. M. (1997). Geometrical and transport properties of random packings of spheres and aspherical particles. *Physical Review E*, **55**(2), 1959–1978.

Colbeck, S. C. (1983a). Ice crystal morphology and growth rates at low supersaturations and high temperatures. *Journal of Applied Physics*, **54**(5), 2677.

Colbeck, S. C. (1983b). Theory of metamorphism of dry snow. *Journal of Geophysical Research*, **88**(C9), 5475–5482.

Colbeck, S. C. (1993). The vapor diffusion coefficient for snow. *Water Resources Research*, **29**(1), 109–115.

Coléou, C., Lesaffre, B., Brzoska, J.-B., Ludwig, W., and Boller, E. (2001). Three-dimensional snow images by X-ray microtomography. *Annals Of Glaciology*, **32**(1), 75–81.

Colorado Department of Transportation (CDOT) (2009). Colorado Department of Transportation 2008-2009 Fact Book. Technical report, Colorado Department of Transportation, Denver.

Cowin, S. C. (1985). Relationship between the elasticity tensor and the fabric tensor. *Mechanics of Materials*, **4**(2), 137–147.

Cowin, S. C. (1986). Wolff's law of trabecular architecture at remodeling equilibrium. *Journal of Biomechanical Engineering*, **108**(1), 83–88.

Cundall, P. A. and Strack, O. D. L. (1979). A discrete numerical model for granular assemblies. *Géotechnique*, **29**(1), 47–65.

de Quervain, M. R. (1963). On the metamorphism of snow. In W. D. Kingery, editor, *Ice and Snow; Properties, Processes and Applications*, pages 377–390, Cambridge, MA. M.I.T. Press.

de Quervain, M. R. (1973). Snow structure, heat, and mass flux through snow. *The Role of Snow and Ice in Hydrology*, **105**(14), 203–226.

Dullien, F. A. L. (1992). *Porous media; fluid transport and pore structure*. Academic Press, San Diego, 2nd edition.

Edens, M. Q. (1997). *An experimental investigation of metamorphism induced microstructure evolution in a "model" cohesive snow*. Ph.D. thesis, Montana State University.

Edens, M. Q. and Brown, R. L. (1995). Measurements of microstructure of snow from surface sections. *Defence Science Journal*, **45**(2), 107–116.

Efron, B. and Tibshirani, R. J. (1994). *An introduction to the bootstrap*. Chapman & Hall/CRC, Boca Raton, FL.

Emeriault, F. and Cambou, B. (1996). Micromechanical modelling of anisotropic nonlinear elasticity of granular medium. *Int. J. Solids Structures*, **33**(18), 2591–2607.

Eshelby, J. D. (1957). The determmination of the elastic field of an ellipsoidal inclusion, and related problems. *Proc. R. Soc. London*, **241**(1226), 376–396.

Friedman, S. P. and Seaton, N. A. (1996). On the transport properties of anisotropic networks of capillaries. *Water Resources Research*, **32**(2), 339–347.

Fullman, R. L. (1953). Measurement of particle sizes in opaque bodies. *Journal of Metals*, **197**, 447–452.

Gibiansky, L. V. and Torquato, S. (1993). Link between the conductivity and elastic moduli of composite materials. *Physical Review Letters*, **71**(18), 2927–2930.

Gibson, L. J. (1985). The mechanical behaviour of cancellous bone. *Journal of Biomechanics*, **18**(5), 317–328.

Gibson, L. J. and Ashby, M. F. (1999). *Cellular solids: structure and properties*. Cambridge Univ Press, Cambridge, 2nd edition.

Giddings, J. C. and LaChapelle, E. (1962). The formation rate of depth hoar. *Journal of Geophysical Research*, **67**(6), 2377–2383.

Goff, J. A. and Gratch, S. (1946). Low-pressure properties of water from -160°F to 212°F. *Trans. American Society Heating and Ventilating Engineers*, **51**, 125–164.

Gubler, H. (1978). Determination of the mean number of bonds per snow grain and of the dependence of the tensile strength of snow on stereological parameters. *Journal of Glaciology*, **20**(83).

Hansen, A. C. and Brown, R. L. (1988). An internal state variable approach to constitutive theories for granular materials with snow as an example. *Mechanics of Materials*, **7**(2), 109–119.

Harrigan, T. P. and Mann, R. W. (1984). Characterization of microstructural anisotropy in orthotropic materials using a second rank tensor. *Journal of Materials Science*, **19**(3), 761–767.

Hashin, Z. V. I. (1983). Analysis of composite materials—a survey. *Journal of Applied Mechanics*, **50**, 481–505.

Helmig, R., Miller, C. T., Jakobs, H., Class, H., Hilpert, M., Kees, C. E., and Niessner, J. (2006). Multiphase flow and transport modeling in heterogeneous porous media. In H.-G. Bock, editor, *Progress in Industrial Mathematics at ECMI 2004*, volume 8 of *Mathematics in Industry*, pages 449–488. Springer Berlin / Heidelberg, Berlin.

Hendrikx, J., Birkeland, K., and Clark, M. (2009). Assessing changes in the spatial variability of the snowpack fracture propagation propensity over time. *Cold Regions Science and Technology*, **56**(2-3), 152–160.

Hill, R. (1963). Elastic properties of reinforced solids: some theoretical principles. *Journal of the Mechanics and Physics of Solids*, **11**(5), 357–372.

Hollister, S. J. and Kikuehi, N. (1992). A comparison of homogenization and standard mechanics analyses for periodic porous composites. *Computational Mechanics*, **10**, 73–95.

Hori, M. and Nemat-Nasser, S. (1999). On two micromechanics theories for determining micro-macro relations in heterogeneous solids. *Mechanics of Materials*, **31**, 667–682.

Hornung, U. (1997). *Homogenization and porous media*. Springer-Verlag, New York.

IEEE Std 442-1981 (1996). *IEE guide for soil thermal resistivity measurements*. The Institute of Electrical and Electronics Engineers, New York.

Jagota, A. and Hui, C. Y. (1990). The effective thermal conductivity of a packing of spheres. *Journal of Applied Mechanics*, **57**(3), 789.

Johnson, J. B. and Schneebeli, M. (1999). Characterizing the microstructural and micromechanical properties of snow. *Cold Regions Science and Technology*, **30**, 91–100.

Jordan, R. E., Hardy, J. P., Perron, F. E., and Fisk, D. J. (1999). Air permeability and capillary rise as measures of the pore structure of snow: an experimental and theoretical study. *Hydrological Processes*, **13**(12-13), 1733–1753.

Kabel, J., Odgaard, A., and Huiskes, R. (1999). Constitutive relationships of fabric, density, and elastic properties in cancellous bone architecture. *Bone*, **25**(4), 481–486.

Kachanov, M. (1980). Continuum model of a medium with cracks. *J. Engineering Mechanics Division*, **106**(5), 1039–1051.

Kachanov, M. and Sevostianov, I. (2005). On quantitative characterization of microstructures and effective properties. *Int. J. Solids Structures*, **42**, 309–336.

Kaempfer, T. U., Schneebeli, M., and Sokratov, S. A. (2005). A microstructural approach to model heat transfer in snow. *Geophysical Research Letters*, **32**(21), 1–5.

Kanatani, K.-I. (1984). Distribution of directional data and fabric tensors. *International Journal of Engineering Science*, **22**(2), 149–164.

Karnopp, D. C., Margolis, D. L., and Rosenberg, R. C. (2000). *System dynamics: modeling and simulation of mechatronic systems*. Wiley, New York, 3rd edition.

Kruyt, N. P. and Rothenburg, L. (2004). Kinematic and static assumptions for homogenization in micromechanics of granular materials. *Mechanics of Materials*, **36**(12), 1157–1173.

Kry, P. R. (1975a). Quantitative stereological analysis of grain bonds in snow. *Journal of Glaciology*, **14**(72), 467–477.

Kry, P. R. (1975b). The relationship between the visco-elastic and structural properties of fine-grained snow. *Journal of Glaciology*, **14**(72), 479–500.

Lamb, H. (1945). *Hydrodynamics*. Cambridge Univ Press, New York, 6th edition.

Lang, R. M. and Harrison, W. L. (1995). Triaxial tests on dry, naturally occurring snow. *Cold Regions Science and Technology*, **23**(2), 191–199.

Lehning, M., Bartelt, P., Brown, B., Fierz, C., and Satyawali, P. (2002). A physical SNOWPACK model for the Swiss avalanche warning Part II. snow microstructure. *Cold Regions Science and Technology*, **35**(3), 147–167.

Li, Y. and Park, C. (2000). Effective medium approximation and deposition of colloidal particles in fibrous and granular media. *Advances in Colloid and Interface Science*, **87**, 1–74.

Liao, C.-L., Chang, T.-P., Young, D.-H., and Chang, C. S. (1997). Stress-strain relationship for granular materials based on the hypothesis of best fit. *Int. J. Solids Struct*, **34**(31), 4087–4100.

Love, A. E. H. (1927). *A treatise on the mathematical theory of elasticity*. Cambridge Univ Press, London, 4th edition.

Lubarda, V. and Krajcinovic, D. (1994). Tensorial representation of the effective elastic properties of the damaged material. *Int. J. Damage Mechanics*, **3**, 38–56.

Lubarda, V. A. and Krajcinovic, D. (1993). Damage tensors and the crack density distribution. *International Journal of Solids and Structures*, **30**(20), 2859–2877.

Luding, S. (2005). Anisotropy in cohesive, frictional granular media. *Journal of Physics: Condensed Matter*, **17**(24), S2623–S2640.

Lundy, C. C., Edens, M. Q., and Brown, R. L. (2002). Measurement of snow density and microstructure using computed tomography. *Journal Of Glaciology*, **48**(161), 312–316.

Mahajan, P. and Brown, R. L. (1993). A microstructure-based constitutive law for snow. *Annals of Glaciology*, **18**, 287–294.

Mallick, P. K. (1993). *Fiber-reinforced composites: materials, manufacturing, and design*. Marcel Dekker, Inc., New York, 2nd edition.

Martins, A., Laranjeira, P. E., Lopes, C. B., and Dias, M. M. (2007). Network modeling of flow in a packed bed. *AIChE Journal*, **53**(1), 91–107.

McClung, D. and Schaerer, P. (2006). *The avalanche handbook*. The Mountaineers Books, Seattle, WA, 3rd edition.

Mehrabadi, M. M. (1982). On statistical description of stress and fabric in granular materials. *Int. J. Numerical and Analytical Methods in Geomechanics*, **6**, 95–108.

Mellor, M. (1975). A review of basic snow mechanics. In *Proc. Int. Symp. Snow Mechanics*, volume 114, pages 251–291, Wallingford. Int. Assoc. Hydrological Sciences Press.

Miller, D. A., Adams, E. E., and Brown, R. L. (2003). A microstructural approach to predict dry snow metamorphism in generalized thermal conditions. *Cold Regions Science and Technology*, **37**(3), 213–226.

Mishra, A. and Mahajan, P. (2004). A constitutive law for snow taking into account the compressibility. *Annals of Glaciology*, **38**, 145–149.

Mori, T. and Tanaka, K. (1973). Average stress in matrix and average elastic energy of materials with misfitting inclusions. *Acta Metallurgica*, **21**(5), 571–574.

Morin, S., Domine, F., Arnaud, L., and Picard, G. (2010). In-situ monitoring of the time evolution of the effective thermal conductivity of snow. *Cold Regions Science and Technology*, **64**(2), 73–80.

Mura, T. (1987). *Micromechanics of defects in solids*. Kluwer Academic Publishers, Norwell, MA, 2nd edition.

Navarre, J., Meyssonnier, J., and Vagnon, a. (2007). 3D numerical model of snow deformation without failure and its application to cold room mechanical tests. *Cold Regions Science and Technology*, **50**(1-3), 3–12.

Nemat-Nasser, S. (2000). A micromechanically-based constitutive model for frictional deformation of granular materials. *Journal of the Mechanics and Physics of Solids*, **48**(6-7), 1541–1563.

Nemat-Nasser, S. and Hori, M. (1999). *Micromechanics: overall properties of heterogeneous materials*, volume 786. Elsevier Science Publishers B.V., Amsterdam, 2nd edition.

Nemat-Nasser, S. and Mehrabadi, M. (1983). Stress and fabric in granular masses. In J. T. Jenkins and M. Satake, editors, *Mechanics of granular materials: new models and constitutive relations*, pages 1–8. Elsevier Science Publishers B.V.

Nicot, F. (2004). Constitutive modelling of snow as a cohesive-granular material. *Granular Matter*, **6**(1), 47–60.

Nield, D. A. and Bejan, A. (2006). *Convection in porous media*. Springer-Verlag, New York, 3rd edition.

Northwest Weather and Avalanche Center (NWAC) (2009). Annual US Avalanche Fatalities by Year, 1950-2009.

Oda, M. and Iwashita, K., editors (1999). *Mechanics of granular materials: an introduction*. A. A. Balkema, Rotterdam.

Odgaard, A. (1997). Three-dimensional methods for quantification of cancellous bone architecture. *Bone*, **20**(4), 315–328.

Odgaard, A., Rietbergen, B. V., Kabel, J., Dalstra, M., and Huiskes, R. (1997). Fabric and elastic principal directions of cancellous bone are closely related. *Journal of Biomechanics*, **30**(5), 487–495.

Petrenko, V. F. and Whitworth, R. W. (1999). *Physics of ice*. Oxford Univ Press, New York.

Pieritz, R., Brzoska, J.-B., Flin, F., Lesaffre, B., and Coléou, C. (2004). From snow X-ray microtomograph raw volume data to micromechanics modeling: first results. *Annals Of Glaciology*, **38**, 52–58.

Rahmoun, J., Kondo, D., and Millet, O. (2009). A 3D fourth order fabric tensor approach of anisotropy in granular media. *Computational Materials Science*, **46**(4), 869–880.

Reddy, J. N. (2008). *An introduction to continuum mechanics: with applications*. Cambridge Univ Press, New York.

Reuss, A. (1929). Berechnung der fließgrenze von mischkristallen auf grund der plastizitätsbedingung für einkristalle . *ZAMM - Zeitschrift für Angewandte Mathematik und Mechanik*, **9**(1), 49–58.

Satake, M. (1983). Fundamental quantities in the graph approach to granular materials. In J. Jenkins and M. Satake, editors, *Mechanics of Granular Materials: New Models and Constitutive Relations*, pages 9–19. Elsevier Science Publishers B.V.

Satyawali, P. K. (2000). Diffusivity and vapor flow into snow during phase change. *Annals of Glaciology*, **31**, 445–450.

Satyawali, P. K. and Singh, A. (2008). Dependence of thermal conductivity of snow on microstructure. *Journal of Earth System Science*, **117**(4), 465–475.

Satyawali, P. K., Singh, A. K., Dewali, S. K., Kumar, P., and Kumar, V. (2008). Time dependence of snow microstructure and associated effective thermal conductivity. *Annals of Glaciology*, **49**, 43–50.

Schneebeli, M. and Sokratov, S. A. (2004). Tomography of temperature gradient metamorphism of snow and associated changes in heat conductivity. *Hydrological Processes*, **18**, 3655–3665.

Sevostianov, I. and Kachanov, M. (2008). Connections between elastic and conductive properties of heterogeneous materials. *Advances in Applied Mechanics*, **42**, 69–252.

Shames, I. H. and Cozzarelli, F. A. (1997). *Elastic and inelastic stress analysis*. Taylor & Francis, Philadelphia.

Shapiro, L. H., Johnson, J. B., Sturm, M., and Blaisdell, G. L. (1997). Snow mechanics: review of the state of knowledge and applications. Technical report, Cold Regions Research and Engineering Lab, Hanover, NH.

SkyScan, N. V. (2009). Structural parameters measured by Skyscan CT-analyzer software. Technical report, Skyscan N. V., Aartselaar.

Slaughter, A. E. and Adams, E. E. (2009). Numerical investigation of factors causing near-surface metamorphism. In J. Schweizer and A. van Herwijnen, editors, *Proc. Int. Snow Science Workshop*, pages 72–76, Davos. Swiss Federal Institute WSL.

Sokratov, S. A. and Maeno, N. (2000). Effective water vapor diffusion coefficient of snow under a temperature gradient. *Water Resources Research*, **36**(5), 1269–1276.

Srivastava, P. K., Mahajan, P., Satyawali, P. K., and Kumar, V. (2010). Observation of temperature gradient metamorphism in snow by X-ray computed microtomography: measurement of microstructure parameters and simulation of linear elastic properties. *Annals Of Glaciology*, **50**(54), 73–82.

Sturm, M. and Johnson, J. B. (1991). Natural convection in the subarctic snow cover. *Journal of Geophysical Research*, **96**(B7), 11,657–11,671.

Sturm, M. and Johnson, J. B. (1992). Thermal conductivity measurements of depth hoar. *Journal of Geophysical Research*, **97**(B2), 2,129–2,139.

Sturm, M., Holmgren, J., Konig, M., and Morris, K. (1997). The thermal conductivity of seasonal snow. *Journal of Glaciology*, **43**(143), 26–41.

Suquet, P. M. (1987). Elements of homogenization for inelastic solid mechancis. *Lecture Notes in Physics*, **272**, 193–278.

Truesdell, C. (1966). *The mechanical foundations of elasticity and fluid dynamics*. Gordon & Breach Science Pub, New York.

Turner, C. H. and Cowin, S. C. (1987). Dependence of elastic constants of an anisotropic porous material upon porosity and fabric. *Journal of Materials Science*, **22**(9), 3178–3184.

Turner, C. H., Cowin, S. C., Rho, J. Y., Ashman, R. B., and Rice, J. C. (1990). The fabric dependence of the orthotropic elastic constants of cancellous bone. *Journal of Biomechanics*, **23**(6), 549–61.

Ugural, A. C. and Fenster, S. K. (1995). *Advanced strength and applied elasticity*. Prentice-Hall, Upper Saddle River, NJ, 3rd edition.

Underwood, E. E. (1970). Quantitative stereology.

Ursino, N., Roth, K., Gimmi, T., and Flühler, H. (2000). Upscaling of anisotropy in unsaturated Miller-similar porous media. *Water Resources Research*, **36**(2), 421.

Vargas, W. L. and McCarthy, J. J. (2001). Heat conduction in granular materials. *AIChE Journal*, **47**(5), 1052–1059.

Vargas-Escobar, W. L. (2002). *Discrete modeling of heat conduction in granular media*. Ph.D. thesis, University of Pittsburgh.

Venkataraman, P. N. (2004). EM851 Lecture Notes: Tensor Algebra.

Voigt, W. (1889). Über die beziehung zwischen den beiden elasticitätsconstanten isotroper körper. *Annalen der Physik*, **274**(12), 573–587.

Voyiadjis, G. Z., Kattan, P. I., and Taqieddin, Z. N. (2007). Continuum approach to damage mechanics of composite materials with fabric tensors. *Int. J. Damage Mechanics*, **16**(3), 301–329.

Vranes, K. and Pielke Jr., R. (2009). Normalized earthquake damage and fatalities in the United States: 1900–2005. *Natural Hazards Review*, **10**(3), 84–101.

Waldner, P. A., Schneebeli, M., Schultze-Zimmermann, U., and Flühler, H. (2004). Effect of snow structure on water flow and solute transport. *Hydrological Processes*, **18**(7), 1271–1290.

Walton, K. (1987). The effective elastic moduli of a random packing of spheres. *J. of the Mechanics and Physics of Solids*, **35**(2), 213–226.

Wang, C.-C. (1970). A new representation theorem for isotropic functions. *Archive for Rational Mechanics and Analysis*, **36**(3), 166–197.

Wang, L. B., Frost, J. D., and Lai, J. S. (2004). Three-dimensional digital representation of granular material microstructure from X-ray tomography imaging. *J. Computing in Civil Engineering*, **18**(1), 28–35.

Wang, X. (1999). Non-Darcy flow through anisotropic porous media. *Chemical Engineering Science*, **54**(12), 1859–1869.

Whitehouse, W. J. (1974). The quantitative morphology of anisotropic trabecular bone. *Journal of Microscopy*, **101**(Pt 2), 153–168.

Williams, J. R., Hocking, G., and Mustoe, G. G. W. (1985). The theoretical basis of the discrete element method. In *Numerical Methods in Engineering, Theory, and Application*, pages 897–906, Swansea. A.A. Balkema Publishers.

Wong, R. C. K. (2003). A model for strain-induced permeability anisotropy in deformable granular media. *Canadian Geotechnical Journal*, **40**(1), 95–106.

Yi, Y.-M., Park, S.-H., and Youn, S.-K. (1998). Asymptotic homogenization of viscoelastic composites with periodic microstructures. *Int. J. Solids Structures*, **35**(17), 2039–2055.

Yosida, Z. (1963). Physical properties of snow. In W. D. Kingery, editor, *Ice and Snow; Properties, Processes and Applications*, pages 485–527, Cambridge, MA. M.I.T. Press.

Zysset, P. K. and Curnier, A. (1995). An alternative model for anisotropic elasticity based on fabric tensors. *Mechanics of Materials*, **21**(4), 243–250.

APPENDICES

APPENDIX A

WATER VAPOR DIFFUSION, PHASE CHANGE & ENERGY FLUX

Water vapor diffusion in snow is evidenced by recrystallization within the snowpack. This mass flux is important not only to crystal growth kinetics within the snowpack, but it is also associated with an energy flux because the H_2O molecules are changing between their vapor and solid phases as sublimation and deposition occur. This energy exchange due to phase change is termed latent heat transfer because it is energy flux at a constant temperature. In quantifying an effective heat transfer coefficient it is important to incorporate this energy flux.

The generally adopted analytical approach was developed by Giddings and LaChapelle (1962); de Quervain (1963); Yosida (1963); de Quervain (1973)—giants in the field of snow mechanics. Over the passing decades it has provided reasonable engineering approximations to the phenomena of mass transfer due to water vapor diffusion, phase change, and the associated energy flux. For the sake of completeness, the purpose here is to review the derivation and its assumptions and simplifications.

A.1 Diffusion in an Ideal Gas Mixture

Diffusion only occurs in mixtures. In dry snow the mixture in an individual pore space is assumed to be comprised two gaseous species: air and water vapor. In such a system the total pressure P (Pa) and total molar concentration or molar density Φ ($^{\mathrm{mol}}/_{\mathrm{m}^3}$) can be determined by the binary constituents as

$$P = p_{air} + p_{vap}, \tag{A.1a}$$

$$\Phi = \Phi_{air} + \Phi_{vap}, \tag{A.1b}$$

where p_{air} and p_{vap} are termed the partial pressures and Φ_{air} and Φ_{vap} are the molar or molecular concentrations of the two species. In its most general form, Fick's 1$^{\mathrm{st}}$

Law describes molar flux $\bar{J}$ ($^{mol}/_{m^2 \cdot s}$) due to a gradient of molar fraction ∇y_{vap} ($^{1}/_{m}$):

$$\overline{J} = \text{-}\Phi D_{vap} \nabla y_{vap}, \tag{A.2}$$

where $y_{vap} = {}^{\Phi_{vap}}/_{\Phi}$, the fraction of moles represented by water vapor in the binary mixture. The diffusivity D_{vap} ($^{m^2}/_{s}$) at this scale is the diffusivity of water vapor through air.

In gaseous mixtures, concentrations are often expressed in terms of partial pressures. It is assumed that the total mixture and the individual species follow the ideal gas model:

$$PV = n_{tot} R\theta, \tag{A.3a}$$

$$p_{vap} V = n_{vap} R\theta, \tag{A.3b}$$

where V is the total volume occupied by the mixture, n is number of moles, R is the universal gas constant ($^{J}/_{mol \cdot K}$) and θ is absolute temperature (K). Now, molar fraction can be written in terms of pressures as(Pa)

$$y_{vap} = \frac{\Phi_{vap}}{\Phi} = \frac{{}^{n_{vap}}/_{V}}{{}^{n_{tot}}/_{V}} = \frac{{}^{p_{vap}}/_{R\theta}}{{}^{P}/_{R\theta}} = \frac{p_{vap}}{P}. \tag{A.4}$$

Fick's 1st Law as driven by a gradient of pressure fraction is then

$$\overline{J} = \text{-}\frac{P}{R\theta} D_{vap} \nabla \left(\frac{p_{vap}}{P} \right). \tag{A.5}$$

Or, multiplying both sides by the molar mass of water vapor results in a mass flux rather than a molar flux:

$$\overline{J} = -\frac{P}{R_{vap}\theta} D_{vap} \nabla \left(\frac{p_{vap}}{P} \right), \tag{A.6}$$

where R_{vap} is the gas constant of water vapor ($^{J}/_{kg \cdot K}$) rather than the universal gas constant. Next, by assuming a constant total pressure the expression becomes

$$\overline{J} = -\frac{1}{R_{vap}\theta} D_{vap} \nabla p_{vap}, \tag{A.7a}$$

or, even more simply in terms of vapor density ρ_{vap}:

$$\overline{J} = -D_{vap} \nabla \rho_{vap}. \tag{A.7b}$$

In assuming constant total pressure, this form of the constitutive relationship is applicable to isobaric systems. Constant total pressure does not imply constant partial pressures, otherwise a partial pressure gradient and the resulting flux of a species in the mixture could not arise. Also, because the gaseous mixture is assumed to obey the ideal gas law, this also necessitates a restriction to isothermal systems. This condition of thermal equilibrium applies to both the mixture and the individual species.

A.2 Temperature Variations and Quasistatic Equilibrium

In view of the goal of eventually characterizing the energy flux associated with the mass flux, it is desirable to express Equation (A.7a) in terms of the temperature gradient, like conductivity. By the chain rule the gradient of partial pressure is related

to the temperature gradient as

$$\nabla p_{vap} = \frac{dp_{vap}}{d\theta} \nabla \theta. \tag{A.8}$$

However, substituting Equation (A.8) into Equation (A.7a) presents a contradiction. This is because Equation (A.7a) applies to a system in thermal equilibrium where temperature gradients are nonexistent. Executing this substitution requires a relaxation of thermal equilibrium.

Real systems rarely exhibit true equilibrium and snow is no exception. Consider the fundamental unit at which these continuum-based vapor diffusion developments apply: an individual pore. At this local scale, dismissing variations in the temperature field as negligible defines a state of quasistatic thermal equilibrium in an individual pore. Because so few real systems ever reach true equilibrium, much of the application of equilibrium thermodynamic principles depends upon accepting the equivalency of quasi-equilibrium and true equilibrium states. Macroscopic gradients of 10 and $100\,{}^{\mathrm{K}}/_{\mathrm{m}}$ translate to microscopic gradients of 0.01 and $0.1\,{}^{\mathrm{K}}/_{\mathrm{mm}}$, respectively. However, at some point deviations in local temperature must violate even a quasistatic equilibrium assumption. Whether that point is $1\,{}^{\mathrm{K}}/_{\mathrm{mm}}$, $0.01\,{}^{\mathrm{K}}/_{\mathrm{mm}}$, or somewhere in between is difficult to determine. The validity of this assumption and the others involved in this derivation are considered later. For now, the existence of a state of quasistatic thermal equilibrium is assumed where small, local temperature gradients are permitted to exist.

Substituting Equation (A.8) into Equation (A.7a) establishes mass flux as driven by a temperature gradient rather than a partial pressure gradient:

$$\overline{J} = -\frac{1}{R_{vap}\theta} D_{vap} \frac{dp_{vap}}{d\theta} \nabla \theta. \tag{A.9}$$

A.3 Application of the Clausius-Clapeyron Relationship

The next assumption is that the derivative of water vapor partial pressure with respect to temperature is defined by the Clausius-Clapeyron relationship. The Clausius-Clapeyron relationship is a differential equation describing the temperature rate of change of the pressure of a substance in a system in which the two phases of the substance are in equilibrium:

$$\frac{dp}{d\theta} = \frac{L}{\theta \delta v}, \tag{A.10}$$

where L is the latent heat associated with the phase change ($^{\mathrm{J}}/_{\mathrm{kg}}$) and δv is the difference in specific volume between the two phases ($^{\mathrm{m}^3}/_{\mathrm{kg}}$). In snow, because a given pore space is immediately adjacent to a surface of ice the substance in question is H_2O and the two phases are ice and water vapor. Consequently the latent heat of this phase change is specifically the latent heat of sublimation L_s.

The concept of equilibrium implies a balance of influences. For compete equilibrium in thermodynamics this broadly includes mechanical, thermal, phase, and chemical equilibrium. Here, the conditions of thermal and phase equilibrium are addressed to evaluate the applicability of the Clausius-Clapeyron equation. Thermal equilibrium dictates that the two phases—ice/water vapor—exist at the same temperature. Phase equilibrium implies that the properties of the two-phase system are uniform but generally different for each phase. For example, the specific volume of the gas phase differs from that of the solid phase. Phase equilibrium is dynamic in that ice may be sublimating to vapor and vapor may be depositing as ice but the exchange is balanced such that there is no net phase change in the system. If a two phase system of solid and vapor is left to equilibrate at a given temperature, such a state of dynamic phase equilibrium will be reached when the vapor phase is saturated.

By the conditions of equilibrium, applying the Clausius-Clapeyron equation in Equation (A.9) requires an assumption that the water vapor in the pore space is saturated. The partial pressure of water vapor, p_{vap}, is therefore taken as equal to the saturated vapor pressure, p_{sat}, and

$$\frac{dp_{vap}}{d\theta} = \frac{dp_{sat}}{d\theta} = \frac{L_s}{\theta \delta v}. \tag{A.11}$$

Also, δv is usually taken as simply the specific volume of the vapor phase, v_{vap}, as it is three orders of magnitude greater than that of the solid phase (e.g., at 273.15 K, $v_{vap} = 1.24\,\mathrm{m^3/kg}$ and $v_{ice} = 1.09 \times 10^{-3}\,\mathrm{m^3/kg}$). Applying the ideal gas model to the vapor species results in $v_{vap} = {}^{R_{vap}\theta}/_{p_{sat}}$ rendering the Clausius-Clapeyron equation as

$$\frac{dp_{sat}}{d\theta} = \frac{L_s p_{sat}}{R_{vap}\theta^2}. \tag{A.12}$$

This differential equation can be solved for p_{sat} (Pa) via separation of variables. The solution to this ice/water vapor version of the Clausius-Clapeyron equation is the sublimation curve on a "$p-T$" phase diagram—it defines the phase boundary between solid and vapor. The latent heat of sublimation varies slightly with temperature, but if assumed constant the solution is

$$p_{sat} = p_o \exp\left[\frac{L_s}{R_{vap}}\left(\frac{1}{\theta_o} - \frac{1}{\theta}\right)\right], \tag{A.13}$$

where p_o is a reference vapor pressure (Pa) at reference temperature θ_o (K). Alternatively, empirical solutions are also available for given temperature ranges. For

example, the classic Goff-Gratch equation (Goff and Gratch, 1946) recommends

$$\log\left(p_{sat}\right) = \text{-}909.718\left(\frac{\theta_o}{\theta} - 1\right) - 356.654\log\left(\frac{\theta_o}{\theta}\right) + 87.6793\left(1 - \frac{\theta}{\theta_o}\right) + \log\left(p_o\right) \tag{A.14}$$

for saturated vapor in equilibrium with ice in the range between 167 and 273 K. Here, p_o and θ_o are a reference pressure and temperature at the triple point.

A.4 Microscopic Mass Flux to Macroscopic Energy Flux

Substituting the Clausius-Clapeyron equation into Equation (A.9) results in

$$\overline{J} = \text{-}\frac{L_s p_{sat}}{R_{vap}^2 \theta^3} D_{vap} \nabla\theta. \tag{A.15}$$

The verbiage behind the process this equation describes is as follows: 1) a relatively warmer ice grain is in equilibrium with the water vapor immediately adjacent to it, 2) across a pore, a relatively cooler ice grain is in equilibrium with the water vapor immediately adjacent to it, 3) by the Clausius-Clapeyron equation, the saturated vapor pressure adjacent to the warmer grain is slightly higher than the saturated vapor pressure adjacent to the cooler grain, 4) thus, temperature differences establish pressure differences, driving mass across the pore space via diffusion.

The local temperature differences are assumed to be slight so as to not violate the assumption of quasistatic thermal equilibrium in any individual pore. The coupled interactions of a network of pores and their surrounding grains, each in a quasistatic equilibrium, dictate the macroscopic mass flux through snow. This idea has been labeled the "simple theory" and the "continuous medium" approach (Colbeck, 1993). The difference in scale is simply captured by a different material property. At the

local scale the material property is D_{vap}, the diffusivity of water vapor through air. However, if applying Equation (A.15) at the macroscopic scale the material property must be $\mathbf{D}^*$, the effective diffusivity of water vapor through snow:

$$\overline{J} = -\frac{L_s p_{sat}}{R_{vap}^2 \theta^3} \mathbf{D}^* \cdot \nabla\theta, \tag{A.16}$$

where diffusivity is in general a 2^{nd} order tensor.

Introducing a property of a heterogeneous, two-phase material adds complication to a constitutive relationship already laden with assumptions and approximations. Equation (A.15) primarily communicates the strong, nonlinear temperature dependence of diffusive vapor flux in snow. Microstructural dependence is introduced in Equation (A.16) through $\mathbf{D}^*$, a primary focus of this research project.

Finally, relating the vapor flux expressed in Equation (A.16) to energy flux is based on the notion that cycles of sublimation and deposition are tied to movement of mass as

$$\bar{q}_{vap} = L_s \overline{J} = -\frac{L_s^2 p_{sat}}{R_{vap}^2 \theta^3} \mathbf{D}^* \cdot \nabla\theta. \tag{A.17}$$

The "apparent conductivity" of water vapor diffusion and phase change is therefore

$$\frac{L_s^2 p_{sat}}{R_{vap}^2 \theta^3} \mathbf{D}^*, \tag{A.18}$$

quantifying the impact of effective diffusivity to overall energy transfer in snow.

A.5 Summary and Validity of Model

Assumptions must be based on sound principles and reinforced by empirical data. The analytical model presented here was developed, reviewed, and edited over the

course of decades. The sublimation, diffusion, and deposition of water vapor within the snowpack is a difficult process to isolate, observe, and measure. Consequently, empirical data neither conclusively confirms nor refutes the model and its assumptions and so the paradigm persists. Summarized below are the major assumptions contributing to the model development and a brief explanation addressing their validity.

- *The binary mixture and individual species of air and water vapor may be treated as an ideal gas*: this is a common thermodynamic assumption at low operating pressures. The total pressure in a given pore should be very close to atmospheric, while the partial pressure of water vapor is much lower than that.

- *The temperature field in an individual pore results in a quasistatic thermal equilibrium state*: this assumption is necessary to apply the relatively simpler concepts of equilibrium thermodynamics. In the high density snow analyzed here the greatest macroscopic gradient is $100\,^{\mathrm{K}}/_{\mathrm{m}} = 0.1\,^{\mathrm{K}}/_{\mathrm{mm}}$—a large temperature gradient—and the pore size is estimated to be 0.15 mm (Schneebeli and Sokratov, 2004). A different microstructural study of similar high density snow measured a mean pore size of 0.30 mm (Waldner *et al.*, 2004). With these estimates the temperature differences across a typical pore are $0.015 - 0.030\,\mathrm{K}$. Low density snow should have larger pores on average. Assuming an order of magnitude increase in pore size—3 mm—results in only a 0.1% temperature difference across a typical pore. This temperature variation is slight and supports the assumption. It is noted that nonequilibrium mass and energy transport concepts have also been recently applied to snow (Bartelt *et al.*, 2004).

- *The partial pressure of water vapor in the pore space is given by the saturated vapor pressure*: this requires that saturated vapor exists everywhere in the pore

space. This is a typical assumption in snow metamorphism given the relatively large surface area of the ice available for phase change. Additionally, the saturated vapor pressure is determined, for a given temperature, with respect to a planar ice surface—ice grain curvature effects on vapor pressure are neglected in this formulation. Colbeck (1983b) illustrates that differences in vapor pressure are much more strongly influenced by temperature than shape.

- *The difference in microscopic and macroscopic application is captured by a change in material property*: this is a fundamental tenet of homogenization for granular materials, reviewed here in Chapters 2 and 3. In this multi-scale approach both the constituents at the microscopic level and the granular material at the macroscopic level are assumed to behave according to the principles of continuum mechanics. This includes constitutive relationships and associated material properties. The appropriate property depends on the scale. Confirmation that both scales follow the proposed constitutive models must ultimately come from empirical data.

APPENDIX B

NOTES ON OTHER ELASTIC STIFFNESS MODELS

At first glance the anisotropic models of Chang *et al.* (1995) and Rahmoun *et al.* (2009) do not look mathematically equivalent. This appendix takes the necessary algebraic steps to demonstrate they are the same model. Equation (5.18b) is taken from Rahmoun *et al.* (2009), Equation (24), and written in the notation of this research project. Rahmoun *et al.* (2009) expand this expression in their Appendix D. Please note that a multiplicative constant of ${}^{4N_{cp}\hat{R}^2}/_{7V}$ is absent from each of the moduli in their Appendix D. Two of these stiffness coefficients are

$$C_{1111} = \frac{4N_{cp}\hat{R}^2}{7V}\left\{\left[6F_{11}-\frac{3}{5}\right]k_n+\left[F_{11}+\frac{3}{5}\right]k_s\right\}, \tag{B.1a}$$

$$C_{1122} = \frac{4N_{cp}\hat{R}^2}{7V}\left\{F_{11}+F_{22}-\frac{1}{5}\right\}\left[k_n-k_s\right]. \tag{B.1b}$$

Equations (B.1a) and (B.1b) are functions of: 1) normal and shear spring stiffnesses k_n and k_s, respectively, 2) the total number of contact planes or bonds N_{cp}, 3) the representative volume V, 4) mean spherical grain radius $\hat{R}$, and 5) the coefficients of the 2$^{\text{nd}}$ order contact tensor F_{ij}.

Chang *et al.* (1995) write these coefficients in their Table 1 as

$$C_{1111} = \frac{4N_{cp}\hat{R}^2}{15V}\left\{\left[3k_n+2k_s\right]+\frac{2a_{20}}{7}\left[6k_n+k_s\right]\right\}, \tag{B.2a}$$

$$C_{1122} = \frac{4N_{cp}\hat{R}^2}{15V}\left\{\left[k_n-k_s\right]+\frac{a_{20}}{7}\left[k_n-k_s\right]+\frac{6a_{22}}{7}\left[k_n-k_s\right]\right\}. \tag{B.2b}$$

a_{20} and a_{22} are coefficients of a deviatoric fabric tensor defined in Chang *et al.* (1995), Equation (51) as

$$\Psi_{ij} = \begin{bmatrix} a_{20} & 0 & 0 \\ 0 & {}^{-a_{20}}/_{2}+3a_{22} & 3b_{22} \\ 0 & 3b_{22} & {}^{-a_{20}}/_{2}-3a_{22} \end{bmatrix}. \tag{B.3}$$

In turn, the fabric tensor $\mathbf{\Psi}$ is used to approximate the distribution density of contact normal vectors $\bar{n}$ in their Equation (50):

$$P(\bar{n}) = \frac{1}{4\pi}\left\{1 + \Psi_{ij} n_i n_j\right\}. \tag{B.4}$$

The above expression is Equation (2.20) in 3-D, meaning that $\mathbf{\Psi}$ is a fabric tensor "of the third kind" first used by Kanatani (1984) in defining $P(\bar{n})$. Consequently, $\mathbf{\Psi}$ and $\mathbf{F}$ are related—specifically in 3-D—as

$$\Psi_{ij} = D_{ij} = \frac{15}{2} F'_{ij} = \frac{15}{2}\left(F_{ij} - \frac{1}{3}\delta_{ij}\right). \tag{B.5}$$

This allows a_{20} and a_{22} to be written in terms of the F_{ij}. For example:

$$\Psi_{11} = a_{20} = \frac{15}{2}\left(F_{11} - \frac{1}{3}\right). \tag{B.6}$$

Using this solution for a_{20} and

$$\Psi_{22} = -\frac{a_{20}}{2} + 3a_{22} = \frac{15}{2}\left(F_{22} - \frac{1}{3}\right), \tag{B.7}$$

and a_{22} can be written as

$$a_{22} = \frac{5}{2}\left(F_{22} - \frac{1}{3}\right) + \frac{1}{6}a_{20} = \frac{5}{2}\left(F_{22} - \frac{1}{3}\right) + \frac{5}{4}\left(F_{11} - \frac{1}{3}\right). \tag{B.8}$$

Substituting Equations (B.6) and (B.8) into Equations (B.2a) and (B.2b) results in exactly Equations (B.1a) and (B.1b).

This example also illustrates that these models yield negative stiffness coefficients in the limiting case of anisotropy where bonds exist only in a single direction. Consider

bonds only in the x_3 direction: $F_{33} = 1$ and $F_{11} = F_{22} = 0$ and Equations (B.1a) and (B.1b) become

$$C_{1111} = \frac{4N_{cp}\hat{R}^2}{V}\left\{\frac{3}{5}\left[k_s - k_n\right]\right\}, \tag{B.9a}$$

$$C_{1122} = \frac{4N_{cp}\hat{R}^2}{V}\left\{\frac{1}{5}\left[k_s - k_n\right]\right\}. \tag{B.9b}$$

As defined in Chapter 5, ${}^{k_s}/_{k_n} = {}^{G_{ice}}/_{E_{ice}}$ and E_{ice} is more than double G_{ice} (Petrenko and Whitworth, 1999). The above expressions are negative for this usual scenario where $k_n > k_s$.

APPENDIX C

EXAMPLE STEREOLOGICAL OUTPUT TABLES

Data assembled from ten different images or slices in the x_2-x_3 plane are presented in the following tables as examples of the stereological outputs. Each element in a 2-D image array corresponds to a pixel. Many of the parameters measured by the software are reported in pixels. They are converted with knowledge of the image resolution.

Table C.1 is truncated so that it fits on a single page. In this table, each row corresponds to information tied to a bond identified in the 2-D image. The columns are:

- rb (pix): 2-D bond radius, labeled in Chapter 6 as $\rho_{(2-D)}$ (pixels),
- rb_angle (deg): orientation of "rb" with respect to the reference axes, labeled in Chapter 6 as ω (deg). Vectors normal to these orientations pointing toward the 1st and 2nd quadrants are used as directional data (see Chapter 2),
- g1x / g1y / g2x / g2y (pix): centroid coordinates of the two circular grains to which the bond is connected,
- rg1 / rg2 (pix): 2-D radii of the aforementioned circular grains, labeled in Chapter 6 as $R_{(2\text{-D})}$ (pixels),
- sdg1 / sdg2 (pix): distance along the skeleton from bond site to centroid of respective grain,
- skeleton Tangent (deg): tangent to the skeleton at the bond site, labeled in Chapter 6 as ϖ (deg).

In Table C.2 the rows correspond to connectivity data: one for each of the ten planar images in this example. The columns are:

Table C.1: Stereology Data File 1: Bonds & Grains

rb (pix)	rb_angle (deg)	g1x (pix)	g1y (pix)	g2x (pix)	g2y (pix)	rg1 (pix)	rg2 (pix)	sdg1 (pix)	sdg2 (pix)	skeleton Tangent (deg)
1	0	97	15	96	19	2	1.41	3	1.41	76.21
1	90	96	19	91	22	1.41	1.41	2.41	5.23	60.19
3.41	36.87	54	17	61	29	5	5.64	8.05	7.64	-56.79
1	0	98	26	91	22	2.82	1.41	7.23	1.41	-45
3	0	119	18	114	33	5	5	6.82	11.87	83.77
1.41	63.44	20	28	11	20	2.82	4.41	5.82	7.64	-48.58
4	-90	76	20	62	29	5.41	4.82	12.87	5.41	-30.66
2.41	33.69	62	29	62	29	4.82	4.82	9.64	11.05	-70.23
1.41	45	102	30	102	30	2.41	2.41	1	1	-9.728
1	0	62	29	62	29	4.82	4.82	15.05	5.64	-37.68
1	0	103	31	92	37	3	3.41	4.23	10.05	42.88
2.41	-18.43	61	29	59	41	5.64	3.41	8.23	5.41	79.7
1	0	42	34	32	43	3.41	3.41	7.23	8.82	-45.92
1	0	59	41	52	43	3.41	2	4.41	3.41	45.97
1	0	77	39	70	56	3	3.82	3.41	22.92	-38.56
2	-63.44	32	43	23	47	3.41	4.23	2.41	8.23	16.7
1	0	92	37	94	49	3.41	4	8.64	5.82	-71.41
1	0	42	34	39	52	3.41	2	19.87	8.05	-54.66
1	0	23	47	12	43	4.23	3	7.82	5.64	-34.96
2.41	-33.69	77	39	70	56	3	3.82	14.05	12.28	49.22
1.41	63.44	95	49	102	51	3	4.41	5.23	4.23	-56.06
1.41	0	107	52	117	54	4.82	2	7.41	4.23	-25.81
1.41	-45	94	49	85	53	4	2.41	6.23	4.41	-8.097

Table C.2: Stereology Data File 2: 2-D Connectivity

NumGrains	0	1	2	3	4	5	6
114	26	34	38	16	0	0	0
103	28	45	21	9	0	0	0
101	19	42	30	10	0	0	0
114	20	45	34	15	0	0	0
109	26	45	33	5	0	0	0
101	22	38	29	12	0	0	0
101	15	42	38	6	0	0	0
105	19	45	30	11	0	0	0
98	26	34	30	8	0	0	0
108	23	39	33	13	0	0	0

- NumGrains: total number of inscribed circular grains identified by the software in the planar image,
- 0, 1,. . ., 6: number of grains having 0, 1,. . ., 6 bonds. A 2-D grain can appear to have no connectivity; it depends on the plane of intersection. The Γ function introduced by Alley (1986) (see Chapter 6) accounts for this probability in estimating 3-D connectivity from 2-D data.

Table C.3 contains parameters derived from test line analyses. Again, a row is produced for one planar image. The columns are:

- Total Intercept Length (pix): those pixels of the test line that coincide with the solid constituent,
- Number Of Grains Intercepted (#): this count registers a tally every time the test line enters *and* exits an idealized 2-D disk identified as a grain, it is possible to count a given grain multiple times in this tally,

Table C.3: Stereology Data File 3: Test Line and Intercept Data

Total Intercept Length (pix)	Number Of Grains Intercepted (#)	Total Test Line Length (pix)	Grains Per Test Area (#pix^-2)	Total Test Analysis Area (pix^2)
8058	1198	21630	0.00743832	11024
7282	1218	21630	0.00598694	11024
9502	1211	21614	0.00662672	11016
8427	1309	22048	0.00765465	11235
7710	1147	21840	0.00673854	11130
8719	1246	21840	0.0066487	11130
8448	1157	22260	0.00643625	11342
9063	1210	22472	0.00681282	11449
8066	1082	20400	0.0066327	10403
9540	1246	21836	0.00700935	11128

- Total Test Line Length (pix): sum of the lengths of the family of parallel line segments that comprise the test line,
- Grains Per Test Area (#pix^-2): number of idealized 2-D disks per unit test area (area of a single pixel),
- Total Test Analysis Area (pix^2): area across which the family of parallel test line segments spans. "Grains Per Test Area" multiplied by this "Total Test Analysis Area" should yield the best estimate of the number of grains in the planar image. However, as mentioned in Chapter 6, estimating the number of grains in the RVE can still vary by an order of magnitude so grain counting techniques are not employed here.

APPENDIX D

CALCULATING 3-D TENSOR COEFFICIENTS FROM ORTHOGONAL PLANES

D.1 Contact Tensor

The first example uses a known 3-D vector to illustrate the method for reconstructing the coefficients of a 3-D contact tensor from 2-D directional data. The methodology does not rely on the absolute values of the tensor coefficients. Instead, the relative values of the planar coefficients drive the 3-D reconstruction. Consider the following 3-D contact normal vector defined in rectangular Cartesian coordinates as in Figure 6.4:

$$\bar{n}^{(3\text{-D})} = n_1\hat{i} + n_2\hat{j} + n_3\hat{k} = 0.487\hat{i} + 0.324\hat{j} + 0.811\hat{k}. \tag{D.1}$$

The 3-D contact tensor coefficients of this vector are:

$$F_{ij}^{(3\text{-D})} = \begin{bmatrix} n_1n_1 & n_1n_2 & n_1n_3 \\ n_2n_1 & n_2n_2 & n_2n_3 \\ n_3n_1 & n_3n_2 & n_3n_3 \end{bmatrix} = \begin{bmatrix} 0.237 & 0.158 & 0.395 \\ 0.158 & 0.105 & 0.263 \\ 0.395 & 0.263 & 0.658 \end{bmatrix}. \tag{D.2}$$

It can easily be verified that the trace of this tensor equals one and its principal direction is coincident with $\bar{n}^{(3\text{-D})}$—characteristics consistent with a fabric tensor constructed from only one piece of directional data.

The projections of $\bar{n}^{(3\text{-D})}$ onto the three reference planes defined by the Cartesian coordinates are:

$$\begin{aligned} \bar{n}^{(1\text{-}2)} &= 0.487\hat{i} + 0.324\hat{j}, \\ \bar{n}^{(1\text{-}3)} &= 0.487\hat{i} + 0.811\hat{k}, \\ \bar{n}^{(2\text{-}3)} &= 0.324\hat{j} + 0.811\hat{k}. \end{aligned} \tag{D.3}$$

As in Chapter 6, the superscript defines the 2-D plane on which the vector is defined. The magnitudes of these planar vectors are less than one because they are projections of $\bar{n}^{(3\text{-D})}$. This magnitude information is exactly what is unknown when starting from 2-D images. With planar images the assumption is that the contact normal vectors are unit vectors of magnitude one. This is accomplished here by normalizing the above projections such that their magnitudes equal one. These vectors are representative of 2-D contact normal vectors:

$$\begin{aligned} \bar{n}_{norm}^{(1\text{-}2)} &= 0.833\hat{i} + 0.554\hat{j}, \\ \bar{n}_{norm}^{(1\text{-}3)} &= 0.515\hat{i} + 0.857\hat{k}, \\ \bar{n}_{norm}^{(2\text{-}3)} &= 0.371\hat{j} + 0.929\hat{k}. \end{aligned} \tag{D.4}$$

The 2-D contact tensor coefficients of these vectors are:

$$\begin{aligned} F_{ij-norm}^{(1\text{-}2)} &= \begin{bmatrix} 0.693 & 0.461 \\ 0.461 & 0.307 \end{bmatrix}, \\ F_{ij-norm}^{(1\text{-}3)} &= \begin{bmatrix} 0.265 & 0.441 \\ 0.441 & 0.735 \end{bmatrix}, \\ F_{ij-norm}^{(2\text{-}3)} &= \begin{bmatrix} 0.137 & 0.345 \\ 0.345 & 0.863 \end{bmatrix}. \end{aligned} \tag{D.5}$$

This numerically illustrates the problem with 2-D unit vectors. For example, were the 2-D tensor coefficients calculated from Equations (D.3), both $F_{11}^{(1\text{-}2)}$ and $F_{11}^{(1\text{-}3)}$ would equal 0.487^2, presenting no ambiguity in reconstructing $F_{11}^{(3\text{-D})}$. Equations (D.5) unfortunately do not exhibit this property.

Applying the methodology developed in Chapter 6 (Equation (6.5)) yields the six independent 3-D coefficients. Recall that the algorithm relies on two features: 1) the ratios of 2-D and 3-D tensor coefficients are equivalent, and 2) the trace of the reconstructed 3-D tensor equals one:

$$\begin{bmatrix} 1 & -\left(0.693/0.307\right) & 0 & 0 & 0 & 0 \\ 1 & 0 & -\left(0.265/0.735\right) & 0 & 0 & 0 \\ 0 & 1 & -\left(0.137/0.863\right) & 0 & 0 & 0 \\ -\left(0.461/0.693\right) & 0 & 0 & 1 & 0 & 0 \\ -\left(0.441/0.265\right) & 0 & 0 & 0 & 1 & 0 \\ 0 & -\left(0.345/0.137\right) & 0 & 0 & 0 & 1 \\ 1 & 1 & 1 & 0 & 0 & 0 \end{bmatrix} \begin{Bmatrix} F_{11}^{(3\text{-D})} \\ F_{22}^{(3\text{-D})} \\ F_{33}^{(3\text{-D})} \\ F_{12}^{(3\text{-D})} \\ F_{13}^{(3\text{-D})} \\ F_{23}^{(3\text{-D})} \end{Bmatrix} = \begin{Bmatrix} 0 \\ 0 \\ 0 \\ 0 \\ 0 \\ 0 \\ 1 \end{Bmatrix}, \text{ and} \tag{D.6a}$$

$$\begin{Bmatrix} F_{11}^{(3\text{-D})} \\ F_{22}^{(3\text{-D})} \\ F_{33}^{(3\text{-D})} \\ F_{12}^{(3\text{-D})} \\ F_{13}^{(3\text{-D})} \\ F_{23}^{(3\text{-D})} \end{Bmatrix} = \begin{Bmatrix} 0.237 \\ 0.105 \\ 0.658 \\ 0.158 \\ 0.395 \\ 0.263 \end{Bmatrix}. \tag{D.6b}$$

Equating 2-D and 3-D ratios is permissible because the planar contact normal vectors adequately capture direction—only magnitude is unknown. For example, $\bar{n}^{(1\text{-}2)}$ and $\bar{n}_{norm}^{(1\text{-}2)}$ point in the same direction but differ in magnitude. Another example is presented to reinforce the concepts.

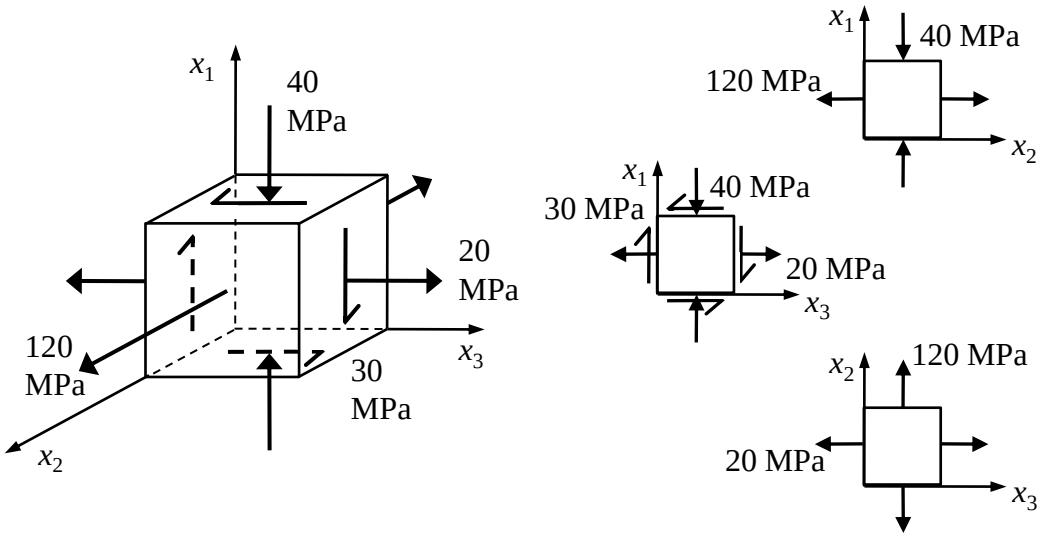


Figure D.1: An example of a possible 3-D state of stress and the associated orthogonal planes in Cartesian coordinates.

D.2 Stress Tensor

This example uses a known 3-D state of stress to illustrate that the method is general and correctly calculates the components of the more familiar stress tensor. The 3-D state of stress in Figure D.1 is defined in rectangular Cartesian coordinates. It is not a principal stress orientation as shearing stress is non-zero. The known coefficients of the 3-D stress tensor $T_{ij}^{(3\text{-D})}$ are

$$T_{ij}^{(3\text{-D})} = \begin{bmatrix} T_{11} & T_{12} & T_{13} \\ T_{21} & T_{22} & T_{23} \\ T_{31} & T_{32} & T_{33} \end{bmatrix}^{(3\text{-D})} = \begin{bmatrix} \text{-40} & 0 & \text{-30} \\ 0 & 120 & 0 \\ \text{-30} & 0 & 20 \end{bmatrix} \text{MPa.} \qquad \text{(D.7)}$$

Because of the symmetry of the 3-D stress tensor there are six independent coefficients. The 2-D coefficients, also MPa, are

$$T_{ij}^{(1-2)} = \begin{bmatrix} \text{-40} & 0 \\ 0 & 120 \end{bmatrix}^{(1-2)},$$
$$T_{ij}^{(1-3)} = \begin{bmatrix} \text{-40} & \text{-30} \\ \text{-30} & 20 \end{bmatrix}^{(1-3)}, \tag{D.8}$$
$$T_{ij}^{(2-3)} = \begin{bmatrix} 120 & 0 \\ 0 & 20 \end{bmatrix}^{(2-3)}.$$

First, the 2-D coefficients are normalized so their first invariant or trace equals the same value on each plane. This is done to draw parallels to the fabric tensor. The trace of each 2-D and 3-D fabric tensor equals one. Similarly, the trace of each 2-D stress tensor is normalized to match the 3-D stress tensor trace, 100 MPa:

$$T_{ij-norm}^{(1-2)} = \begin{bmatrix} \text{-50} & 0 \\ 0 & 150 \end{bmatrix}^{(1-2)},$$
$$T_{ij-norm}^{(1-3)} = \begin{bmatrix} 200 & 150 \\ 150 & \text{-100} \end{bmatrix}^{(1-3)}, \tag{D.9}$$
$$T_{ij-norm}^{(2-3)} = \begin{bmatrix} 85.7 & 0 \\ 0 & 14.3 \end{bmatrix}^{(2-3)}.$$

Normalizing the coefficients does not change any directional information. Because all coefficients are normalized by the same scalar value the principal *directions* of each 2-D tensor remain the same. However, normalizing the coefficients does alter the

principal *values* of each 2-D tensor, recreating the fundamental crux in assembling 3-D fabric tensor coefficients from orthogonal planes.

Note that the value of a coefficient relative to its planar companions also remains fixed. It is this fact—that the ratios of coefficients from any 2-D tensor equal the ratios of their counterparts in the 3-D tensor—that drives the ensuing algorithm. Because of the reliance on only the ratios, normalizing Equation (D.8) is unnecessary in demonstrating the methodology. It is useful only in relating to the nature of the problem in dealing with directional data.

Highlighting the $x_1 - x_3$ plane, the premise behind the reconstruction algorithm relies on the fact that the ratio $\left(T_{11}/T_{33}\right)^{\text{(3-D)}}$ of unknown values is equal to the measured $\left(T_{11}/T_{33}\right)^{(1-3)}$. Similarly, planar off-diagonals obey $\left(T_{13}/T_{11}\right)^{\text{(3-D)}} = \left(T_{13}/T_{11}\right)^{(1-3)}$ and $\left(T_{13}/T_{33}\right)^{\text{(3-D)}} = \left(T_{13}/T_{33}\right)^{(1-3)}$, either of which could be used to solve for the unknown off-diagonal $T_{13}^{\text{(3-D)}}$. As mentioned in Chapter 6, this identically holds true only if the 2-D tensors "fit" well together, a point which is discussed in the main body of this dissertation. The fit is evaluated with Equation (6.9):

$$\left(\frac{\text{-}50}{150}\right)^{(1-2)} \cdot \left(\frac{85.7}{14.3}\right)^{(2-3)} \cdot \left(\frac{\text{-}100}{200}\right)^{(1-3)} = 1, \tag{D.10}$$

indicating that these planar data fit perfectly.

Collecting ratios from three orthogonal planes results in six equations with linear dependence for six unknowns (Equations (6.3)). Consequently, an additional equation is required to create a well-posed linear algebra problem. In the case of fabric tensors this equation arises from the fact that the trace of the 3-D fabric tensor must equal one. Here, the trace of the stress tensors equals 100 MPa. This equation could replace any one of the six linearly dependent equations. In practice, it is added as a seventh equation because the other six equations might not exhibit linear dependence

to working numerical precision due to "fit". The pivot operations involved with seven equations and six unknowns is not computationally difficult for modern computers.

Finally, applying Equation (6.5) results in the six unknown 3-D coefficients:

$$\begin{bmatrix} 1 & -\left({}^{-50}/_{150}\right) & 0 & 0 & 0 & 0 \\ 1 & 0 & -\left({}^{200}/_{-100}\right) & 0 & 0 & 0 \\ 0 & 1 & -\left({}^{85.7}/_{14.3}\right) & 0 & 0 & 0 \\ -\left({}^{0}/_{-50}\right) & 0 & 0 & 1 & 0 & 0 \\ -\left({}^{150}/_{200}\right) & 0 & 0 & 0 & 1 & 0 \\ 0 & -\left({}^{0}/_{85.7}\right) & 0 & 0 & 0 & 1 \\ 1 & 1 & 1 & 0 & 0 & 0 \end{bmatrix} \begin{Bmatrix} T_{11}^{(3\text{-D})} \\ T_{22}^{(3\text{-D})} \\ T_{33}^{(3\text{-D})} \\ T_{12}^{(3\text{-D})} \\ T_{13}^{(3\text{-D})} \\ T_{23}^{(3\text{-D})} \end{Bmatrix} = \begin{Bmatrix} 0 \\ 0 \\ 0 \\ 0 \\ 0 \\ 0 \\ 100 \end{Bmatrix}, \text{ and} \tag{D.11a}$$

$$\begin{Bmatrix} T_{11}^{(3\text{-D})} \\ T_{22}^{(3\text{-D})} \\ T_{33}^{(3\text{-D})} \\ T_{12}^{(3\text{-D})} \\ T_{13}^{(3\text{-D})} \\ T_{23}^{(3\text{-D})} \end{Bmatrix} = \begin{Bmatrix} -40 \\ 120 \\ 20 \\ 0 \\ -30 \\ 0 \end{Bmatrix} \text{MPa}. \tag{D.11b}$$

Obviously in the case of stress this system of equations is unnecessary in arriving at this conclusion. Stress is used simply as an additional example. This approach assumes that the 2-D tensor coefficients are calculated on three orthogonal planes and that—in the case of the diagonals—these measured values "fit" together well. With these assumptions, the algorithm requires: 1) the measured ratios of 2-D tensor coefficients, and 2) a numerical constraint on the first invariant of the resulting 3-D tensor. These data are defined for the contact tensors calculated in this dissertation.

APPENDIX E

MATLAB CODE

E.1 Overview

The MATLAB code is organized as a root level script—mother.m—from which several functions are called. Each of the subsequent sections is an individual file, beginning with the root level script. The heading of each file contains a brief description and purpose of the code. These brief narratives correspond to the methods outlined in Chapter 6. What is not included here are the various input files: the stereological data generated by the software in Edens (1997) and the EHC data presented in Schneebeli and Sokratov (2004).

E.1.1 mother.m

```
%Root level script to read directional data and calculate stereological parameters
clear all
close all
clc

% "flag" used to set the source of directional data:
%   1 = center-to-center angle between connected grains
%   2 = angle of segment identified as bond
%   3 = tangent to the skeleton of the ice structure at the bond site
flag = 1;

sample = 4; %High Density Sample 4 or 6

% Call function that defines grain-to-bond threshold used to generate
% Mike's stereological output files
g_b_sel = GrainBondThresh(sample);

if sample == 4
    endday = 7;
    excp = [7 3];
    idx = 1/6:1/3:23/3;
elseif sample == 6
    endday = 4;
    excp = [2 3];
    idx = 1/6:1/3:15/3;
else
    disp('Error: sample must be either 4 or 6')
    return
end

days = 0:endday;
runs = 1:3;

h = waitbar(0,'Please wait...');
k = 1;
for i = 1:length(days)
    for j = 1:length(runs)
        if days(i) == excp(1) && runs(j) == excp(2)
            k = k + 1;
            continue
        end
        waitbar(i/length(days),h);
        disp(['Day' num2str(days(i)) ' Run' num2str(runs(j))])

        % Generate directional data from Mike Edens stereology output
        %_____________________________________________________________%
        [angle,nbonds,r,rbar(k),harmmn(k),rb3(k),Rbar(k),Rg3(k)] = EdensBondFinder(sample,days
            (i),runs(j),g_b_sel,flag);

        % Estimate Vol Frac of ice from stereology
        %_____________________________________________________________%
```

```
51          phii(k) = StereoPhi(sample,days(i),runs(j),g_b_sel);
52               phiixy(k) = phii(k).xy;
53               phiixz(k) = phii(k).xz;
54               phiiyz(k) = phii(k).yz;
55
56          % Generate 2-D Coord Number from Mike Edens stereology output
57          %_____________________________________________________________%
58          [N2m(k),N2(k),NgVm(k),NgV,NbVm(k)] = TwoDCoordNum(sample,days(i),runs(j),nbonds,harmmn
                (k),g_b_sel);
59               N2xy(k) = N2(k).xy;
60               N2xz(k) = N2(k).xz;
61               N2yz(k) = N2(k).yz;
62
63          % Estimate 3-D Coord Number from Alley, 1986 algorithm
64          %_____________________________________________________________%
65          [N3a(k),N3b(k),Rg3a(k),alpha(k),gamma(k)] = ThreeDCoordNum(N2m(k),rb3(k),Rg3(k),NgVm(k
                ),NbVm(k),phiixy(k));
66
67          % Use directional data, angle and potentially rho, to calculate the
68          % 2-D and 3-D 2nd order contact tensor coefficients and their
69          % associated statistical uncertainty
70          %_____________________________________________________________%
71          [twoD(k), LUnc(k), UUnc(k), C(:,:,k), Unc(:,:,k,:), Ci(:,:,k), Unci(:,:,k,:), ecc,
                eccUnc] = Contact2D3D(angle);
72
73          % Iteratively save 2-D tensor coefficients and bounds
74          %_____________________________________________________________%
75          Bxy(:,:,k) = twoD(k).xy;
76          Bxz(:,:,k) = twoD(k).xz;
77          Byz(:,:,k) = twoD(k).yz;
78               LUncXY(:,:,k) = LUnc(k).xy;
79               UUncXY(:,:,k) = UUnc(k).xy;
80               LUncXZ(:,:,k) = LUnc(k).xz;
81               UUncXZ(:,:,k) = UUnc(k).xz;
82               LUncYZ(:,:,k) = LUnc(k).yz;
83               UUncYZ(:,:,k) = UUnc(k).yz;
84  %          Bxys(:,:,k) = twoDs(k).xy;
85  %          Bxzs(:,:,k) = twoDs(k).xz;
86  %          Byzs(:,:,k) = twoDs(k).yz;
87  %               LUncXYs(:,:,k) = LUncs(k).xy;
88  %               UUncXYs(:,:,k) = UUncs(k).xy;
89  %               LUncXZs(:,:,k) = LUncs(k).xz;
90  %               UUncXZs(:,:,k) = UUncs(k).xz;
91  %               LUncYZs(:,:,k) = LUncs(k).yz;
92  %               UUncYZs(:,:,k) = UUncs(k).yz;
93
94          % Iteratively save Harrigan & Mann's "stretch" factor and bounds
95          %_____________________________________________________________%
96          E(k) = ecc;
97          EUnc(k,:) = eccUnc;
98  %          Es(k) = eccs;
99  %          EUncs(k,:) = eccUncs;
100
101         % Degree of Anistropy to compare with Martin's Data
102         DA(k) = max(diag(C(:,:,k)))/min(diag(C(:,:,k)));
103              if max(diag(C(:,:,k))) == C(1,1,k) || max(diag(C(:,:,k))) == C(2,2,k)
104                   mrkr(k) = false;
105              else
106                   mrkr(k) = true;
107              end
108         % Degree of Anistropy to compare with Martin's Data
109 %          DAs(k) = max(diag(Cs(:,:,k)))/min(diag(Cs(:,:,k)));
110 %               if max(diag(Cs(:,:,k))) == Cs(1,1,k) || max(diag(Cs(:,:,k))) == Cs(2,2,k)
111 %                    mrkrs(k) = false;
112 %               else
113 %                    mrkrs(k) = true;
114 %               end
115
116         k = k + 1;
117     end
118 end
119
120 close(h)
121
122 % filename = 'HDS4_Fabric_Mike0_4new3D';
123 % save(filename, 'C', 'Calt', 'Unc');
124
125 %Plots
126 %_____________________________________________________________________%
127 % Scalar thermal conductivity parameters
128 % Solid Volume Fraction
129 figure
130 plot(idx,phiixy,'ko','MarkerSize',4); grid
131 yl = ylabel('Solid Volume Fraction (-)');
132 xl = xlabel('Days from Experiment Start');
133 set([yl xl],'FontName','Times New Roman','FontSize',11)
134 axis([0 (endday+1) 0.3 0.5])
```

```
135
136 % 3-D Coordination Number
137 figure
138 plot(idx,N3a,'ko','MarkerSize',4); grid
139 yl = ylabel('Mean 3-D Coordination Number (-)');
140 xl = xlabel('Days from Experiment Start');
141 set([yl xl],'FontName','Times New Roman','FontSize',11)
142 axis([0 (endday+1) 2.6 3.6])
143
144 % Bond and Grain Radii
145 figure
146 ax(1) = subplot(1,3,1);
147 plot(idx,rb3*36,'ko','MarkerSize',4); grid
148 axis([0 (endday+1) 95 110])
149 yl(1) = ylabel('\rho: Mean 3-D Bond Radius (\mum)');
150 ax(2) = subplot(1,3,2);
151 plot(idx,Rg3*36,'ko','MarkerSize',4); grid
152 axis([0 (endday+1) 165 185])
153 yl(2) = ylabel('R: Mean 3-D Grain Radius (\mum)');
154 xl = xlabel('Days from Experiment Start');
155 ax(3) = subplot(1,3,3);
156 plot(idx,rb3./Rg3,'ko','MarkerSize',4); grid
157 axis([0 (endday+1) 0.52 0.64])
158 yl(3) = ylabel('Mean 3-D Bond-to-Grain Ratio (-)');
159 set([yl xl],'FontName','Times New Roman','FontSize',11)
160 set(ax,'FontName','Times New Roman','FontSize',11)
161 %_____________________________________________________________________________%
162
163
164 % 2-D tensor coefficients and bounds: DIAGONALS
165 figure
166 ax(1) = subplot(1,3,1); hold on
167 errorbar(idx,Bxy(1,1,:),Bxy(1,1,:)-LUncXY(1,1,:),UUncXY(1,1,:)-Bxy(1,1,:),'rsquare','
      MarkerSize',4)
168 errorbar(idx,Bxy(2,2,:),Bxy(2,2,:)-LUncXY(2,2,:),UUncXY(2,2,:)-Bxy(2,2,:),'gdiamond','
      MarkerSize',5)
169 yl = ylabel('2-D Tensor Diagonals (-)');
170 set(yl,'FontName','Times New Roman','FontSize',11)
171 % xlabel('Days from Experiment Start')
172 legend('\it{x}\rm{_2}', '\it{x}\rm{_3}'); grid, box on
173 axis([0 (endday+1) 0.35 0.75])
174
175 ax(2) = subplot(1,3,2); hold on
176 errorbar(idx,Bxz(2,2,:),Bxz(2,2,:)-LUncXZ(2,2,:),UUncXZ(2,2,:)-Bxz(2,2,:),'bo','MarkerSize',4)
177 errorbar(idx,Bxz(1,1,:),Bxz(1,1,:)-LUncXZ(1,1,:),UUncXZ(1,1,:)-Bxz(1,1,:),'rsquare','
      MarkerSize',4)
178 % ylabel('x_1-x_2 Diagonals')
179 xl = xlabel('Days from Experiment Start');
180 set(xl,'FontName','Times New Roman','FontSize',11)
181 legend('\it{x}\rm{_1}', '\it{x}\rm{_2}'); grid, box on
182 axis([0 (endday+1) 0.35 0.75])
183
184 ax(3) = subplot(1,3,3); hold on
185 errorbar(idx,Byz(2,2,:),Byz(2,2,:)-LUncYZ(2,2,:),UUncYZ(2,2,:)-Byz(2,2,:),'bo','MarkerSize',4)
186 errorbar(idx,Byz(1,1,:),Byz(1,1,:)-LUncYZ(1,1,:),UUncYZ(1,1,:)-Byz(1,1,:),'gdiamond','
      MarkerSize',5)
187 % ylabel('x_1-x_3 Diagonals')
188 % xlabel('Days from Experiment Start')
189 legend('\it{x}\rm{_1}', '\it{x}\rm{_3}'); grid, box on
190 axis([0 (endday+1) 0.35 0.75])
191 set(ax,'FontName','Times New Roman','FontSize',11)
192
193 % 2-D tensor coefficients and bounds: DIAGONALS ROTATED & STRETCHED
194 % figure
195 % ax(1) = subplot(1,3,1); hold on
196 % errorbar(idx,Bxys(1,1,:),Bxys(1,1,:)-LUncXYs(1,1,:),UUncXYs(1,1,:)-Bxys(1,1,:),'rsquare','
      MarkerSize',4)
197 % errorbar(idx,Bxys(2,2,:),Bxys(2,2,:)-LUncXYs(2,2,:),UUncXYs(2,2,:)-Bxys(2,2,:),'gdiamond','
      MarkerSize',5)
198 % ylabel('2-D Tensor Diagonals: Rot & Str'),
199 % % xlabel('Days from Experiment Start')
200 % legend('x_2', 'x_3'), grid
201 % axis([0 (endday+1) 0.3 0.7])
202 %
203 % ax(2) = subplot(1,3,2); hold on
204 % errorbar(idx,Bxzs(2,2,:),Bxzs(2,2,:)-LUncXZs(2,2,:),UUncXZs(2,2,:)-Bxzs(2,2,:),'bo','
      MarkerSize',4)
205 % errorbar(idx,Bxzs(1,1,:),Bxzs(1,1,:)-LUncXZs(1,1,:),UUncXZs(1,1,:)-Bxzs(1,1,:),'rsquare','
      MarkerSize',4)
206 % % ylabel('x_1-x_2 Diagonals: Rot & Str')
207 % xlabel('Days from Experiment Start')
208 % legend('x_1', 'x_2'), grid
209 % axis([0 (endday+1) 0.3 0.7])
210 %
211 % ax(3) = subplot(1,3,3); hold on
212 % errorbar(idx,Byzs(2,2,:),Byzs(2,2,:)-LUncYZs(2,2,:),UUncYZs(2,2,:)-Byz(2,2,:),'bo','
      MarkerSize',4)
```

```
% errorbar(idx,Byzs(1,1,:),Byzs(1,1,:)-LUncYZs(1,1,:),UUncYZs(1,1,:)-Byz(1,1,:),'gdiamond','MarkerSize',5)
% % ylabel('x_1-x_3 Diagonals: Rot & Str')
% % xlabel('Days from Experiment Start')
% legend('x_1', 'x_3'), grid
% axis([0 (endday+1) 0.3 0.7])
%_____________________________________________________________________%

% 2-D tensor coefficients and bounds: OFF-DIAGONALS
figure
ax(1) = subplot(1,3,1); hold on
errorbar(idx,Bxy(1,2,:),Bxy(1,2,:)-LUncXY(1,2,:),UUncXY(1,2,:)-Bxy(1,2,:),'ko','MarkerSize',4)
yl = ylabel('2-D Tensor Off-Diagonals (-)');
set(yl,'FontName','Times New Roman','FontSize',11)
% xlabel('Days from Experiment Start')
legend('\it{x}\rm{_2_3}'); grid, box on
axis([0 (endday+1) -0.1 0.1])

ax(2) = subplot(1,3,2); hold on
errorbar(idx,Bxz(1,2,:),Bxz(1,2,:)-LUncXZ(1,2,:),UUncXZ(1,2,:)-Bxz(1,2,:),'ko','MarkerSize',4)
% ylabel('x_1-x_2 Off-Diagonal')
xl = xlabel('Days from Experiment Start');
set(xl,'FontName','Times New Roman','FontSize',11)
legend('\it{x}\rm{_1_2}'); grid, box on
axis([0 (endday+1) -0.1 0.1])

ax(3) = subplot(1,3,3); hold on
errorbar(idx,Byz(1,2,:),Byz(1,2,:)-LUncYZ(1,2,:),UUncYZ(1,2,:)-Byz(1,2,:),'ko','MarkerSize',4)
% ylabel('x_1-x_3 Off-Diagonal')
% xlabel('Days from Experiment Start')
legend('\it{x}\rm{_1_3}'); grid, box on
axis([0 (endday+1) -0.1 0.1])
set(ax,'FontName','Times New Roman','FontSize',11)

% 2-D tensor coefficients and bounds: ROTATED & STRETCHED OFF-DIAGONALS
% figure
% ax(1) = subplot(1,3,1); hold on
% errorbar(idx,Bxys(1,2,:),Bxys(1,2,:)-LUncXYs(1,2,:),UUncXYs(1,2,:)-Bxys(1,2,:),'rsquare','MarkerSize',4)
% ylabel('x_2-x_3 Off-Diagonal: Rot & Str')
% xlabel('Days from Experiment Start')
% legend('x_2_3'), grid
% axis([0 (endday+1) -0.1 0.1])
%
% ax(2) = subplot(1,3,2); hold on
% errorbar(idx,Bxzs(1,2,:),Bxzs(1,2,:)-LUncXZs(1,2,:),UUncXZs(1,2,:)-Bxzs(1,2,:),'bo','MarkerSize',4)
% ylabel('x_1-x_2 Off-Diagonal: Rot & Str')
% xlabel('Days from Experiment Start')
% legend('x_1_2'), grid
% axis([0 (endday+1) -0.1 0.1])
%
% ax(3) = subplot(1,3,3); hold on
% errorbar(idx,Byzs(1,2,:),Byzs(1,2,:)-LUncYZs(1,2,:),UUncYZs(1,2,:)-Byzs(1,2,:),'gdiamond','MarkerSize',5)
% ylabel('x_1-x_3 Off-Diagonal: Rot & Str'),
% xlabel('Days from Experiment Start')
% legend('x_1_3'), grid
% axis([0 (endday+1) -0.1 0.1])
%_____________________________________________________________________%

% Harrigan & Mann "stretch" factor and bounds
figure
errorbar(idx,E',E'-EUnc(:,1),EUnc(:,2)-E','ko','MarkerSize',4), hold on
plot(0:k/3,ones(1,length(0:k/3)),'b--')
xl = xlabel('Days from Experiment Start');
set(xl,'FontName','Times New Roman','FontSize',11)
yl = ylabel('"fit"');
set(yl,'Fontname','Times New Roman','FontSize',11)
legend('Planar Fit','Ideal','Location','Northwest')
axis([0 (endday+1) 0.3 1.7])
set(gca,'Fontname','Times New Roman','FontSize',11)
% figure
% errorbar(idx,Es',Es'-EUncs(:,1),EUncs(:,2)-Es','bo'), hold on
% plot(0:k/3,ones(1,length(0:k/3)),'r-')
% legend('Stretched','Ideal')
% axis([0 (endday+1) 0.3 1.7])
%_____________________________________________________________________%

% 3-D tensor diagonals and bounds
figure
errorbar(idx,C(3,3,:),C(3,3,:)-Unc(3,3,:,1),Unc(3,3,:,2)-C(3,3,:),'bo','MarkerSize',4), hold on
errorbar(idx,C(1,1,:),C(1,1,:)-Unc(1,1,:,1),Unc(1,1,:,2)-C(1,1,:),'rsquare','MarkerSize',4), hold on
errorbar(idx,C(2,2,:),C(2,2,:)-Unc(2,2,:,1),Unc(2,2,:,2)-C(2,2,:),'gdiamond','MarkerSize',5)
grid, axis([0 (endday+1) 0.2 0.5])
```

```
yl = ylabel('3-D Tensor Diagonals (-)');
set(yl,'Fontname','Times New Roman','FontSize',11)
xl = xlabel('Days from Experiment Start');
set(xl,'Fontname','Times New Roman','FontSize',11)
legend('\it{x}\rm{_1}','\it{x}\rm{_2}','\it{x}\rm{_3}','Location','NorthWest','Orientation','horizontal')
set(gca,'Fontname','Times New Roman','FontSize',11)

% 3-D tensor diagonals and bounds: idealized transversely isotropic
% symmetry
figure
errorbar(idx,Ci(3,3,:),Ci(3,3,:)-Unci(3,3,:,1),Unci(3,3,:,2)-Ci(3,3,:),'bo','MarkerSize',4), hold on
errorbar(idx,Ci(1,1,:),Ci(1,1,:)-Unci(1,1,:,1),Unci(1,1,:,2)-Ci(1,1,:),'rsquare','MarkerSize',4), hold on
errorbar(idx,Ci(2,2,:),Ci(2,2,:)-Unci(2,2,:,1),Unci(2,2,:,2)-Ci(2,2,:),'gdiamond','MarkerSize',5)
grid, axis([0 (endday+1) 0.2 0.5])
yl = ylabel('3-D Tensor Diagonals (-): Idealized');
xl = xlabel('Days from Experiment Start');
set([yl xl],'Fontname','Times New Roman','FontSize',11)
legend('\it{x}\rm{_1}','\it{x}\rm{_2}','\it{x}\rm{_3}','Location','NorthWest')
set(gca,'Fontname','Times New Roman','FontSize',11)
%_____________________________________________________________________________%

% 3-D tensor off-diagonals and bounds
figure
ax(1) = subplot(1,3,1); hold on
errorbar(idx,Ci(1,2,:),Ci(1,2,:)-Unci(1,2,:,1),Unci(1,2,:,2)-Ci(1,2,:),'ko','MarkerSize',4)
yl = ylabel('3-D Tensor Off-Diagonals (-)');
legend('\it{x}\rm{_2_3}'); grid, box on
axis([0 (endday+1) -0.1 0.1])

ax(2) = subplot(1,3,2); hold on
errorbar(idx,Ci(1,3,:),Ci(1,3,:)-Unci(1,3,:,1),Unci(1,3,:,2)-Ci(1,3,:),'ko','MarkerSize',4)
xl = xlabel('Days from Experiment Start');
legend('\it{x}\rm{_1_2}'); grid, box on
axis([0 (endday+1) -0.1 0.1])

ax(3) = subplot(1,3,3); hold on
errorbar(idx,Ci(2,3,:),Ci(2,3,:)-Unci(2,3,:,1),Unci(2,3,:,2)-Ci(2,3,:),'ko','MarkerSize',4)
legend('\it{x}\rm{_1_3}'); grid, box on
axis([0 (endday+1) -0.1 0.1])
set([yl xl],'Fontname','Times New Roman','FontSize',11)
set(ax,'FontName','Times New Roman','FontSize',11)
%_____________________________________________________________________________%

% Degree of Anisotropy: derived (from above) and reported (Swiss CT)
if sample ==4
    figure
    plot(1/6+[0 2],[1.17 1.07],'rsquare','MarkerSize',4), hold on
    plot(idx(~mrkr),DA(~mrkr),'bo','MarkerSize',4)
    plot(1/6+[4 6],[1.12 1.12],'rsquare','MarkerFaceColor','r','MarkerSize',4)
    plot(idx(mrkr),DA(mrkr),'bo','MarkerFaceColor','b','MarkerSize',4)
    grid, axis([0 (endday+1) 0.6 1.8])
    yl = ylabel('Degree of Anisotropy (-)');
    xl = xlabel('Days from Experiment Start');
    legend('Schneebeli and Sokratov (2004)-Horizontal','Derived from Contact Tensor-Horizontal',...
        'Schneebeli and Sokratov (2004)-Vertical','Derived from Contact Tensor-Vertical')
    set([yl xl],'Fontname','Times New Roman','FontSize',11)
    set(gca,'FontName','Times New Roman','FontSize',11)
else
    figure
    plot(idx(~mrkr),DA(~mrkr),'bo','MarkerSize',4), hold on
    plot(idx(mrkr),DA(mrkr),'bo','MarkerFaceColor','b','MarkerSize',4)
    grid, axis([0 (endday+1) 0.6 1.8])
    yl = ylabel('Degree of Anisotropy (-)');
    xl = xlabel('Days from Experiment Start');
    legend('Derived from Contact Tensor-Horizontal','Derived from Contact Tensor-Vertical')
    set([yl xl],'Fontname','Times New Roman','FontSize',11)
    set(gca,'FontName','Times New Roman','FontSize',11)
end
%_____________________________________________________________________________%

SwissKFunc(C,Unc(:,:,:,1),Unc(:,:,:,2),alpha,N3a,sample,phiixy);

%EOF
```

E.1.2 GrainBondThresh.m

```
function g_b_sel = GrainBondThresh(sample)
%This function defines the grain-to-bond threshold that was used in
%generating the stereological input data. Currently, Sample 4 was run with
%a 0.90 ratio and Sample 6 was run with a 0.75. The results seem
%insensitive to the treshold. The various images could be completely re-run
%for different thresholds.

%"g_b_opt" - data produced for 3 different stereology thresholds
g_b_opt = [50 75 90];

if sample == 4
    g_b_flag = 3;
elseif sample == 6
    g_b_flag = 2;
else
    disp('Error: sample must be either 4 or 6')
    return
end

g_b_sel = g_b_opt(g_b_flag);
end

%EOF
```

E.1.3 EdensBondFinder.m

```
function [dirdata, nbonds, r, rbar, m, rbar3, Rbar, Rbar3] = EdensBondFinder(samp,d,r,g_b,flag
    )
% this function reads data generated by Mike Eden's software specific to
% the grains and bonds. The information is used to estimate grain and bond
% sizes and to build arrays of directional data to calculate contact tensor
% coefficients.

theta.xy = [];
theta.xz = [];
theta.yz = [];
d2r = pi/180;

fn = fieldnames(theta);
n = length(fn);

for m = 1:n
    % Read files of stereological data generated by Mike Eden's S/W
    fid = fopen(['M:\Research\SnowModeling\GranularFabric\MATLAB\Dissertation\Text Files\',
        num2str(samp),'Day'...
        ,num2str(d),'_',num2str(r),'_',fn{m},num2str(g_b),'_8.txt'], 'r');
    hdr = textscan(fid, '%s %s %s %s %s %s %s %s %s %s %s %s',1); % scans first row
    bonds = textscan(fid, '%f %f %f %f %f %f %f %f %f %f %f %f'); % scans the numbers
    fclose(fid);

    % Build data structure of output
    for i = 1:length(hdr);
        idx = strfind(hdr{i},'(');
        data.(hdr{i}{1}(1:idx{1}-1)) = bonds{i};
    end

    %_____________________________________________________________________%
    % #1 Source of Directional Data: center-to-center angle of connected
    % grains
    %_____________________________________________________________________%
    dely = data.g2y - data.g1y; %grain 2 - grain1 centers (y-coords)
    delx = data.g2x - data.g1x; %grain 2 - grain1 centers (x-coords)
    Theta_c = atan(dely./delx);

    % Remove NaN from resulting directional data
    Theta_c = Theta_c(~isnan(Theta_c));
    bond_rad_c = data.rb(~isnan(Theta_c));

    % Process data
    for i = 1:length(Theta_c)
        if Theta_c(i) > pi || Theta_c(i) < 0
            % 1) Theta's in I and IV quadrants - transpose IV to II
            Theta_c(i) = Theta_c(i) + pi;
        end
    end

```

```
    %_____________________________________________________________________%
    % #2 Source of Directional Data: "rb_angle" directly from stereology
    % output file. It is the angle of the segment identified as a bond
    % ("rb") w.r.t. the reference axes
    %_____________________________________________________________________%
    % Retain only bonds greater than 1 pixel in length - can't form a line,
    % and therefore angle, with only 1 point!

%     numbonds.(fn{m}) = length(data.rb); %tally bonds before indexing
    idx2 = data.rb > 1;
    Theta_alt = d2r*data.rb_angle(idx2);
    numbonds.(fn{m}) = length(data.rb(idx2)); %tally bonds after indexing

    %_____________________________________________________________________%
    % #3 Source of Directional Data: "skeltonTangent" directly from
    % stereology output file. It is the tangent to the skeletonized ice
    % structure in the neighborhood of the identified bond "rb"
    %_____________________________________________________________________%
    Theta = d2r*data.skeltonTangent(idx2);

    % Process data
    for i = 1:length(Theta)
        if Theta(i) > pi || Theta(i) < 0
            % 1) Theta's in I and IV quadrants - transpose IV to II
            Theta(i) = Theta(i) + pi;
        end
        if Theta(i) > 2*pi
            % 2) large Theta's (10^4) should be 90 degrees
            Theta(i) = pi/2;
        end
    end

    %_____________________________________________________________________%
    % Define a vector of 2-D bond radii and 2-D grain radii
    bond_rad = data.rb(idx2);
    grain_rad = [data.rg1(idx2); data.rg2(idx2)];

    %_____________________________________________________________________%
    % Store planar data in a structure
    theta.(fn{m}) = Theta;
    theta_alt.(fn{m}) = Theta_alt;
    theta_c.(fn{m}) = Theta_c;
    % rho and rho_c are from the same "rb" data, just indexed differently
    % so their size matches their corresponding directional data vectors
    rho.(fn{m}) = bond_rad;
    rho_c.(fn{m}) = bond_rad_c;
    R.(fn{m}) = grain_rad;

end

if flag == 1
    dirdata = theta_c;
    r = rho_c;
    nbonds = numbonds;
elseif flag == 2
    dirdata = theta_alt;
    r = rho;
    nbonds = numbonds;
elseif flag == 3
    dirdata = theta;
    r = rho;
    nbonds = numbonds;
else
    disp('dir data flag out of bounds')
    dirdata = [];
end

% Arithmetic Mean 2-D bond radius
rbar = mean([rho.xy; rho.xz; rho.yz]);
% Harmonic Mean 2-D bond radius
m = harmmean([2*rho.xy; 2*rho.xz; 2*rho.yz]);
% Estimate of 3-D bond radius
rbar3 = pi/4*m; % Edens & Brown, 1991
% Arithmetic Mean 2-D grain radius
Rbar = mean([R.xy; R.xz; R.yz]);
% Estimate of 3-D grain radius
Rbar3 = 4*Rbar/pi; % Alley, 1986

%EOF
```

E.1.4 StereoPhi.m

```
function phii = StereoPhi(samp,d,r,gb)
%this function calculates the solid volume fraction of the solid
%constituent in a 2-D binary image. The only constraint is that the images
%used to calculate phi should be known isotropic arrangements.

phii.xy = [];
phii.xz = [];
phii.yz = [];

fn = fieldnames(phii);
n = length(fn);

for m = 1:n
    % Read files of stereological data generated by Mike Eden's S/W
    fid = fopen(['M:\Research\SnowModeling\GranularFabric\MATLAB\Dissertation\Text Files\
        Stereo\',num2str(samp),'Day'...
        ,num2str(d),'_',num2str(r),'_MIL',fn{m},num2str(gb),'_8.txt'], 'r');
    data = textscan(fid, '%f %f %f %f %f','HeaderLines',1); % scans the numbers
    fclose(fid);

    % Save cell arrays
    TotIntL = data{1}; %Total Intercept Length (pixels)
    TotLnL = data{3}; %Total Line Probe Length (pixels)

    % If the microstructure is isotropic - which the xy plane is as close as
    % it's going to get - then vol fraction is equal to line fraction
    temp = TotIntL./TotLnL;
    phii.(fn{m}) = mean(temp);
end
end

%EOF
```

E.1.5 TwoDCoordNum.m

```
function [N2m,N2,NgVm,NgV,NbVm] = TwoDCoordNum(samp,d,r,numbonds,harmmn,g_b)
%this function calculates the mean 2-D coordination number based on
%connectivity information generated by Mike Eden's software. The
%"alternate" method uses a grain counting technique to estimate mean number
%of bonds per grain by counting the total number of grains in the planar
%images. This was not pursued as the resulting 3-D coordination number was
%in the twenties - much too high to be realistic. The code is included in
%case grain counting techniques are improved.

N2.xy = [];
N2.xz = [];
N2.yz = [];

fn = fieldnames(N2);
n = length(fn);

for m = 1:n
    % Read files of stereological data generated by Mike Eden's S/W
    fid = fopen(['M:\Research\SnowModeling\GranularFabric\MATLAB\Dissertation\Text Files\N\',
        num2str(samp),'Day'...
        ,num2str(d),'_',num2str(r),'_N',fn{m},num2str(g_b),'_8.txt'], 'r');
    hdr = textscan(fid, '%s %s %s %s %s %s %s %s %s',1); % scans first row
    stereo = textscan(fid, '%f %f %f %f %f %f %f %f %f'); % scans the numbers
    stereo = cell2mat(stereo);
    fclose(fid);

    % Find totals for each column
    numgrains = sum(stereo,1);
    w = numgrains(2:end)/numgrains(1);

    for i = 2:length(hdr);
        cnct(i-1) = str2double(hdr{i}{1});
    end
    N = sum(w.*cnct);

%     numg.(fn{m}) = numgrains(1);
    N2.(fn{m}) = N;

    %_____________________________________________________________________%
    % Alternate Stereology Method: relies on a grain counting technique
    % Read files of stereological data generated by Mike Eden's S/W
```

```
    fid = fopen(['M:\Research\SnowModeling\GranularFabric\MATLAB\Dissertation\Text Files\
        Stereo\',num2str(samp),'Day'...
        ,num2str(d),'_',num2str(r),'_MIL',fn{m},num2str(g_b),'_8.txt'], 'r');
    data = textscan(fid, '%f %f %f %f %f','HeaderLines',1); % scans the numbers
    fclose(fid);

    % Save cell arrays
    TotIntL = data{1}; %Total Intercept Length (pixels)
    NumGInt = data{2}; %Number of Grains Intercepted (#)
    TotLnL = data{3}; %Total Line Probe Length (pixels)
    NgA = data{4}; %Num of Grains Intc'd per Unit Test Area (#/pix^2)
    Atot = data{5}; %Total Test Analysis Area (pix^2)
    % Derived Quantities
    NgL = NumGInt./TotLnL;
    NgVvec = (NgA.^2)./NgL;
    NgV.(fn{m}) = mean(NgVvec); %Num of Grains per Unit Vol - mean value from all considered
        planes
    % Derive NbV as well
    NbA = numbonds.(fn{m})/length(Atot); % mean # bonds per plane
    NbA = NbA/(1.4*mean(Atot)); % mean # bonds per area - amplify test analysis area by 1.4 to
        account for cropping that Mike does
    NbV.(fn{m}) = 8*harmmn*NbA/(pi^2); % Fullman (1953)

end

N2m = mean([N2.xy N2.xz N2.yz]);
NgVm = mean([NgV.xy NgV.xz NgV.yz]);
NbVm = mean([NbV.xy NbV.xz NbV.yz]);

%EOF
```

E.1.6 ThreeDCoordNum.m

```
function [N3a,N3b,R,alpha,gamma] = ThreeDCoordNum(N2,r,Rm,NgV,NbV,phii)
%this function uses the algorithm of Alley, 1986 to estimate 3-D
%coordination number from 2-D coordination number and the estimated 3-D
%bond-to-grain radius ratio

% set flag to determine source of grain radius estimate
%   Gflag = 1: estimate from fixed vol frac (phii) and num dens of grains (NgV)
%   Gflag = 2: estimate from arithmetic mean (Edens_Bond_Finder.m)
Gflag = 2;

% Calculate Ralt based on vol frac of spheres
Ralt = (phii*3/4/pi/NgV)^(1/3);

% Set grain radius
if Gflag == 1
    R = Ralt;
elseif Gflag == 2
    R = Rm;
else
    disp('Grain Flag set out of bounds')
    return
end

% Calculate mean 3-D bond-to-grain ratio
alpha = r/R;
alpha_p = alpha/sqrt(1+alpha^2);

% Apply Alley, 1986 algorithm for estimating 3-D Coord #
gamma_ins = pi*alpha/4;
gamma_tan = pi*alpha_p/4;
gamma = (gamma_ins + gamma_tan)/2;
N3a = N2/gamma;

% Apply Hansen/Edens algorithm for estimating 3-D Coord #
N3b = 2*NbV/NgV;

end

%EOF
```

E.1.7 Contact2D3D.m

```
function [N2, LUnc, UUnc, threeD, Unc, threeDi, Unci, ecc, eccUnc] = Contact2D3D(theta)
% CONTACT2D3D calculates the 2-D & 3-D 2nd order contact tensors
%_____________________________________________________________________________
% SYNTAX:
%   [N2, threeD, Unc] = Contact2D3Dnew(theta);
%
% INPUTS:
%   theta - structure array with 3 fields, one for each orthogonal plane:
%       theta.xy, theta.xz, theta.yz
%       * each field must be a COLUMN vector for the resampling statistical
%       method (bootstrap) to work
%       theta's are unit vector angles from [0, pi] radians
%
% OUTPUTS:
%   N2 - structure array with 3 fields, one for each orthogonal plane:
%       N2.xy, N2.xz, N2.yz
%       * each field is a 2x2 array of the contact tensor coefficients for
%       that plane
%   LUnc/UUnc - lower and upper bounds of the 95% confidence intervals
%   calculated from the resampled 2-D coefficients
%   threeD - 3x3 array of the 3-D contact tensor coefficients
%   Unc - 3x3x2 array of the upper and lower bounds of the 95% confidence
%   interval on the contact tensor coefficients in "threeD"
%   threeDi/Unci - same as above but related instead to the idealized data
%   that assumes a perfect transversely isotropic textural symmetry
%   ecc/eccUnc - the "fit" factor of the 2-D contact tensor coefficients
%   and their associated uncertainties. From Harrigan & Mann, 1984.
%
%This function is organized as:
%   1) Initialize variables
%
%   2) Build 2nd order Contact Tensors (both 2D and 3D) from directional
%   data. Resample the given input data to develop confidence intervals
%   (bootstrap method).
%
%   3) Build 2nd order Contact Tensors (both 2D and 3D) from directional
%   data. Calculate from complete data set to get expected values.
%
%   4) Calculate deviatoric parts of 2nd and 4th order contact tensors. A
%   comparison of these via a hypothesis test estimates the significance of
%   the 4th order coefficients in estimating the PDF of the directional
%   data.
%
%   5) Executes the hypothesis test from Kanatani, 1984. The test returns
%   the critical test statistic (zc) as well as the test statistics
%   associated with the 2nd and 4th order coefficients.

%_____________________________________________________________________________%
% 1) Initialize variables
%_____________________________________________________________________________%

fn = fieldnames(theta); %store "xy" "xz" and "yz" strings
n = length(fn);
N = 0; %initialize total observations in all three planes
nboot = 1000; %number of resampling iterations for confidence intervals
D3 = zeros(3,3,nboot); %initialize confidence interval array

%_____________________________________________________________________________%
% 2) Build confidence intervals on resampled data
%_____________________________________________________________________________%
for i = 1:nboot
    % resample directional data before calculating tensor coefficients
    for m = 1:n
        angle.(fn{m}) = randsample(theta.(fn{m}),length(theta.(fn{m})),true);
    end

    % calculate 2-D tensor coefficients and for each bootstrap iteration
    % save tensor coefficients from orthogonal planes -- used to build
    % confidence intervals
    [N2, N4, W] = CT2D(angle,fn,n,N);
    XY(:,:,i) = N2.xy;
    XZ(:,:,i) = N2.xz;
    YZ(:,:,i) = N2.yz;

    % Calculate quantity relating diagonal values of 2-D arrays
    ecc(i) = N2.xy(1,1)*N2.yz(1,1)*N2.xz(2,2)/N2.xy(2,2)/N2.yz(2,2)/N2.xz(1,1);

    % Call function to rotate 2-D orthogonal planes into principal
    % orientation within a specified tolerance
%     N2r = Principal(N2);

    % Call function that stretches 2-D planes, forcing "ecc" == 1
%     N2s = stretch(N2r,ecc(i));
%     XYs(:,:,i) = N2s.xy;
```

```
%     XZs(:,:,i) = N2s.xz;
%     YZs(:,:,i) = N2s.yz;

    % Calculate quantity relating diagonal values of 2-D arrays
%     eccs(i) = N2s.xy(1,1)*N2s.yz(1,1)*N2s.xz(2,2)/N2s.xy(2,2)/N2s.yz(2,2)/N2s.xz(1,1);

    % For raw set of 2-D orthogonal fabric tensors, calculate the
    % corresponding 3-D tensor coefficients
    threeD = two2three(N2);
    D3(:,:,i) = threeD;

    % For rotated and stretched set of 2-D coefficients, calculate the
    % corresponding 3-D tensor coefficients
%     threeDs = two2three(N2s);
%     D3s(:,:,i) = threeDs;

    % For ideally transversely isotropic 2-D fabric tensors, calculate the
    % correseponding 3-D tensor coefficients
    threeDi = two2threeideal(N2);
    D3i(:,:,i) = threeDi;

end

% Calculate the 95% confidence intervals on the resampled coefficients
UncXY = prctile(XY,[5 95],3);
    LUnc.xy = UncXY(:,:,1);
    UUnc.xy = UncXY(:,:,2);
UncXZ = prctile(XZ,[5 95],3);
    LUnc.xz = UncXZ(:,:,1);
    UUnc.xz = UncXZ(:,:,2);
UncYZ = prctile(YZ,[5 95],3);
    LUnc.yz = UncYZ(:,:,1);
    UUnc.yz = UncYZ(:,:,2);
Unc = prctile(D3,[5 95],3);
Unci = prctile(D3i,[5 95],3);

% Calculated the 95% C.I. on the rotated & stretched coefficients
% UncXYs = prctile(XYs,[5 95],3);
%     LUncs.xy = UncXYs(:,:,1);
%     UUncs.xy = UncXYs(:,:,2);
% UncXZs = prctile(XZs,[5 95],3);
%     LUncs.xz = UncXZs(:,:,1);
%     UUncs.xz = UncXZs(:,:,2);
% UncYZs = prctile(YZs,[5 95],3);
%     LUncs.yz = UncYZs(:,:,1);
%     UUncs.yz = UncYZs(:,:,2);
% Uncs = prctile(D3s,[5 95],3);

eccUnc = prctile(ecc,[5 95]);
% eccUncs = prctile(eccs,[5 95]);

%-------------------------------------------------------------------------%
% 3) Calculate expected tensor coefficients from complete data set
%-------------------------------------------------------------------------%
% Call function again to calcualte tensor coefficients for entire given
% data set (i.e., not resampled)
[N2, N4, W] = CT2D(theta,fn,n,N);
ecc = N2.xy(1,1)*N2.yz(1,1)*N2.xz(2,2)/N2.xy(2,2)/N2.yz(2,2)/N2.xz(1,1);
% N2r = Principal(N2);
% N2s = stretch(N2r,ecc);
% eccs = N2s.xy(1,1)*N2s.yz(1,1)*N2s.xz(2,2)/N2s.xy(2,2)/N2s.yz(2,2)/N2s.xz(1,1);
threeD = two2three(N2);
% threeDs = two2three(N2s);
threeDi = two2threeideal(N2);

%-------------------------------------------------------------------------%
% 4) Calculate Deviatoric part of Contact Tensors - required for N2 vs N4
%-------------------------------------------------------------------------%
[D2,D4] = MnDev(N2,N4,fn,n);

%-------------------------------------------------------------------------%
% 5) Convergence of Series approximations - Statistical Check
%-------------------------------------------------------------------------%
alpha = 0.05;   %Significance of test - "95%"
[zc,z2,z4] = ConvgTest(W,2,D2,D4,alpha,fn,n);

%-------------------------------------------------------------------------%
function [N2, N4, W] = CT2D(theta,fn,n,N)
% Function builds Contact Tensor Coefficients
% Based on average of tensor products
%-------------------------------------------------------------------------%
%2nd and 4th order Tensor Coefficients in 2-D
    %
    for m = 1:n
    current = theta.(fn{m});
    p = length(current);
    W.(fn{m}) = p;
```

```
172     N = N + p;
173     if isempty(current)
174         N2.(fn{m}) = zeros(2,2);
175         continue
176     end
177         for l = 1:p
178             if current(l) < 0
179                 current(l) = current(l) + pi;
180             else
181                 current(l) = current(l);
182             end
183         end
184     % Direction Cosines: 1st row w.r.t. x1 axis / 2nd row w.r.t. x2 axis
185     T = cos(current');
186     T = [T; sin(current')];
187         for i = 1:2
188             for j = 1:2
189                 % (1/p): vol avg based on "p" observations in a given plane
190                 N2.(fn{m})(i,j) = (1/p)*sum(T(i,:).*T(j,:)); %
191                 for k = 1:2
192                     for l = 1:2
193                         N4.(fn{m})(i,j,k,l) = (1/p)*sum(T(i,:).*T(j,:).*T(k,:).*T(l,:));
194                     end
195                 end
196             end
197         end
198     end
199
200 %_____________________________________________________________________%
201 function N2s = stretch(N2,ecc)
202 % Function applies distortion "a_i" to the axes of each 2-D plane. The
203 % "a_i" permit adjusting the coefficients to drive "ecc" toward equality
204
205 Q = (1/ecc)^(1/3);
206
207 A = [N2.xy(1,1) N2.xy(2,2) 0 0 0 0; 0 0 N2.yz(1,1) N2.yz(2,2) 0 0; ...
208     0 0 0 0 N2.xz(1,1) N2.xz(2,2); 1 -Q 0 0 0 0; 0 0 1 -Q 0 0; ...
209     0 0 0 0 -Q 1];
210 b = [1 1 1 0 0 0]';
211 a2 = A\b;
212 a = sqrt(a2);
213
214 % reassemble stretched 2-D tensor coefficients
215 N2s.xy = [N2.xy(1,1)*a(1)^2 N2.xy(1,2)*a(1)*a(2); N2.xy(2,1)*a(1)*a(2) N2.xy(2,2)*a(2)^2];
216 N2s.xz = [N2.xz(1,1)*a(5)^2 N2.xz(1,2)*a(5)*a(6); N2.xz(2,1)*a(5)*a(6) N2.xz(2,2)*a(6)^2];
217 N2s.yz = [N2.yz(1,1)*a(3)^2 N2.yz(1,2)*a(3)*a(4); N2.yz(2,1)*a(3)*a(4) N2.yz(2,2)*a(4)^2];
218
219 %_____________________________________________________________________%
220 function N3 = two2three(N2)
221 % Function assembles the 3-D tensor coefficients from three, orthogonal 2-D
222 % planes. The theory relies on the ratios of pricipal values and the
223 % function assumes that the 2-D planes not only form a basis, but are also
224 % principal planes
225 %_____________________________________________________________________%
226 % Ratios of 2-D principal values
227 Rxy = N2.xy(1,1)/N2.xy(2,2);
228 Rxz = N2.xz(1,1)/N2.xz(2,2);
229 Ryz = N2.yz(1,1)/N2.yz(2,2);
230
231 % Set up system of equations that estalishes the same ratios of principal
232 % values in 3-D and satisfies constraint that the trace of the tensor = 1
233 A = [1 -Rxy 0; 1 0 -Rxz; 0 1 -Ryz; 1 1 1];
234 b = [0 0 0 1]';
235 N3 = diag(A\b);
236 N3(1,2) = mean([N3(1,1)/N2.xy(1,1) N3(2,2)/N2.xy(2,2)])*N2.xy(1,2); N3(2,1) = N3(1,2);
237 N3(1,3) = mean([N3(1,1)/N2.xz(1,1) N3(3,3)/N2.xz(2,2)])*N2.xz(1,2); N3(3,1) = N3(1,3);
238 N3(2,3) = mean([N3(2,2)/N2.yz(1,1) N3(3,3)/N2.yz(2,2)])*N2.yz(1,2); N3(3,2) = N3(2,3);
239
240 %_____________________________________________________________________%
241 function N3 = two2threeideal(N2)
242 % Function assembles the 3-D tensor coefficients from three, orthogonal 2-D
243 % planes. The theory relies on the ratios of pricipal values and the
244 % function assumes that the 2-D planes not only form a basis, but are also
245 % principal planes
246 %_____________________________________________________________________%
247 % Ratios of 2-D principal values
248 Rxy = 1;
249 Rxz = N2.xz(1,1)/N2.xz(2,2);
250 Ryz = N2.yz(1,1)/N2.yz(2,2);
251 Rnz = mean([Rxz Ryz]);
252
253 % Set up system of equations that estalishes the same ratios of principal
254 % values in 3-D and satisfies constraint that the trace of the tensor = 1
255 A = [1 -Rxy 0; 1 0 -Rnz; 0 1 -Rnz; 1 1 1];
256 b = [0 0 0 1]';
257 N3 = diag(A\b);
258 N3(1,2) = mean([N3(1,1)/N2.xy(1,1) N3(2,2)/N2.xy(2,2)])*N2.xy(1,2); N3(2,1) = N3(1,2);
```

```
N3(1,3) = mean([N3(1,1)/N2.xz(1,1) N3(3,3)/N2.xz(2,2)])*N2.xz(1,2); N3(3,1) = N3(1,3);
N3(2,3) = mean([N3(2,2)/N2.yz(1,1) N3(3,3)/N2.yz(2,2)])*N2.yz(1,2); N3(3,2) = N3(2,3);

%EOF
```

E.1.8 MnDev.m

```
function [Dev2,Dev4] = MnDev(varargin)
%Mn_Dev.m
%This function computes the mean and deviatoric parts of the symmetric
%2nd and 4th rank contact tensors (arrays)
%INPUT:
%   N2 - symmetric, 2nd rank contact tensor
%   N4 - symmetric, 4th rank contact tensor
%OUTPUTS:
%   Mn - the scalar, mean value of input N2
%   Dev2 - the deviatoric part of N2, also a 2nd rank tensor (array)
%   Dev4 - the deviatoric part of N4, also a 4th rank tensor (array)

if length(varargin) ~= 4
    disp('Too many input arguments for function')
    Mn = []; Dev2 = []; Dev4 = [];
    return
end

N2 = varargin{1};
N4 = varargin{2};
fn = varargin{3};
n  = varargin{4};
dim = 2;
I = eye(dim); %define 2nd rank identity/kronecker tensor

for m = 1:n
% CALCULATE 2nd RANK MEAN
    mn = trace(N2.(fn{m}))/dim;
    Mn = trace(N2.(fn{m}));      %Density Distribution Mean is 1st invariant of N2
    % CALCULATE 2nd RANK DEVIATOR
    DevN = N2.(fn{m}) - mn*I;
    % CALCULATE 4th RANK DEVIATOR
    for i = 1:dim
        for j = 1:dim
            for k = 1:dim
                for l = 1:dim
                    K(i,j,k,l) = 1/3*(I(i,j)*I(k,l) + I(i,k)*I(j,l) +...
                        I(i,l)*I(j,k));
                    A(i,j,k,l) = 1/6*(I(i,j)*N2.(fn{m})(k,l) + I(k,l)*N2.(fn{m})(i,j) +...
                        I(i,k)*N2.(fn{m})(j,l) + I(i,l)*N2.(fn{m})(j,k) + I(j,k)*N2.(fn{m})(i,
                            l) +...
                        I(j,l)*N2.(fn{m})(i,k));
                end
            end
        end
    end

    if dim == 2
        Dev2.(fn{m}) = (dim^2)*DevN;
        Dev4.(fn{m}) = (dim^4)*(N4.(fn{m}) - A + 1/8*K);
    elseif dim == 3
        Dev2.(fn{m}) = 15/2*DevN;
        Dev4.(fn{m}) = 315/8*(N4.(fn{m}) - 6/7*A + 3/35*K);
    else
        disp('oops')
    end
end
end

%EOF
```

E.1.9 ConvgTest.m

```
function [zcrit,z2,z4] = ConvgTest(N,dim,D2,D4,alpha,fn,n)
%ConvgTest.m
%This function performs a hypothesis test to determine whether the higher
%rank tensors are required to more accurately describe the distribution
%density
%INPUT:
%   N - # of samples (contact normal vectors)
%   dim - 2 for 2-D problem
%   D2 - symmetric, 2nd order deviatoric tensor
%   D4 - symmetric, 4th order deviatoric tensor
%   alpha - user defined significance of hypothesis test
%   fn - field names of the three orthogonal planes: xy, xz, yz
%   n - dimension of problem, e.g., n = 3 for 3-D
%OUTPUTS:
%   zcrit - critical value
%   z2 - test statistic for 2nd rank tensor
%   z4 - test statistic for 4th rank tensor
%-------------------------------------------------------------------------%
% 1) Null Hypothesis: true distribution has anisotropy characterized by D2
% (or D4)
%-------------------------------------------------------------------------%
% 2) Alt Hypothesis: true distribution is uniform/isotropic --> D2 is not
% required (or D4 is not required)
%-------------------------------------------------------------------------%
%3) Calculate Test Statistic: liklihood ratio --> Prob that data come from
%uniform distro. / Prob that data come from a "D2" distro.
%-------------------------------------------------------------------------%

for m = 1:n
    z2.(fn{m}) = N.(fn{m})/(dim^2)*sum(sum(D2.(fn{m}).^2));
    z4.(fn{m}) = [];    %for now...
    %---------------------------------------------------------------------%
    %4) Look Up Critical Value: liklihood ratio behaves according to Chi-squre
    %---------------------------------------------------------------------%
    zcrit = chi2inv(1-alpha,2);
    %---------------------------------------------------------------------%
    %5) Compare test stat to crit value and repeat for 4th rank if necessary
    %---------------------------------------------------------------------%
    if z2.(fn{m}) <= zcrit
%         disp('D2 and D4 not required')
        continue
    elseif z2.(fn{m}) > zcrit
        disp(['  D2 required - ' num2str(fn{m})])
        z4.(fn{m}) = N.(fn{m})/(dim^4)*sum(sum(sum(sum(D4.(fn{m}).^2))));
        if z4.(fn{m}) <= zcrit
%             disp('D4 not required')
        elseif z4.(fn{m}) > zcrit
            disp(['  D4 required - ' num2str(fn{m})])
        end
    end
end
end

%EOF
```

E.1.10 SwissKFunc.m

```
function  SwissKFunc(C,LUnc,UUnc,r_R_rat,N3,sample,phii)

% File to reproduce Schneebeli's thermal conductivity results
load Swiss_EHC_HDS_4_6

%Reconstruct Ice Network Thermal Conductivity
% INPUTS
rhos = 490;     %snow density - kg/m^3
b_g_rat = 0.15;  %bond/grain ratio

% Define crystal properties
rg = .1;       %arbitrary grain radius - mm
gvol = 4/3*pi*rg^3; %grain vol
rb = b_g_rat*rg; %bond radius - mm

% Define material properties
T = 265;         %absolute temperature - K
rhoi = 920;      %ice density - kg/m^3
ki = 651/T;       %ice thermal conductivity - W/m*K
```

```
%above empirical relationship from Petrenko, eqn (3.11), p43
ka = 23e-3;     %air thermal conductivity - W/m*K

% Intermediates
alpha = ki/ka;  %ratio of constituent thermal conductivities
beta = alpha*b_g_rat;  %non-dim quantity used by Batchelor
phii = mean(phii); %rhos/rhoi;  %vol fraction of ice
phia = 1-phii;  %vol fraction of air = porosity
N = 3.565 - 7.435*phii + 24.825*(phii^2); %estimate of coordination number
nc = 1*phii/gvol;   %# of cells in unit sample vol
ncL = nc^(1/3); %# of cells in length of sample cube
ncA = ncL^2;    %avg # of cells in x-sect of sample cube

% Adams & Sato (1993) effective ice network thermal conductivity
kn = pi^2*rb*ki*N*ncA/32/ncL;

%Batchelor (1977) analytical eqn
if beta >= 1
    H = 2*beta/pi;
else
    H = 0.2*beta^2;
end
kstar = 0.5*phii*N*ka*H;

b_g_rat = r_R_rat;
kstr1 = phii*N3.*ki.*b_g_rat/pi;

%Data from Martin's paper
HDS4_k_3 = HDS(:,2);
HDS6_k_3 = HDS(:,3);
t = HDS(:,1);
idx1 = 1:1:length(t);   %Index data if desired

%Use fabric coefficient and construct keff data for HDS4
C_11 = squeeze(C(1,1,:));
C_22 = squeeze(C(2,2,:));
C_33 = squeeze(C(3,3,:));
LUnc_11 = squeeze(LUnc(1,1,:));
UUnc_11 = squeeze(UUnc(1,1,:));
LUnc_22 = squeeze(LUnc(2,2,:));
UUnc_22 = squeeze(UUnc(2,2,:));
LUnc_33 = squeeze(LUnc(3,3,:));
UUnc_33 = squeeze(UUnc(3,3,:));
k_f1 = 3*kstr1.*C_11';
k_f2 = 3*kstr1.*C_22';
k_f3 = 3*kstr1.*C_33';
LE_1 = 3*kstr1.*LUnc_11';
UE_1 = 3*kstr1.*UUnc_11';
LE_2 = 3*kstr1.*LUnc_22';
UE_2 = 3*kstr1.*UUnc_22';
LE_3 = 3*kstr1.*LUnc_33';
UE_3 = 3*kstr1.*UUnc_33';

%Plot indices
idx2 = 48:96:length(t);
idx3 = idx2(1:length(C_33));
% idx4 = idx2(1:length(C6_33));

%Plots
if sample == 4
    y1 = HDS4_k_3(idx1);
    ttl = 'Sample 4 - 100 K/m';
elseif sample ==6
    y1 = HDS6_k_3(idx1);
    ttl = 'Sample 6 - 50 K/m';
else
    disp('oops')
end

figure
plot(t(idx1),y1,'k.'); hold on
errorbar(t(idx3),k_f3,k_f3-LE_3,UE_3-k_f3,'bo','MarkerSize',4)
% plot(t(idx1),fk33,'g-.',t(idx3),fkf,'r-.')
axis([0 8 .3 0.8])
yl = ylabel('\bf{k}\rm{^\ast component in \it{x}\rm{_1} direction (W/m\cdotK)}','interpreter',
    'tex'); grid
xl = xlabel('Days from Experiment Start','interpreter','tex');
legend('Derived EHC','Modeled \bf{k}\rm{^\ast Tensor Component}','Location','NorthWest')
set([yl xl],'FontName','Times New Roman','FontSize',11)
set(gca,'FontName','Times New Roman','FontSize',11)
% title(ttl)

figure
errorbar(t(idx3),k_f3,k_f3-LE_3,UE_3-k_f3,'bo','MarkerSize',4); hold on
errorbar(t(idx3),k_f1,k_f1-LE_1,UE_1-k_f1,'rs','MarkerSize',4);
errorbar(t(idx3),k_f2,k_f2-LE_2,UE_2-k_f2,'gdiamond','MarkerSize',5);
axis([0 8 .3 0.8])
```

```
yl = ylabel('\bf{k}\rm{^\ast diagonal components (W/m\cdotK)}','interpreter','tex'); grid
xl = xlabel('Days from Experiment Start','interpreter','tex');
legend('\it{x}\rm{_1}','\it{x}\rm{_2}','\it{x}\rm{_3}','Location','NorthWest')
set([yl xl],'FontName','Times New Roman','FontSize',11)
set(gca,'FontName','Times New Roman','FontSize',11)
% title(ttl)

figure
plot(t(idx1),y1,'k.'); hold on
plot(t(idx3),kstr1,'bo','MarkerSize',4)
axis([0 8 .3 .8])
yl = ylabel('\it{k}\rm{^\ast in \it{x}\rm{_1} direction (W/m\cdotK)}','interpreter','tex');
     grid
xl = xlabel('Days from Experiment Start','interpreter','tex');
legend('Derived EHC','Modeled Scalar \it{k}\rm{^\ast}','Location','NorthWest')
set([yl xl],'FontName','Times New Roman','FontSize',11)
set(gca,'FontName','Times New Roman','FontSize',11)

%EOF
```